Dissertation zur Erlangung des Doktorgrades

der Fakultät für Chemie und Pharmazie

der Ludwig-Maximilians-Universität München

Chemical Modifications of Covalent Organic Frameworks for Tunable Optoelectronic Properties, Surface Chemistry, and Photocatalytic Performance

Klaudija Paliušytė

aus

Palanga, Litauen

2025

Erklärung

Diese Dissertation wurde im Sinne von § 7 der Promotionsordnung vom 28. November 2011 von Herrn Professor Dr. Thomas Bein betreut.

Eidesstattliche Versicherung

Diese Dissertation wurde eigenständig und ohne unerlaubte Hilfe bearbeitet.

München, 18.12.2025

Klaudija Paliušytė

Dissertation eingereicht am	18.12.2025
1. Gutachter:	Prof. Dr. Thomas Bein
2. Gutachter:	Prof. Dr. Achim Hartschuh
Mündliche Prüfung am	23.02.2026

Abstract

Covalent organic frameworks (COFs) are crystalline, porous polymers constructed from organic building blocks linked by covalent bonds, providing remarkable stability, low density, and tunable porosity. Initially introduced in 2005 by Yaghi and colleagues, COFs merge structural accuracy with chemical adaptability, allowing for the customization of pore dimensions, shapes, and electronic characteristics for uses in gas storage, catalysis, sensing, separation, and drug delivery. A range of bonding chemistries, including boronate esters, imines, β-ketoenamines, hydrazones, polyimides, amides, and triazines, permit meticulous control over stability and functionality, while synthetic techniques such as solvothermal, microwave-assisted, ionothermal, and mechanochemical methods enhance their availability. Among these, imine-linked COFs, formed via Schiff base condensation, continue to attract significant attention due to their structural flexibility and straightforward synthesis.

Promising strategies to tailor the structure, properties, and performance of COFs include pre-synthetic, post-synthetic and hybrid modifications. Pre-synthetic modification involves altering the monomers or adjusting reaction conditions prior to framework formation, enabling control over topology, porosity, and stability. Post-synthetic modification enables the incorporation of new chemical functionalities into pre-formed COFs, offering access to features that are difficult or impossible to achieve through direct synthesis. Hybrid modifications involve one-pot approaches in which guest components are incorporated into the COF structure during synthesis, enabling simultaneous tuning of framework composition and functionality. This thesis presents a balanced investigation of pre-synthetic, post-synthetic and hybrid modification strategies. The first part of the thesis (Chapters 3 and 4) investigates the pre-synthetic functionalization of N,N,N′,N′-tetraphenyl-1,4-phenylen (Wurster, W)-anthracene(A)-based COFs, denoted as W-A-X (X = H, Cl, Br, I). The second part (Chapters 5) explores post-synthetic modifications of a thiophene-based COF, constructed from benzo[1,2- b:4,5-b′]-dithiophene-2,6-dicarboxaldehyde (BDT) and 4-fold amine functionalized tetraphenylethylene (1,1′,2,2′-tetra-p-aminophenylethylene) (ETTA), referred to as BDT-ETTA, aimed at enhancing its catalytic performance. The third part (Chapter 6) explores hybrid modification of the BDT-ETTA COF, aimed at controlling its charge- and energy-transfer behavior.

Following this conceptual line of research, Chapter 3 focuses on the effect of pre-synthetic single-atom functionalization of W-A-X COFs. Anthracene is an electron-rich building block with versatile photophysical characteristics, making it an ideal candidate for the construction of optoelectronically active COFs. Introducing a single substituent at the 2-position of the anthracene core prior to framework formation yielded a series of highly crystalline COFs, enabling systematic investigations of how subtle chemical modifications influence crystallinity, domain size, and optoelectronic behavior. Comprehensive experimental characterization, complemented by theoretical modeling, revealed clear correlations between substituent identity, framework morphology, and optical response, demonstrating the potential of pre-synthetic single-atom modification as a strategy for tuning COF properties. These findings provide a fundamental understanding of structure-property relationships in functional COFs and offer a platform for their rational design toward applications in optoelectronics and photocatalysis.

Chapter 4 builds on the previous work and examines how pre-synthetic halogen functionalization affects host-guest interactions in W-A-X COFs. Single-atom modifications on the peripheral anthracene rings allow subtle control over structural features and local electrostatics, influencing CO_2 adsorption behavior. Experimental CO_2 sorption measurements showed that all halogen-functionalized COFs exhibit significantly higher CO_2 uptake and increased isosteric heats of adsorption compared to the non-functionalized W-A-H COF. Computational modeling identified two main adsorption regions: the imine linkage and the trigonal pores between anthracene units. Halogenation reduces nitrogen basicity and porosity but introduces σ-hole regions that enhance CO_2 binding, with interaction strength increasing in the order I > Br > Cl. The combination of favorable electronic interactions and framework crystallinity results in W-A-Br achieving the highest CO_2 uptake. These findings highlight how single-atom pre-synthetic functionalization can tailor electrostatics over the polymeric network, fine-tune adsorption sites and optimize COFs for host-guest interactions.

Chapter 5 presents a post-synthetic modification strategy of the COF in which linkage conversion is employed to tune the interfacial and photocatalytic properties of the (BDT-ETTA). Conversion of imine to amide linkages alters the COF surface charge due to their distinct protonation behaviors, as confirmed by zeta potential measurements, which in turn directs in-situ Pt photodeposition. The imine-linked COF yields uniformly small Pt

nanoparticles, while the amide-linked COF forms larger Pt particles and acts as an electron-transport antenna, enhancing charge separation, proton adsorption, and overall hydrogen evolution, achieving a 300 % increase in photocatalytic activity compared to the imine form.

Section 5.6 in this chapter describes complementary mechanistic studies on Pt photodeposition in the imine-based COF BDT-ETTA. Transmission electron microscopy images confirm the homogeneous distribution of Pt particles within the polymeric matrix and reveal that the deposited particles replicate the COF structure, evidencing their incorporation into the COF pores. Experimental observations suggest that Pt formation within the COF pores is a multistep process requiring both photoexcitation and a sacrificial electron donor, with sulfur atoms in the BDT unit serving as active sites for hole trapping and oxidation, and the imine bonds coordinating and reducing the Pt precursor. Although these studies were preliminary, they provided valuable mechanistic insight and informed the subsequent investigation of linkage conversion as a strategy to modulate COF photocatalytic behavior. These results highlight that post-synthetic modulation of surface charge and a mechanistic understanding of active sites together offer a powerful approach to control interfacial processes and expand the functional versatility of COFs in photocatalysis.

Finally, Chapter 6 explores a hybrid modification strategy of the BDT-ETTA COF, focusing on doping with carbon dots (CDs). Microwave-derived, photoluminescent, metal-free CDs were incorporated into the COF in a one-pot synthesis, enabling precise control over the COF:CDs ratio. Structural and optoelectronic characterization revealed that the CD loading governs the interaction mechanism between the two components. At low loadings (up to 20 wt%), strong interfacial contact promotes charge transfer, evident from photoluminescence quenching of both COF and CDs and accelerated exciton decay kinetics. At higher loadings (30 wt% and above), reduced contact favors Förster resonance energy transfer from CDs to COF, enhancing COF photoluminescence. The study shows how controlled incorporation of CDs allows tuning of charge- and energy-transfer pathways. These findings provide fundamental insights into structure-property relationships in the BDT-ETTA COF/CDs composites, informing the design of multifunctional materials for photocatalysis, optoelectronics, and sensing.

In conclusion, this thesis has been focused on the functionalization strategies of imine-linked COFs employing pre-synthetic, post-synthetic and hybrid modification strategies to tailor structural, optoelectronic, and interfacial properties for enhanced gas sorption and photocatalysis. Single-atom halogenation, linkage conversion, Pt and carbon dot incorporation were employed to systematically investigate and control local electrostatics, adsorption behavior, photodeposition mechanisms, and charge- and energy-transfer pathways. These studies provide fundamental insights into structure-property relationships in COFs and demonstrate versatile strategies for tuning their functionality, highlighting their potential for applications in gas capture, photocatalysis, and optoelectronic applications.

Table of contents

1. Introduction 1
1.1. Metal-organic frameworks (MOFs) 1
1.1.1. Discovery and development 1
1.1.2. Synthesis methods 3
1.2. Covalent organic frameworks (COFs) 6
1.2.1. Linkage types 7
1.2.2. Different topologies 11
1.3. From molecule to material: aligning building blocks with function 12
1.3.1. Anthracene - a multifunctional building block 14
1.3.2. Incorporation of anthracene into COF architectures 15
1.4. Pre-synthetic modifications 17
1.4.1. Halogen functionalized COFs: Effects on functional performance 18
1.4.2. Electronegativity vs. atomic size 19
1.5. Post-synthetic modifications 22
1.5.1. Linkage conversion 22
1.5.2. Nobel metal incorporation 23
1.6. Hybrid modifications 25
1.6.1. Carbon dots (CDs) 26
1.6.2. Synthesis methods 26
1.6.3. CDs doped-COFs for functional applications 28
1.7. Photocatalytic hydrogen evolution reaction (HER) 29
1.7.1. COFs as photocatalysts for HER 30
1.7.2. Progress in COF-based photocatalysis 34
1.8. Motivation 38
1.9. References 39
2. Characterization techniques 53
2.1. Powder X-ray diffraction (PXRD) 53
2.2. Gas sorption 55
2.3. Thermogravimetric analysis (TGA) 60

2.4. Scanning electron microscopy (SEM) 60
2.5. Transmission electron microscopy (TEM) 63
2.6. Infrared spectroscopy (IR) 64
2.7. Ultraviolet-visible spectroscopy (UV-Vis) 65
2.8. Photoluminescence spectroscopy (PL) 67
2.9. Time-correlated single-photon counting (TCSPC) 69
2.10. Zeta potential 70
2.11. X-ray photoelectron spectroscopy (XPS) 72
2.12. Cyclic voltammetry (CV) 73
2.13. Gas chromatography (GC) 75
2.14. Nuclear magnetic resonance spectroscopy (NMR) 75
2.15. Elemental analysis 77
2.16. Mass spectrometry (MS) 77
2.17. References 78
3. Pre-synthetic modification of Wurster-Anthracene COF: tuning the structural and optoelectronic properties 82
3.1. Abstract 82
3.2. Introduction 83
3.3. Results and discussion 85
3.4. Conclusion 97
3.5. References 98
3.6. Appendix 103
3.6.1. Experimental section 103
3.6.2. Linker synthesis 107
3.6.3. COF synthesis 128
3.6.4. Structural analysis 132
3.6.5. Simulations of different halogen positions 152
3.6.6. TEM images 153
3.6.7. ESP calculations 154
3.6.8. SEM images 155
3.6.9. Sorption and porosity parameters 156

3.6.10. FT-IR analysis of COFs 158
3.6.11. Solid-state ^{13}C NMR of COFs 158
3.6.12. TGA analysis 159
3.6.13. Experimental optical properties 159
3.6.14. Calculated optical properties 161
3.6.15. References 162
4. Pre-synthetic modification of Wurster-Anthracene COF: tuning the intermolecular interactions 165
4.1. Abstract 165
4.2. Introduction 166
4.3. Results and discussion 168
4.3.1. CO_2 adsorption in Wurster-Anthracene-Based COFs 170
4.3.2. DFT modeling on CO_2 interaction with molecular fragments 172
4.3.3. DFT modeling of CO_2 interaction with extended COF structure 175
4.4. Conclusions 180
4.5. References 180
4.6. Appendix 185
4.6.1. Experimental section 185
4.6.2. Syntheses of halogenated anthracene building blocks 188
4.6.3. Syntheses of COFs 194
4.6.4. BET surface areas 195
4.6.5. Isosteric heat calculations 196
4.6.6. ESP of 2-X-anthracene (X = H, Cl, Br, I) 198
4.6.7. Representative conformers for W-A-X-CO_2 complexes 200
4.6.8. Proton affinity studies for the imine bonds in adsorption units of W-A-X 206
4.6.9. ESP of adsorption units of W-A-X 208
4.6.10. Visualization of iso-surface, non-covalent interactions and atom-wise contributions for adsorption units of W-A-X 209
4.6.11. Comparative energetic properties of the triangle unit of W-A-X and CO_2 in different adsorption sites 211
4.6.12. References 212

5. Post-synthetic modification of BDT-ETTA-COF: Linkage conversion 214
5.1. Abstract 214
5.2. Introduction 215
5.3. Results and discussion 216
5.3.1. Structural and morphological characterization 216
5.3.2. Photocatalytic hydrogen evolution 222
5.3.3. Physical characterization 223
5.3.4. Interfacial characterization 225
5.3.5. Post-Characterization and Proposed Reaction Mechanism 230
5.4. Conclusions 233
5.5. References 233
5.6. Appendix A 239
5.6.1. Initial idea and hypotheses 240
5.6.2. Platinum photodeposition 240
5.6.3. Results and investigation 240
5.6.4. References 247
5.7. Appendix B 250
5.7.1. Materials and Methods 250
5.7.2. Synthetic procedures 254
5.7.3. Structural analysis 257
5.7.4. References 275
6. Hydrid modification of BDT-ETTA-COF: Carbon Dots doping 276
6.1. Abstract 276
6.2. Introduction 277
6.3. Methods 279
6.3.1. Synthesis of CDs 279
6.3.2. Synthesis of BDT-ETTA COF and COF/CDs composite 279
6.3.3. PXRD 280
6.3.4. Physisorption 280
6.3.5. UV-vis spectroscopy 281
6.3.6. Steady-state and time-resolved photoluminescence measurements 281

6.3.7. Cyclic Voltammetry 281
6.4. Results 281
6.5. Discussion 291
6.6. Conclusions 294
6.7. References 295
6.8. Appendix 298
6.8.1. Photoluminescence (PL) anisotropy approach to estimate the CDs particle size 299
6.8.2. Electrochemical characterization 305
6.8.3. References 306
7. Conclusion and outlook 307
8. Appendix 311
8.1. Publications 311
8.2. Conference Contributions 312

List of abbreviations

2D	two-dimensional
ADCH	Atomic Dipole
AIM	Atoms in Molecules
APT	Atomic Polar Tensor
BDT	Benzodithiophene
BET	Brunauer Emmet Teller
BPEI	Branched Polyethylenimine
CA	Citric acid
CDs	Carbon Dots
CCD	Charge Coupled Device
CHELPG	Charges from Electrostatic Potentials using a Grid-based method
CLSM	Confocal Laser Scanning Microscope
COF	Covalent Organic Framework
CPMAS	^{13}C Cross-Polatization Magic Angle Spinning
CREST	Conformer-Rotamer Ensemble Sampling Tool
CT	Charge Transfer
CV	Cyclic Voltammetry
DFT	Density Functional Theory
DMF	Dimethylformamide
DMSO	Dimethyl sulfoxide
EtOH	Ethanol
ESP	Electrostatic Potential
FRET	Förster Resonance Energy Transfer
FWHM	Full Width at Half Maximum
GC	Gas Chromatography
GFN2	Geometry Frequency Noncovalent version 2
Gnuplot	Graphical Utility for Plotting Data
equiv.	quivalents
H_2A	Ascorbic Acid

H2O	Water
HER	Hydrogen Evolution Reaction
IR	Infrared Spectroscopy
ITO	Indium Tin Oxide
LABVIEW	Laboratory Virtual Instrument Engineering Workbench
MK	Merz Kollmann
MOF	Metal Organic Framework
Multiwfn	Multifunctional Wavefunction Analyzer
MS	Mass Spectroscopy
MeOH	Methanol
NCV	Non-Covalent
NLDFT Non	Local Density Functional Theory
NMR	Nuclear Magnetic Resonance
NPA	Natural Population Analysis
N_2	Nitrogen
PAW	Projector Augmented Wave
PL	Photoluminescence
Pt	Platinum
PMAC	Photomultiplier Assembly Controller
ppm	parts per million
PXRD	Powder X-ray Diffraction
QSDFT	Quenched Solid Density Functional Theory
SED	Sacrificial Electron Donor
SEM	Scanning Electron Microscopy
STEM	Scanning Transmission Electron Microscopy
TCSPC	Time Correlated Single Photon Counting
TD-DFT	Time-Dependent Density Functional Theory
TEOA	Triethanolamine
TEM	Transmission electron microscopy
TGA	Thermogravimetric analysis
THF	Tetrahydrofuran

UV-vis	Ultraviolet-visible
VASP	Vienna Ab Initio Simulation Package
vdW	van der Waals
VMD	Visual Molecular Dynamics
XPS	X-ray Photoelectron Spectroscopy

1. Introduction

Porous substances have become essential in contemporary life. Zeolites are a class of crystalline microporous materials known for their unique structural properties, which include a high surface area, uniform porosity, and interconnected pore systems. They are highly versatile and widely applied today, whether in the petrochemical sector for hydrocarbon separation, for catalyzing chemical reactions, or in household applications as ion exchangers for water softening.[1,2] In addition to zeolites, other highly porous materials such as aerogels, made from silica or metal oxides, along with porous carbons, are utilized as adsorbents, catalysts, thermal insulators, or for energy storage.[3] The extensive array of potential uses and their commercial viability have also inspired research into novel nanoporous material classes, including porous organic polymers, metal-polymer hybrid materials, and porous liquids. Of notable interest are materials that demonstrate a high degree of order, allowing for large surface areas and accurately defined pore sizes. By integrating organic components into the porous structure of these materials, a broad spectrum of physical and chemical properties can be achieved.[4] In the following sections, two such classes of materials - metal-organic frameworks and covalent organic frameworks - are discussed.

1.1. Metal-organic frameworks (MOFs)

Metal-organic frameworks (MOFs) are a class of crystalline porous substances formed by metal ions or clusters linked with organic ligands, resulting in extended one-, two-, or three-dimensional structures. Their architecture consists of metal nodes connected by organic linkers, allowing precise control over properties such as porosity, surface area, and chemical stability. Unique characteristics like high tunability, structural diversity, and exceptionally high surface areas make MOFs promising candidates for various applications, including gas storage, separation, catalysis, and sensing.[5]

1.1.1. Discovery and development

The first notable metal-organic frameworks (MOFs), HKUST-1[6] and MOF-5[7] were reported in 1999, defining a benchmark in the field of MOF chemistry. In HKUST-1, copper

paddlewheel secondary building units are linked through 1,3,5-benzenetricarboxylate (BTC) to create three-dimensional porous cubic structures (**Figure 1.1**). In contrast, MOF-5, with the chemical formula $Zn_4O(BDC)_3 \cdot (DMF)_8(C_6H_5Cl)$, where BDC refers to terephthalic acid and DMF denotes dimethylformamide, is made up of Zn_4O clusters connected by ditopic linear BDC linkers (**Figure 1.2**).

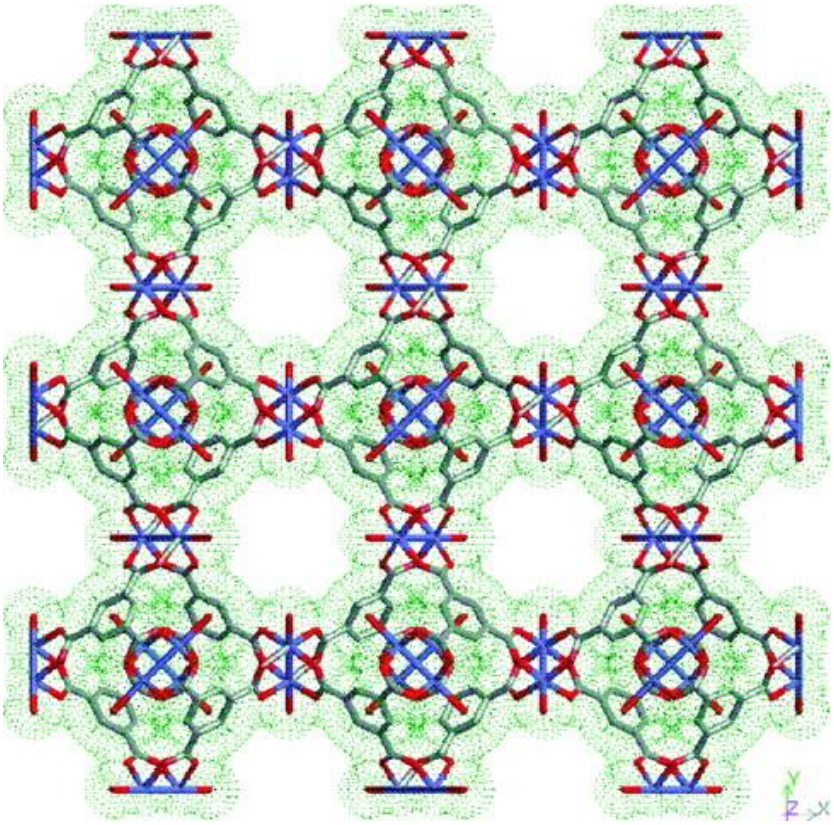

Figure 1.1. Structure of HKUST-1 - $[Cu_3(TMA)_2(H_2O)_3]_n$ polymer framework viewed down the [100] direction, showing nanochannels with fourfold symmetry. Reprinted with permission from Chui *et al* [6]. Copyright 1999 American Association for the Advancement of Science.

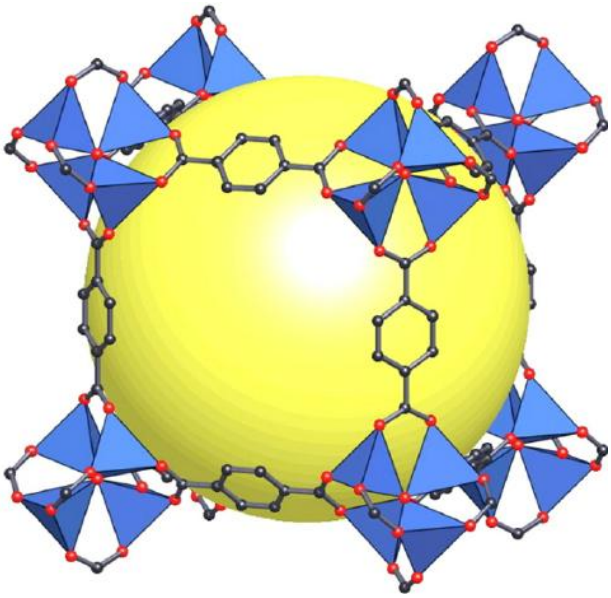

Figure 1.2. Structure of MOF-5 shown as Zn_4O tetrahedra (blue polyhedra) joined by benzene dicarboxylate linkers (O: red and C: black) to give an extended 3D cubic framework. Reprinted with permission from Kaye *et al.*[8] Copyright 2007 American Chemical Society.

These substances demonstrate significant porosity and surface areas, offering potential uses in gas separation, storage, catalysis, sensing, and drug delivery. The advancement of MOFs has been greatly shaped by Yaghi's contributions, which established the groundwork for the discipline of reticular chemistry and the modular construction approach in the development of novel porous materials. In recognition of their pioneering work, Omar M. Yaghi, Susumu Kitagawa, and Richard Robson were awarded the Nobel Prize in Chemistry in 2025.

1.1.2. Synthesis methods

The synthesis of MOFs has progressed remarkably, with numerous innovative techniques being introduced to improve their scalability, eco-friendliness, and usability. Each method presents distinct benefits and obstacles, adding to the varied field of MOF production. The main synthesis methods are discussed below.

- **Solvothermal synthesis.** This method involves reacting metal ions with organic linkers in a solvent under elevated temperatures and pressures to form crystalline MOFs. It is highly versatile, offering control over particle size and morphology by adjusting reaction conditions. However, it typically requires long reaction times and may involve toxic solvents.[9]

- **Ionothermal synthesis.** This synthesis utilizes ionic liquids instead of organic solvents. Ionic liquids act as catalysts, charge-balancing agents, and templates, facilitating the introduction of ions into the cavities of the MOF, maintaining ionic charge balance, and guiding the structure of the framework, which includes the creation of homochiral MOFs featuring particular chiral anions. The usage of ionic liquids provides a wide temperature range and structural directing roles, enabling the formation of novel MOF structures with unique properties. However, the method may be limited by the availability and cost of suitable ionic liquids, and the potential complexity in recovering and recycling these liquids after synthesis.[10]

- **Electrochemical synthesis.** To synthesize MOFs on the desired substrates, various electrochemical techniques can be employed:[11]

  - **Anodic dissolution.** The dissolution of a metal anode in an electrolyte solution containing organic linkers. The metal ions released from the anode react with the organic linkers to form MOFs.[12]

  - **Reductive electrosynthesis.** Metal ions are reduced at the cathode in the presence of organic linkers, leading to the formation of MOFs.[13]

  - **Electrophoretic deposition**. This process involves the movement of charged particles (metal ions and organic linkers) under an electric field towards an electrode, where they deposit and form MOFs.[14]

  - **Galvanic displacement.** In galvanic displacement, an active metal (e.g., copper) contacts a solution containing more noble metal ions (e.g., silver). The difference in reduction potentials drives the reduction and deposition of the noble metal, while the active metal is oxidized and supplies electrons for the cathodic reaction. Unlike electrodeposition, no external voltage or current is needed. The released metal ions can also serve as metal sources for MOF synthesis.[15,16]

  The key advantages of electrochemical synthesis include significantly shorter synthesis times, precise control over the properties of the resulting MOFs (such as

thickness and morphology through adjustment of current and voltage), and mild reaction conditions, which are particularly beneficial for preserving the functionality of sensitive components. The challenges in electrochemical synthesis of MOFs include anode erosion, electrolyte issues affecting MOF structure, limited metal selection for anodes, and difficulties in maintaining control over synthesis at high current densities.[11]

- **Mechanochemical synthesis.** Mechanochemical synthesis involves grinding the reactants together, without any or just a minimal presence of a small amount of solvent, thus promoting the formation of MOFs. This method allows using MOF precursors with low solubility and is fast and cost-efficient. However, its main limitation is scalability, as it is typically a low-throughput, batch process.[17,18]

- **Microwave-assisted synthesis.** This method used uses electromagnetic waves to rapidly and directly heat reactants, enabling fast and efficient MOF crystallization. It offers shorter reaction times, higher yields, smaller particle sizes, and better control over crystal quality compared to conventional heating. Microwave synthesis is also useful for defect engineering and gram-scale production. However, it can face challenges with reproducibility, limited scalability, and requires specialized equipment.[17,19,20]

Due to their diverse synthesis methods and promising properties, such as high crystallinity and large surface area, MOFs have already been widely applied in various fields, including pollution remediation,[21,22] gas storage,[23,24] and sensing[25,26]. One major issue in the area of MOFs is the difficulty of ensuring chemical stability, especially in severe environments like acidic, basic, and aqueous environments,[27,28] which can sometimes limit their real-world applications. Ongoing research and the development of novel approaches to improve MOF stability show promise and have already resulted in the synthesis of MOFs that exhibit enhanced resistance to severe conditions.[29–31]

1.2. Covalent organic frameworks (COFs)

Covalent organic frameworks (COFs) are a class of crystalline porous materials that are constructed from organic building blocks linked by covalent bonds. Initially introduced by Yaghi *et al*. in 2005,[32] COFs represented a significant advancement in the creation of crystalline cross-linked polymers. Yaghi and co-workers successfully achieved the synthesis of COF-1 and COF-5 through the reaction of phenyl diboronic acid with itself or with hexahydroxytriphenylene, thus addressing a persistent challenge within the realm of polymer chemistry (see **Figure 1.3**).

COFs possess a wide range of valuable characteristics, including:

- **Stability**. Thanks to their covalent bonding, COFs can demonstrate significantly greater thermal and chemical stability compared to the metal-ligand coordination bonds found in MOFs.[33]

- **High surface area and porosity**. The large internal surface area and porosity of COFs offer abundant space for interactions with guest molecules. This makes them especially effective for applications such as gas storage, catalysis, and drug delivery, where surface interactions are crucial.[34,35]

- **Low density**. Composed primarily of light elements such as carbon, nitrogen, hydrogen, and sulfur, COFs are inherently low in density. This feature, along with the absence of metal ions, can enhance their biocompatibility and reduce toxicity, making them potential candidates for biomedical applications like drug delivery and cancer therapy.[36]

- **High crystallinity**. The well-ordered, crystalline structure of COFs supports applications that rely on precise molecular alignment, such as sensing, optoelectronics, catalysis and separation technologies.[33]

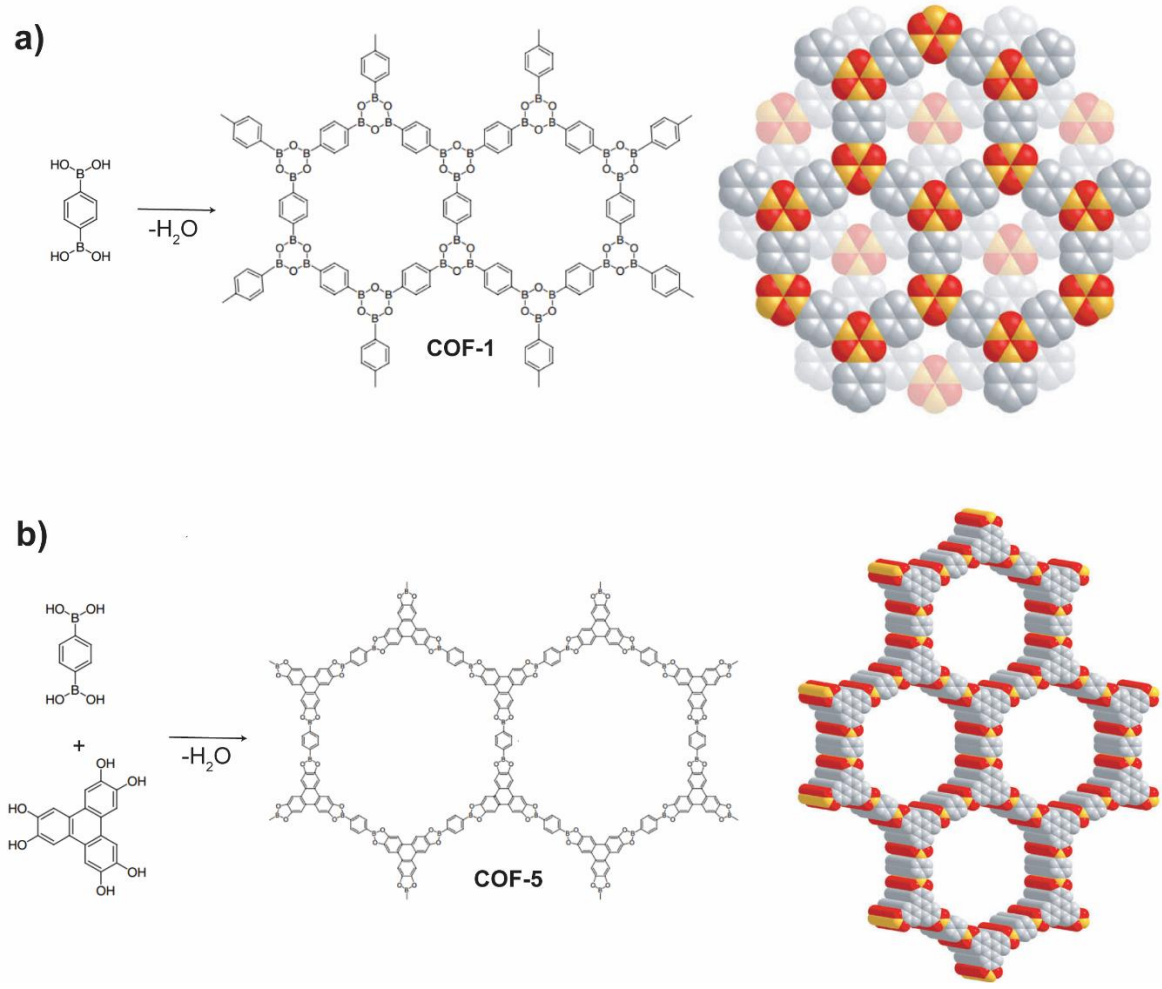

Figure 1.3. Condensation reactions of boronic acids used to produce (a) COF-1 and (b) COF-5. Adapted with permission from Côté *et al.*[32] Copyright 2005 American Association for the Advancement of Science.

1.2.1. Linkage types

COFs can be connected through various linkage types, which affect their structural and functional characteristics. The selection of linkages in COFs is a key element that influences their photophysical properties, catalytic performance, electronic configurations, and overall durability. This variety in linkage chemistry enables the creation of COFs with customized functionalities suitable for a range of applications.[37]

Many widely used linkages of COFs are presented in **Table 1.1**. The majority of them, such as boroxine, boronate, imide, imine, alkene, hydrazone, ketoenamine, and triazine, are typically obtained through direct and (slightly) reversible synthetic routes from monomers. In addition, a

few linkage types (such as amine, amide, and thiazole) can be formed via indirect synthetic routes, that is, through linkage conversion processes of pre-synthesized imine linkages, usually involving irreversible reactions. Specifically, the imine-to-amide linkage conversion is discussed in detail in Section 0.

Table 1.1. Different types of COF linkages and their common synthetic routes.

Linkage type	Reaction conditions
Boroxine, boronate (B-O) 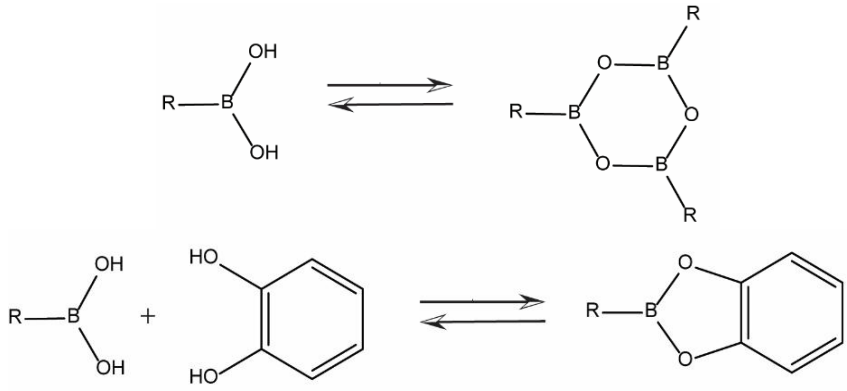	Self-condensation of boronic acids to produce boroxine rings, or via the co-condensation of boronic acids with catechols to yield boronate ester linkages.[32]
Polyimide (C-N) 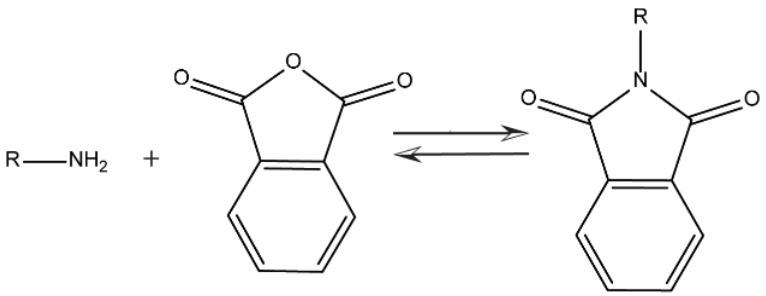	Condensation between acid anhydrides and amino groups.[38]
Imine (C=N) 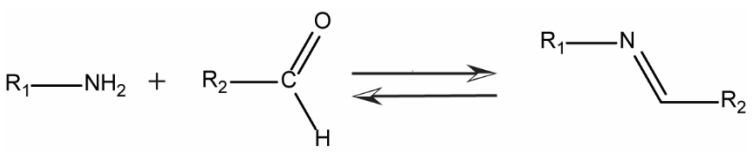	Schiff base condensation between amines and aldehydes.[39]

Alkene (C=C) 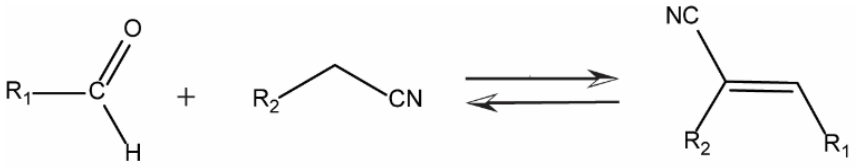	Knoevenagel condensation between aldehyde-substituted monomer and cyano-containing compound.[40]
Hydrazine (C=N) 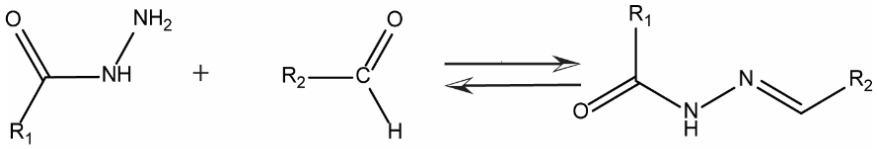	Condensation of hydrazine with carbonyl-containing compounds such as aldehydes or ketones.[41]
Ketonenamine (C-N) 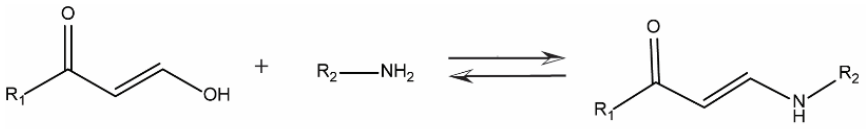	Schiff base condensation between amines and carbonyl compounds. The resulting imine linkages then undergo irreversible enol-to-keto tautomerization, leading to a stable β-ketoenamine structure.[42]
Triazine (C=N) 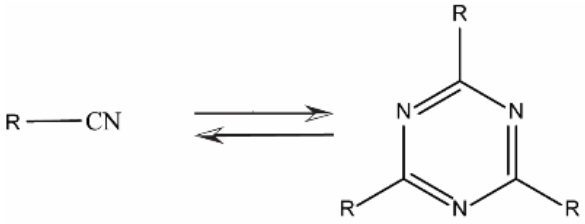	Cyclotrimerization of cyano-containing monomers.[43]

Amine (C-N) 	Linkage conversion from pre-synthesized imine linkage to amine linkage using formic acid.[44]
Amide (C-N) 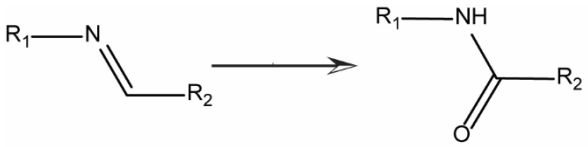	Linkage conversion from pre-synthesized imine linkage to amide linkage using suitable oxidizing agents.[45–49]
Thiazole (C-S) 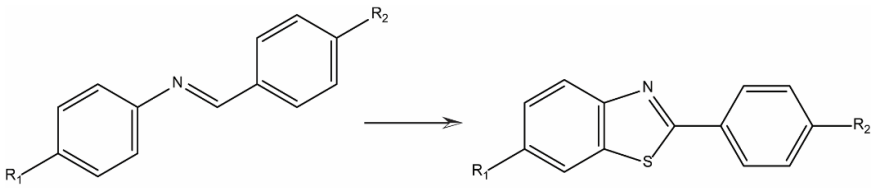	Linkage conversion from pre-synthesized imine linkage to amide linkage using elemental sulfur.[50]

COFs can typically be synthesized employing methodologies analogous to those utilized for MOFs, including solvothermal,[51] microwave-assisted,[52,53] ionothermal,[54,55] and mechanochemical[56,57] techniques. Of all the techniques, the solvothermal strategy is still the most frequently used method for the formation of imine-based COFs, which are the main focus of this thesis. Generally, these reactions occur via a Schiff base condensation, conducted in designated organic solvents accompanied by acetic acid, which functions as a Brønsted acid catalyst. The role of acetic acid is crucial, as it donates a proton to the carbonyl group of the aldehyde, increasing its electrophilicity and facilitates the nucleophilic attack by the amine.[58]

This nucleophilic attack initiates the Schiff base reaction (**Figure 1.4**), which proceeds through the formation of the imine (C=N) bond, accompanied by the elimination of water.[59]

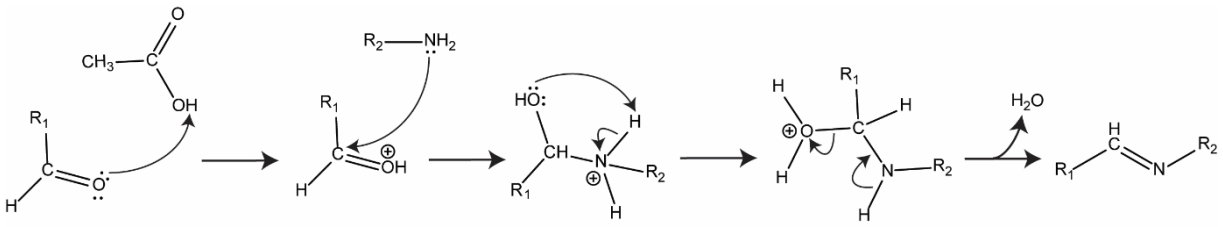

Figure 1.4. Mechanism of Schiff base (imine) formation.

A key factor in achieving high crystallinity in COFs is the use of (slightly) reversible reactions during synthesis. This reversibility allows for dynamic error correction and self-repair, enabling the formation of highly ordered frameworks.[60] Nonetheless, high crystallinity is not limited to systems only formed via reversible linkages, as alternative synthetic approaches (for example, previously mentioned linkage conversion strategies)[44,45] and optimized reaction conditions can also yield well-ordered COFs.

1.2.2. Different topologies

Topology refers to the geometric arrangement and connectivity pattern of the building units within the extended 2D or 3D framework. In 2D COFs, layers are formed through in-plane covalent linkages and stacked via π–π interactions between planar sheets, whereas in 3D COFs, building units are covalently connected in all directions to generate fully extended frameworks. The primary focus of this thesis was on 2D COFs. Typical topological design types for 2D COFs include "C2 + C2," "C2 + C3," "C3 + C3," "C2 + C4," "C4 + C4," and "C6 + C2" (**Figure 1.5**). In the design process of 2D COFs, it is essential to consider not only the structure and geometry of the building units but also their stacking configurations. Generally, the potential stacking modes of two-dimensional COFs include layered overlapping stacking and layered staggered stacking, randomly disordered stacking, and staircase stacking. The powder X-ray diffraction (PXRD) patterns of these stacked configurations can be simulated and computed using Materials Studio software, often allowing for the determination of the most probable structure of 2D COFs by comparing them with the PXRD patterns obtained from experimental data.[43,61,62]

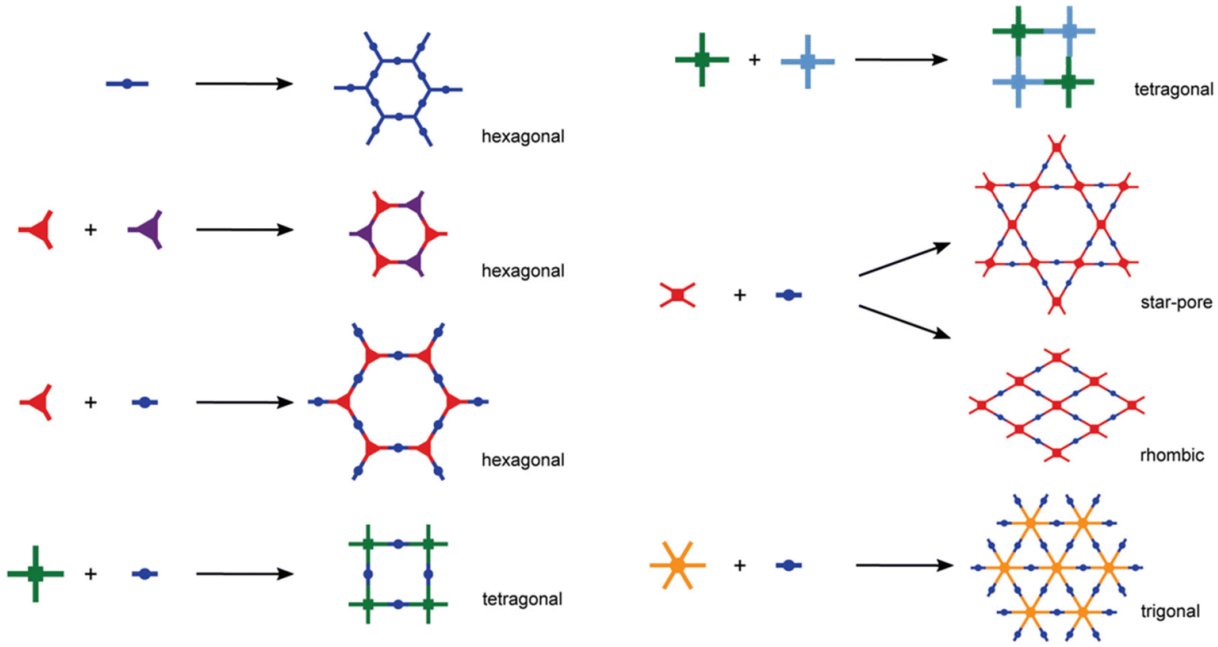

Figure 1.5. Different topological structures of 2D COFs. Adapted with permission from Lohse *et al.*[63] Copyright 2018 Wiley-VCH.

1.3. From molecule to material: aligning building blocks with function

Choosing building blocks for COFs is an important step, as the structural and chemical properties of the building blocks such as geometry, functionality, and electronic characteristics play a critical role in determining the framework's overall structure, stability, porosity, and potential for specific applications.

- **Rigidity**. Rigid building blocks are typically preferred because they maintain their defined geometric arrangement within the crystal lattice, promoting the formation of highly crystalline structures with well-defined pores.[64] Their limited conformational flexibility ensures correct bonding orientations during polymerization, further supporting ordered framework formation.[65]

- **Flexibility.** In contrast to rigidity, flexibility is often associated with a higher number of single bonds, allowing free rotation within the structure. This structural adaptability imparts unique properties, such as breathing behavior and reversible expansion or contraction, enabling the formation of dynamic and responsive pore environments.[64,65]

For example, flexible frameworks can switch their porosity state in response to external stimuli such as guest molecules, pressure, or temperature.[65]

- **Extended π-conjugation.** It typically involves longer aromatic systems or linearly connected conjugated units. Such systems are particularly useful for modulating optical properties, such as tuning the bandgap energy. This is especially important in applications like photocatalysis, where tuning the energy levels is a key step in enhancing photocatalytic performance.[66,67]

- **Fluorescence.** This feature is strongly influenced by the π-conjugation degree of the building unit. When fluorescent building blocks are integrated into COFs, their emissive ability can be transferred to the extended polymeric network. Such fluorescent COFs are particularly promising for sensing applications, as they can exhibit high sensitivity and selectivity toward specific target molecules.[68] In some cases, this is manifested as a selective "turn-off" fluorescence response, enabling detection through measurable changes in emission.[69,70]

- **Electroactivity.** It refers to the ability to conduct, store or transfer charge through the extended polymeric network of COFs.[71–73] Incorporation of electroactive building blocks into COFs is highly beneficial for applications such as organic electronics[74] including photodetectors, photovoltaics, transistors and light-emitting diodes (OLEDs), as well as for energy storage applications[75] like supercapacitors.

- **Quadrupole character**. This property arises from a non-spherically symmetric charge distribution within a system. In COFs, this feature is particularly useful for tuning the electrostatic potential across the framework. By modifying this potential, it becomes possible to influence how gas molecules interact with and are adsorbed within the material's pores. Such control is essential for optimizing applications like ion and gas uptake, where the local electrostatic environment plays a critical role in performance.[76]

In the following sections, we highlight the potential of the anthracene building block for constructing novel COF structures. In Chapters 3 and 4, this building unit was used to synthesize multifunctional COFs with novel structural and functional features.

1.3.1. Anthracene - a multifunctional building block

Anthracene is a polycyclic aromatic hydrocarbon molecule consisting of three benzene rings. Anthracene is well-known for its fluorescence properties which makes it particularly useful in organic electronics such as OLEDs or visualization and analysis of molecular structures.[77–79] Another interesting property of anthracene is its ability to generate dimers upon illumination, which constitutes one of the oldest documented photochemical reactions (see **Figure 1.6**)[80]. Dimerization represents a reversible reaction - dimers can readily undergo decomposition and revert to their original anthracene configuration via thermal activation. Given that the anthracene molecule exhibits a highly conjugated structure and the dimerized products experience a loss of conjugation in the central ring, the dimerization process profoundly modifies the electronic characteristics of the compound, thereby influencing its luminescence and charge transport capabilities.[81] This distinctive behavior renders anthracene a significant candidate for a various applications such as photoresponsive sensors and memory materials.[82–85]

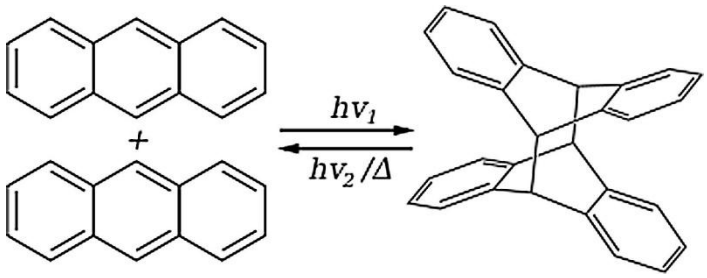

Figure 1.6. Anthracene dimerization reaction. Reprinted with permission from Novak *et al.*[86] Copyright 2019 Elsevier.

Anthracene is also well known for its high reactivity, particularly at the central ring (the 9 and 10 positions), while the outer rings typically show diminished reactivity.[87,88] The high reactivity at these positions is often exploited in synthetic chemistry to introduce functional groups. This behavior is especially evident in anthracene's strong tendency to undergo Diels-Alder and photocycloaddition reactions.[89–91] The underlying reason lies in its electronic structure - specifically, the distribution of π-electrons across the molecule. In contrast, the outer rings are less reactive due to lower electron density and the stabilizing effects of resonance throughout the system.[92,93]

1.3.2. Incorporation of anthracene into COF architectures

Anthracene-based building blocks have been widely explored in the field of MOFs for a range of applications, including sensing and light-emitting devices.[94–98] Based on this success, anthracene has also become an increasingly popular building block in the design of COFs. Below we present several reported anthracene-based COFs, where various unique properties of anthracene have enabled the development of functional materials for diverse applications.

- **Photocatalytic applications.** The extended π-conjugated system of anthracene plays a central role in enhancing the material's optoelectronic properties. The three linearly fused benzene rings of anthracene form a long conjugation pathway that broadens visible light absorption, lowers the bandgap, and improves charge transport. These combined features are particularly beneficial for photocatalytic applications.[99,100] As a result, anthracene-based COFs can efficiently harvest light and promote effective charge separation and mobility. In addition, anthracene units can serve as effective anchoring sites through their strong π–π interactions (see **Figure 1.7**), which facilitate the immobilization of metal complexes and consequently enhance photocatalytic performance by promoting more efficient charge transfer, broadening the light absorption range, and optimizing interfacial reaction pathways.[101]

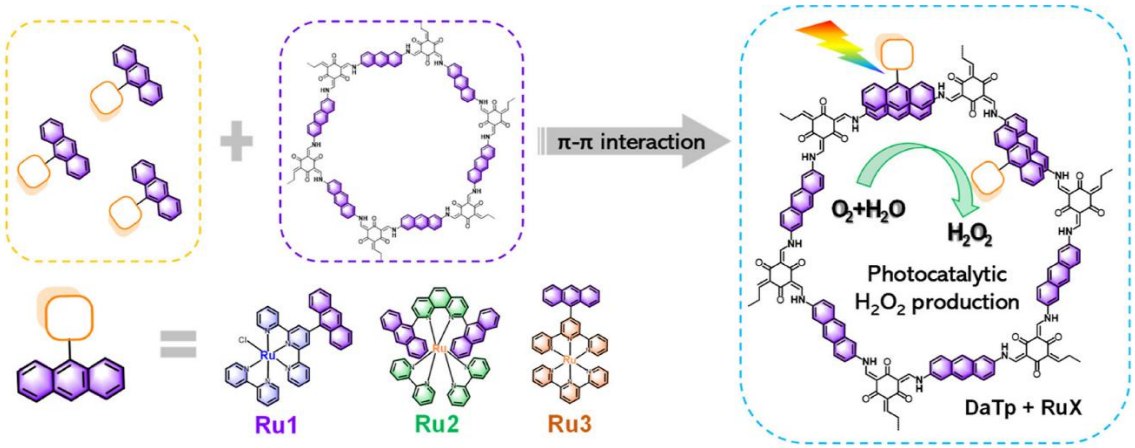

Figure 1.7. Preparation of anthracene-based COFs (DaTp) with ruthenium complexes (RuX) for photocatalytic H_2O_2 production. Reprinted with permission from Jiang *et al.*[101] Copyright 2024 American Chemical Society.

- **Sensing applications.** The planar structure of anthracene facilitates robust π–π interactions with target analytes, permitting sensitive fluorescence quenching and elevated selectivity in chemo-sensing applications.[102] This sensing performance is further augmented thanks to anthracene's capability to execute reversible photodimerization through a [4π+4π] cycloaddition mechanism upon UV light exposure, which temporarily quenches fluorescence and is restored upon heating (see **Figure 1.8**).[103] In addition to fluorescence switching, this dimerization process also triggers notable alterations in the UV-Vis absorption spectra, which can act as an additional optical signal for sensing or for observing the photoresponsive state of the material.[104] These combined attributes make anthracene-based COFs highly suitable for sensitive, reusable, and light-controlled sensing systems, with further potential in advanced optoelectronic and synaptic applications.

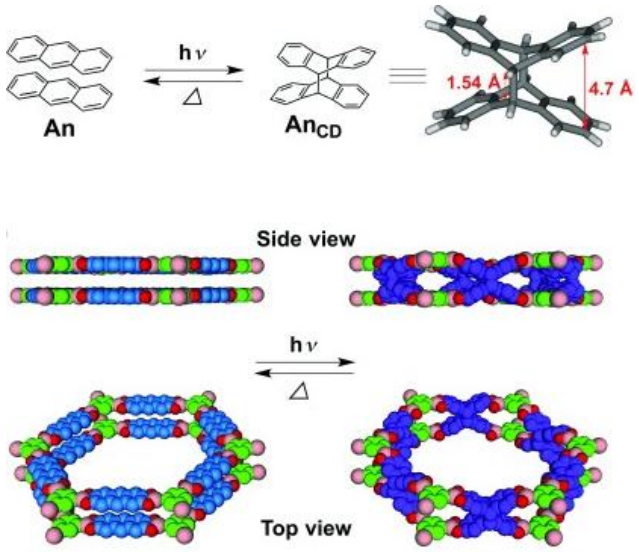

Figure 1.8. Reversible photodimerization of anthracene unit in anthracene-based COF upon light exposure causes interruption of the conjugated system. Adapted with permission from Huang *et al.*[103] Copyright 2015 Wiley-VCH.

- **Structural tuning.** The spatial arrangement of anthracene units can strategically control the dimensionality of the final material and its resulting optical properties. In some frameworks, anthracene units are oriented vertically relative to the 2D layers, introducing steric hindrance that prevents excessive layer stacking and facilitates the formation of 3D

COF structures (see **Figure 1.9**).[105] This vertical alignment not only promotes 3D growth but can also contribute to fluorescence modulation. Additionally, in other designs, the planar eclipsed stacking of anthracene units supports efficient exciton migration, which is essential for light-emitting processes.[106] This stacking mode enhances the structural stability of the COF while also boosting photoluminescent efficiency.

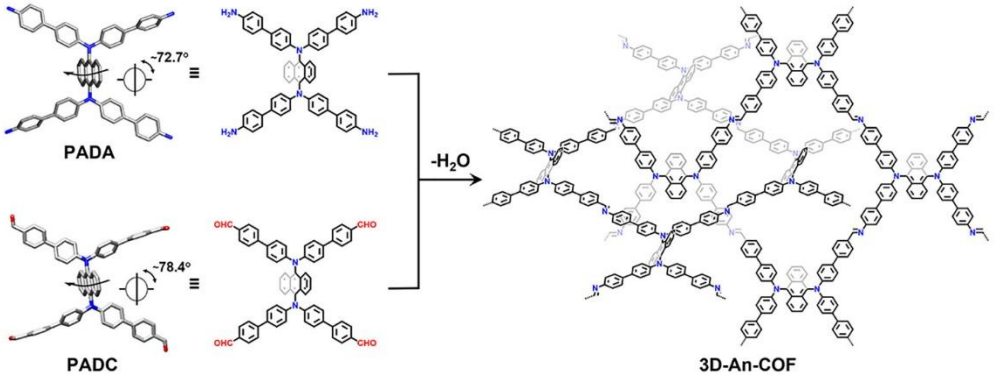

Figure 1.9. Synthesis of 3D COF using sterically demanding anthracene unit. Reprinted with permission from Cheng *et al.*[105] Copyright 2023 American Chemical Society.

1.4. Pre-synthetic modifications

Pre-synthetic modifications in COFs involve altering the building blocks or adjusting the synthesis process before the framework is fully formed. This strategy is fundamental in COF chemistry as it enables the design of frameworks with tailored functionalities that are often not achievable through direct synthesis or post-synthetic modifications. A key approach is the incorporation of heteroatoms into the building blocks prior to framework assembly.

The introduction of heteroatoms must be carefully controlled to avoid undesirable reactions that could compromise the building blocks or the final COF structure. This requires a thorough understanding of the chemical reactivity of the selected heteroatoms and the conditions under which the COF is synthesized. Ensuring the compatibility of heteroatoms with the synthesis environment is essential, as their influence on the stability and integrity of the framework can be significant.[107]

When thoughtfully chosen, heteroatoms can introduce active sites for catalysis, enhance interactions with guest molecules, and improve the overall functional performance of the COF.[108] In the following sections, we present the incorporation of halogens as heteroatoms into the COF structure, which served as the main strategy in Chapters 3 and 4 of this thesis.

1.4.1. Halogen functionalized COFs: Effects on functional performance

Halogen functionalization for the building blocks that are further used for COF synthesis is one of the most promising strategies to modulate final properties of the COFs and to broaden their applications. While typical elements of COF structures are carbon, nitrogen, hydrogen, sulfur and oxygen, incorporation of unusual strongly electronegative atoms such as halogens can significantly influence the electronic properties and reactivity of the building blocks, allowing for tailored interactions within the COF framework.

Here we elaborate a few aspects demonstrating the impact of halogen functionalization of COFs:

- **Electronic properties tuning.** The incorporation of halogen atoms can generate active sites within the COF framework and modify the band structure. This is advantageous in chemical reactions where COFs are used as catalysts, as the presence of halogens can promote electron transfer mechanisms and elevate performance in applications such as photocatalysis, where effective light absorption and emission are crucial.[109–111]

- **Increased stability.** Halogen functionalization can enhance the chemical stability of COFs. The high electronegativity of halogen atoms, specifically fluorine, increases the hydrophobicity of COFs by reducing surface tension. This improves their stability in harsh aqueous chemical environments, including acidic and alkaline conditions.[112] Additionally, halogen bonding promotes denser molecular packing, further enhancing chemical and thermal resistance which is an important advantage for applications in extreme conditions.[113]

- **Intermolecular interactions.** Halogen functionalization can enhance the adsorption properties of COFs by strengthening intermolecular interactions. The incorporation of

halogen atoms modifies surface characteristics, increasing the material's ability to capture specific molecules by introduction of additional binding sites. This is particularly valuable for gas storage and separation applications.[114–117]

1.4.2. Electronegativity vs. atomic size

In the context of halogen atom categories, their different electronegativities and atomic sizes can result in distinct characteristics of halogen-containing COFs.

The most electronegative halogen, fluorine, frequently demonstrates superior efficacy owing to its capability to efficiently modulate electronic structure, which is particularly useful for photocatalytic and electrochemical applications.[113,118] A good example is the work of Cao *et al.*,[110] who synthesized COFs functionalized with fluorine, chlorine, and bromine (**Figure 1.10**a) and evaluated them for photocatalytic Cr^{6+} reduction to Cr^{3+} (**Figure 1.10**c). The fluorinated COF showed the highest activity, consistent with the increasing electronegativity trend (Br < Cl < F), which generated more negative conduction band potentials (**Figure 1.10**b) and improved charge separation. Together, these factors provided a stronger driving force for efficient Cr^{6+} photoreduction.

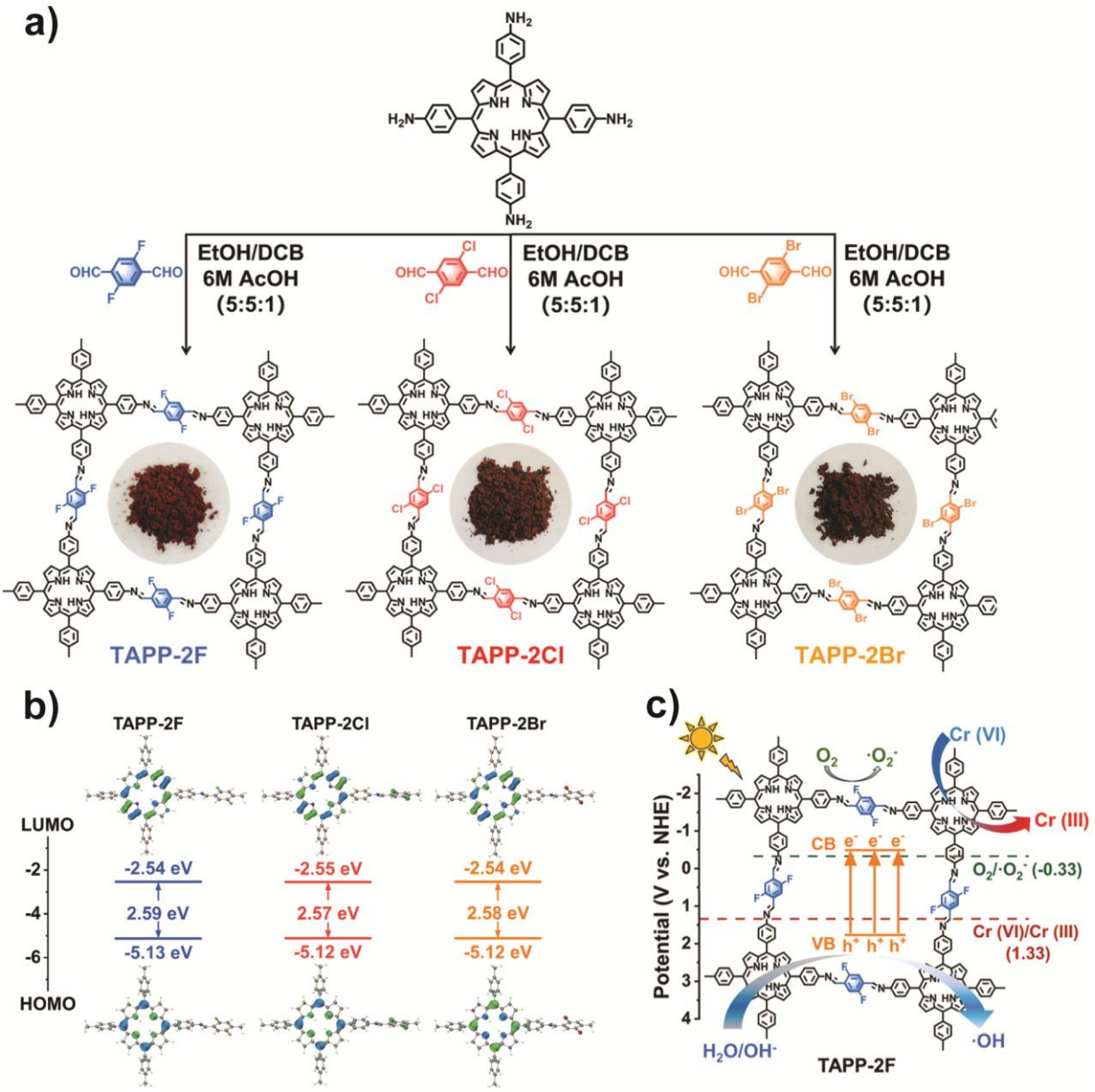

Figure 1.10. (a) Synthesis and chemical structures of halogen-functionalized COFs: fluorinated(TAPP-2F), chlorinated (TAPP-2Cl), and brominated (TAPP-2Br). (b) Energy gaps of the HUMO/LUMO for TAPP-2F, TAPP-2Cl and TAPP-2Br. (c) Schematic illustration of the photoreduction of Cr^{6+} to Cr^{3+}. by TAPP-2F. Adapted with permission from Cao *et al.*[110] Copyright 2024 Elsevier.

However, in certain cases, the incorporation of larger and less electronegative halogens may be more advantageous. Therefore, before choosing the halogen, it is important to consider the specific application and desired properties. While fluorine functionalization may amplify electron-withdrawing effects,[119–121] halogens with higher polarizability such as iodine exhibit

stronger halogen bonding capabilities, which can be advantageous in applications where intermolecular interactions play a significant role. For example, Hu *et al*.[116] synthesized COFs with double halogen substitutions (chlorine, bromine, and iodine) and evaluated their methane sorption performance. The iodinated COF demonstrated a superior isosteric heat of adsorption, attributed to the strongest I-CH_4 interaction among the tested halogens. Although this and other related studies[122] from the same group confirm the superior gas-sorption affinity of larger halogen atoms compared to smaller ones (I > Br > Cl), detailed investigations and comprehensive explanations of the interaction mechanisms between halogen atoms and gas molecules remain unexplored. Here, another interesting phenomenon known as *σ*-hole, which was already has been well characterized in supramolecular systems[123] but not yet in COFs, is worth to consider.

The *σ*-hole concept is a fundamental principle in chemistry that describes a low electron-density region that exists along the extension of a covalent bond, particularly in molecules containing electronegative atoms such as halogens. The *σ*-hole is generated by the polarization of electron density towards the electronegative atom, creating a positive electron-deficient area.[124] The characteristics of the *σ*-hole are significantly impacted by the atomic number of the halogen.[125] Bromine and iodine, being heavier halogens, display more pronounced *σ*-holes compared to lighter halogens like chlorine.[126] Fluorine is frequently regarded as an exception among halogens concerning the formation of *σ*-holes. Due to fluorine's high electronegativity, small atomic size, and considerable sp-hybridization, it often leads to an influx of electronic charge that neutralizes the *σ*-hole, resulting in its absence.[125]

An important facet regarding the *σ*-hole is its capacity to participate in non-covalent interactions such as halogen bonding (**Figure 1.11**). In this type of bonding, the *σ*-hole in the halogen atom acts as an electrophile and interacts with electron-rich sites (nucleophiles).[127] Examples of nucleophiles include π-electrons of unsaturated systems, negatively charged ions or lone pairs on atoms such as nitrogen, oxygen, and sulfur.[127,128] Halogen bonding typically occurs along the C-X axis (where X is a halogen atom), which predicts a 180-degree angle; however, studies have already demonstrated that variations of the angle can also occur.[124,129,130]

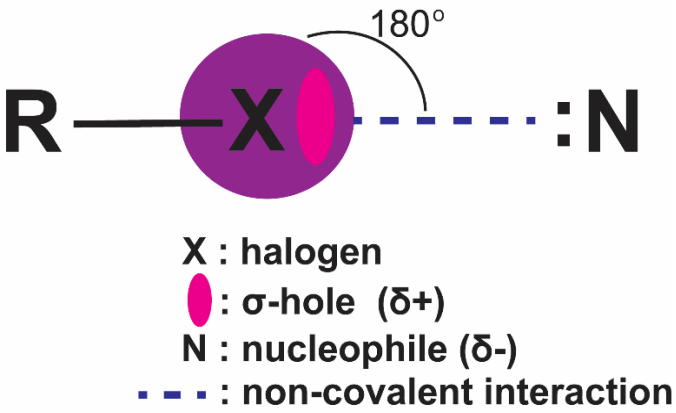

Figure 1.11. *σ*-hole interacting with a nucleophile via non-covalent bonding.

1.5. Post-synthetic modifications

Post-synthetic modification of COFs is an important strategy for introducing novel chemical functionalities, modulating their properties, and thereby broadening their application potential beyond the initial synthesis. Post-modification strategies include approaches such as metal integration into the polymeric structure (for example, via photodeposition, chemical reduction or electrochemical modification) and chemical transformation of linkages. The following section summarizes several post-modification strategies employed for COFs in this thesis.

1.5.1. Linkage conversion

Post-synthetic linkage conversion from imine to amide linkages has been so far the most popular linkage conversion technique used for COFs.[45–49,131] This method allows to alter COF properties without changing the overall framework structure, thus retaining crystallinity and porosity.[45]

To convert imine bonds into amide bonds, mild reaction conditions are typically sufficient - the transformation usually occurs at room temperature and often without the need for stirring. The key to this process is the use of oxidizing agents such as sodium chlorite,[45] N-heterocyclic carbenes[46,47] or $KHSO_5$[48,49].

The conversion of imine linkages to amide bonds in COFs offers significant advantages:

- **Enhanced chemical stability.** Amide-linked COFs have higher resistance to degradation compared to their imine-based counterparts, which is especially important for applications in harsh chemical environments.[45,132] This improved stability arises from the formation of stable amide bonds, which significantly enhance the structural durability of the COFs and make them more suitable for long-term use.[133]

- **Improved polarity and dispersibility.** Introducing an oxygen atom into the framework through amide formation can markedly influence the polarity and dispersibility of the COFs. This can be particularly beneficial in processes like photocatalysis, where effective intermolecular interactions with target molecules is essential.[45,131,134]

While the transformation of imine to amide linkages in COFs presents several advantages, there are obstacles and factors to consider. The selection of oxidizing agent and reaction parameters must be optimized to avoid damage to the COF framework or the loss of functional groups. Aggressive oxidizing agents often reduce crystallinity.[134,135] Additionally, like many other post-modification techniques, linkage conversion can lead to a decrease in surface area.[45,136,137]

1.5.2. Nobel metal incorporation

Noble metals, such as gold (Au), palladium (Pd) and platinum (Pt), are often integrated into COFs to exploit their unique electronic and catalytic properties. This incorporation benefits from well-ordered COF channels allowing for stabilization of metal nanoparticles, thus enhancing their catalytic efficiency and reusability.[138,139]

The main objective of integrating Pt into the polymeric COF network is to enhance photocatalytic activity in reactions such as CO_2 reduction and water splitting. Various studies have explored different approaches for Pt integration into the COF structure.

- **Photodeposition.** During the photodeposition reaction, the COF is illuminated with light of suitable energy to generate electrons that reduce Pt precursors such as H_2PtCl_6 to Pt^0. The photogenerated holes undergo reaction with a sacrificial electron donor. Since the COF provides both electrons and holes, the formation of Pt particles occurs

within the framework. Hence, under optimal conditions this process yields COF with evenly distributed platinum particles, serving as co-catalytic sites for hydrogen production.[140]

- **Chemical reduction.** In this approach, platinum was introduced into a COF containing bipyridine units, which are well known for their metal-chelating ability. The COF suspension was treated with the Pt precursor K_2PtCl_4, allowing coordination between the bipyridine sites and Pt^{2+} ions. Subsequent addition of sodium borohydride reduced Pt^{2+} to metallic Pt^0 nanoparticles. The resulting Pt/COF composite exhibited excellent catalytic performance in the hydrogen evolution reaction as well as in the simultaneously tested 4-nitrophenol reduction reaction.[141] A similar strategy has been applied in other studies using different COFs and the Pt precursor H_2PtCl_6, where sodium borohydride similarly reduced Pt^{4+} to Pt^0. In these cases, the resulting Pt/COF materials were employed in electrocatalytic methanol oxidation and peroxidase-like reactions.[142]

- **Electrochemical modification.** In this study, a nitrogen-rich COF with high conductivity and acid stability was employed as a support for platinum deposition. Platinum was introduced from the H_2PtCl_6 precursor via a mild electrochemical deposition process in an acidic electrolyte using cyclic voltammetry. Characterization of the resulting Pt/COF material revealed that platinum existed in a mixed oxidation state, intermediate between metallic platinum (Pt^0) and fully oxidized platinum (Pt^{4+}), indicating partial reduction. In situ analyses and theoretical studies further showed the formation of a distinct Pt-N_2 coordination environment, which enhanced metal-support interactions, promoted electron transport, and improved the structural stability of the material under acidic conditions.[143]

- **Vacuum-assisted Pt loading.** In this method, Pt nanoparticles were incorporated into the COF framework via a vacuum-assisted incipient wetness impregnation technique. The COF was impregnated with a calculated amount of the Pt precursor H_2PtCl_6, followed by reduction under a H_2/Ar atmosphere at 200 °C. This post-synthetic treatment resulted in the uniform dispersion of Pt nanoparticles within the COF matrix.

The resulting Pt/COF composite exhibited excellent catalytic performance in the selective reductive amination of benzaldehyde to secondary amines.[144]

- **Facile dispersion**. In this approach, the Pt precursor (H_2PtCl_6) was introduced into the COFs simply by exposing the precursor solution to the COF suspension under constant stirring for 12 hours. The COFs were specifically designed with a high density of oxygen and nitrogen atoms in their frameworks to provide effective anchoring sites for Pt species. The resulting Pt exhibited a valence state intermediate between metallic platinum (Pt^0) and oxidized platinum (Pt^{2+}), indicating partial reduction. The final Pt/COF composite was then employed for photocatalytic water splitting, where the presence of Pt facilitated charge separation during the reaction.[145]

While various synthetic strategies have enabled significant progress in incorporating platinum into COFs and improving both catalytic activity and structural stability, the complexity of these hybrid systems often requires a carefully tailored integration approach. Incorporating Pt within the porous framework of COFs presents several challenges, particularly in achieving precise control over particle size, dispersion, and chemical compatibility. Successful integration is essential for catalytic applications, where the efficiency and durability of the catalyst depend on the interplay between the structural features of the COF and the chemical nature of the Pt species. In Chapter 5, we introduce a novel strategy based on surface charge modulation of COFs to guide the *in situ* photodeposition of Pt. This method allows for controlled growth of platinum particles and reveals how surface charge influences the photocatalytic hydrogen evolution performance of Pt/COF composites.

1.6. Hybrid modifications

Apart from pre- and post-synthetic modifications, there are other strategies that can be considered hybrid because they do not fit into either category. For example, certain modifications can be introduced during COF synthesis when guest components that are not part of the precursor structures are added together with the COF precursors. This approach is often applied through a one-pot method, which refers to combining all reactants in a single reaction vessel to obtain the desired composite material. The one-pot method allows the COF structure

to form while the guest component is simultaneously incorporated. One promising type of guest component is carbon dots, which are discussed in detail in the following sections.

1.6.1. Carbon dots (CDs)

Carbon dots (CDs) are a novel group of carbon-centric nanomaterials, usually measuring below 10 nanometers, along with a number of favorable optical, electronic, and chemical features. Owing to their strong photoluminescence, high photostability, and resistance to photobleaching, CDs are excellent candidates for long-term fluorescence imaging and sensing applications.[146,147] Their good electrical conductivity and effective charge separation also make them suitable for use in solar cells and other energy-related technologies.[148] Additionally, CDs exhibit high water solubility, low toxicity, and good biocompatibility, positioning them as promising materials for biomedical applications such as drug delivery and bioimaging [149] Considered a green alternative, CDs can also serve as a substitute for standard nanomaterials including inorganic quantum dots, as they can be synthesized from biomass without involving toxic metals.[150–152] CDs are often doped with nitrogen, which, due to its electronegativity, can significantly alter the electronic structure of CDs, leading to improved fluorescence, quantum yield, and other desirable properties.[153]

1.6.2. Synthesis methods

CD synthesis methods are generally classified as top-down or bottom-up, depending on the carbon course. Top-down methods rely on breaking down bulk carbon materials, whereas bottom-up methods produce CDs through the pyrolysis or carbonization of small organic molecules. Compared to top-down routes, bottom-up strategies offer higher yields, milder conditions, simpler operation, and easy tunability through precursor selection. As a result, they are typically more cost-effective, scalable, and environmentally friendly, making them preferable for industrial applications.[154] Below we present the main synthesis strategies.

- **Conventional pyrolysis.** Pyrolysis involves heating precursors to induce dehydration, polymerization, and carbonization, forming CDs. It is widely used due to its simplicity, short reaction time, broad precursor compatibility, and low cost. Common precursors for the pyrolysis process include citric acid, glucose, or monoethanolamine.[154,155] An

example of rapid (10 min) pyrolysis to obtain nitrogen-doped carbon dots (NCDs) is presented in **Figure 1.12**a.[156] The main challenges of this method are high energy consumption, slow or uneven heat transfer, and complex purification**,** which still limit large-scale production.

- **Hydrothermal/solvothermal methods.** The hydrothermal or solvothermal method involves heating precursors in a sealed vessel at elevated temperatures and pressures, promoting uniform particle formation in CDs, using various precursors such as 1,3,6-trinitropyrene, sodium alginate (SA), or indigo.[154,157,158] This approach allows high conversion rates, often simplifying separation and purification, and can produce CDs with tailored surface chemistry by selecting appropriate precursors or solvents. An example of the hydrothermal method, in which SA, a naturally occurring clustering-induced emission luminogen (CLUEgen), forms a gel in the presence of ethylenediamine as the "molecular glue", is presented in **Figure 1.12**b.[159] The main limitations of hydrothermal/solvothermal synthesis are long reaction times and high energy consumption, which can restrict efficiency in large-scale applications.[154]

- **Microwave-assisted synthesis.** Microwave-assisted synthesis utilizes the interaction of polar molecules with alternating electric and magnetic fields, producing rapid molecular-level heating. It allows uniform heating and fast reaction rates.[160,161] Various precursors can utilized to form CDs using this method, such as polyethylene glycol, glucose, or isophorone diisocyanate (IPDI).[154] An example of a microwave-assisted reaction is shown in **Figure 1.12**c, where NCDs were formed using IPDI as a carbon source under microwave irradiation.[162] The main limitations of microwave-assisted synthesis are the current size restrictions of commercial equipment, which hinder large-scale production.[154]

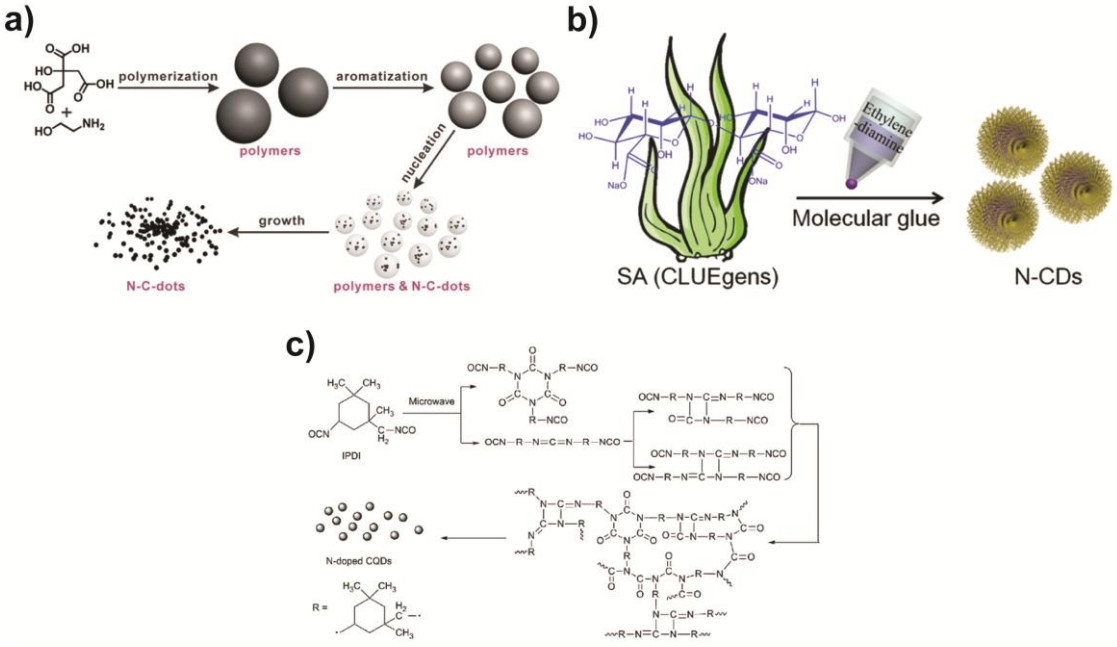

Figure 1.12. (a) Preparation of NCDs from citric acid in monoethanolamine via rapid synthesis at 170 °C. The mechanism incluses polymerization, aromatization, nucleation, and growth. Adapted with permission from Yu *et. al*.[156] Copyright 2015 Royal Society of Chemistry. (b) Preparation of NCDs from SA via hydrothermal method. SA and ethylendiamine aqueous solution formed hydrogel upon addition of Ca^{2+}. Adapted with permission from Wang *et. al*.[159] Copyright 2012 American Chemical Society. (c) Preparation of NCDs from IPDI under microwave irradiation. The mechanism involves self-polymerization and condensation of IPDI. Adapted with permission from Tan *et. al.*[162] Copyright 2016 Royal Society of Chemistry.

1.6.3. CDs doped-COFs for functional applications

There have already been several successful integrations of CDs into COFs to enhance functional applications such as:

- **Sensing applications.** NCDs were incorporated into the COF constructed from 2,4,6-tris(4-aminophenyl)-1,3,5-triazine (TAPT) and thieno[3,2-b]thiophene-2,5-dicarboxaldehyde (TT) to create a ratiometric fluorescent sensor for Cu^{2+}. While the COF itself exhibits weak fluorescence, the NCDs provide a strong reference signal and, through hydrogen bonding, become encapsulated within the COF. This interaction reduces interlayer forces, inducing self-exfoliation into two-dimensional nanosheets with improved stability and dispersion. In the presence of Cu^{2+}, NCD fluorescence is

quenched while the COF emission is enhanced, enabling sensitive and selective "off-on" detection of copper.[163]

- **Photocatalytic applications.** Carbon quantum dots (CQDs) were incorporated into a TAPT-TFP COF (built from 2,4,6-tris(4-aminophenyl)-1,3,5-triazine and 2,4,6-trihydroxybenzene-1,3,5-tricarbaldehyde) to enhance its photocatalytic hydrogen evolution performance. The addition of CDs can enhance the visible light absorption and decrease the recombination rate of photogenerated electron-hole pairs, thus improving the photocatalytic performance of COFs.[164]

- **Enhanced electrical conductivity and energy storage.** NCDs were incorporated into the COF constructed from 1,3,5-benzenetricarbohydrazide (BTH) and TT to produce a hollow rod-like composite for lithium-ion battery applications. When used as an anode material**,** the hollow COF architecture facilitates Li^+ transport and exposes a large number of active Li-storage sites**,** while the integrated NCDs significantly improve the composite's electrical conductivity and strengthen π–π interactions within the framework. Together, these features enhance charge transfer and structural stability during cycling, enabling high reversible capacity and long-term performance in lithium-ion batteries.[165]

In Chapter 6, we introduce a novel method for adjusting the interaction between CDs and COFs to regulate energy and charge transfer mechanisms, which are particularly important for applications that rely on controlled photophysical processes, such as photocatalysis and chemical sensing.

1.7. Photocatalytic hydrogen evolution reaction (HER)

Serving as the reduction half-reaction in water splitting, the HER entails the conversion of protons (H^+) into molecular hydrogen (H_2) through electron transfer, making it vital for achieving the goal of a clean hydrogen economy. The production of hydrogen from water, driven by renewable energy sources such as solar light, presents an environmentally benign alternative to conventional hydrogen generation methods, which are typically based on fossil fuel reforming and emit significant greenhouse gases.[166] As a promising strategy to obtain

hydrogen - an environmentally friendly and efficient energy fuel - photocatalytic HER has been extensively studied for decades. In 1972, Fujishima and Honda demonstrated the splitting of water to generate H_2 with a Pt-TiO_2 photo-electrode under ultraviolet light irradiation.[167] More efficient HER relies on photocatalytic systems that absorb visible light to drive the reaction. These systems typically involve a light absorber (photocatalyst) and a noble metal part (co-catalyst).[166]

1.7.1. COFs as photocatalysts for HER

In 2014, Lotsch *et al.* demonstrated a hydrazone-based COF capable of photocatalytic hydrogen production from water under visible light, representing the first application of COFs as photocatalysts.[168] Since then, COFs have emerged as promising candidates for efficient HER due to their unique structural and functional properties, such as:

- **Crystallinity and structural integrity.** The ordered and predictable structures of COFs minimize defects and promote efficient charge separation and transport which is crucial for photocatalytic reactions. This structural quality ensures that active sites are accessible and optimally arranged.[169] A good example is the study by Zhuo *et al*.,[170] who demonstrated that improving COF crystallinity can more than double its photocatalytic performance. In their work, two COFs were synthesized from the same building blocks - 1,3,5-triformylphloroglucinol and 4,4'-diaminobiphenyl. One material was obtained using the traditional acetic acid catalyst, while the other was synthesized using an organic base catalyst, which resulted in significantly higher crystallinity. When tested in photocatalytic tests, the more crystalline COF exhibited more than twice the activity of its less crystalline counterpart.

- **High porosity and surface area.** The crystalline porous nature of COFs offers an extensive surface area for catalytic reactions. This structural attribute aids in the adsorption and diffusion of reactants and boosts overall photocatalytic efficiency.[171] For example, Ding *et al.*[172] reported a three-dimensional COF built from a triptycene-based aldehyde and a porphyrin-based amine unit. Its large interconnected pores (4.6 nm) and high surface area (2204 $m^2\ g^{-1}$) optimize reactant diffusion, mass transport, and

active site accessibility. These porosity parameters directly enable the high exposure of porphyrin moieties, resulting in great photocatalytic performance.

- **Tunability.** The electronic band structure of COFs can be tuned by modulating the degree of π-conjugation within their frameworks through the selection of appropriate linkers and building blocks. Extended π-conjugation and ordered π–π stacking enable the modulation of the band gap and broaden visible-light absorption, thereby enhancing light harvesting and facilitating efficient charge separation for photocatalytic processes.[171] A good example of π-conjugation tuning was reported by Lin *et al.*,[173] who synthesized two analogous COFs using different triangular aldehyde linkers: 1,3,5-tris(4-formylbiphenyl)benzene (TFBPB) to form BPh-COF, and 1,3,5-tri(3-hydroxy-4-formyl-ethynylphenyl)benzene (THFEB) to form AC-COF. While the BPh-COF featured an extended phenyl network, the AC-COF incorporated an ethynyl-containing linker that increased structural planarity and strengthened π-conjugation across the framework. As a result, AC-COF exhibited broader visible-light absorption, a narrower optical band gap, and more efficient photoinduced charge separation and transfer. These features enabled significantly improved photocatalytic activity. Additional strategies, such as the incorporation of donor-acceptor units, can further promote intramolecular charge transfer and improve overall charge separation and transport within the framework.[174] For example, donor-acceptor design was reported by Liu *et al.*,[175] who synthesized COFs combining benzothiadiazole units as electron acceptors and triphenylamine units as electron donors. In this donor-acceptor framework, the HOMO is mainly localized on the donor segments (triphenylamine), while the LUMO resides on the acceptor units (benzothiadiazole), ensuring clear spatial separation of electrons and holes. This arrangement extends π-electron delocalization, reduces the band gap, enhances visible-light absorption, and promotes efficient photogenerated charge separation and transfer, leading to significantly improved photocatalytic performance.

In a COF-supported photocatalytic system (**Figure 1.13**) for hydrogen production, the COF photocatalyst, noble metal co-catalyst, and sacrificial electron donor (SED) collectively participate to drive the hydrogen evolution reaction. Platinum is a commonly used co-catalyst in photocatalytic systems.[176] For example, Li *et al.*[177] reported the *in situ* incorporation of Pt

into a pyrene-based COF, specifically designed with adjacent hydroxyl groups serving as anchoring sites to direct Pt cluster photodeposition. They also evaluated various Pt loadings (0.5-5 wt%) to study their influence on photocatalytic hydrogen evolution. The activity generally increased with higher Pt loading and reached its maximum at 3 wt%**,** after which a decline was observed at 5 wt%**.** This reduced performance was attributed to light-shielding effects caused by excessive Pt deposition.

Typically, Pt is introduced in the form of precursor complexes (for example H_2PtCl_6, $H_2Pt(OH)_6$, $Pt(NO_3)_2$, $Pt(acac)_2$) followed by reduction to metallic platinum particles. The SEDs are crucial in photocatalytic systems, where they donate electrons to the photocatalyst and enable the scavenging of photogenerated holes, thereby preventing charge recombination. In COF-supported photocatalytic hydrogen production, common SEDs include triethanolamine, ascorbic acid (H_2A), and methanol. The choice of SED significantly influences system performance and must be tailored to the photocatalyst and reaction conditions. Effective SEDs should donate electrons efficiently at high rate, form stable intermediates, and avoid interfering with the photocatalytic process.[178,179]

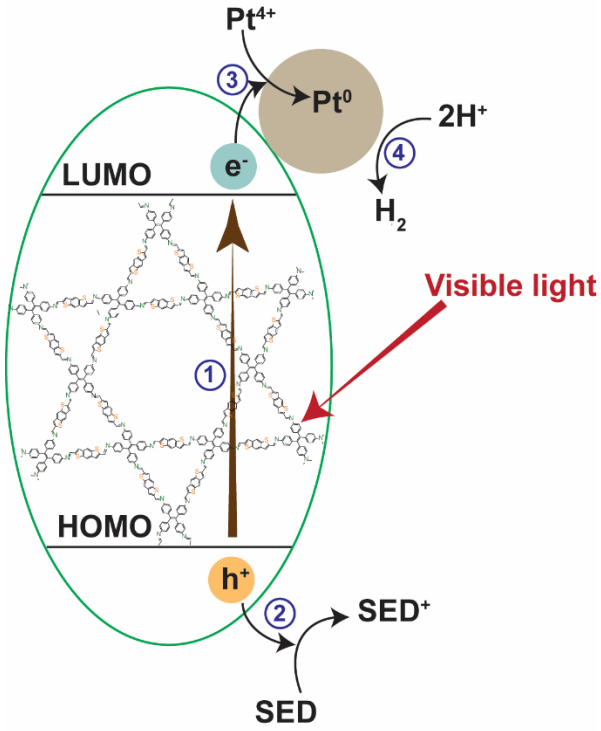

Figure 1.13. Mechanism of the HER in COF-supported photocatalytic systems. Key reaction steps are highlighted in blue: 1) Photon absorption and generation of charge carriers; 2) oxidation of SED by holes; 3) electron transfer to Pt particle; 4) H_2 formation.

In general, the overall photocatalytic reaction is governed by a sequence of key steps, each crucial for the efficient production of hydrogen. In COF-supported systems, these steps are as follows:

1) **Photon absorption and charge carrier generation.** Under visible light irradiation, the COF (photocatalyst) absorbs photons, generating photoexcited electrons (e^-) and holes (h^+). Photoexcited electrons move from the HOMO to the LUMO level.

$$COF \xrightarrow{h\nu} e^- + h^+ \qquad (1.1)$$

2) **Hole-driven oxidation.** The photogenerated holes oxidize the sacrificial electron donor (SED). In the following example H_2A is oxidized to dehydroascorbic acid, A, either

directly by two-electron transfer or by one-electron oxidation *via* formation of ascorbyl radical, $HA^{\bullet}$, as an intermediate (equation 1.2 and equation 1.3).

$$H_2A + h^+ \rightarrow HA^{\bullet} + H^+ \quad (1.2)$$

$$HA^{\bullet} + h^+ \rightarrow A + H^+ \quad (1.3)$$

3) **Electron transfer to co-catalyst.** First step: photogenerated electrons reduce Pt^{4+} precursor, leading to the formation of Pt^0 particles (equation 1.4). Second step: photogenerated electrons are subsequently transferred from the COF to the *in-situ* formed Pt^0 particles (equation 1.5).

$$COF(4e^-) + Pt^{4+} \rightarrow COF + Pt^0 \quad (1.4)$$

$$COF(e^-) + Pt^0 \rightarrow Pt(e^-) + COF \quad (1.5)$$

4) **H_2 formation.** Volmer step:[180] it involves the transfer of H^+ from the solution to the Pt surface, where it is reduced to form an adsorbed hydrogen atom H_{ads} (equation (1.). This is followed by H_2 evolution either via Tafel[181] (equation 1.7) or Heyrovsky[182] (equation 1.8) steps.

$$Pt(e^-) + H^+ \rightarrow Pt\text{-}H_{ads} \quad (1.6)$$

$$Pt\text{-}H_{ads} + Pt\text{-}H_{ads} \rightarrow H_2 + Pt \quad (1.7)$$

$$Pt\text{-}H_{ads} + H^+ + e^- \rightarrow H_2 + Pt \quad (1.8)$$

1.7.2. Progress in COF-based photocatalysis

COFs were first employed for photocatalytic HER in 2014, when Lotsch *et al.* demonstrated a water-stable hydrazine-based COF (see **Figure 1.14**a) for HER that achieved reaction rates of 1.98 mmol g^{-1} h^{-1}.[168] This marked a significant milestone in COF-based photocatalysis, paving the way for the development of COFs as platforms for solar fuel production. Over the

past decade, COFs have been extensively investigated for a variety of photocatalytic applications.

Recent studies have focused on enhancing the photocatalytic efficiency of COFs by optimizing their structural and electronic properties. In 2021, Yang *et al.*[183] reported a high HER efficiency of 20.7 mmol g^{-1} h^{-1} using a COF constructed from strong acceptor (triazine) and donor (triphenylamine) moieties (see **Figure 1.14**b). The study highlighted the crucial role of imine linkage protonation in acidic environments, facilitated by H_2A used as an SED during the photocatalytic reaction. Protonation of the imine linkages was found to significantly enhance light absorption, promote charge separation, and increase hydrophilicity, collectively leading to improved photocatalytic performance. More recently, in 2023, Altinisik *et al*.[184] reported a hydrogen evolution rate of 1.03 mmol g^{-1} h^{-1}. While this value may appear modest compared to other studies, it is important to emphasize that the performance was achieved using entirely metal-free, viologen-based COFs with varying alkyl chain lengths (**Figure 1.14**c), and notably, without the assistance of any co-catalyst such as platinum. This work highlighted the intriguing role of alkyl chains, which acted as an insulating barrier between electroactive COF moieties, suppressing electron-hole recombination within the COF scaffold and thereby improving charge separation and transfer. Overall, this work underscored the potential of structural tuning in metal-free systems for enhanced HER performance. A year later, a similar metal-free approach was further advanced by Yao *et al*.,[185] who reported a thiophene-based COF (**Figure 1.14**d) with HER rate of 2.87 mmol g^{-1} h^{-1}. Their study introduced a novel design concept, demonstrating that incorporating more electronegative groups into the framework or constructing donor-acceptor architectures can effectively modulate electronic properties and boost photocatalytic efficiency, even in the absence of a co-catalyst.

Meanwhile, studies involving co-catalysts but introducing new conceptual advances also progressed significantly. For instance, in 2024, Hassan *et. al.*[186] designed a heterostructure composed of a COF and graphitic carbon nitride (CN) (**Figure 1.14**e), achieving an impressive HER rate of 27.5 mmol g^{-1} h^{-1}. This outstanding performance was attributed to enhanced light-harvesting ability, effective separation of charge carriers, and the synergistic effect between COF and CN. A similar heterostructure approach was reported by Liu *et. al*.,[187] who combined a cadmium sulfide (CdS) semiconductor with a COF to form a hybrid heterojunction

system (**Figure 1.14**f). Their design achieved HER efficiency of 21.8 mmol g^{-1} h^{-1}, primarily due to the rapid charge carrier transfer at the COF-CdS interface.

Apart from constructing hybrid systems, another promising strategy is precise molecular engineering. A notable example is a recent study by Xiao *et. al*.,[188] which highlighted the critical influence of both the content and spatial arrangement of nitrogen atoms within COF frameworks on their photoelectronic properties (**Figure 1.14**g). Increasing nitrogen incorporation was found to modulate π–π stacking interactions and to tune the electronic structure, leading to improved charge separation and photogenerated electron transfer. Although higher nitrogen content slightly reduced crystallinity, it ultimately enhanced photocatalytic hydrogen evolution, illustrating how targeted molecular-level design can effectively control the structure-property-activity relationship in COFs. This team demonstrated that varying the nitrogen content can lead to a two- to threefold increase in photocatalytic performance.

Despite these notable advancements, several fundamental challenges remain in the development of COF-based photocatalysts. Relatively low charge carrier mobility, high exciton binding energy, and somewhat limited stability in aqueous environments during photocatalytic testing continue to restrict long-term efficiency and scalability.[189–191] However, promising strategies have emerged to address these issues. For instance, extending π-conjugation and introducing heteroatoms or metal complexes can enhance charge transport,[189] while the incorporation of donor-acceptor motifs[189,192,193] or exciton-modulating elements such as nickel[190] can improve charge separation and exciton dissociation. Additionally, replacing reversible linkages with more robust covalent bonds significantly improves durability and stability,[194] which is especially important during the HER when COFs are continuously exposed to aqueous conditions.

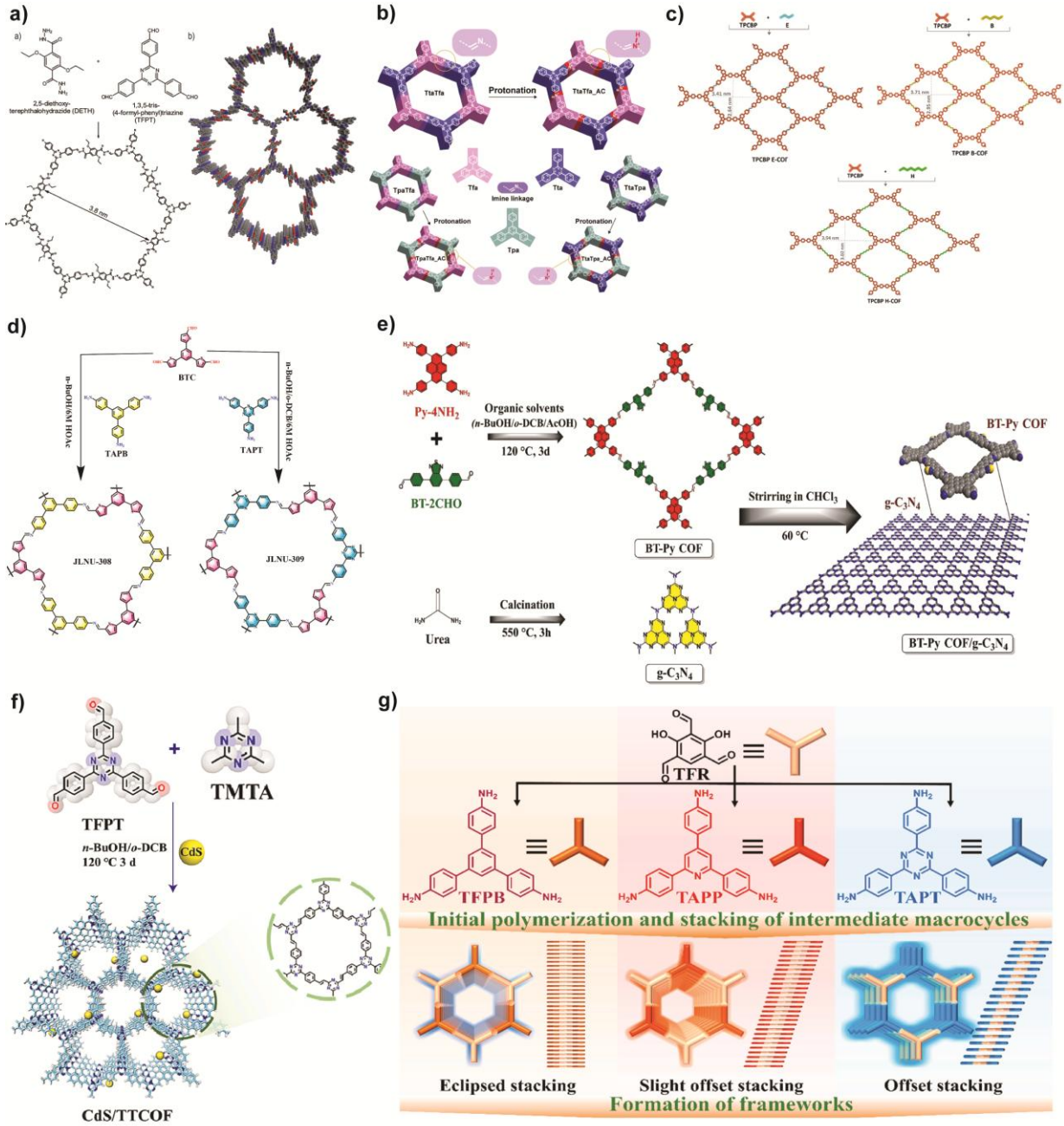

Figure 1.14. (a) Hydrazine-based COFs first time used for as HER catalysts. Adapted with permission from Lotsch *et al.*[168] Copyright 2014 Royal Society of Chemistry. This article is an open access article distributed under the terms and conditions of the Creative Commons Attribution (CC BY 3.0) license (https://creativecommons.org/licenses/by/3.0/). (b) Triazine and triphenylamine based-COFs used for HER, highlighting the importance of imine-linkage protonation. Adapted with permission from Yang *et al.*[183] Copyright 2021 Wiley-VCH GmbH. This article is an open access article distributed under the terms and conditions of the Creative

Commons Attribution (CC BY) license (http://creativecommons.org/licenses/by/4.0/). (c) Viologen-based COFs with alkyl-chain insulating spacers enhancing metal-free HER performance. Adapted with permission from Altinisik *et al*.[184] Copyright 2023 American Chemical Society. This article is an open access article distributed under the terms and conditions of the Creative Commons Attribution (CC BY) license (http://creativecommons.org/licenses/by/4.0/). (d) Thiophene-based COFs with (JLNU-309) and without (JLNU-308) electronegative nitrogen atoms in the benzene rings, designed for metal-free HER catalysis. Adapted with permission from Yao *et al*.[185] Copyright 2024 Elsevier. (e) Hybrid composite of COF and CN for HER catalysis. Adapted with permission from Hassan *et. al*.[186] Copyright 2023 Elsevier. (f) Hydrid composite of COF and CdS for HER catalysis. Adapted with permission from Liu *et. al*.[187] Copyright 2024 Elsevier. (g) COFs with different numbers of nitrogen atoms for structural tuning toward optimal HER performance. Adapted with permission from Xiao *et. al*.[188] Copyright 2024 Elsevier.

1.8. Motivation

A promising strategy to tune COF electronic and optical properties is the pre-synthetic incorporation of halogen atoms into π-conjugated building blocks. Halogens can modulate electron distribution thereby benefiting optoelectronic and photocatalytic applications. Most reported halogenated COFs use simple building blocks, while incorporation into larger π-extended systems is rare due to synthetic challenges. The first project (Chapter 3) aims to functionalize anthracene building units with halogen atoms, to explore how halogen substitution on a π-extended framework influences COF formation and optoelectronic properties. To the best of our knowledge, no studies have reported COFs featuring halogenated anthracene units. Given anthracene's highly conjugated nature, even the introduction of a single halogen atom can significantly alter the electronic properties of the linker and, consequently, the functionality of the entire COF. This unexplored design avenue presents a promising opportunity to further expand the structural and functional diversity of COFs.

Apart from tuning optoelectronic properties, halogen atoms also offer a powerful strategy to enhance intermolecular interactions. In COFs, their incorporation can introduce additional binding sites for target guest molecules such as CO_2. A particularly intriguing feature of halogens is their ability to form *σ*-holes - electron-deficient regions that act as Lewis acids, enabling directional interactions with electron-rich moieties. While *σ*-hole interactions have been extensively studied in supramolecular systems, their influence within halogen-functionalized COFs has not yet been reported. This unexplored phenomenon presents an

exciting opportunity to develop new design strategies for tailoring host-guest chemistry in COFs, which the second project (Chapter 4) seeks to uncover.

Post- synthetic modification of COFs offers a versatile strategy to introduce functionalities that are difficult to achieve through direct synthesis. Transformations of framework linkages, such as imine-to-amide conversion, can significantly enhance structural stability and photocatalytic efficiency. Although their beneficial impact on photocatalytic performance is well documented, certain aspects - such as the role of surface charge and intermolecular interactions between COFs and other components during photocatalytic reactions - remain poorly understood. This knowledge gap presents an opportunity to gain deeper insight into the influence of surface charge on photocatalysis in COFs, an aspect explored in the third project (Chapter 5).

A hybrid COF modification approach involves incorporating carbon dots (CDs) into COFs during their synthesis to create composites with enhanced light-harvesting and charge-transfer properties. CDs are nanoscale, carbon-based materials with tunable photoluminescence and strong electron-donating ability. While they can broaden visible-light absorption and improve charge separation, the effect of CD concentration on COF/CD structure and electronic properties is largely unknown. This gap provides an opportunity to establish structure-property relationships governing charge-transfer dynamics in such composites, which the last project (Chapter 6) aims to explore.

1.9. References

[1] F. Ramoa Ribeiro, F. Lemos, C. Henriques, M. F. Ribeiro, in *Ion Exch. Sci. Technol.*, Springer Netherlands, Dordrecht, **1986**, pp. 513–525.

[2] P. Baile, E. Fernández, L. Vidal, A. Canals, *Analyst* **2019**, *144*, 366–387.

[3] H. D. Gesser, P. C. Goswami, *Chem. Rev.* **1989**, *89*, 765–788.

[4] P. J. Langley, J. Hulliger, *Chem. Soc. Rev.* **1999**, *28*, 279–291.

[5] C. Zhou, *Highlights Sci. Eng. Technol.* **2024**, *90*, 147–152.

[6] S. S.-Y. Chui, S. M.-F. Lo, J. P. H. Charmant, A. G. Orpen, I. D. Williams, *Science (80-.).* **1999**, *283*, 1148–1150.

[7] H. Li, M. Eddaoudi, M. O'Keeffe, O. M. Yaghi, *Nature* **1999**, *402*, 276–279.

[8] S. S. Kaye, A. Dailly, O. M. Yaghi, J. R. Long, *J. Am. Chem. Soc.* **2007**, *129*, 14176–14177.

[9] F. Wang, C.-C. Wang, S. Yi, *Chem. Eng. J.* **2024**, *495*, 153398.

[10] Z. ul Nisa, N. A. Ashashi, H. N. Sheikh, in *Synth. Met. Fram. Via Water-Based Routes*, Elsevier, **2024**, pp. 143–158.

[11] A. Ghoorchian, A. Afkhami, T. Madrakian, M. Ahmadi, in *Met. Fram. Biomed. Appl.*, Elsevier, **2020**, pp. 177–195.

[12] E. Stavitski, M. Goesten, J. Juan-Alcañiz, A. Martinez-Joaristi, P. Serra-Crespo, A. V. Petukhov, J. Gascon, F. Kapteijn, *Angew. Chemie Int. Ed.* **2011**, *50*, 9624–9628.

[13] M. Li, M. Dincă, *J. Am. Chem. Soc.* **2011**, *133*, 12926–12929.

[14] P. Sarkar, P. S. Nicholson, *J. Am. Ceram. Soc.* **1996**, *79*, 1987–2002.

[15] A. Gutés, C. Carraro, R. Maboudian, *J. Am. Chem. Soc.* **2010**, *132*, 1476–1477.

[16] R. Ameloot, L. Pandey, M. Van der Auweraer, L. Alaerts, B. F. Sels, D. E. De Vos, *Chem. Commun.* **2010**, *46*, 3735.

[17] M. Rubio-Martinez, C. Avci-Camur, A. W. Thornton, I. Imaz, D. Maspoch, M. R. Hill, *Chem. Soc. Rev.* **2017**, *46*, 3453–3480.

[18] D. Crawford, J. Casaban, R. Haydon, N. Giri, T. McNally, S. L. James, *Chem. Sci.* **2015**, *6*, 1645–1649.

[19] M. Gharibeh, G. A. Tompsett, K. S. Yngvesson, W. C. Conner, *J. Phys. Chem. B* **2009**, *113*, 8930–8940.

[20] I. Bilecka, M. Niederberger, *Nanoscale* **2010**, *2*, 1358.

[21] U. Farwa, Z. A. Sandhu, A. Kiran, M. A. Raza, S. Ashraf, H. Gulzarab, M. Fiaz, A. Malik, A. G. Al-Sehemi, *RSC Adv.* **2024**, *14*, 37164–37195.

[22] H. Musarurwa, N. T. Tavengwa, *Mater. Today Commun.* **2022**, *33*, 104823.

[23] B. M. Connolly, D. G. Madden, A. E. H. Wheatley, D. Fairen-Jimenez, *J. Am. Chem. Soc.* **2020**, *142*, 8541–8549.

[24] W. Xie, Q. Fu, L. Yang, L. Yan, J. Zhang, X. Zhao, *ChemSusChem* **2025**, *18*, e202401382.

[25] P. N. Blessy Rebecca, D. Durgalakshmi, R. A. Rakkesh, *Anal. Sens.* **2025**, *5*, e202400078.

[26] Shubhangi, I. Nandi, S. K. Rai, P. Chandra, *Talanta* **2024**, *266*, 125124.

[27] Y. An, X. Lv, W. Jiang, L. Wang, Y. Shi, X. Hang, H. Pang, *Green Chem. Eng.* **2024**, *5*, 187–204.

[28] L. Feng, K.-Y. Wang, G. S. Day, M. R. Ryder, H.-C. Zhou, *Chem. Rev.* **2020**, *120*, 13087–13133.

[29] J. Senker, *Nat. Chem.* **2018**, *10*, 1079–1081.

[30] M. Ding, X. Cai, H.-L. Jiang, *Chem. Sci.* **2019**, *10*, 10209–10230.

[31] T. He, X.-J. Kong, J.-R. Li, *Acc. Chem. Res.* **2021**, *54*, 3083–3094.

[32] A. P. Côté, A. I. Benin, N. W. Ockwig, M. O'Keeffe, A. J. Matzger, O. M. Yaghi, *Science (80-.).* **2005**, *310*, 1166–1170.

[33] P. Najmi, N. Keshmiri, B. Ramezanzadeh, M. Ramezanzadeh, in *Covalent Org. Fram.*, CRC Press, Boca Raton, **2022**, pp. 431–448.

[34] H. R. Abuzeid, A. F. M. EL-Mahdy, S.-W. Kuo, *Giant* **2021**, *6*, 100054.

[35] A. Esrafili, A. Wagner, S. Inamdar, A. P. Acharya, *Adv. Healthc. Mater.* **2021**, *10*, 2002090.

[36] Y. Shi, J. Yang, F. Gao, Q. Zhang, *ACS Nano* **2023**, *17*, 1879–1905.

[37] D. Blätte, F. Ortmann, T. Bein, *J. Am. Chem. Soc.* **2024**, *146*, 32161–32205.

[38] Q. Fang, Z. Zhuang, S. Gu, R. B. Kaspar, J. Zheng, J. Wang, S. Qiu, Y. Yan, *Nat. Commun.* **2014**, *5*, 4503.

[39] J. L. Segura, M. J. Mancheño, F. Zamora, *Chem. Soc. Rev.* **2016**, *45*, 5635–5671.

[40] S. Wang, X.-X. Li, L. Da, Y. Wang, Z. Xiang, W. Wang, Y.-B. Zhang, D. Cao, *J. Am. Chem. Soc.* **2021**, *143*, 15562–15566.

[41] X. Mu, S. Xie, X. Ye, S. Tao, J. Li, D. Jiang, *J. Am. Chem. Soc.* **2024**, *146*, 25118–25124.

[42] Y. Li, M. Liu, J. Wu, J. Li, X. Yu, Q. Zhang, *Front. Optoelectron.* **2022**, *15*, 38.

[43] P. Kuhn, M. Antonietti, A. Thomas, *Angew. Chemie Int. Ed.* **2008**, *47*, 3450–3453.

[44] L. Grunenberg, G. Savasci, M. W. Terban, V. Duppel, I. Moudrakovski, M. Etter, R. E. Dinnebier, C. Ochsenfeld, B. V. Lotsch, *J. Am. Chem. Soc.* **2021**, *143*, 3430–3438.

[45] P. J. Waller, S. J. Lyle, T. M. Osborn Popp, C. S. Diercks, J. A. Reimer, O. M. Yaghi, *J. Am. Chem. Soc.* **2016**, *138*, 15519–15522.

[46] W. Wang, D. Huang, W. Zheng, X. Zhao, K. He, H. Pang, Y. Xiang, *Chem. Mater.* **2023**, *35*, 7154–7163.

[47] S. Yu, L. Cheng, L. Liu, *ChemistrySelect* **2024**, *9*, e202304668.

[48] R. Xue, Y. Liu, M. Wang, H. Guo, W. Yang, J. Guo, G. Yang, *ChemSusChem* **2024**, *17*, e202400732.

[49] Z.-B. Zhou, X.-H. Han, Q.-Y. Qi, S.-X. Gan, D.-L. Ma, X. Zhao, *J. Am. Chem. Soc.* **2022**, *144*, 1138–1143.

[50] V. Singh, J. Kim, B. Kang, J. Moon, S. Kim, W. Y. Kim, H. R. Byon, *Adv. Energy Mater.* **2021**, *11*, 2003735.

[51] Y. Su, M. Qin, J. Kong, Q. Zhai, D. Yuan, Z. Liu, Y. Fang, *Adv. Funct. Mater.* **2024**, *34*, 2400433.

[52] Z. Alsudairy, N. Brown, C. Yang, S. Cai, F. Akram, A. Ambus, C. Ingram, X. Li, *Precis. Chem.* **2023**, *1*, 233–240.

[53] A. Dey, S. Chakraborty, A. Singh, F. A. Rahimi, S. Biswas, T. Mandal, T. K. Maji, *Angew. Chemie Int. Ed.* **2024**, *63*, e202403093.

[54] K. Seob Song, P. W. Fritz, D. F. Abbott, L. Nga Poon, C. M. Caridade, F. Gándara, V. Mougel, A. Coskun, *Angew. Chemie* **2023**, *135*, e202309775.

[55] X. Guan, Y. Ma, H. Li, Y. Yusran, M. Xue, Q. Fang, Y. Yan, V. Valtchev, S. Qiu, *J. Am. Chem. Soc.* **2018**, *140*, 4494–4498.

[56] E. Hamzehpoor, F. Effaty, T. H. Borchers, R. S. Stein, A. Wahrhaftig-Lewis, X. Ottenwaelder, T. Friščić, D. F. Perepichka, *Angew. Chemie* **2024**, *136*, e202404539.

[57] K. Asokan, M. K. Patil, S. P. Mukherjee, S. B. Sukumaran, T. Nandakumar, *Chem. – An Asian J.* **2022**, *17*, e202201012.

[58] A. B. Thomas, P. N. Tupe, R. V. Badhe, R. K. Nanda, L. P. Kothapalli, O. D. Paradkar, P. A. Sharma, A. D. Deshpande, *Green Chem. Lett. Rev.* **2009**, *2*, 23–27.

[59] X. Han, K. Gong, X. Huang, J. Yang, X. Feng, J. Xie, B. Wang, *Angew. Chemie Int. Ed.* **2022**, *61*, e202202912.

[60] Y. Yu, S. Lei, in *Encycl. Interfacial Chem.*, Elsevier, **2018**, pp. 414–423.

[61] T. Zhang, G. Zhang, L. Chen, *Acc. Chem. Res.* **2022**, *55*, 795–808.

[62] S. Kandambeth, K. Dey, R. Banerjee, *J. Am. Chem. Soc.* **2019**, *141*, 1807–1822.

[63] M. S. Lohse, T. Bein, *Adv. Funct. Mater.* **2018**, *28*, 1705553.

[64] J. Song, J. Liu, C. Tuo, J. Zhang, S. Huang, S. Lu, J. He, L. Liao, Q. Fang, *Chem. – An Asian J.* **2025**, *20*, e202401608.

[65] Z. Zhou, H. Sun, Q. Qi, X. Zhao, *Angew. Chemie Int. Ed.* **2023**, *62*, e202305131.

[66] Y. Wan, P. Sun, L. Shi, X. Yan, X. Zhang, *J. Phys. Chem. Lett.* **2023**, *14*, 7411–7420.

[67] S. Ghosh, H. Küçükkeçeci, R. P. Paitandi, V. Weigelt, V. Dippold, S. Seki, A. Thomas, *J. Mater. Chem. A* **2024**, *12*, 247–255.

[68] D. Wei, W. Zhao, C. Xing, Y. Zhang, H. Li, Y. Zhi, *ACS Appl. Polym. Mater.* **2024**, *6*, 8498–8504.

[69] J. Zhu, W. Li, X. Qi, C. Sun, W. Li, Z. Chang, *J. Mol. Struct.* **2024**, *1301*, 137414.

[70] Y. Zhang, G. Wang, *Spectrochim. Acta Part A Mol. Biomol. Spectrosc.* **2024**, *318*, 124483.

[71] S. Kim, H. Jung, M. S. Okyay, H. Noh, S. Chung, Y. H. Kim, J. Jeon, B. M. Wong, K. Cho, J. Seo, J. Yoo, J. Baek, *Angew. Chemie* **2023**, *135*, e202310560.

[72] X. Zhang, F. Li, S. Yang, B. Song, R. Luo, R. Xiong, W. Xu, *SusMat* **2024**, *4*, 4–33.

[73] W. Li, W. Xie, F. Shao, J. Qian, S. Han, P. Wen, J. Lin, M. Chen, X. Lin, *Chem* **2023**, *9*, 117–129.

[74] Y. Yang, K. Börjesson, *Trends Chem.* **2022**, *4*, 60–75.

[75] A. M. Khattak, Z. A. Ghazi, B. Liang, N. A. Khan, A. Iqbal, L. Li, Z. Tang, *J. Mater. Chem. A* **2016**, *4*, 16312–16317.

[76] E.-A. Bittner, K. Merkel, F. Ortmann, *npj 2D Mater. Appl.* **2024**, *8*, 58.

[77] J. Huang, J.-H. Su, H. Tian, *J. Mater. Chem.* **2012**, *22*, 10977.

[78] J.-L. H. A. Duprey, D. M. Bassani, E. I. Hyde, C. Ludwig, A. Rodger, J. S. Vyle, J. Wilkie, Z.-Y. Zhao, J. H. R. Tucker, *Supramol. Chem.* **2011**, *23*, 273–277.

[79] J.-L. H. A. Duprey, G. A. Bullen, Z. Zhao, D. M. Bassani, A. F. A. Peacock, J. Wilkie, J. H. R. Tucker, *ACS Chem. Biol.* **2016**, *11*, 717–721.

[80] M. O'Donnel, *Nature* **1968**, *218*, 460–461.

[81] V. M. Tapilin, N. N. Bulgakov, A. P. Chupakhin, A. A. Politov, *J. Struct. Chem.* **2008**, *49*, 581–586.

[82] K. S. Wei, R. Livingston, *Photochem. Photobiol.* **1967**, *6*, 229–232.

[83] G. W. Breton, X. Vang, *J. Chem. Educ.* **1998**, *75*, 81.

[84] K. Kondratenko, I. Carlescu, P.-E. Danjou, Y. Boussoualem, A. Simion, B. Duponchel, J. F. Blach, C. Legrand, N. Hurduc, A. Daoudi, *Phys. Chem. Chem. Phys.* **2021**, *23*, 13885–13894.

[85] H. Bouas-Laurent, J.-P. Desvergne, A. Castellan, R. Lapouyade, *Chem. Soc. Rev.* **2000**,

29, 43–55.

[86] I. Novak, L. Klasinc, S. P. McGlynn, *Chem. Phys. Lett.* **2019**, *728*, 50–52.

[87] R. E. Pickering, E. J. Eisenbraun, D. Doughty, M. M. Strube, B. E. Gammon, *J. Label. Compd. Radiopharm.* **1988**, *25*, 83–87.

[88] S. Takenaka, K. Ohtuka, H. Miyahara, T. Nojima, M. Takagi, *Nucleic Acids Symp. Ser.* **2002**, *2*, 291–292.

[89] S. Fukuzumi, J. Yuasa, T. Miyagawa, T. Suenobu, *J. Phys. Chem. A* **2005**, *109*, 3174–3181.

[90] C. Zhou, Z. Liu, G. Liang, Y.-Q. Zhang, T. Lei, B. Chen, R.-Z. Liao, C.-H. Tung, L.-Z. Wu, *Org. Lett.* **2024**, *26*, 1116–1121.

[91] V. N. Huynh, M. Leitner, A. Bhattacharyya, L. Uhlstein, P. Kreitmeier, P. Sakrausky, J. Rehbein, O. Reiser, *Commun. Chem.* **2020**, *3*, 158.

[92] J. Van Damme, F. Du Prez, *Prog. Polym. Sci.* **2018**, *82*, 92–119.

[93] R. F. Costa, M. S. Oliveira, A. S. N. Aguiar, J. M. F. Custodio, P. Di Mascio, J. R. Sabino, G. V. Verde, J. C. P. de Souza, L. G. Santin, A. J. Camargo, I. C. Barbosa, S. S. Oliveira, H. B. Napolitano, *Crystals* **2021**, *11*, 934.

[94] F. Liu, L. Zhang, R. Wang, J. Sun, J. Yang, Z. Chen, X. Wang, D. Sun, *CrystEngComm* **2014**, *16*, 2917–2928.

[95] K. Konstas, K. F. Taupitz, D. R. Turner, D. F. Kennedy, M. R. Hill, *CrystEngComm* **2014**, *16*, 8937–8940.

[96] J.-R. Zhang, H.-Y. Zhang, J.-H. Guo, Z.-H. Liu, C.-Y. Ma, X.-G. Yang, X.-Y. Lu, J.-H. Qin, L.-F. Ma, *Dalt. Trans.* **2022**, *51*, 1769–1774.

[97] X. Liu, B. Liu, G. Li, Y. Liu, *J. Mater. Chem. A* **2018**, *6*, 17177–17185.

[98] Q. An, S. Bao, X. Li, J. Sun, Z. Su, *New J. Chem.* **2022**, *46*, 11377–11381.

[99] Y. Liu, Z. Zhao, W. Xu, W. Gong, *Catal. Sci. Technol.* **2024**, *14*, 3211–3218.

[100] L. Li, Q. Shan, J. Zang, L. Yu, D. J. Young, Z.-G. Ren, H.-X. Li, *Catal. Sci. Technol.* **2024**, *14*, 7212–7218.

[101] X. Jiang, A. Wang, J. Peng, X. Song, L. Wang, *Inorg. Chem.* **2024**, *63*, 23028–23035.

[102] M. Faheem, S. Aziz, X. Jing, T. Ma, J. Du, F. Sun, Y. Tian, G. Zhu, *J. Mater. Chem. A* **2019**, *7*, 27148–27155.

[103] N. Huang, X. Ding, J. Kim, H. Ihee, D. Jiang, *Angew. Chemie Int. Ed.* **2015**, *54*, 8704–8707.

[104] L. Zhao, Y. Gao, X. Fu, Y. Chen, B. Zhang, F. Xuan, *Small Methods* **2025**, *9*, 2401341.

[105] Y. Cheng, J. Xin, L. Xiao, X. Wang, X. Zhou, D. Li, B. Gui, J. Sun, C. Wang, *J. Am. Chem. Soc.* **2023**, *145*, 18737–18741.

[106] S. Haldar, D. Chakraborty, B. Roy, G. Banappanavar, K. Rinku, D. Mullangi, P. Hazra, D. Kabra, R. Vaidhyanathan, *J. Am. Chem. Soc.* **2018**, *140*, 13367–13374.

[107] M. Rose, R. Palkovits*, in *Met. Org. Fram. as Heterog. Catal.*, The Royal Society Of Chemistry, **2013**, pp. 384–405.

[108] O. M. Yaghi, M. J. Kalmutzki, C. S. Diercks, in *Introd. to Reticular Chem.*, Wiley, **2019**, pp. 245–266.

[109] C.-F. Fu, C. Zhao, Q. Zheng, X. Li, J. Zhao, J. Yang, *Sci. China Chem.* **2020**, *63*, 1134–1141.

[110] D. Cao, J. Guan, J. Du, Q. Sun, J. Ma, J. Li, J. Liu, G. Sheng, *J. Hazard. Mater.* **2024**, *476*, 134956.

[111] K. Zhao, H. Qiao, S. Wang, X. Xu, C. Wang, M. Jiao, L. Yang, X. Kong, Z. Zhu, N. Qin, L. Zhai, *ACS Mater. Lett.* **2024**, *6*, 212–221.

[112] X. Wu, Y. Hong, B. Xu, Y. Nishiyama, W. Jiang, J. Zhu, G. Zhang, S. Kitagawa, S. Horike, *J. Am. Chem. Soc.* **2020**, *142*, 14357–14364.

[113] W. Li, Y. Cheng, D. Yang, Y. Liu, B. Han, *Macromol. Rapid Commun.* **2023**, *44*, 2200778.

[114] R. Singh, V. Kaur, in *Covalent Org. Fram.*, CRC Press, Boca Raton, **2022**, pp. 361–378.

[115] G. O. Aksu, S. Keskin, *ACS Appl. Mater. Interfaces* **2024**, *16*, 19806–19818.

[116] J. Hu, J. Zhao, T. Yan, *J. Phys. Chem. C* **2015**, *119*, 2010–2014.

[117] Q. Li, Y. Xu, Z. Lin, Z. Sun, Y. Liu, *Sep. Purif. Technol.* **2025**, *367*, 132992.

[118] M. Wang, Z. Wang, M. Shan, J. Wang, Z. Qiu, J. Song, Z. Li, *Chem. Mater.* **2023**, *35*, 5368–5377.

[119] B. Ma, X. Lin, T. Zhu, X. Zheng, J. Zhu, *Colloids Surfaces B Biointerfaces* **2024**, *242*, 114101.

[120] M. Yang, L. Fang, J. Li, Z. Yuan, D. Yu, X. Chen, *Adv. Photonics Res.* **2022**, *3*, 2200008.

[121] M. Martínez-Fernández, E. Martínez-Periñán, A. de la Peña Ruigómez, J. J. Cabrera-Trujillo, J. A. R. Navarro, F. Aguilar-Galindo, D. Rodríguez-San-Miguel, M. Ramos, R. Vismara, F. Zamora, E. Lorenzo, J. L. Segura, *Angew. Chemie* **2023**, *135*, e202313940.

[122] J. Zhao, T. Yan, *RSC Adv.* **2014**, *4*, 15542–15551.

[123] R. Siddiqui, J. Rani, H. M. Titi, R. Patra, *Coord. Chem. Rev.* **2024**, *517*, 215994.

[124] P. Politzer, J. S. Murray, in *Pract. Asp. Comput. Chem.*, Springer Netherlands, Dordrecht, **2009**, pp. 149–163.

[125] T. Clark, M. Hennemann, J. S. Murray, P. Politzer, *J. Mol. Model.* **2007**, *13*, 291–296.

[126] M. H. Kolář, D. Suchá, M. Pitoňák, *Int. J. Quantum Chem.* **2020**, *120*, 1–12.

[127] P. Politzer, J. S. Murray, T. Clark, *Phys. Chem. Chem. Phys.* **2010**, *12*, 7748.

[128] N. Guo, R. Maurice, D. Teze, J. Graton, J. Champion, G. Montavon, N. Galland, *Nat. Chem.* **2018**, *10*, 428–434.

[129] P. Auffinger, F. A. Hays, E. Westhof, P. S. Ho, *Proc. Natl. Acad. Sci.* **2004**, *101*, 16789–16794.

[130] H. Pinto de Magalhães, A. Togni, H. P. Lüthi, *J. Org. Chem.* **2017**, *82*, 11799–11805.

[131] J. Kang, J. Hang, B. Chen, L. Chen, P. Zhao, Y. Xu, Y. Luo, C. Xia, *ACS Appl. Mater. Interfaces* **2022**, *14*, 57225–57234.

[132] L. Cusin, H. Peng, A. Ciesielski, P. Samorì, *Angew. Chemie Int. Ed.* **2021**, *60*, 14236–14250.

[133] Q. Yu, W. Zhang, H. Chen, J. Wang, Z. Wang, Q. Ding, L. Zhang, *Anal. Chim. Acta* **2023**, *1284*, 342002.

[134] Q. Yan, H. Xu, X. Jing, H. Hu, S. Wang, C. Zeng, Y. Gao, *RSC Adv.* **2020**, *10*, 17396–17403.

[135] A. Khojastehnezhad, A. Samie, A. Bisio, H. M. El-Kaderi, M. Siaj, *ACS Appl. Mater. Interfaces* **2025**, *17*, 11415–11442.

[136] X. Han, J. Huang, C. Yuan, Y. Liu, Y. Cui, *J. Am. Chem. Soc.* **2018**, *140*, 892–895.

[137] Z. B. Zhou, X. H. Han, Q. Y. Qi, S. X. Gan, D. L. Ma, X. Zhao, *J. Am. Chem. Soc.* **2022**, *144*, 1138–1143.

[138] M. Dinari, Z. Golshadi, P. Asadi, A. E. Norton, K. R. Reid, B. Karimi, *Nanomaterials* **2024**, *14*, 1458.

[139] N. Wang, X. Qi, F. Xiao, *Colloids Surfaces A Physicochem. Eng. Asp.* **2024**, *697*, 134440.

[140] Y. Li, L. Yang, H. He, L. Sun, H. Wang, X. Fang, Y. Zhao, D. Zheng, Y. Qi, Z. Li, W. Deng, *Nat. Commun.* **2022**, *13*, 1355.

[141] E. Park, J. Jack, Y. Hu, S. Wan, S. Huang, Y. Jin, P. C. Maness, S. Yazdi, Z. Ren, W. Zhang, *Nanoscale* **2020**, *12*, 2596–2602.

[142] L. Zhang, C. Han, P. Zhang, W. Fu, Y. Nie, Y. Wang, *Nanoscale* **2021**, *13*, 18665–18676.

[143] Z. Zhang, Z. Zhang, C. Chen, R. Wang, M. Xie, S. Wan, R. Zhang, L. Cong, H. Lu, Y. Han, W. Xing, Z. Shi, S. Feng, *Nat. Commun.* **2024**, *15*, 2556.

[144] N. Wang, J. Liu, L. Tang, C. Wang, X. Li, L. Ma, *ChemCatChem* **2022**, *14*, e202101587.

[145] T. Sun, H. Zhang, Y. Wang, N. Zhang, L. Shao, H. Dong, F. Zhang, *Angew. Chemie* **2025**, *202515397*, e202515397.

[146] S. Divya, P. Singh, S. Hashmi, A. Kumar, A. Misra, N. Singh, R. Dixit, P. K. Katiyar, *Curr. Drug ther.* **2025**, *20*, 742–753.

[147] M. Jorns, D. Pappas, *Nanomaterials* **2021**, *11*, 1448.

[148] H. F. Etefa, A. A. Tessema, F. B. Dejene, *C* **2024**, *10*, 60.

[149] S. Kumar, J. Gaur, S. Kaushal, J. Dalal, M. Misra, H. Kaur, S. Kaur, N. Kaur, G. Singh, G. Singh, *Crystals* **2025**, *15*, 320.

[150] M. Fu, F. Ehrat, Y. Wang, K. Z. Milowska, C. Reckmeier, A. L. Rogach, J. K. Stolarczyk, A. S. Urban, J. Feldmann, *Nano Lett.* **2015**, *15*, 6030–6035.

[151] S. K. Kulkarni, A. S. Ethiraj, S. Kharrazi, D. N. Deobagkar, D. D. Deobagkar, *Biosens. Bioelectron.* **2005**, *21*, 95–102.

[152] A. Deb, D. Chowdhury, *Curr. Med. Chem.* **2024**, *31*, 3899–3924.

[153] C. Olla, A. Cappai, S. Porcu, L. Stagi, M. Fantauzzi, M. F. Casula, F. Mocci, R. Corpino, D. Chiriu, P. C. Ricci, C. M. Carbonaro, *Nanomaterials* **2023**, *13*, 1344.

[154] L. Chen, C. Wang, C. Liu, S. Chen, *Small* **2023**, *19*, 2206671.

[155] R. Wang, K.-Q. Lu, Z.-R. Tang, Y.-J. Xu, *J. Mater. Chem. A* **2017**, *5*, 3717–3734.

[156] Y. Hu, J. Yang, J. Tian, J.-S. Yu, *J. Mater. Chem. B* **2015**, *3*, 5608–5614.

[157] W. Zhu, X. Feng, M. Zhao, Z. Wei, Z. Liu, G. Wang, Q. Guo, D. Chen, *Diam. Relat. Mater.* **2021**, *116*, 108395.

[158] L. Wang, Y. Wang, T. Xu, H. Liao, C. Yao, Y. Liu, Z. Li, Z. Chen, D. Pan, L. Sun, M. Wu, *Nat. Commun.* **2014**, *5*, 5357.

[159] P. Wang, C. Liu, W. Tang, S. Ren, Z. Chen, Y. Guo, R. Rostamian, S. Zhao, J. Li, S. Liu, S. Li, *ACS Appl. Mater. Interfaces* **2019**, *11*, 19301–19307.

[160] H. B. A. Sousa, C. S. M. Martins, J. A. V. Prior, *Nanomaterials* **2021**, *11*, 611.

[161] K. Tungare, M. Bhori, K. S. Racherla, S. Sawant, *3 Biotech* **2020**, *10*, 540.

[162] J. Tan, R. Zou, J. Zhang, W. Li, L. Zhang, D. Yue, *Nanoscale* **2016**, *8*, 4742–4747.

[163] S. Wang, L. Guo, L. Chen, L. Wang, Y. Song, *ACS Appl. Nano Mater.* **2022**, *5*, 1339–1347.

[164] J. Zang, Y. Zhao, L. Yu, D. J. Young, Z.-G. Ren, H.-X. Li, *J. Mater. Chem. A* **2025**, *13*, 1932–1941.

[165] Y. Li, K. Chen, H. Yu, Y. Song, Y. Du, *Ionics (Kiel).* **2024**, *30*, 95–103.

[166] S. M. Arachchige, K. J. Brewer, in *Encycl. Inorg. Chem.*, Wiley, **2005**.

[167] A. Fujishima, K. Honda, *Nature* **1972**, *238*, 37–38.

[168] L. Stegbauer, K. Schwinghammer, B. V. Lotsch, *Chem. Sci.* **2014**, *5*, 2789–2793.

[169] L. Qin, C. Ma, J. Zhang, T. Zhou, *Adv. Funct. Mater.* **2024**, *34*, 2401562.

[170] C. Zhou, L. Tao, J. Gao, J. Dong, Q. Zhu, C. Liao, *J. Environ. Sci.* **2025**, *153*, 172–181.

[171] Q. Yang, M. Luo, K. Liu, H. Cao, H. Yan, *Appl. Catal. B Environ.* **2020**, *276*, 119174.

[172] J. Ding, X. Guan, J. Lv, X. Chen, Y. Zhang, H. Li, D. Zhang, S. Qiu, H.-L. Jiang, Q. Fang, *J. Am. Chem. Soc.* **2023**, *145*, 3248–3254.

[173] Q. Lin, Y. Yusran, J. Xing, Y. Li, J. Zhang, T. Su, L. Yang, J. Suo, L. Zhang, Q. Li, H. Wang, Q. Fang, Z.-T. Li, D.-W. Zhang, *ACS Appl. Mater. Interfaces* **2024**, *16*, 5869–5880.

[174] H. Liu, S. Zhu, Y. Zhi, H. Yue, X. Liu, *Chem. Sci.* **2025**, *16*, 12768–12803.

[175] J. Liu, C. Tuo, W. Xiao, M. Qi, Y. Yusran, Z. Wang, H. Li, C. Guo, J. Song, S. Qiu, Y. Xu, Q. Fang, *Angew. Chemie Int. Ed.* **2025**, *64*, e202416240.

[176] S. Golunski, *JOM* **2001**, *53*, 22–24.

[177] Y. Li, L. Yang, H. He, L. Sun, H. Wang, X. Fang, Y. Zhao, D. Zheng, Y. Qi, Z. Li, W. Deng, *Nat. Commun.* **2022**, *13*, 1355.

[178] D. W. Bahnemann, J. Schneider, *ECS Meet. Abstr.* **2015**, *MA2015-01*, 1982.

[179] U. Pal, S. Ghosh, D. Chatterjee, *Transit. Met. Chem.* **2012**, *37*, 93–96.

[180] J. C. Wilson, S. Caratzoulas, D. G. Vlachos, Y. Yan, *Nat. Commun.* **2023**, *14*, 2384.

[181] E. E. Siddharthan, S. Ghosh, R. Thapa, *ACS Appl. Energy Mater.* **2023**, *6*, 8941–8948.

[182] E. Santos, P. Hindelang, P. Quaino, W. Schmickler, *Phys. Chem. Chem. Phys.* **2011**, *13*, 6992.

[183] J. Yang, A. Acharjya, M. Ye, J. Rabeah, S. Li, Z. Kochovski, S. Youk, J. Roeser, J. Grüneberg, C. Penschke, M. Schwarze, T. Wang, Y. Lu, R. van de Krol, M. Oschatz, R. Schomäcker, P. Saalfrank, A. Thomas, *Angew. Chemie Int. Ed.* **2021**, *60*, 19797–19803.

[184] S. Altınışık, G. Yanalak, İ. Hatay Patır, S. Koyuncu, *ACS Appl. Mater. Interfaces* **2023**, *15*, 18836–18844.

[185] Y. Yao, Y. Han, S. Qi, D. Sun, J. Lang, B. Hu, Y. Ma, C. Liu, *Int. J. Hydrogen Energy* **2024**, *63*, 184–192.

[186] A. E. Hassan, A. M. Elewa, M. S. A. Hussien, A. F. M. EL-Mahdy, I. M. A. Mekhemer, I. S. Yahia, T. A. Mohamed, H.-H. Chou, Z. Wen, *J. Colloid Interface Sci.* **2024**, *653*, 1650–1661.

[187] D. Liu, C. Zhu, G. Yuan, *Mater. Lett.* **2024**, *365*, 136417.

[188] Y. Xiao, K. Wang, W. Dong, L. Li, *Polymer (Guildf).* **2024**, *300*, 126980.

[189] N. Khan, C. Azad, M. Luo, J. Chen, T. Kesharwani, A. Badshah, D. Wang, *Energies* **2023**, *16*, 5888.

[190] R. Shen, X. Li, C. Qin, P. Zhang, X. Li, *Adv. Energy Mater.* **2023**, *13*, 2203695.

[191] L. Hao, R. Shen, C. Huang, Z. Liang, N. Li, P. Zhang, X. Li, C. Qin, X. Li, *Appl. Catal. B Environ.* **2023**, *330*, 122581.

[192] Z. Mi, T. Zhou, W. Weng, J. Unruangsri, K. Hu, W. Yang, C. Wang, K. A. I. Zhang, J. Guo, *Angew. Chemie Int. Ed.* **2021**, *60*, 9642–9649.

[193] L. Zou, D. Si, S. Yang, Z. Chen, Y. Huang, R. Cao, *Angew. Chemie Int. Ed.* **2025**, *64*, e202418319.

[194] H. Qian, F. Meng, C. Yang, X. Yan, *Angew. Chemie Int. Ed.* **2020**, *59*, 17607–17613.

2. Characterization techniques

2.1. Powder X-ray diffraction (PXRD)

The characterization of Covalent Organic Frameworks (COFs) usually begins with an evaluation of their structural order, crystalline structure, and morphological characteristics. Powder X-ray diffraction (PXRD) is the primary method utilized for examining the crystallinity of COFs. This analytical approach evaluates the crystallinity and structural properties of powders, films, and single crystals across a diverse range of compounds, while also enabling the characterization of phase compositions. The PXRD technique stands out as an excellent tool for characterization of COFs, covering aspects like topology, lattice parameters and stacking arrangement.

The discovery of X-rays, which possess typical wavelengths between 5 pm and 100 pm, was made by Wilhelm Conrad Röntgen in 1895.[1] Fundamentally, X-rays are generated when accelerated and focused electrons collide with a metallic target. This process typically leads to an empty spot forming in the atom's inner electron shells, which is then occupied by an electron from an outer shell, resulting in the release of an X-ray photon that matches the energy difference between the two configurations. The wavelength and intensity of the emitted X-rays are contingent upon the specific metal target utilized, with variations attributable to the differing electron shell structures of various target materials, as articulated by Moseley's law.

$$\frac{1}{\lambda} = \frac{K}{(Z-\sigma)^2} \qquad (2.1)$$

λ is the X-ray wavelength; Z is the atomic number; K and σ are constants associated with a particular spectral line.

To isolate a prominent segment of the spectrum, typically Kα radiation, distinct metal filters and a collimator are employed. Upon interaction with a collimated X-ray beam, the crystalline phases present within the specimen cause diffraction of the rays in accordance with Bragg's law:[2]

$$n\lambda = 2d\sin\theta \qquad (2.2)$$

n is an integer; d is the spacing between the lattice planes; θ is the angle between the incident X-rays and the lattice planes.

This methodology is based on the concept that X-rays are influenced by scattering at crystallite lattice planes characterized by a spacing similar to that of the X-ray wavelength. The angle at which X-rays strike can result in various scattering phenomena, implying that the scattered X-rays may interfere either in a constructive or destructive manner. The conditions under which constructive interference can be observed are elucidated through Bragg's law. As a result, the resultant pattern of constructive interference can be converted into a graphical representation of intensity as a function of the diffraction angle 2θ, commonly referred to as a diffraction pattern, which provides insights into the atomic arrangement within the crystal. Within this one-dimensional diffraction pattern, the constructive interference of diffracted X-rays is characterized by a peak, identified as a reflection, for which the measured intensities largely depend on the lattice atoms and their specific spatial arrangements (**Figure 2.1**).

The resulting diffraction data can significantly depend on the size of crystalline domains. In cases where the domains are small, the diffraction patterns exhibit a broadening of the reflections in contrast to those from larger domains. Evaluating peak broadening through the full width at half maximum (FWHM) makes it possible to estimate the size of crystallite domains.[3] The relationship between peak broadening and the domain size D is articulated in the Scherrer equation:[4]

$$D = \frac{k\,\lambda}{\beta\,cos\,\Theta} \qquad (2.3)$$

D is the domain size, k is a form-dependent factor, β is the FWHM of the reflection.

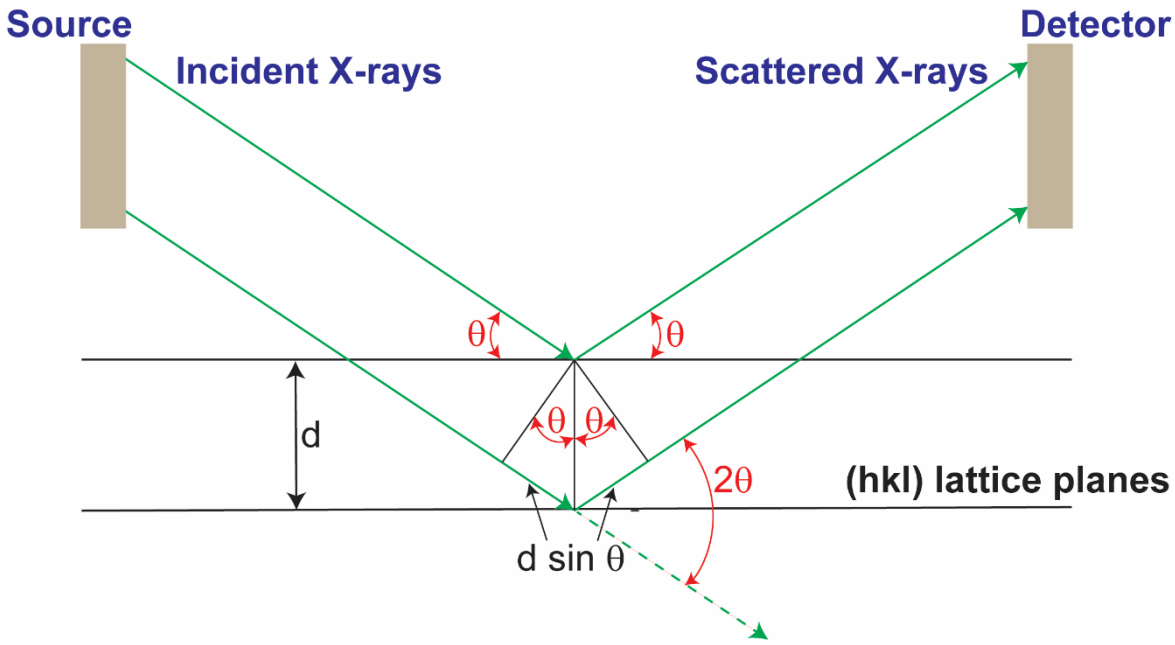

Figure 2.1. Schematic representation of diffraction and Bragg's law. Two X-ray beams are directed at a crystalline sample, reflecting off the crystal planes and being captured by a detector positioned to ensure that the angles of the incident and scattered X-rays are identical (θ-θ geometry).

This method was used to determine the crystallinity and structure of the samples and to calculate Pt particle size. The PXRD measurements were performed with a Bruker D8 Discover with Ni-filtered Cu-Kα- radiation and a position-sensitive semiconductor detector (LynxEye).

2.2. Gas sorption

The gas sorption analysis is method used to characterize porous materials like COFs and to determine porosity properties including surface area, pore size and pore volume. The ratio of the complete pore volume to the mass or volume of solid particles quantitatively defines the porosity of a particular sample. Throughout the adsorption phase, molecules or ions frequently accumulate close to an interface. Two primary categories of adsorption can be identified, that is, physisorption (without forming bonds), and chemisorption, defined by the establishment of chemical bonds. In chemisorption, the molecules that are adsorbed create bonds with certain regions of the surface, generally (but not always) leading to a single layer formation. This process is frequently associated with elevated heats of adsorption, in contrast to physisorption,

which is merely linked to minimal thermal exchanges with the surrounding environment. Furthermore, in physisorption surface coverage generally is not restricted to a single layer and may manifest as multilayer adsorption at elevated relative pressures. Besides, the chemical arrangement of the adsorbent is unaffected as physisorption takes place. The physical interactions that occur between the gas or vapor (adsorptive) and the surface of the sample (adsorbent) are predominantly governed by van der Waals forces. The surface of the sample (adsorbent) may be externally covered by the adsorptive, occurring outside the pores, as well as internally, within the pores. Another distinguishing characteristic between the two main adsorption types is that the physisorbed molecules (adsorbate) exist in a state of dynamic equilibrium with the adsorptive. Owing to the reversible nature of the interaction between adsorptive and adsorbent, the fluid phase can revert to its original form post-desorption. In contrast, a chemisorbed molecule is typically not recoverable through desorption due to reactions or dissociations that transpire during the adsorption process, thus rendering the sorption isotherms irreversible.[5,6]

To classify porous materials, the IUPAC established definitions in 1985 based on their pore diameter, categorizing macropores as those with widths greater than approximately 50 nm, mesopores as having sizes ranging from 2 to 50 nm, and micropores as being no more than 2 nm. The IUPAC has identified six major categories of physisorption isotherms, which can be generated by plotting the relative pressure of the adsorptive against the volume of gas adsorbed at a standard pressure and constant temperature.[7]

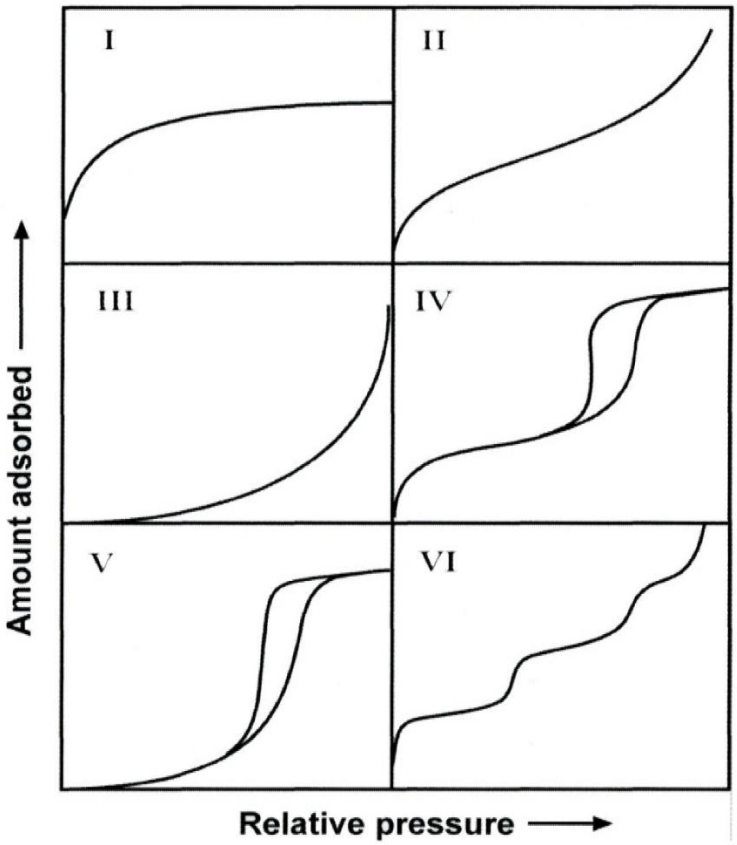

Figure 2.2. Classification of the physisorption isotherms according to IUPAC. Adapted with permission from Alothman.[8] Copyright 2012 MDPI. This article is an open access article distributed under the terms and conditions of the Creative Commons Attribution (CC BY) license (http://creativecommons.org/licenses/by/4.0/).

Type I isotherms are characteristic of microporous adsorbents. They exhibit a steep increase in adsorption at low relative pressures P/P_0 (with P_0 being the saturation pressure and P the actual pressure of the adsorptive) due to micropore filling, which eventually reaches saturation determined by the micropore volume.

Type II isotherm is associated with nonporous or macroporous adsorbents. The initial uptake results from monolayer coverage, which is succeeded by multilayer adsorption.

Type III isotherms characterize nonporous or macroporous substances that exhibit weak interactions with the adsorbate.

Type IV isotherms illustrate the behavior of mesoporous adsorbents. At first, a single layer forms and then multiple layers start to accumulate, eventually leading to condensation in the pores, which culminates in the complete filling of the pores by the adsorbate. Pore condensation involves the process where a gas inside a pore changes into a liquid-like form. Hysteresis in mesoporous gas adsorption can arise because gas condenses and evaporates in pores at different pressures (capillary condensation, typically in pores > 4 nm diameter). It can occur if pore shapes (ink-bottle, cylindrical, interconnected networks) alter the filling/emptying mechanism, or if energy barriers for liquid nucleation and metastability (of the meniscus) delay evaporation relative to condensation.

Type V isotherms are observed for water adsorption on hydrophobic microporous or mesoporous materials. In general, these situations involve weak interactions between the adsorbent and the adsorbate, along with the process of pore filling and the aspect of hysteresis.

Type VI isotherms are frequently seen in nonporous materials that display a highly uniform surface. Each step in the uptake corresponds to an adsorbed monolayer.[7]

The Brunauer-Emmett-Teller (BET) technique is widely recognized as a standard method for determining the surface area of porous substances. In order to facilitate the modeling of the intricate interactions that occur between adsorbate molecules and solid surfaces, this methodology is predicated upon several simplifying assumptions:

- **Monolayer formation.** Gas molecules initially form a monolayer on the surface of the adsorbent prior to the onset of multilayer adsorption. This aspect is paramount for accurately assessing the surface area of the adsorbent.[9]

- **Uniform surface energy.** All adsorption sites across the surface exhibit equivalent energy levels, resulting in a consistent adsorption potential throughout the surface.[9]

- **Non-interacting adsorbates**. Adsorbed molecules do not interact (laterally) with each other, thus simplifying the calculations related to adsorption isotherms.[10]

- **Equilibrium conditions.** The BET equation's derivation is contingent upon the assumption that equilibrium exists between the adsorbed and gaseous phases, which is significant for precise modeling.[11]

The application of the BET method involves two stages:[7]

1) Converting a physisorption isotherm into the 'BET plot' and from this deriving the value of the BET monolayer capacity. It is standard practice to apply the BET equation in its linear form:

$$\frac{P/P_0}{n(1-P/P_0)} = \frac{1}{n_m C} + \frac{C-1}{n_m C}(P/P_0) \qquad (2.4)$$

P/P_0 is the relative pressure; P is the equilibrium pressure; P_0 is the saturation pressure; n is the amount adsorbed per gram adsorbent; n_m is the specific monolayer capacity; C is BET constant.

The linearity interval of the BET plot remains consistently limited to a particular segment of the isotherm, typically found within the P/P_0 range of roughly 0.05-0.30 for Type II and Type IV isotherms.

2) Calculation of specific BET surface area a(BET) from n_m by using an appropriate molecular cross-sectional area, σ_m.

$$a(BET) = \frac{n_m * N_a * \sigma_m}{m} \qquad (2.5)$$

N_a is the Avogadro number; m is the mass of the adsorbent.

The typical gas used for gas sorption in determining the BET surface area of COFs is nitrogen (N_2) at 77 K, as it is a non-reactive gas that interacts predictably with various porous materials.

In addition, sorption isotherms allow for the calculation of pore size through simulations based on density functional theory (DFT). In this process, the interactions between adsorbates and various pore shapes and surface characteristics were simulated, leading to the creation of

several models known as kernels. These kernels enable the theoretical modeling of isotherms, which can be adjusted to align with experimental data by modifying pore sizes. This system can use either non-local density functional theory (NLDFT) or the more innovative quenched-solid density functional theory (QSDFT), as NLDFT misses surface roughness and changes. The choice between these methods often depends on the specific characteristics of the material being studied and the level of accuracy required for modeling the adsorption process.[12]

Nitrogen sorption experiments were performed to determine BET surface area, pore size and pore volume. Isotherms were recorded on a Quantachrome Autosorb 1 at 77 K within a pressure range from P/P_0 = 0.001 to 0.98. Prior to the measurement of the sorption isotherms, the samples were heated for 24 h at 120 °C under turbo-pumped vacuum.

2.3. Thermogravimetric analysis (TGA)

Thermogravimetric analysis (TGA) is a method used to examine changes in the mass of a sample over time as the temperature increases. The sample is heated in a selected atmosphere (such as synthetic air, inert gases, vacuum, etc.), while a precise balance measures any mass losses or gains that may occur due to processes such as evaporation, decomposition, oxidation, or reduction. In the field of COFs, this technique is primarily used to assess the thermal stability of various COF materials and to identify solvent molecules that may be confined within the channel structure.[13]

In this thesis, TGA method was utilized to determine the thermal stability of the synthesized COFs. TGA measurements were performed on a Netzsch Jupiter ST 449 C instrument equipped with a Netzsch TASC 414/4 controller ((heating rate of 10 °C min^{-1} in a stream of synthetic air or nitrogen of about 25 mL min^{-1}).

2.4. Scanning electron microscopy (SEM)

Scanning electron microscopy (SEM) is a surface imaging method that utilizes a focused electron beam to gather information about the sample's topography and composition. This approach achieves a much higher resolution compared to light microscopes, owing to the significantly smaller de Broglie wavelength associated with electrons. An electron beam is systematically scanned over the sample, producing either backscattered or secondary electrons

that are subsequently detected. The variation in the quantity of detected electrons at distinct scanning locations allows for the generation of an image.

Two primary types of electron sources can be employed for SEM: a thermal emitter or a field emission gun (FEG). In this context, the emission of electrons can be initiated either thermally or through a strong electric field from a source like a tungsten cathode situated in a vacuum. The electrons are then guided towards the anode. Electromagnetic lenses generate a non-uniform magnetic field that focuses the electrons, which are then scanned over the sample. The SEM setup schematic is illustrated in **Figure 2.3**. When the electrons strike the sample, various interactions may occur, as depicted in **Figure 2.3**b. These processes take place within a pear-shaped interaction volume whose dimensions depend on the acceleration voltage and the atomic number of the material.

The key interactions for imaging in SEM include secondary electrons (SE) and backscattered electrons (BSE). SE originate from the top few nanometers of the sample due to their very low energies (<50 eV), which limits their escape depth. Therefore, SE imaging provides high-resolution topographic information. In contrast, BSE have significantly higher energies and can exit the sample from deeper regions of the interaction volume. Because the BSE yield increases with the average atomic number (Z) of the material, BSE imaging provides Z-contrast, enabling compositional or phase differentiation. Together, SE and BSE signals enable SEM to deliver both surface topography and elemental contrast.

The signals generated in SEM can be collected using different detector types, each designed for a specific class of emitted electrons. Due to their very low energies, SE are typically detected with scintillator-photomultiplier detectors. The most common is the Everhart-Thornley (ET) detector. This detector employs a positively biased collector that attracts the low-energy SE toward a scintillator, where they are converted into photons. The resulting light is amplified by a photomultiplier tube and used as the intensity signal for image formation, enabling high-resolution surface topography. BSE are typically detected using semiconductor detectors or scintillator-photomultiplier detectors. In a semiconductor detector, a doped silicon single crystal featuring a p-n-junction beneath the surface generates electron-hole pairs when illuminated by electrons. An external voltage or field is applied to separate these charge

carriers, allowing the signal to be detected and monitored. Utilizing a scintillator-photomultiplier detector, electrons are accelerated into the scintillator that generates photons, which are converted in the photomultiplier into a cascade of electrons, thereby producing the signal.[14]

In this thesis, the SEM technique was used to examine the morphological properties of the synthesized COFs. SEM images were recorded using an FEI Helios NanoLab G3 UC microscope at acceleration voltages of 1-30 kV.

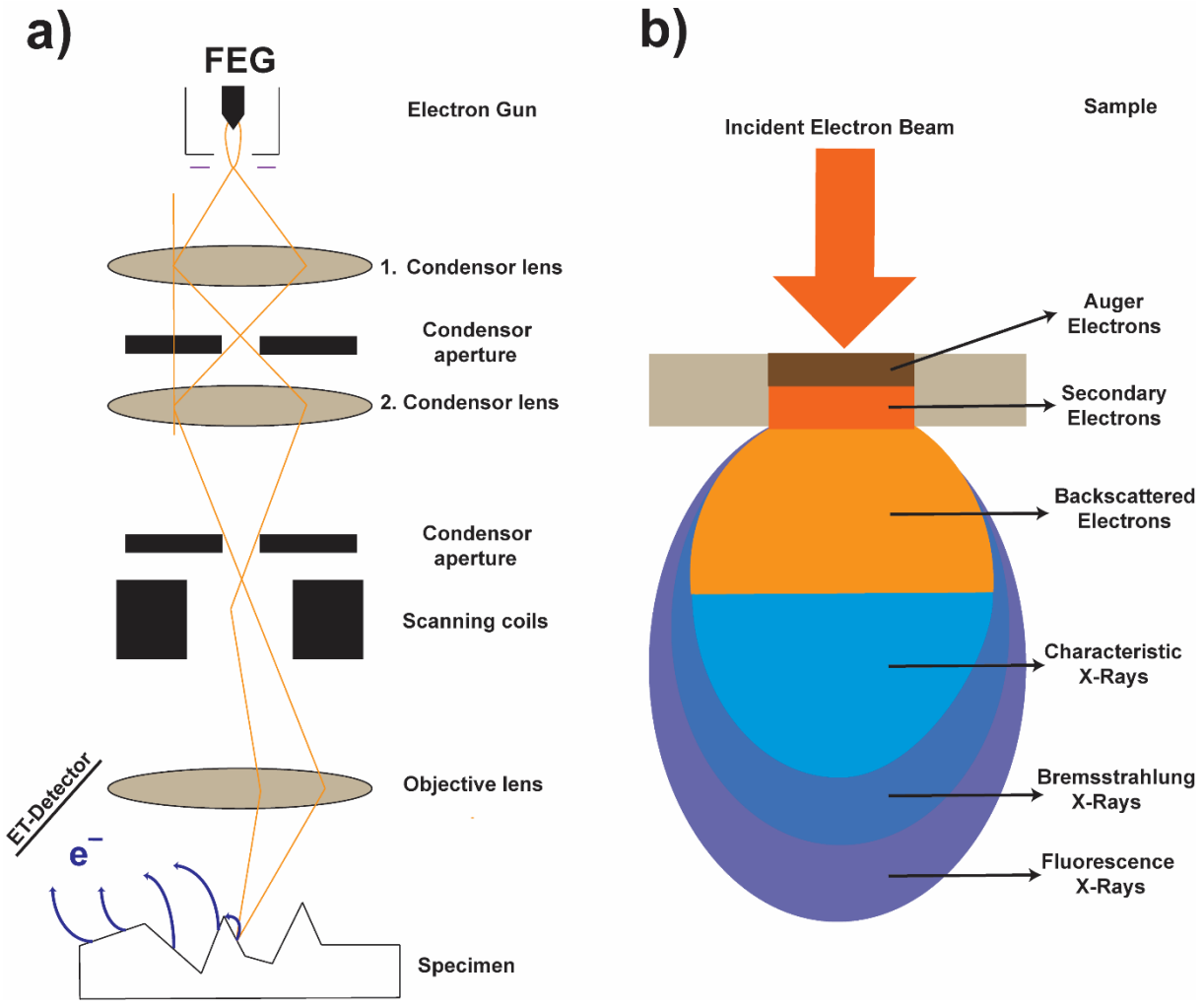

Figure 2.3. (a) Diagram illustrating the operational principles of SEM. Free electrons are produced within the electron gun and propelled towards the specimen. A series of condenser lens systems and apertures concentrates the electron beam onto the sample. The scanning coils manipulate the trajectory of the beam, thereby enabling the scanning process across the specimen. (b) The interaction volume established between the incident electron beam and the

sample (schematic), resulting in the generation of Auger electrons, secondary electrons, backscattered electrons, as well as characteristic X-rays and fluorescence.

2.5. Transmission electron microscopy (TEM)

Transmission electron microscopy (TEM) is a powerful analytical tool used to image and analyze objects far smaller than 10 nm and to obtain information about the internal structure of a material and for imaging of the internal structure. Through electron diffraction, data regarding samples can also be collected in reciprocal space. A key requirement for analyzing samples using TEM is their durability in the beam. Because high voltages ranging from 60 kV to 400 kV are employed during measurements, less stable samples may deteriorate or break down, resulting in reduced resolution and compromised image quality.[15]

The working principle of TEM is complementary to that of SEM. In the case of TEM, electrons that pass through the specimen are directed onto a detector area to create a visual representation. This method necessitates thin specimens (with thicknesses typically under 100 nm) and offers significantly higher resolution compared to SEM. Furthermore, unlike traditional SEM, TEM yields both imaging and diffraction data about the sample. **Figure 2.4** illustrates a schematic representation of the two different modes, which vary only in the imaging configuration of the intermediate lens. In both modes, the sample is illuminated by a nearly parallel beam of electrons, generated by the condenser lenses and a condenser aperture. Electrons detected could either be those that traveled through the sample without any scattering or those that experienced scattering from interactions with the sample. Inelastic scattering arises from the interactions between the primary electron beam and the electrons within the sample, influenced by variations such as composition and morphology. Consequently, electrons of differing intensities are captured and utilized for imaging purposes. Diffraction data from the sample can be gathered using the elastically scattered electrons, which do not experience energy loss. This technique enables the study of the crystal structure along with the morphology.[16]

In this thesis, the TEM technique was utilized to investigate the crystalline structure of the synthesized COFs, determine the sizes of crystalline domains, and to analyze the distribution

and size of Pt particles within the polymeric matrix. TEM images were recorded on an FEI Titan Themis transmission electron microscope equipped with a FEG run at 300 kV.

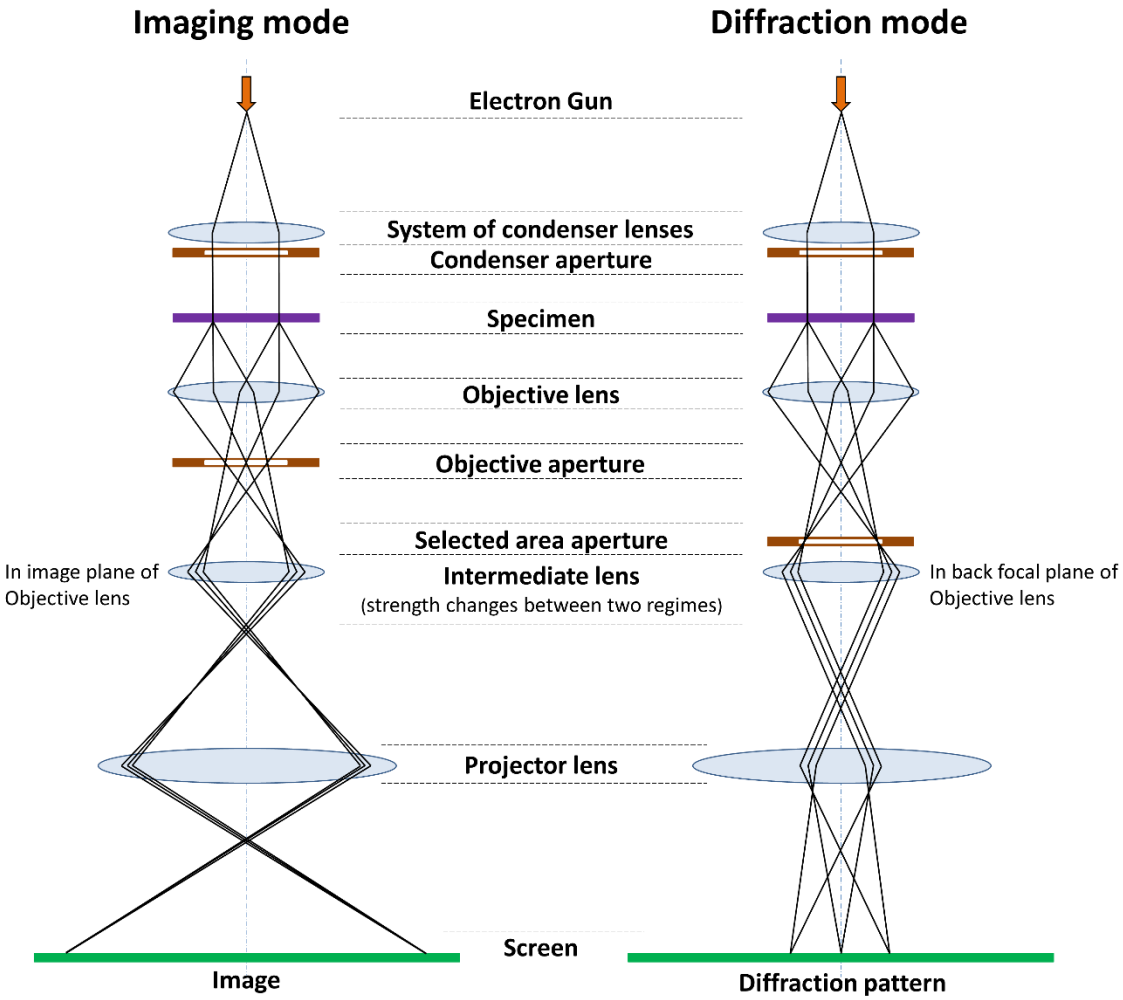

Figure 2.4. Schematic view of imaging and diffraction modes in TEM. Adapted from Ralf Mikut, Karlsruhe Institute of Technology (KIT).[17] Licensed under the Creative Commons Attribution-Share Alike (CC BY-SA 4.0) license. Available at https://commons.wikimedia.org/wiki/File:Schematic_view_of_imaging_and_diffraction_modes_in_TEM..tif

2.6. Infrared spectroscopy (IR)

Infrared spectroscopy (IR) is an analytical technique that can be used to identify and characterize the functional molecular groups within a material. This method is based on the interaction between infrared radiation and matter. Molecules absorb infrared radiation

according to their chemical composition and structure, with the corresponding resonant frequencies aligning with the vibrational or rotational excitations of the molecules. These frequencies are determined by the masses of the individual atoms as well as the nature and strength of the chemical bonds (coupling) within the molecules. A vibrational mode is considered IR-active only if there is a change in the dipole moment during the vibration. The number of vibrational modes can be calculated using the formula 3N-5 for linear molecules and 3N-6 for non-linear molecules, where N is the number of atoms. IR spectral analysis encompasses three regions: near-IR (14,000-4,000 cm^{-1}, associated with overtone or harmonic vibrations), mid-IR (4,000-400 cm^{-1}, corresponding to fundamental vibrations), and far-IR (400-10 cm^{-1}, relevant to rotational spectroscopy). Among these, the mid-IR region is primarily used in IR spectroscopy.

Fourier transform infrared (FT-IR) spectroscopy is commonly employed to collect IR spectra. Starting with a broad spectrum of wavelengths, the light beam passes through a Michelson interferometer - a specific arrangement of moving mirrors and a beam splitter. By adjusting the position of one mirror, the spectrum is modulated through wave interference. After passing through the sample, the beam is attenuated due to absorption and then detected. Computational (Fourier transform) analysis is used to determine absorption at each wavelength, thereby generating the IR spectrum. This technique enables efficient, precise measurements with an excellent signal-to-noise ratio.[18,19]

In this thesis, the IR method was employed to confirm the formation of linkages in the synthesized COFs from the monomers and to identify newly formed linkages resulting from the linkage conversion reactions. IR spectra were recorded using a PerkinElmer Spectrum BX II FT-IR system equipped with a diamond attenuated total reflectance (ATR) unit.

2.7. Ultraviolet-visible spectroscopy (UV-Vis)

Ultraviolet-visible (UV-vis) spectroscopy is a powerful analytical technique used to measure the absorbance or transmittance of ultraviolet and visible light by a sample, providing valuable information about the extent of π-conjugation and electronic transitions within the system. This method is based on the principle that different substances absorb light at specific wavelengths, allowing, for example, the identification and quantification of various compounds in a mixture.

The electromagnetic radiation in the UV-Vis range interacts with absorbing substances, leading to electronic transitions (wherein electrons transition from their ground state to an elevated energy state). In addition to liquids, solid samples can also be assessed both quantitatively and qualitatively via absorption.[20]

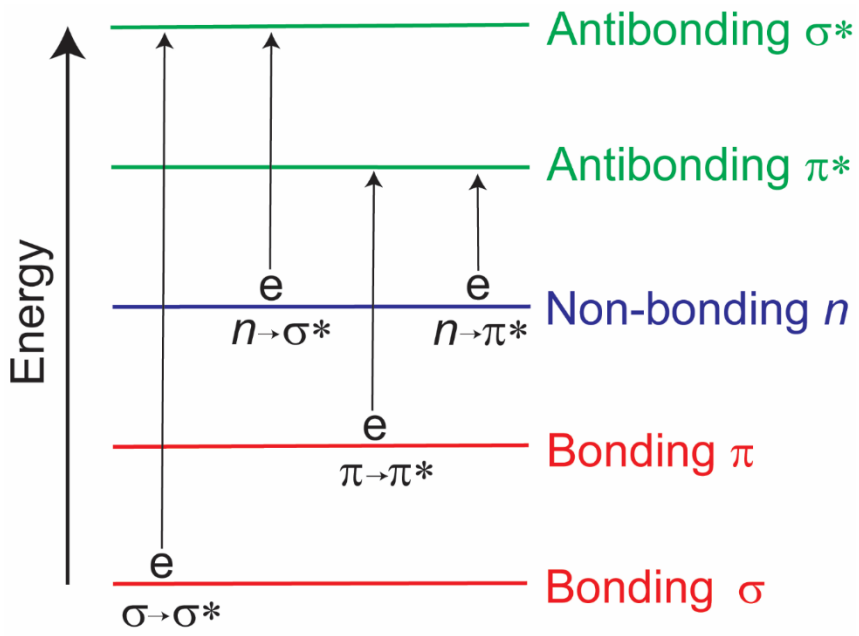

Figure 2.5. Expected electronic transitions in substances involving *σ, π,* and *n* electrons.

The connection between the intensity of transmitted light that is observed, the concentration of the absorbing medium, and the length of the optical path is defined by the Lambert-Beer law:[21]

$$A = -log_{10}\frac{I}{I_0} = \varepsilon * c * L \qquad (2.6)$$

A is the absorbance; I is the intensity of transmitted light; I_0 is the intensity of incident light; ε is the extinction coefficient; c is the concentration of the absorbing sample; L is the length of the medium.

Conversely, the absorption can be determined by measuring both the transmittance (T) and reflectance (R) using the formula:[22]

$$\%T + \%R + \%A = 1 \qquad (2.7)$$

In this work, UV-Vis spectroscopy was used to measure absorbance and reflectance of the precursors (soluble monomers) and COFs (insoluble powders). To calculate absorption spectra for the solids (powders), the Kubelka-Munk (KM) theory is used.[23] The theory assumes that

the sample is an (optically) infinitely thick, homogeneous, and isotropic scattering medium (absorption coefficient *K* and scattering coefficient *S* are assumed to be constant throughout). Light propagation is described by only two diffuse fluxes, one downward into the sample, the other upward into the detector, and specular reflection (and luminescence) are considered negligible. Under these conditions, the Kubelka–Munk function (Equation 2.8) *KM=R/S* relates the measured diffuse reflectance *R* to the absorption coefficient *K* and the scattering coefficient *S*, thereby enabling semiquantitative estimation of band gaps. For the powder measurements, pure barium sulfate served as a reference standard for diffuse reflectance. During the measurement, a minimal quantity of the sample was meticulously ground with barium sulfate to create a homogenous mixture suitable for analysis. The measured *R* can be transformed using the Kubelka-Munk equation into a spectrum that closely approximates the absorption characteristics:

$$KM = \frac{(1-R)^2}{2R} \qquad (2.8)$$

Reflectance data, converted using the Kubelka-Munk function, or direct absorbance measurements can also be used to determine the optical bandgap of a material via the Tauc plot method:[24]

$$(\alpha h\nu)^{1/r} = A(h\nu - E_g) \qquad (2.9)$$

α (or *K* above) is the absorption coefficient or absolute absorbance; *v is* the frequency of light; *h is* Planck's constant; *r* is a constant that defines the type of electronic transition in a material, determining whether it is direct (r = 0.5) or indirect (r = 2); E_g is the optical bandgap; *A* is the proportionality constant.

UV-Vis-NIR spectra were recorded using a Perkin-Elmer Lambda 1050 spectrometer equipped with a 150 mm integrating sphere and photomultiplier tube and InGaAs detectors. Diffuse reflectance spectra were collected with a Praying Mantis (Harrick) accessory.

2.8. Photoluminescence spectroscopy (PL)

Photoluminescence spectroscopy (PL) is a powerful optical technique used to characterize the electronic and optical properties of semiconductors and their nanostructures. The working principle of PL is presented in a Jablonski diagram,[25] involving the observation of the spontaneous emission of electromagnetic radiation within the visible spectrum subsequent to

the absorption of photons, thereby serving as a complementary technique to UV-Vis spectroscopy. Conceptually, two distinct phenomena can be discerned through PL spectroscopy, specifically fluorescence and phosphorescence (**Figure 2.6**). Fluorescence represents the radiative transition from the excited electronic state S_1 to the ground electronic state S_0 and typically transpires with short temporal delays (at the order of ps to ns) in comparison to the absorption process. Conversely, phosphorescence transpires when the excited singlet state S_1 experiences a non-radiative intersystem crossing to the triplet state T_1 (or its higher vibrational states), which subsequently transitions radiatively to the ground electronic state. Given that transitions involving a change in multiplicity are formally prohibited, phosphorescence manifests over extended timescales relative to fluorescence and generally exhibits diminished intensity levels.[26]

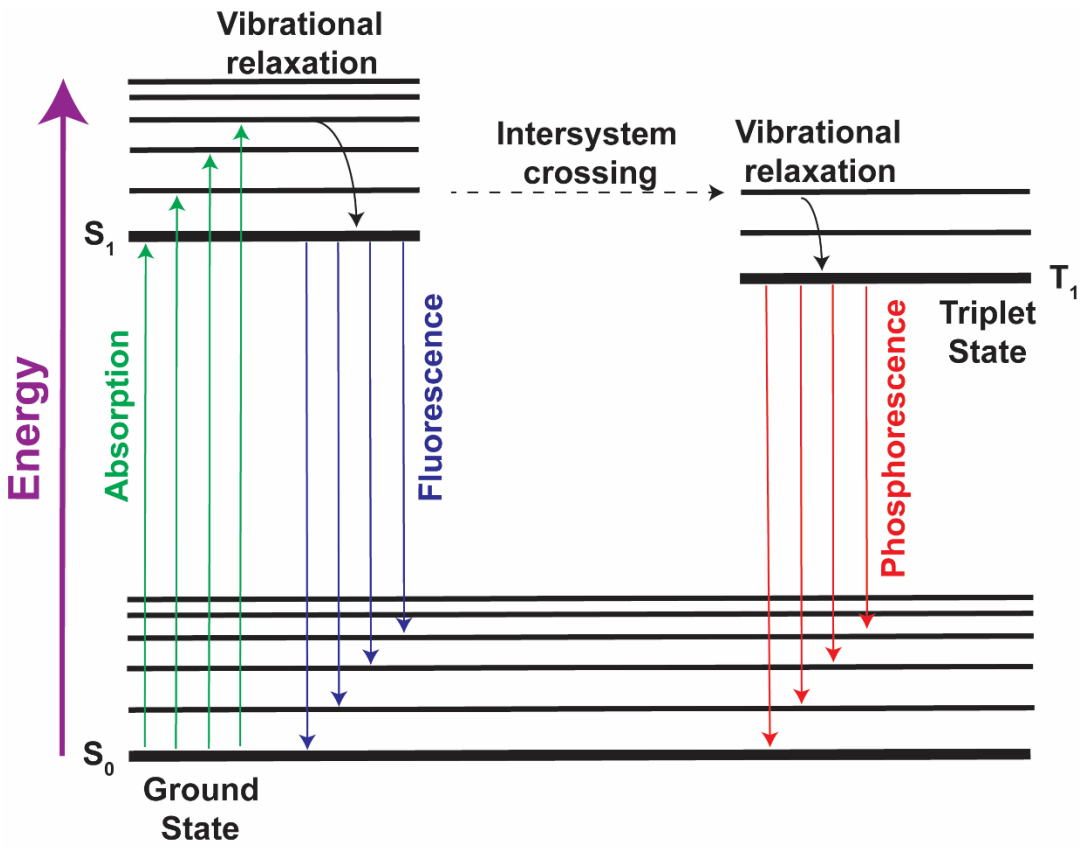

Figure 2.6. Jablonski diagram showing possible transitions between the ground state and excited states.

In this thesis, the PL method was used to evaluate the luminescence properties of the synthesized linkers and COFs. PL measurements were performed using two different setups: a home-built confocal laser scanning microscope (CLSM) equipped with a spectrometer (ANDOR SHAMROCK SRi303) and CCD camera (ANDOR NEWTON DU920), and a FluoTime 300 system (PicoQuant GmbH) for PL and PL anisotropy measurements, using pulsed excitation at 378 nm and 510 nm (~100 ps pulses, 500 kHz, ~300 μJ cm^{-2}/pulse) with detection via a high-resolution monochromator and photomultiplier (PMAC 192-N-M, PicoQuant GmbH).

2.9. Time-correlated single-photon counting (TCSPC)

Time-Correlated Single Photon Counting (TCSPC) represents a sophisticated methodology for the time-resolved examination of photoemission, instead of the absolute energy and intensity of the emitted photons in the case of steady-state PL measurements.

A pulsed laser is employed to activate the sample, potentially leading to the emission of a single photon. The detector logs the temporal intervals, referred to as start-stop times, during which a solitary photon is detectable. It is imperative to ensure that only one or no photon is emitted throughout the duration of a single laser pulse cycle. The count of detected photons is then graphically represented against the corresponding time interval from excitation to emission. As illustrated in **Figure 2.7**, this process is reiterated multiple times to accumulate adequate data for the assessment of fluorescence lifetimes.[27]

Utilizing a pulsed laser operating at frequencies ranging from 100 kHz to 80 MHz facilitates this highly repetitive photon registration, resulting in histograms that exhibit the exponential decay of excitation along with the associated lifetimes. The half-life of the excited species can be deduced from the exponential decay depicted in the subsequent histogram (**Figure 2.7**).

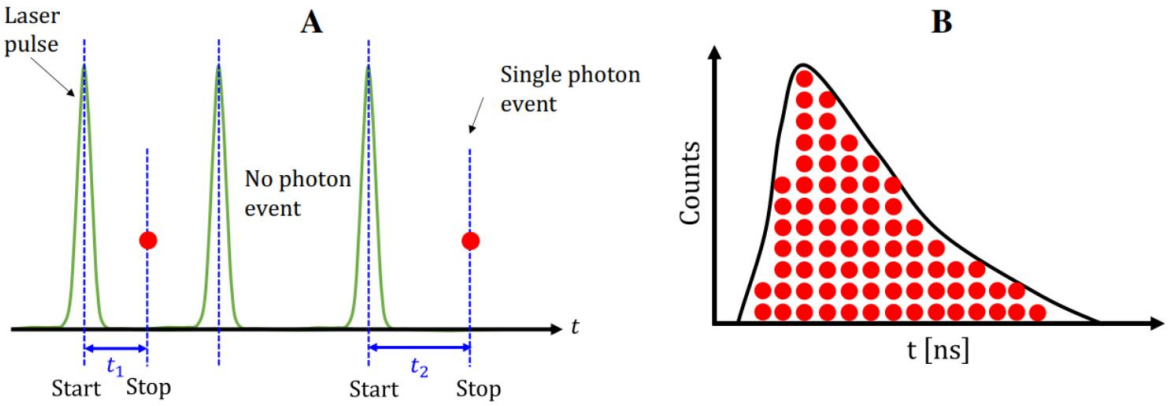

Figure 2.7. The principle of the lifetime measurement with TCSPC. (a) the TCSPC device typically measures the time between one START event and one STOP event (like a stopwatch). (b) A histogram of startstop times is reconstructed by counting a high number of photon events to reach statistical convergence. Reprinted with permission from Wang *et al*.[28] Copyright 2022 Springer Nature.

In this thesis, TCSPC measurements were employed to determine the lifetime of excited states in the synthesized COFs. TCSPC measurements were performed using an avalanche photodiode (MPD PDM) and TCSPC electronics (BECKER UND HICKL) integrated into the same CLSM setup, with samples excited at 476 nm.

2.10. Zeta potential

Zeta potential (also described with the Greek letter ζ) is a surface characteristic of nanomaterials that estimates the surface charge and and is related to colloidal stability in a medium. In aqueous environments, nanoparticles are predominantly defined by a (slight) charge induced by the dissociation of surface functional groups or the adsorption of charged solvent molecules. Therefore, ions of differing charges from the dispersion medium stick to the nanoparticle's surface, resulting in the development of an electric double layer (**Figure 2.8**). The inner layer comprises counter ions that are firmly bound, referred to as the Stern layer, whereas the outer layer contains counter ions that are more loosely bound (extending to the slipping plane). This double layer (up to the slipping plane) remains associated with the nanoparticle and moves in accordance with its Brownian motion. The electrical potential gradient existing between this dual layer and the adjacent dispersive medium is referred to as the zeta potential.[30,31]

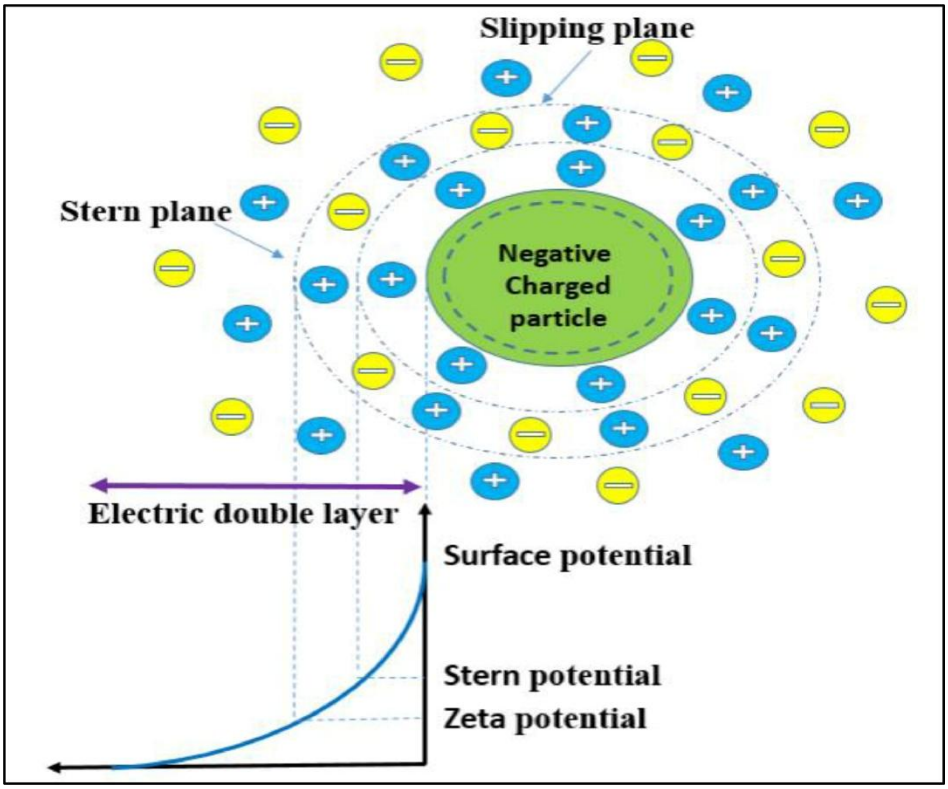

Figure 2.8. Block diagram of surface charge zeta potential. Reprinted with permission from Yadav *et al.*[32] Copyright 2022 Elsevier. This article is an open access article distributed under the terms and conditions of the Creative Commons Attribution (CC BY) license (http://creativecommons.org/licenses/by/4.0/).

The determination of zeta potential can be conducted in a cuvette equipped with two gold electrodes, wherein laser illumination is used to track the motion of the particles as an external electric field is applied. The laser detects the movement of the particles by measuring shifts in the scattered light caused by their velocity, allowing accurate determination of electrophoretic mobility. Charged particles will migrate toward the electrode bearing the opposing charge. The velocity of this action, termed the electrophoretic mobility of the particles, relates to the zeta potential through the Henry equation:[33,34]

$$\zeta = \frac{3\eta U_e}{2\varepsilon f(\kappa a)} \qquad (2.10)$$

ζ is the zeta potential; η is the viscosity of the medium; U_e is the electrophoretic mobility; ε is the dielectric constant; $f(\kappa a)$ is Henry's function.

The magnitude of the zeta potential indicates how stable colloidal systems are, showing the degree of repulsive interactions among charged particles in the mixture. High zeta potential values, whether positive or negative, suggest enhanced colloidal stability due to the pronounced electrostatic repulsion acting on individual particles. On the other hand, diminished zeta potential readings, associated with lowered colloidal stability, can result in particle clustering and flocculation, as insufficient repulsive forces enable particles to agglomerate due to dispersive forces.[35]

In this thesis, zeta potential measurements were utilized to evaluate the surface charge of the synthesized COFs and to study their protonation behavior in an acidic environment. Zeta potential measurements were performed on Malvern Zetasizer Nano equipped with a 4 mW He-Ne laser (λ = 633 nm) and an avalanche photodetector.

2.11. X-ray photoelectron spectroscopy (XPS)

X-ray photoelectron spectroscopy (XPS) is a technique widely used in fields such as material science, chemistry, and nanotechnology for determining the elemental composition, oxidation states, and electronic states of materials with outstanding surface sensitivity. This method utilizes the expulsion of photoelectrons into a vacuum from a sample, triggered by the bombardment with X-rays released from an Al Kα1 or Mg Kα1 source. Upon striking the surface of the sample, the incident X-ray beam generates elastically scattered electrons. These electrons are subsequently analyzed using an electron analyzer, which measures their kinetic energy. Utilizing the evaluated kinetic energy allows for the computation of the binding energy (BE) of the electrons, thereby analyzing the material's chemical characteristics. XPS is particularly sensitive to surface layers, with a penetration depth that barely reaches 0.5 to 2 nm. because only electrons originating from very close to the surface can escape without losing energy through inelastic scattering. Electrons emitted from deeper layers lose energy through interactions with other atoms and therefore do not contribute to the sharp, well-defined peaks used for analysis. To alleviate the energy loss of electrons resulting from scattering phenomena in the gas phase, XPS is performed in ultra-high vacuum (UHV) conditions, usually spanning from 10^{-9} to 10^{-8} Pa. Maintaining these ultra-high vacuum conditions is crucial for minimizing

contamination and ensuring accurate measurements, as even trace amounts of atmospheric gases can significantly affect the results obtained during XPS.[36,37]

The foundation of XPS is linked to the equation established by Ernest Rutherford in 1914:[38]

$$E_k = \lambda\upsilon - E_b \qquad (2.11)$$

E_k is the kinetic energy of the photoelectron; $h\nu$ is the energy of the X-ray; E_b is the binding energy of the electron.

From XPS results, one can gain insights into chemical details by interpreting the BE values that come from the captured electron spectrum. Given that the BE of electrons is thoroughly examined, XPS provides the capability to investigate the electronic core levels of various atoms, including s, p, and d levels along with their respective splitting due to spin-orbit coupling. Furthermore, the valence state of the corresponding atoms can be evaluated, as a reduction in valence charge (for instance, oxidation) results in elevated BE values, whereas an increase (for example, reduction) corresponds to diminished BE values.[39] This can be described by the formula:[37]

$$\Delta E = k\Delta q + \Delta V \qquad (2.12)$$

ΔE is the change in BE of a core level; k is a constant; Δq is the charge change; ΔV is the potential difference.

In this thesis, the XPS method was used to investigate the changes of the oxidation states of the elements of COFs before and after linkage conversion. The XPS measurements were performed with a VSW TA10 X-ray source providing non-monochromatized Al Kα radiation ($h\nu$ = 1486.6 eV) set at 15 mA and 12 kV and a VSW HA100 hemispherical analyzer. The spectra were recorded with a pass energy of 22 eV and a dwell time of 0.1 s per measurement point. The obtained spectra were fitted in Igor Pro 6.0.2.4 using a convolution of Doniach-Ŝunjić and Gaussian functions after a linear background subtraction.

2.12. Cyclic voltammetry (CV)

Cyclic voltammetry (CV) is an electrochemical technique that provides insights into the redox behavior of chemical species by measuring the current response to a linearly varying potential. CV is employed to investigate electrochemical phenomena occurring at and within electrodes.

With this experimental set-up, a regular three-electrode design is applied, incorporating a working electrode (the material of interest), a counter electrode, and a reference electrode, all positioned within an electrochemical cell filled with an electrolyte solution. The electrodes are interfaced with a potentiostat connected to a computer for comprehensive data analysis. Typically, the potential is systematically varied over a predetermined range, and the resultant current is recorded. By manipulating various parameters such as scan rate, scan direction, or step size, one can examine both oxidation and reduction processes within the electrochemical cell. By employing CV, various types of data can be extracted such as capacitance, cycle stability, photocurrent values, and the reversibility of redox reactions. In the context of organic molecules, determination of the HOMO energy level is particularly significant, given that the LUMO level can be readily determined by adding the optical band gap derived from UV-Vis absorption measurements to the electrochemically derived HOMO level. Understanding the HOMO and LUMO levels facilitates the incorporation of organic compounds into various devices that necessitate precise energy alignment, including solar cells, transistors, and hole-only devices.

The CV technique applied to organic semiconductors facilitates the estimation of the HOMO level by analyzing the initial oxidation event within the scan. Ferrocene serves as the reference for the electrochemical process. HOMO level can be calculated using the following equation:[40–42]

$$E(HOMO) = -e[E_{ox1}^{onset} + 4.8 - E_{FC/FC+}] \qquad (2.13)$$

E(HOMO) is the estimated HOMO level; *e* is the elementary charge (the minus sign ensures HOMO energy is negative); E_{ox1}^{onset} is the oxidation onset potential, $E_{FC/FC+}$ is the HOMO energy of ferrocene.

In this thesis, the CV method was utilized to determine HOMO levels of the COFs with a further evaluation of LUMO levels. The CV measurements were carried out on an Autolab PGSTAT204 potentiostat/galvanostat at 0.1 V s^{-1} scan speed. The electrochemical setup was made of a single chamber electrochemical cell, filled with 0.1 M NBu_4PF_6 in acetonitrile, using a Pt wire as counter electrode and Ag as pseudo-reference standardized to the ferrocene/ferrocenium couple.

2.13. Gas chromatography (GC)

Gas chromatography (GC) is an analytical method used for the separation, identification, and quantification of components in a mixture of volatile compounds. The procedure entails the introduction of a minute volume of the sample into a carrier gas (predominantly helium or nitrogen), which facilitates the transit of the sample through a capillary column that is lined with a stationary phase.

As the sample advances through the column, its constituents engage in varying interactions with the stationary phase, influenced by their intrinsic chemical characteristics, including polarity and boiling point. Such disparities lead to differential migration rates of the components within the column, thereby achieving their separation.

Upon reaching the terminal end of the column, a detector (frequently a flame ionization detector or thermal conductivity detector) quantifies the separated entities as they emerge from the column, thereby generating a chromatogram - a graphical representation delineating signal intensity against time. Each peak present on the chromatogram signifies a distinct compound found within the sample. The area under each peak corresponds to the concentration of that specific compound, allowing for quantitative analysis and comparison between different samples.[43]

In this thesis, the GC method was used determine the hydrogen production rate during the photocatalytic test. GC measurements were performed using a PerkinElmer Clarus 580 gas chromatograph equipped with a thermal conductivity detector (TCD).

2.14. Nuclear magnetic resonance spectroscopy (NMR)

Nuclear magnetic resonance (NMR) spectroscopy is an analytical technique used for the characterization of chemical molecular structures. This method facilitates the determination of molecular architectures as well as the examination of dynamic processes within organic, inorganic, and biological matter. Furthermore, the electronic environments surrounding magnetic isotopes within molecules and their interactions with adjacent atoms can be systematically investigated. The elucidation of molecular structure is achievable, as the

interaction between an oscillating radio-frequency electromagnetic field and a collection of nuclei situated within a strong external magnetic field is quantifiable. Atoms possessing nuclear spin exhibit distinctive behaviors when subjected to an external magnetic field, contingent upon their respective chemical environments. NMR spectroscopy enables the measurement of nuclei with intrinsic spin; consequently, the nuclei of interest must contain an odd number of protons, neutrons, or both, exemplified by ^{1}H, ^{13}C, or ^{19}F. These nuclei have a spin, linked to a spin angular momentum vector $\rightarrow S$, and this relationship is described by the gyromagnetic ratio γ, as shown in equation 2.14:

$$\rightarrow \mu = \gamma \rightarrow S \qquad (2.14)$$

$\rightarrow \mu$ is the magnetic moment.

When subjected to an external magnetic field, the potential orientations of atomic magnetic moments are constrained. Only specific quantum states are permissible, which are governed by the spin quantum number I. For any given spin quantum number, there exist $2I+1$ possible orientations. These spin states are non-degenerate in an external magnetic field and consequently experience a splitting into discrete energy levels. When electromagnetic radiation in the radio frequency range is absorbed, it can cause transitions between these states, as long as the following equations are satisfied:

$$\nu = \frac{\gamma B_0}{2\pi} \qquad (2.15)$$

$$\nu = \gamma B_{loc} = \gamma(B_0 + B_{int}) \qquad (2.16)$$

ν is the resonance frequency; B_0 is the external magnetic field; B_{loc} is the local magnetic field; B_{int} is the internal magnetic field.

The varying electronic environments of the atoms will induce a difference between the external and local magnetic fields, which in turn will result in a variation in resonance frequency. This variation is measurable and can consequently yield significant insights into the electronic structure and chemical environment surrounding the nuclei under investigation.

In this thesis, liquid-state ^{1}H and ^{13}C NMR methods were used to analyze the chemical composition and structure of the synthesized building blocks, while solid-state ^{13}C CP/MAS NMR (MAS = magic angle spinning) was employed to evaluate chemical composition and

structure of synthesized COFs. Liquid-state ^{1}H and ^{13}C NMR spectra were recorded using Bruker AV 400 and AV 400 TR spectrometers. Solid-state ^{13}C CP/MAS NMR spectra were acquired on a Bruker Avance III-500 spectrometer equipped with a 4 mm double resonance MAS probe, using a MAS rate of 10.0 kHz, contact time of 2-5 ms, and a pulse delay of 4 s.

2.15. Elemental analysis

Elemental analysis is a method used to determine the atomic composition of a given substance by identifying the presence and quantity of elements such as carbon, hydrogen, nitrogen, sulfur, or chlorine. This analysis relies on transforming the sample into an analyzable form, typically through combustion in an oxygen-rich environment. This procedure liberates gaseous products, which are subsequently captured and quantified to ascertain the concentrations of particular elements, including carbon, hydrogen, and nitrogen (CHN analysis). This method, initially developed by Fritz Pregl, can exhibit a high degree of precision and can be used at the microscale, necessitating only milligram quantities of the specimen. The precision of elemental analysis is imperative for validating the atomic composition and overall purity of substances.[44]

In this thesis, CHNSCl analysis was used to determine the percentages of carbon (C), hydrogen (H), nitrogen (N), sulfur (S), and chlorine (Cl) in the synthesized building blocks and COFs, providing information on the elemental composition and enabling comparison with the theoretical values based on the proposed molecular structures. Elemental analysis was performed using the vario EL and vario micro cube systems from Elementar, with high-temperature digestion, dynamic gas component separation, and detection in a single apparatus. Samples were weighed in tin boats. Combustion of the samples occurred at 1150 °C in an oxygen-enriched helium atmosphere. The resulting combustion products were collected and separated with gas chromatography.

2.16. Mass spectrometry (MS)

Mass spectrometry (MS) is a tool for identifying a compound based on the molecular or atomic mass(es) of its components. Using this method, the elements present and the molecular formula of the molecule can be identified. The idea behind mass spectrometry is rather straightforward:

first, ions are created from the sample of interest. These ions are then separated and measured based on their different mass-to-charge (m/z) ratios.

In practice, a very small amount of the sample is vaporized and sent into an ionization chamber, where it gets bombarded by an electron beam, turning the molecules into positively charged ions. A small positive voltage pushes these ions out of the ionization chamber, and they are then accelerated by an electrostatic field toward the analyzer. Inside the analyzer, the ions are separated. A strong magnetic field, placed perpendicular to their motion, bends their paths into curves - lighter ions bend more, heavier ions bend less - depending on their mass-to-charge ratio. Finally, the ions pass through an exit slit and hit a collector electrode, creating a small electric current. This current is then amplified and recorded, showing up as a function of either the magnetic field strength or the accelerating voltage.[45,46]

In this thesis, the MS method was used to evaluate the molecular masses of the synthesized compounds. Compounds were analyzed using electron ionization (EI),[47] also known as electron impact ionization or simply electron impact. MS were recorded using an Advion expression compact mass spectrometer (CMS) with the atmospheric solid analysis probe (ASAP) technique. The ion source was set to “low temperature and low fragmentation” and spectra were acquired with a mass range of 500 m/z at a speed of 104 m/z units per second. Analysis was performed using Advion's CheMS Express 5.1.0.2 software after background subtraction.

2.17. References

[1] B. K. Teo, in *X-Rays and Electrons*, Springer Berlin Heidelberg, Heidelberg, **1986**, pp. 1–20.

[2] C. G. Pope, *J. Chem. Educ.* **1997**, *74*, 129.

[3] V. Hauk, in *Struct. Residual Stress Anal. by Nondestruct. Methods*, Elsevier, Aachen, **1997**, pp. 216–229.

[4] A. Monshi, M. R. Foroughi, M. R. Monshi, *World J. Nano Sci. Eng.* **2012**, *02*, 154–160.

[5] K. S. W. Sing, *Pure Appl. Chem.* **1985**, *57*, 603–619.

[6] M. M. Dubinin, *Russ. Chem. Rev.* **1982**, *51*, 605–611.

[7] M. Thommes, K. Kaneko, A. V. Neimark, J. P. Olivier, F. Rodriguez-Reinoso, J. Rouquerol, K. S. W. Sing, *Pure Appl. Chem.* **2015**, *87*, 1051–1069.

[8] Z. ALOthman, *Materials (Basel).* **2012**, *5*, 2874–2902.

[9] J. Rouquerol, P. Llewellyn, F. Rouquerol, in *Stud. Surf. Sci. Catal.*, **2007**, pp. 49–56.

[10] G. . Berezin, A. . Kiselev, *J. Colloid Interface Sci.* **1966**, *22*, 161–164.

[11] D. Zeng, W. Voigt, *Calphad* **2003**, *27*, 243–251.

[12] P. I. Ravikovitch, A. V. Neimark, in *Stud. Surf. Sci. Catal.*, **2000**, pp. 597–606.

[13] C. Earnest, in *Compos. Anal. by Thermogravim.*, ASTM International100 Barr Harbor Drive, PO Box C700, West Conshohocken, PA 19428-2959, **1988**, pp. 1–18.

[14] J. I. Goldstein, D. E. Newbury, J. R. Michael, N. W. M. Ritchie, J. H. J. Scott, D. C. Joy, *Scanning Electron Microscopy and X-Ray Microanalysis*, Springer New York, New York, NY, **2018**.

[15] P. Qiu, L. Wang, C. B. Mao, in *Transm. Electron Microsc. Charact. Nanomater.*, Springer Berlin Heidelberg, Berlin, Heidelberg, **2014**, pp. 1–41.

[16] B. Fultz, J. Howe, *Transmission Electron Microscopy and Diffractometry of Materials*, Springer Berlin Heidelberg, Berlin, Heidelberg, **2013**.

[17] B. Tubus, "Schematic view of imaging and diffraction modes in TEM.tif," can be found under https://commons.wikimedia.org/wiki/File:Schematic_view_of_imaging_and_diffraction_modes_in_TEM..tif, **n.d.**

[18] S. N. Ghosh, in *Handb. Anal. Tech. Concr. Sci. Technol.*, Elsevier, **2001**, pp. 174–204.

[19] É. Dufour, in *Infrared Spectrosc. Food Qual. Anal. Control*, Elsevier, **2009**, pp. 1–27.

[20] Z. Chen, T. G. Deutsch, H. N. Dinh, K. Domen, K. Emery, A. J. Forman, N. Gaillard, R. Garland, C. Heske, T. F. Jaramillo, A. Kleiman-Shwarsctein, E. Miller, K. Takanabe, J. Turner, **2013**, pp. 49–62.

[21] D. Calloway, *J. Chem. Educ.* **1997**, *74*, 744.

[22] C. Summonte, *MRS Proc.* **1993**, *297*, 395.

[23] R. Alcaraz de la Osa, I. Iparragirre, D. Ortiz, J. M. Saiz, *ChemTexts* **2020**, *6*, 2.

[24] P. R. Jubu, E. Danladi, U. I. Ndeze, O. Adedokun, S. Landi, A. J. Haider, A. T. Adepoju, Y. Yusof, O. S. Obaseki, F. K. Yam, *Results Opt.* **2024**, *14*, 100606.

[25] D. Frackowiak, *J. Photochem. Photobiol. B Biol.* **1988**, *2*, 399.

[26] M. H. Gordon, R. Macrae, in *Instrum. Anal. Biol. Sci.*, Springer US, Boston, MA, **1987**, pp. 117–132.

[27] M. Wahl, in *Adv. Phot. Count.*, **2014**, pp. 1–21.

[28] M. Wang, M. Stiti, H. Chaynes, S. Becker, E. Berrocal, F. Lemoine, G. Castanet, *Exp. Fluids* **2022**, *63*, 1–20.

[29] K. P. Ghiggino, A. J. Roberts, D. Phillips, *J. Phys. E Sci. Instruments* **1979**, 98–100.

[30] D. Varsou, A. Afantitis, A. Tsoumanis, A. Papadiamantis, E. Valsami-Jones, I. Lynch, G. Melagraki, *Small* **2020**, *16*, 1906588.

[31] J. D. Clogston, A. K. Patri, **2011**, pp. 63–70.

[32] M. A. Chowdhury, M. M. K. Uddin, M. B. A. Shuvho, M. Rana, N. Hossain, *Appl. Surf. Sci. Adv.* **2022**, *11*, 100308.

[33] H. Ohshima, *J. Colloid Interface Sci.* **1996**, *180*, 299–301.

[34] G. Giupponi, I. Pagonabarraga, *Philos. Trans. R. Soc. A Math. Phys. Eng. Sci.* **2011**, *369*, 2546–2554.

[35] W. Huo, X. Zhang, K. Gan, Y. Chen, J. Xu, J. Yang, *J. Eur. Ceram. Soc.* **2019**, *39*, 574–583.

[36] R. K. Vempati, T. R. Hess, D. L. Cocke, Beaumont, Texas, United States, **2018**, pp. 357–375.

[37] J. Lefebvre, F. Galli, C. L. Bianchi, G. S. Patience, D. C. Boffito, *Can. J. Chem. Eng.*

2019, *97*, 2588–2593.

[38] P. M. A. Sherwood, in *Handb. Surf. Imaging Vis.*, CRC Press, Boca Raton, **2022**, pp. 875–887.

[39] A. Levasseur, P. Vinatier, D. Gonbeau, *Bull. Mater. Sci.* **1999**, *22*, 607–614.

[40] P. Chooto, in *Voltammetry*, IntechOpen, **2019**.

[41] J. R. Smith, S. A. Campbell, F. C. Walsh, *Trans. IMF* **1995**, *73*, 72–78.

[42] J. Heinze, *Angew. Chemie Int. Ed. English* **1984**, *23*, 831–847.

[43] A. Braithwaite, F. J. Smith, in *Chromatogr. Methods*, Springer Netherlands, Dordrecht, **1985**, pp. 137–211.

[44] S. Proctor, S. Lovera, A. Tomich, V. Lavallo, *ACS Cent. Sci.* **2022**, *8*, 874–876.

[45] L. D. S. Yadav, in *Org. Spectrosc.*, Springer Netherlands, Dordrecht, **2005**, pp. 250–294.

[46] R. Wait, in *Spectrosc. Methods Anal.*, Humana Press, New Jersey, **1993**, pp. 191–214.

[47] T. D. Mark, *Plasma Phys. Control. Fusion* **1992**, *34*, 2083–2090.

3. Pre-synthetic modification of Wurster-Anthracene COF: tuning the structural and optoelectronic properties

This chapter is based on the following article:

Single-Atom Tuning of Structural and Optoelectronic Properties in Halogenated Anthracene-Based Covalent Organic Frameworks

Submitted to "Journal of Material Chemistry A"

Klaudija Paliušytė, Laura Fuchs, Zehua Xu, Kuangjie Liu, Kornel Roztocki, Shuo Sun, Hendrik Zipse, Achim Hartschuh, Frank Ortmann* and Jenny Schneider*

Department of Chemistry and Center for NanoScience (CeNS), University of Munich (LMU), Munich 81377, Germany

Department of Chemistry, TUM School of Natural Sciences, and Atomistic Modeling Center, Munich Data Science Institute, Technische Universität München, 85748 Garching b. München, Germany

Faculty of Chemistry, Adam Mickiewicz University, 61-614 Poznań, Poland

*Corresponding authors

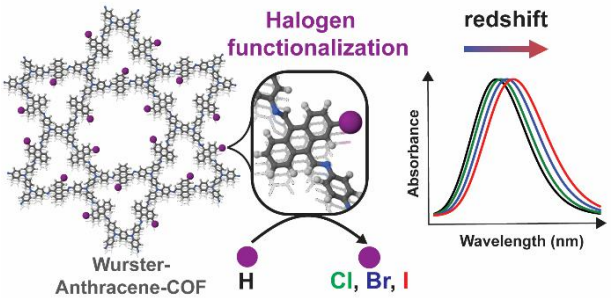

3.1. Abstract

In this study, we report the synthesis and comprehensive characterization of a series of halogenated anthracene-based covalent organic frameworks (COFs), W-A-X (X = H, Cl, Br, I), obtained through Schiff-base condensation with a N,N,N′,N′-tetraphenyl-1,4-phenylen (Wurster-type) building block. Systematic substitution of a single halogen atom at the 2-

position of the anthracene core revealed significant effects on the resulting COFs' structural and optoelectronic properties. Powder X-ray diffraction and transmission electron microscopy analyses demonstrate that halogenation influences both crystallinity and domain size, with W-A-Br COF exhibiting notably larger crystalline domains (200–400 nm), while W-A-Cl formed much smaller ones (~50 nm). This variation was attributed to both the choice of solvent and the electrostatic potential of the halogen substituents, as supported by density functional theory (DFT) calculations. Optical absorption and photoluminescence measurements revealed a clear redshift in both UV-vis absorption and emission maxima across the halogen series (H < Cl < Br < I), consistent with enhanced π-conjugation and increased polarizability. These trends were further validated and complemented by theoretical calculations, including DFT-based electronic and optical band gap analysis of the molecular fragments and COF's structure. Collectively, our results underscore the critical role of single-atom halogen substitution in tailoring the morphology and optoelectronic response of anthracene-based COFs, offering a modular strategy for precision design of organic framework materials.

3.2. Introduction

Covalent organic frameworks (COFs) are porous crystalline polymers constructed from a diverse set of molecular organic building blocks, linked through covalent bonds in a periodic arrangement.[1] This structural regularity enables precise control over their properties, resulting in a rich spectrum of functionalities. The ability to design COFs with high structural precision allows for a direct connection between their architecture and (opto-)electronic properties, establishing well-defined structure–property relationships that are critical for the development of novel functional materials. These frameworks can be designed with numerous organic molecules capable of engaging in extensive chemical interactions, further broadening their utility.[2] The choice of molecular building units is therefore pivotal in defining structural, electronic, and chemical characteristics of COFs, directly influencing their applicability in fields such as photocatalysis,[3] photovoltaics,[4] sensing,[5] and gas storage.[6]

A particularly compelling molecular building block for the synthesis of COFs is anthracene, an aromatic polycyclic compound composed of three linearly fused benzene rings. While it has been extensively utilized in metal-organic frameworks,[7–10] its integration into COFs remains

relatively limited. First anthracene-based COFs have been applied in photocatalysis,[11–13] fluorescence quenching,[14,15] sensing,[16,17] supercapacitors,[18] and optoelectronic devices.[19,20] Given anthracene's intrinsic optoelectronic properties including strong photoluminescence,[21] efficient intramolecular charge transfer[21] and mechanochromic[22] behavior, it holds significant promise as a versatile building block for the development of advanced COF materials.

In its native form, anthracene primarily absorbs and emits in the UV region, which limits its direct applicability in visible-light-driven technologies. To fully exploit its potential in solar energy conversion systems, a redshift in its optical response is required.[23,24] This can be achieved by integrating anthracene units into extended π-conjugated frameworks such as COFs, or through peripheral chemical functionalization that preserves the integrity of the aromatic core.[25,26] However, the inherent planarity and rigidity of anthracene, combined with the positions of its functional groups, often impede the formation of crystalline COFs, as it may cause imperfect layer alignment and steric hindrance.[27,28]

In this context, N,N,N′,N′-tetraphenyl-1,4-phenylen (Wurster-type) building blocks offer a particularly attractive option for COF synthesis due to their structural flexibility, which stems from free rotation around single bonds.[29,30] This adaptability allows them to conform to more rigid components such as anthracene, facilitating the formation of well-ordered, crystalline frameworks. Notably, the additional aromatic rings in Wurster-type building blocks enhance π-conjugation enabling fine-tuning of the (opto-)electronic properties and expanding the design space for modular and functional COF architectures.[29,31] Specifically, the combination of electron-donating Wurster-type units with electron-accepting anthracene moieties can promote the formation of donor-acceptor COFs, a design strategy known to enhance charge carrier separation and improve the efficiency of light-induced processes.[32]

One effective strategy for modulating the properties of COFs is the integration of functional groups or atoms, among which halogen functionalization stands out as particularly impactful. The incorporation of halogens into the COF backbone can enhance charge separation and transfer efficiency owing to their electron-withdrawing characteristics[33,34] or tune the COF's electrostatic potential.[35] Additionally, halogen modifications have been shown to directly impact charge carrier mobility and electrical conductivity.[36] Furthermore, halogen-framework

interactions can induce changes in both the electronic structure and the molecular geometry of the framework, making halogenation a powerful tool for tuning materials properties.[37] To the best of our knowledge, no studies have reported COFs featuring halogenated anthracene units. Given anthracene's highly conjugated nature, even the substitution of a single halogen atom can significantly alter the electronic properties of the linker and, consequently, the functionality of the entire COF.[38] This unexplored design avenue presents a promising opportunity to further expand the structural and functional diversity of COFs.

In this study, we present a series of novel anthracene-based COFs functionalized with various halogen atoms on the peripheral position of the anthracene core and incorporating Wurster-type building blocks. We demonstrate that even a single-atom substitution leads to significant changes in crystallite size, morphology, and optoelectronic properties. Furthermore, we provide comprehensive insights into the electronic and optical behavior of these systems, supported by extensive theoretical calculations performed on functionalized building blocks, extended molecular fragments and the corresponding COF structures.

3.3. Results and discussion

Novel anthracene-based linkers, functionalized with different halogens at the 2-position, were synthesized following a general synthetic route outlined in **Scheme 3.1**.[39] The synthesis involves a Diels-Alder reaction between halogenated anthracene precursors (2-X-anthracene (A-X); X = Cl, Br, I) and vinylene carbonate to form a cyclic carbonate intermediate. This intermediate is subsequently converted into the corresponding diol, which is then oxidized to yield the target compound: 2-halogen-9,10-anthracenedialdehyde (A-X-CHO; X = Cl, Br, I). Details on the synthesis are provided in the Appendix (**Figure 3.6** - **Figure 3.21**).

The freshly synthesized halogenated A-X-CHO linkers, along with the commercially available non-halogenated analog, were employed to construct four novel crystalline COFs (W-A-X, where X = H, Cl, Br, I) via a Schiff-base condensation reaction with the electron-rich N,N,N′,N′-tetrakis(4-aminophenyl)-1,4-phenylenediamine (W-NH_2) building block (see **Figure 3.1**a, **Figure 3.22** to **Figure 3.25**). Powder X-ray diffraction (PXRD) analysis reveals well-ordered structures of all synthesized COFs **(**see **Figure 3.1**b-d). All four COFs exhibit

prominent diffraction peaks corresponding to the (100), (110) and (210) lattice planes at similar positions. Additionally, (200) and (310) peaks were observed for W-A-H, W-A-Cl and W-A-Br. Intense and sharp diffraction peaks for W-A-H, W-A-Cl, and W-A-Br COFs establish high crystallinity, while the W-A-I COF features somewhat lower crystallinity.

Building on the PXRD characterization, we further investigated the structure of all four W-A-X COFs using density functional theory (DFT) simulations. For better comparison of the four models, we assumed hexagonal lattice symmetry with a Kagome structure in all cases. Each unit cell comprised six mono-halogenated anthracene and three Wurster units per layer, arranged in an eclipsed vertical stacking geometry. Due to the asymmetric structure of the functionalized anthracene building blocks, various orientations and combinations of the halogenated units relative to the smaller and larger pores are possible. Multiple halogen atom arrangements were explored (see **Figure 3.26**), yielding the most energetically favorable configuration (shown in **Figure 3.1**a), which also exhibited the best agreement with the experimental PXRD data. In this structural model, two halogen atoms per unit cell are oriented toward the smaller trigonal pore (highlighted with pink arrows), while the remaining four halogen atoms are facing the larger hexagonal pore (blue arrows). For comparison, the non-halogenated analog (W-A-H), in which halogen atoms were replaced by hydrogen, was used as a reference structure in the simulations.

Based on the structural DFT-models and the PXRD patterns (**Figure 3.1**b-e, **Table 3.1** to **Table 3.4**), we performed Pawley refinement of the four COFs, adopting P-3 symmetry for W-A-H and P-1 for W-A-X (X = Cl, Br, I), as detailed in the SI. The refined unit cell parameters are: W-A-H ($a = b = 4.236$ nm, $c = 0.411$ nm), W-A-Cl ($a = b = 4.265$ nm, $c = 0.408$ nm), and W-A-Br ($a = b = 4.263$ nm, $c = 0.409$ nm). These COFs exhibited excellent agreement between the simulated and experimental diffraction peaks with R_p values of 4.66%, 5.09%, and 5.64%, respectively. All observed diffraction peaks were successfully indexed to specific lattice planes, confirming the high crystallinity of the synthesized frameworks. The W-A-I ($a = b = 4.263$ nm, $c = 0.408$ nm) COF exhibits slightly lower crystallinity compared to the other three COFs. Nevertheless, its experimental PXRD pattern shows a good agreement with the simulated pattern of the dual-pore hexagonal structural model, with refinement factor of $R_p = 3.34\%$.

We note that minor additional reflections were observed in the PXRD patterns of the W-A-Cl and W-A-Br COFs. Specifically, diffraction peaks at 5.25° and 5.30°, respectively, could not be assigned to the simulated dual-pore hexagonal model, suggesting the presence of a minor phase impurity in these frameworks, possibly caused by the asymmetry of the halogenated anthracene linker.

To gain deeper insight into the structural properties of the synthesized COFs, transmission electron microscopy (TEM) was performed for W-A-H, -Cl, -Br COFs as representatives of the series. Hereby, the images confirm the Kagome-type hexagonal lattice. The crystalline domain sizes were found to range from 50–100 nm for W-A-H COF, up to 50 nm for W-A-Cl, and as large as 200-400 nm for W-A-Br, see Figure 3**.1**f-h. Additional TEM images for W-A-Br are shown in **Figure 3.27**, clearly exhibiting lattice fringes.

The observed differences in crystalline domain sizes can be rationalized by nucleation and growth dynamics. Slower nucleation rates tend to promote the growth of larger domains, as fewer nucleation sites are formed, allowing each crystal domain to grow more extensively. In contrast, faster nucleation rates typically lead to smaller crystallite sizes due to the formation of numerous nucleation sites, which limits individual crystal growth.[40–42]

Addressing the potential impact of halogenation, the introduction of a single halogen atom into anthracene-based linkers can induce polarization due to the high electronegativity of halogens, creating regions of distinct electrostatic potential (ESP). This polarization can influence monomer interactions during COF formation, thereby affecting nucleation. To explore this point further, we performed ESP calculations of the four A-X-CHO linkers (X = H, Cl, Br, I), as well as for the W-NH_2 linker (**Figure 3.28**). The calculations show that halogen atoms covalently bonded to the anthracene unit in a C-X fashion, particularly Br and I, exhibit a region of positive ESP opposite the C-X bond axis, which are known as the σ-hole (ESP = +0.011, +0.021, and +0.038 a.u. for Cl, Br, and I, respectively).[43,44] This σ-hole can engage in directional halogen bonding with electron-rich species, such as the amino groups of the W-NH_2 building block used for COF synthesis.[45,46] To hypothesize, such non-covalent interactions may play a crucial role in stabilizing the early stages of COF nucleation. Their directionality and specificity can lead to more ordered supramolecular assemblies, potentially slowing down

nucleation and allowing larger crystallite growth.[47,48] Consistent with literature[49,50], **Figure 3.28** shows that the size and strength of the σ-hole increase with halogen polarizability (I > Br > Cl), enhancing interactions with nucleophiles.[49,50] This trend may explain why W-A-Br COF, containing the more polarizable Br, exhibits large crystalline domains (200–400 nm), while W-A-Cl COF does not show a comparable effect. In the case of W-A-I COF, the very strong halogen bonding associated with iodine's large σ-hole may act as an "overmodulating" factor, somewhat disrupting regular framework formation and contributing to its slightly reduced crystallinity.[51–53] Notably, the large σ-hole of iodine can engage in directional noncovalent interactions with electron-rich amino groups, either through halogen bonding or charge-transfer complexation,[54] potentially leading to off-target interactions that interfere with the intended framework connectivity. In contrast, the more moderate σ-hole of bromine may act as a gentler modulator, supporting controlled interactions that enhance crystallinity, while the stronger interactions of iodine may slightly interfere with ordered framework growth.[55,56]

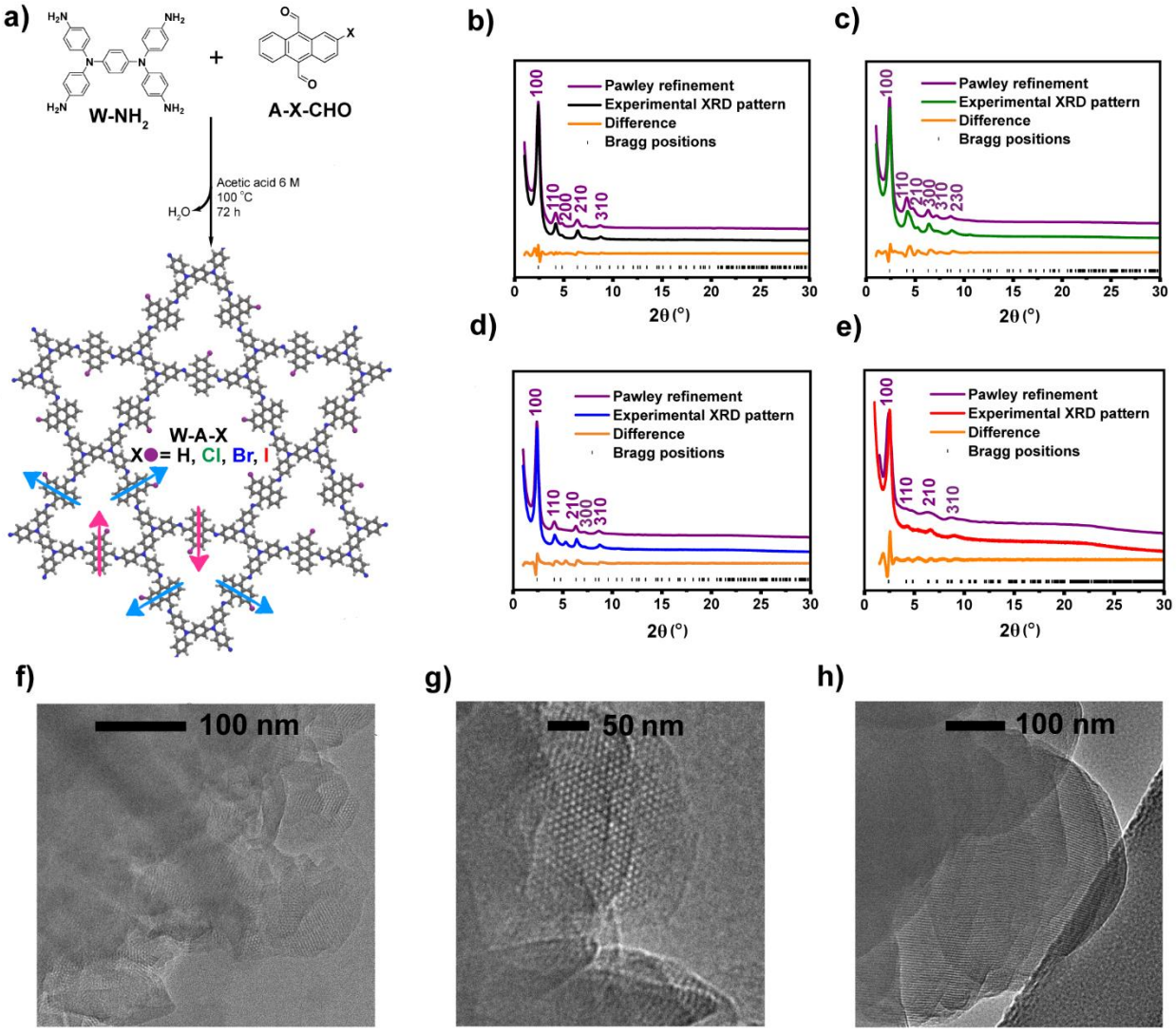

Figure 3.1. (a) Schematic representation of Schiff-base reaction to obtain W-A-X COFs (X = H, Cl, Br, I). Arrows indicate the orientation of the halogen atoms of the energetically most stable configuration with two halogens facing the smaller trigonal pore (pink) and the remaining four halogens directed toward the larger hexagonal pore shown in blue. Simulated and experimental PXRD patterns of (b) W-A-H, (c) W-A-Cl, (d) W-A-Br, (e) W-A-I. TEM images of (f) W-A-H, (g) W-A-Cl, (h) W-A-Br.

The morphologies of the COFs were evaluated via scanning electron microscopy (SEM). SEM images demonstrate that despite the similar crystal structure, morphologies of all four COFs differ (**Figure 3.29**). The pristine W-A-H COF consists of small platelets, W-A-Cl COF contains a mixture of platelets and spherical particles, W-A-Br COF is composed mainly of spherical particles and W-A-I COF exhibits rods. The morphology of COFs can be significantly influenced by solvent polarity and electrostatic repulsion, the latter of which may arise from the

presence of electronegative halogen atoms.[57,58] These factors affect layer spacing and solvation, possibly leading to different morphologies.

Nitrogen sorption isotherms were recorded to analyze the porosity of all four COFs (**Figure 3.30**). A gradual reduction in surface area is observed with increasing atomic radius of the halogen *r* (*r*(H) < *r*(Cl) < *r*(Br) < *r*(I)): W-A-H 548 $m^2 g^{-1}$, W-A-Cl 490 $m^2 g^{-1}$, W-A-Br 187 $m^2 g^{-1}$ and W-A-I 170 $m^2 g^{-1}$. These values are considerably lower than the theoretical network-accessible surface areas per gram calculated from perfect crystal structures using PoreBlazer:[59] W-A-H, 897 $m^2 g^{-1}$; W-A-Cl, 806 $m^2 g^{-1}$; W-A-Br, 674 $m^2 g^{-1}$; and W-A-I, 653 $m^2 g^{-1}$ (Table S5). Nevertheless, the experimental pore volumes for W-A-H (0.35 $cm^3 g^{-1}$) and W-A-Cl (0.33 $cm^3 g^{-1}$) are in good agreement with the theoretical values of 0.364 $cm^3 g^{-1}$ and 0.317 $cm^3 g^{-1}$, respectively, indicating good crystallinity and stability during activation prior to the N_2 adsorption experiment. By contrast, W-A-Br and W-A-I COFs show both substantially lower experimental pore volumes (0.18 $cm^3 g^{-1}$ and 0.13 $cm^3 g^{-1}$, respectively) and BET surface area than their theoretical counterparts. For the iodine derivative, this is attributed to reduced crystallinity compared with the other three materials (**Figure 3.1**e). Furthermore, the activation process (vacuum drying) of COFs may cause partial pore collapse. Due to steric hindrance, this effect may be more pronounced in materials functionalized with larger atoms, such as Br and I, compared to H and Cl,[60,61] leading to a further reduction in the overall BET surface area and accessible pore volume.

Using non-local density functional theory (NLDFT)[62] for slit and cylindrical pores for evaluation of the isotherms, average pore sizes were calculated to be 1.1 nm and 1.7 nm for W-A-H, 1.1 nm and 2.0 nm for W-A-Cl, 1.1 nm and 2.0 nm for W-A-Br, and 1.1 nm and 2.0 nm for W-A-I, respectively. Additionally, porosity parameters were simulated using Zeo++ software[63] (**Table 3.5** and **Figure 3.31**), providing theoretical pore sizes and pore volumes. The results indicated pore sizes of 0.7 nm and 2.0 nm for W-A-H, 0.7 nm and 1.9 nm for W-A-Cl, 0.7 nm and 1.9 nm for W-A-Br, and 0.7 nm and 1.8 nm for W-A-I. The deviations between the experimental and theoretical pore sizes can be attributed to the idealized nature of the theoretical models, which assume a perfectly ordered and defect-free COF structure. In reality, structural imperfections, defects, distortions, and variations in the distribution of halogen substituents can occur, leading to differences in the experimentally observed porosity

parameters. Additionally, the same Zeo++ software was applied to calculate average unit cell densities, yielding 0.67 g cm^{-3} for W-A-H, 0.74 g cm^{-3} for W-A-Cl, 0.81 g cm^{-3} for W-A-Br, and 0.90 g cm^{-3} for W-A-I. The increase in unit cell density for halogenated COFs compared to the non-halogenated W-A-H COF is attributed to the incorporation of halogen atoms, which increase the overall framework density.[64] A comparison of theoretical and experimental porosity parameters is presented in **Table 3.5**.

Fourier Transform Infrared Spectroscopy (FTIR) analysis was conducted to confirm the formation of imine bonds following the condensation reaction of the monomers (**Figure 3.32**). All four COFs show an FTIR-band at 1609 cm^{-1} which is assigned to the newly formed imine (C=N) bonds.[65,66] We note that the stretching vibrations of the carbon-halogen bonds are hidden in the fingerprint region (< 600-840 cm^{-1} C-Cl, < 700 cm^{-1} C-Br, < 600 cm^{-1} C-I),[67] therefore these vibration bands are not presented in FTIR spectra.

To further characterize the chemical structure of the four COFs, ^{13}C cross-polarization magic angle spinning (CPMAS) analysis was performed (**Figure 3.33**). All COFs exhibited a distinct peak at 157 ppm, confirming imine bond formation. An additional peak at 93 ppm in the ^{13}C spectrum of the W-A-I COF indicates the presence of a C-I bond. In contrast, the ^{13}C NMR signals corresponding to carbons bonded to chlorine (123.14 ppm) and bromine (122.87 ppm) in the W-A-Cl and W-A-Br COFs, respectively, were less distinct due to overlap with other carbon resonances in the 109-140 ppm region of the spectrum.

A good thermal stability of the COFs was confirmed by thermogravimetric analysis (TGA), **Figure 3.34**. A weight loss of 10% under the dynamic TGA conditions was observed at 403 °C, 419 °C, 404 °C and 378 °C for W-A-H, W-A-Cl, W-A-Br and W-A-I COFs, respectively.

The optical properties of the COFs were examined using in UV-vis diffuse reflectance absorption spectroscopy and are presented as the Kubelka-Munk function (F(R)) for solid materials.[68] W-A-H and W-A-Cl COF exhibit an absorption maximum at 580 nm, W-A-Br at 611 nm and W-A-I at 572 nm (**Figure 3.2**a). Assuming direct optical transitions for all COFs, the optical bandgap energies were determined using Tauc plots, yielding 1.70 eV for W-A-H COF, 1.66 eV for W-A-Cl, 1.62 eV for W-A-Br and 1.61 eV for W-A-I eV (**Figure 3.2**a, inset). The observed decrease in the optical band gap energy correlates with the increasing size

of the halogen atom, consistent with previously published results.[34,38,69,70] This results from changes in orbital participation.[71,72] Additionally, the optical properties of the W-A-H COF were compared to the previously reported[73] Wurster-terephthalaldehyde (W-TA) COF, which is structurally similar to the anthracene moiety but lacks the additional fused benzene rings (**Figure 3.35**). UV-vis spectra revealed that the W-A-H COF exhibits a redshift of 97 nm relative to the W-TA COF, along with a significantly reduced optical gap energy (1.70 eV vs. 1.89 eV). The transition towards longer wavelengths and the concomitant reduction in bandgap can be attributed to the augmented conjugation provided by the tri-fused benzene rings present in anthracene.[11,74]

To further investigate the optical properties of the materials, photoluminescence (PL) spectroscopy was performed on the series of W-A-X COFs (**Figure 3.2**b). All anthracene-based frameworks exhibited strong emission in the red to near-infrared region, with emission maxima at 755 nm for W-A-H, 757 nm for W-A-Cl, 771 nm for W-A-Br, and 776 nm for W-A-I. Consistent with the trend observed in the UV-vis spectra, the emission profiles display a gradual redshift with increasing halogen atomic size, indicating enhanced π-conjugation and modulated electronic interactions within the framework. Additionally, PL measurements were performed for the W-TA COF to serve as a reference (**Figure 3.36**). In contrast to the anthracene-containing systems, W-TA exhibited a markedly blue-shifted emission maximum at 670 nm, consistent with its reduced conjugation. This mirrors the trend seen in the UV-vis data. The consistent redshift across both absorption and emission spectra highlights the impact of the extended π-system provided by the anthracene core in lowering the energy of electronic transitions.[14,75]

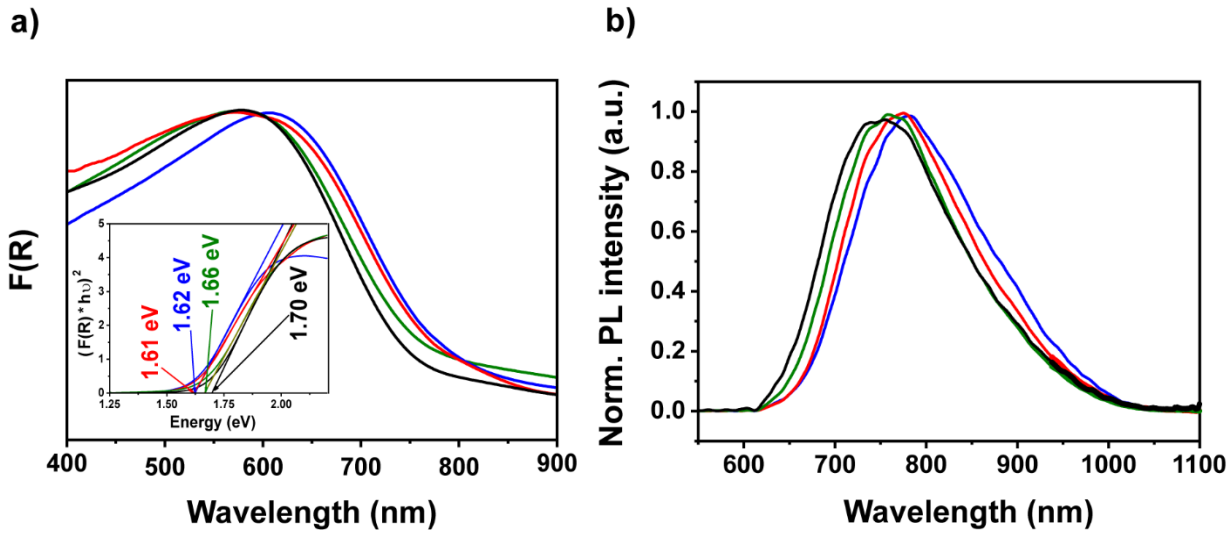

Figure 3.2. Optical properties of W-A-H (black), W-A-Cl (green), W-A-Br (blue), W-A-I (red): (a) F(R) and Tauc plots (inset), (b) PL spectra.

Transient PL spectroscopy measurements were performed for the W-A-X COFs to investigate the excited-state lifetimes as a function of the halogen atom present in the anthracene linker, with the W-TA COF included as a reference (**Figure 3.37**). The W-A-Cl COF exhibits a significantly longer average lifetime of 7 ps, whereas the lifetimes of the other COFs fall below the resolution limit of 3 ps. Chlorine is the most electronegative halogen among those used in these COF systems, and the extended luminescence lifetime can be attributed to its enhanced electron-withdrawing character. The combination of the A-Cl-CHO linker with an electron donor such as W-NH_2 enhances donor-acceptor interactions within the COF, thereby stabilizing the excited state and extending its lifetime.[76]

To understand the observed redshift in UV-vis absorption and the corresponding decrease in optical band gap energy across the W-A-X COF series (X = H, Cl, Br, I), DFT calculations were first performed to determine their electronic band structures. The band structure of W-A-H (**Figure 3.3**b) shows typical Kagome-like band features[77] along the in-plane high-symmetry path (Γ – M – K – Γ) with moderate band widths, while the band dispersions in the out-of-plane direction (Γ – A) are significantly stronger. Consistent with the strategy of tuning anthracene's (opto-)electronic properties through framework integration, the electronic band gap is observed to be relatively low, indicative of semiconducting behavior. The W-A-H COF has a direct band gap of 0.85 eV. The halogenated COF derivatives exhibit the same electronic band features as

well as a direct band gap of similar size (W-A-Cl: 0.85 eV, W-A-Br: 0.84 eV, W-A-I: 0.85 eV; see **Figure 3.3**e and **Figure 3.38**). However, the asymmetric halogenated anthracene moieties break the threefold symmetry that underlies the distinct Kagome-band-like features. This becomes noticeable in the band structure by a gap opening of the Dirac-cone at the K point in the Brillouin zone (**Figure 3.3**a) in the halogenated COFs as well as the emergence of small band dispersions for the former flat bands (**Figure 3.3**e, highlighted in green).

More detailed analyses of the HOMO and LUMO states show that they are highly localized on the electron-rich donor (Wurster) and electron-deficient acceptor (anthracene) fragments, as exemplarily shown in **Figure 3.3** d and c for W-A-H, respectively. The same localization tendencies are found in the halogenated COFs (see **Figure 3.38**), emphasizing the donor-acceptor character of all four COFs. The energetic comparison of the W-NH_2 and (non-)halogenated anthracene (A-X, X = H, Cl, Br, I) building blocks in the gas phase (**Figure 3.39**) confirms the profound donor character of W-NH_2 with an energetically high HOMO and the acceptor character of the A-X fragments (energetically low lying LUMO).

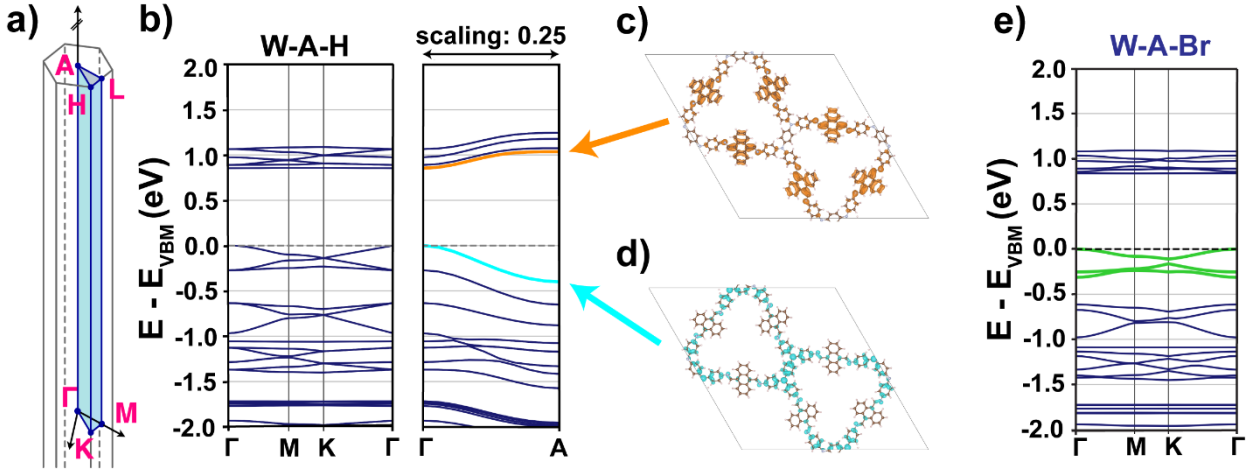

Figure 3.3. (a) Schematic representation of the high symmetry path in the Brillouin Zone of a primitive hexagonal unit cell. (b) Electronic band structure of W-A-H with the partial charge densities of (c) LUMO band in orange and (d) HOMO band in blue. (e) Electronic band structure of W-A-Br with Kagome-like band feature highlighted in green.

After the analysis of the electronic band gap we focus on the optical band gap. Note that the reduced electronic band gaps of the W-A-X COFs as compared to the COF building blocks W-NH_2 and A-X (**Figure 3.39**) do not in general permit a quantitative prediction of an optical

band gap. Unfortunately, optical simulations of the W-A-X COFs are computationally not feasible due to size limitations. Therefore, to study the impact of anthracene halogenation on the optical properties of the W-A-X COFs, we simulated the UV-vis absorption spectrum of the halogenated and non-halogenated anthracene molecules A-X (**Figure 3.4**a) with time-dependent density functional theory (TD-DFT, more details in the experimental section of the Appendix). The spectra show a distinct redshift in the absorption maximum from anthracene (A-H) to the halogenated derivatives (A-Cl ≈A-Br < A-I). These maxima are dominated by transitions between the HOMO and LUMO of the molecules, while other energetically close orbitals have substantially lower weights in these transitions. The energetic shift of the absorption maxima (A-Cl: - 35 meV, A-Br: - 40 meV, A-I: - 59 meV) with respect to anthracene is consistent with the observed trend in the electronic HOMO - LUMO gaps of the halogenated anthracenes with respect to A-H (A-Cl: - 31 meV, A-Br: - 34 meV, A-I: - 49 meV). In order to extrapolate these findings to the larger COF systems, a systematic extension of anthracene towards a combined anthracene-Wurster fragment of W-A-H, as present in the COF (see **Figure 3.4**b), was studied next. Already at the level of extension with phenyl groups, we observe a redshift of the absorption maxima into the visible region (**Figure 3.4**c). Concomitantly, the LUMO energy is significantly lowered, while the energetic position of the HOMO remains unaffected (more details in the Appendix, **Figure 3.40**). The same redshift trend is also observed for the halogenated AX-2(CN-Ph) fragments, although on a smaller scale (**Figure 3.41**), shifts of optical excitation energy w.r.t. A-H-2(CN-Ph) for Cl: - 13 meV, Br: - 16meV, I: - 27 meV). Following this trend, we expect the COFs to inherit the absorption properties of their fragments (i.e., the redshift of halogenated anthracenes) in the low-energy regime.

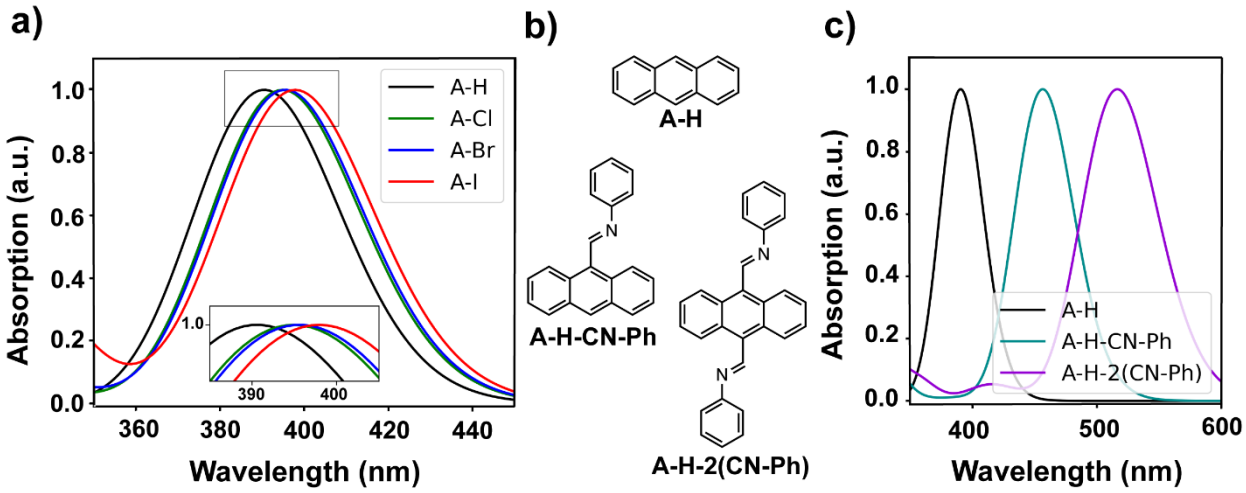

Figure 3.4. (a) Theoretical absorption spectrum of anthracene (A-H, black) and its halogenated derivatives (A-X, X = Cl (green), Br (blue), I (red)) with an inset showing the absorption maxima. (b) Molecular structure and (c) theoretical absorption spectrum of extended anthracene molecules A-H (black), A-H-CN-Ph (turquoise) and A-H-2(CN-Ph) (purple) simulating a combined Wurster-anthracene fragment.

We finally note that the experimental optical band gaps of the COFs (1.60–1.70 eV) do not coincide with the calculated electronic band gaps (~0.85 eV). Typically, one would expect a significant exciton binding energy to reduce the electronic band gap toward the optical band gap. In the present case, however, the calculated electronic band gap is substantially lower than the observed optical band gap, and a negative exciton binding energy is physically implausible. To gain insight into this apparent discrepancy, we analyzed the spatial localization of the HOMO and LUMO states (see **Figure 3.3**d and c). This would indicate a charge-transfer-type transition at the lowest energy, i.e. around the electronic band gap, which however is typically dark. In contrast, our theoretical results from the gradual extension of the anthracene units suggest a predominantly local, anthracene-based excitation rather than a charge-transfer-type transition. In a, the electronic bands formed by atomic orbitals located on the anthracene units in W-A-H are colored in dark red, while those dominated by contributions from Wurster units are shown in dark blue. A local, anthracene-dominated transition from the highest valence band to the lowest conduction band in W-A-H (with anthracene character) requires about 1.91 eV. Accounting for the exciton binding energy, this value is close to and consistent with the experimental optical band gap. Similar conclusions can be drawn for the halogenated COFs (see **Figure 3.5**b-c; local halogenated-anthracenes transitions for W-A-Cl: 1.93 eV, W-A-Br:

1.93 eV, W-A-I: 1.93 eV), while the influence of the halogen atoms is more clearly discernible in the optical simulation data.

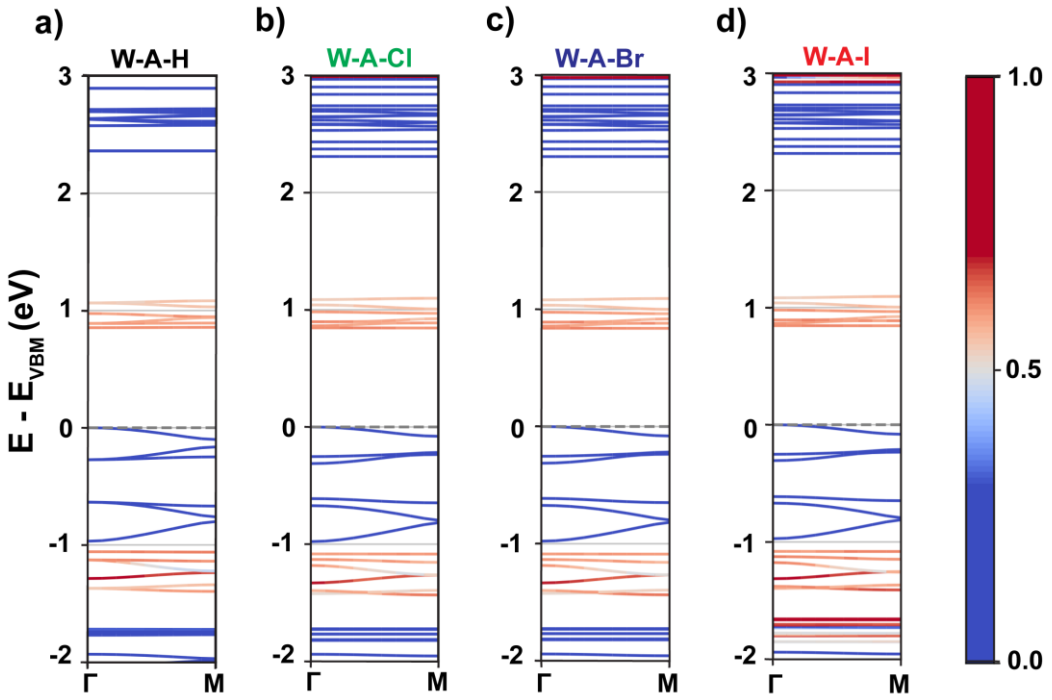

Figure 3.5. Projected band structure of (a) W-A-H, (b) W-A-Cl, (c) W-A-Br and (d) W-A-I with bands solely located on (halogenated) anthracene fragments colored in dark red.

3.4. Conclusion

This work presents the first detailed investigation into the effects of single-atom halogen substitution on the structure and optoelectronic properties of anthracene-based covalent organic frameworks. Through systematic synthesis and characterization of W-A-X COFs (X = H, Cl, Br, I), we demonstrate that even minimal structural modifications, namely, the introduction of a single halogen atom, induce pronounced changes in crystallite size, morphology, and optical properties. Our findings reveal that larger halogens such as bromide promote the formation of larger crystalline domains, while smaller or more electronegative halogens lead to reduced domain growth. We hypothesize that this behavior is closely linked to reaction conditions and halogen-mediated electrostatic interactions, as confirmed by electrostatic potential surface modeling. Furthermore, both UV-vis absorption and photoluminescence measurements exhibit a redshift across the halogen series, correlating with increased polarizability and extended

conjugation, in excellent agreement with theoretical simulations. Importantly, the band structure calculations affirm the donor-acceptor nature of these frameworks and highlight the role of local anthracene-based transitions in determining the optical bandgap. This joint theoretical-experimental study provides comprehensive insight into structure–property relationships in halogenated COFs, establishing halogenation as a powerful design tool for modulating the physical and functional properties of COFs and paving the way for their rational design in optoelectronic and photocatalytic applications.

3.5. References

[1] A. P. Côté, A. I. Benin, N. W. Ockwig, M. O'Keeffe, A. J. Matzger, O. M. Yaghi, *Science* **2005**, *310*, 1166–1170.

[2] X. Feng, X. Ding, D. Jiang, *Chem. Soc. Rev.* **2012**, *41*, 6010.

[3] S. He, B. Yin, H. Niu, Y. Cai, *Appl. Catal. B Environ.* **2018**, *239*, 147–153.

[4] G. C. Welch, L. A. Perez, C. V. Hoven, Y. Zhang, X.-D. Dang, A. Sharenko, M. F. Toney, E. J. Kramer, T.-Q. Nguyen, G. C. Bazan, *J. Mater. Chem.* **2011**, *21*, 12700.

[5] X. Liu, D. Huang, C. Lai, G. Zeng, L. Qin, H. Wang, H. Yi, B. Li, S. Liu, M. Zhang, R. Deng, Y. Fu, L. Li, W. Xue, S. Chen, *Chem. Soc. Rev.* **2019**, *48*, 5266–5302.

[6] Q. Gao, X. Li, G.-H. Ning, H.-S. Xu, C. Liu, B. Tian, W. Tang, K. P. Loh, *Chem. Mater.* **2018**, *30*, 1762–1768.

[7] K. Konstas, K. F. Taupitz, D. R. Turner, D. F. Kennedy, M. R. Hill, *CrystEngComm* **2014**, *16*, 8937–8940.

[8] J.-R. Zhang, H.-Y. Zhang, J.-H. Guo, Z.-H. Liu, C.-Y. Ma, X.-G. Yang, X.-Y. Lu, J.-H. Qin, L.-F. Ma, *Dalt. Trans.* **2022**, *51*, 1769–1774.

[9] X. Liu, B. Liu, G. Li, Y. Liu, *J. Mater. Chem. A* **2018**, *6*, 17177–17185.

[10] Q. An, S. Bao, X. Li, J. Sun, Z. Su, *New J. Chem.* **2022**, *46*, 11377–11381.

[11] Y. Liu, Z. Zhao, W. Xu, W. Gong, *Catal. Sci. Technol.* **2024**, *14*, 3211–3218.

[12] J. Jeon, Y. J. Kim, S. H. Joo, H. Noh, S. K. Kwak, J. Baek, *Angew. Chemie* **2023**, *135*,

e202217416.

[13] W. Y. Geng, S. F. Guo, H. Zhang, Y. H. Luo, X. X. Lu, F. Y. Chen, Z. X. Wang, D. E. Zhang, *J. Solid State Chem.* **2022**, *310*, 123004.

[14] M. Faheem, S. Aziz, X. Jing, T. Ma, J. Du, F. Sun, Y. Tian, G. Zhu, *J. Mater. Chem. A* **2019**, *7*, 27148–27155.

[15] N. Huang, X. Ding, J. Kim, H. Ihee, D. Jiang, *Angew. Chemie Int. Ed.* **2015**, *54*, 8704–8707.

[16] X. Ma, J. Kang, W. Cao, Y. Wu, C. Pang, S. Li, Z. Yi, Y. Xiong, C. Li, M. Wang, Z. Xu, J. Li, *J. Colloid Interface Sci.* **2024**, *659*, 665–675.

[17] Y. Cheng, J. Xin, L. Xiao, X. Wang, X. Zhou, D. Li, B. Gui, J. Sun, C. Wang, *J. Am. Chem. Soc.* **2023**, *145*, 18737–18741.

[18] M. C. Lin, S. W. Kuo, M. G. Mohamed, *Mater. Adv.* **2024**, *5*, 6222–6233.

[19] L. Zhao, Y. Gao, X. Fu, Y. Chen, B. Zhang, F. Xuan, *Small Methods* **2025**, *9*, 2401341.

[20] S. Haldar, D. Chakraborty, B. Roy, G. Banappanavar, K. Rinku, D. Mullangi, P. Hazra, D. Kabra, R. Vaidhyanathan, *J. Am. Chem. Soc.* **2018**, *140*, 13367–13374.

[21] M. Aydemir, G. Haykir, H. Selvitopi, O. C. Yildirim, M. E. Arslan, B. Abay, F. Turksoy, *J. Mater. Chem. B* **2023**, *11*, 4287–4295.

[22] W. Zhu, B. Zhao, S. Fang, H. Zhu, F. Huang, *Chem. Sci.* **2024**, *15*, 16300–16306.

[23] J. W. Jung, F. Liu, T. P. Russell, W. H. Jo, *Adv. Energy Mater.* **2015**, *5*, 1500065.

[24] F. A. Faraghally, A. F. Musa, C. Chen, Y. Chen, Y. Chen, C. Yeh, T. Wei, *Small Struct.* **2024**, *5*, 2400236.

[25] J. Zuo, K. Liu, J. Harrell, L. Fang, P. Piotrowiak, D. Shimoyama, R. A. Lalancette, F. Jäkle, *Angew. Chemie* **2024**, *136*, e202411855.

[26] S. Kyushin, Y. Suzuki, *Molecules* **2022**, *27*, 2241.

[27] C. Kitamura, H. Tsukada, T. Kawase, T. Kobayashi, H. Naito, *X-ray Struct. Anal. Online*

2010, *26*, 65–66.

[28] L. Ascherl, T. Sick, J. T. Margraf, S. H. Lapidus, M. Calik, C. Hettstedt, K. Karaghiosoff, M. Döblinger, T. Clark, K. W. Chapman, F. Auras, T. Bein, *Nat. Chem.* **2016**, *8*, 310–316.

[29] J. M. Rotter, R. Guntermann, M. Auth, A. Mähringer, A. Sperlich, V. Dyakonov, D. D. Medina, T. Bein, *Chem. Sci.* **2020**, *11*, 12843–12853.

[30] H.-G. Zhang, W.-T. Yu, S.-N. Yan, C. Cheng, X.-T. Tao, *Acta Crystallogr. Sect. E Struct. Reports Online* **2006**, *62*, o5236–o5238.

[31] R. Guntermann, D. Helminger, L. Frey, P. M. Zehetmaier, C. Wangnick, A. Singh, T. Xue, D. D. Medina, T. Bein, *Angew. Chemie Int. Ed.* **2024**, *63*, e202407166.

[32] L. Wang, J. Chakraborty, M. Deng, J. Sun, P. Van Der Voort, *ChemCatChem* **2024**, *16*, e202400200.

[33] L. Zhai, S. Cui, B. Tong, W. Chen, Z. Wu, C. Soutis, D. Jiang, G. Zhu, L. Mi, *Chem. - A Eur. J.* **2020**, *26*, 5784–5788.

[34] M. Wang, Z. Wang, M. Shan, J. Wang, Z. Qiu, J. Song, Z. Li, *Chem. Mater.* **2023**, *35*, 5368–5377.

[35] E.-A. Bittner, K. Merkel, F. Ortmann, *npj 2D Mater. Appl.* **2024**, *8*, 58.

[36] R. Matheu, J. A. Vigil, E. J. Crace, H. I. Karunadasa, *Trends Chem.* **2022**, *4*, 206–219.

[37] Y. Yang, L. Guo, X. Wang, Z. Li, W. Zhou, *Adv. Powder Mater.* **2024**, *3*, 100178.

[38] K. A. Othman, Y. H. Azeez, R. A. Omer, R. O. Kareem, *Kondens. sredy i mezhfaznye granitsy = Condens. Matter Interphases* **2024**, *26*, 280–294.

[39] Otto Phanstiel, *Fluorescent Cytotoxic Compounds Specific for the Cellular Polyamine Transport System*, **2001**.

[40] K.-I. Yamashita, M. Tsuboi, M. S. Asano, K.-I. Sugiura, *Synth. Commun.* **2012**, *42*, 170–175.

[41] B. Yang, A. S. Abyzov, E. Zhuravlev, Y. Gao, J. W. P. Schmelzer, C. Schick, *J. Chem.*

Phys. **2013**, *138*, 054501.

[42] Y. Zheng, *Molecules* **2023**, *29*, 141.

[43] M. Seidler, N. K. Li, X. Luo, S. Xuan, D. Prendergast, R. N. Zuckermann, N. P. Balsara, X. Jiang, *Microsc. Microanal.* **2022**, *28*, 2206–2208.

[44] K. J. Donald, in *Explor. Chem. Concepts Through Theory Comput.*, Wiley, **2024**, pp. 285–316.

[45] R. M. Gomila, T. J. Mooibroek, A. Frontera, in *Hot Top. Cryst. Eng.*, Elsevier, **2021**, pp. 119–155.

[46] P. Politzer, J. S. Murray, T. Clark, *J. Phys. Chem. A* **2019**, *123*, 10123–10130.

[47] X.-H. Ding, Y.-Z. Chang, C.-J. Ou, J.-Y. Lin, L.-H. Xie, W. Huang, *Natl. Sci. Rev.* **2020**, *7*, 1906–1932.

[48] V. Nemec, K. Lisac, M. Liović, I. Brekalo, D. Cinčić, *Materials (Basel).* **2020**, *13*, 2385.

[49] T. Ju, M. Liu, X. Shi, A. Xiao, Z. Zhang, J. Wang, Y. Zhang, Y. Wang, *ACS Nano* **2023**, *17*, 23784–23793.

[50] M. A. A. Ibrahim, A. M. M. Mahmoud, M. N. I. Shehata, R. R. A. Saeed, N. A. M. Moussa, S. R. M. Sayed, M. K. Abd El-Rahman, T. Shoeib, *ACS Omega* **2024**, *9*, 10391–10399.

[51] T. Lang, X. Zhang, L. Meng, Y. Zeng, *Struct. Chem.* **2016**, *27*, 927–937.

[52] E. Dautzenberg, F. W. Claassen, L. C. P. M. de Smet, *Microporous Mesoporous Mater.* **2023**, *350*, 112318.

[53] M. Calik, T. Sick, M. Dogru, M. Döblinger, S. Datz, H. Budde, A. Hartschuh, F. Auras, T. Bein, *J. Am. Chem. Soc.* **2016**, *138*, 1234–1239.

[54] V. Safarifard, A. Morsali, *CrystEngComm* **2014**, *16*, 8660–8663.

[55] I. A. Lázaro, N. Almora-Barrios, S. Tatay, C. Martí-Gastaldo, *Chem. Sci.* **2021**, *12*, 2586–2593.

[56] S. Hou, G. Zhang, Z. Qiao, Y. Bai, H. Di, Y. Hua, T. Hao, H. Xu, *Angew. Chemie Int. Ed.* **2025**, *64*, e202421555.

[57] N. Zhang, T. Wang, X. Wu, C. Jiang, F. Chen, W. Bai, R. Bai, *RSC Adv.* **2018**, *8*, 3803–3808.

[58] A. Varadwaj, H. M. Marques, P. R. Varadwaj, *Molecules* **2019**, *24*, 379.

[59] L. Sarkisov, R. Bueno-Perez, M. Sutharson, D. Fairen-Jimenez, *Chem. Mater.* **2020**, *32*, 9849–9867.

[60] K. Zhao, H. Qiao, S. Wang, X. Xu, C. Wang, M. Jiao, L. Yang, X. Kong, Z. Zhu, N. Qin, L. Zhai, *ACS Mater. Lett.* **2024**, *6*, 212–221.

[61] B. Song, R. E. Sikma, C. McKeown, K. Leung, D. F. Sava Gallis, A. G. Ilgen, *ACS Appl. Nano Mater.* **2025**, *8*, 15791–15798.

[62] G. Kupgan, T. P. Liyana-Arachchi, C. M. Colina, *Langmuir* **2017**, *33*, 11138–11145.

[63] T. F. Willems, C. H. Rycroft, M. Kazi, J. C. Meza, M. Haranczyk, *Microporous Mesoporous Mater.* **2012**, *149*, 134–141.

[64] N. V. Pervukhina, S. V. Borisov, S. A. Magarill, *Кристаллография* **2023**, *68*, 566–574.

[65] P. J. Waller, Y. S. Alfaraj, C. S. Diercks, N. N. Jarenwattananon, O. M. Yaghi, *J. Am. Chem. Soc.* **2018**, *140*, 9099–9103.

[66] Y. Zhang, W. Shi, Y. Zhao, C. Zhang, Y. Zhi, *Macromol. Rapid Commun.* **2023**, *44*, 1–7.

[67] D. r. Palleros, *"Infrared Spectroscopy" in Experimental Organic Chemistry.*, Wiley, New York, **2000**.

[68] R. Alcaraz de la Osa, I. Iparragirre, D. Ortiz, J. M. Saiz, *ChemTexts* **2020**, *6*, 2.

[69] D. Cao, J. Guan, J. Du, Q. Sun, J. Ma, J. Li, J. Liu, G. Sheng, *J. Hazard. Mater.* **2024**, *476*, 134956.

[70] C. F. Fu, C. Zhao, Q. Zheng, X. Li, J. Zhao, J. Yang, *Sci. China Chem.* **2020**, *63*, 1134–1141.

[71] P. R. Varadwaj, A. Varadwaj, H. M. Marques, K. Yamashita, *J. Comput. Chem.* **2018**, *39*, 1902–1912.

[72] A. Labdelli, F. Bendahma, M. Mana, N. Benderdouche, *Rev. Mex. Física* **2023**, *69*, 061001.

[73] J. M. Rotter, R. Guntermann, M. Auth, A. Mähringer, A. Sperlich, V. Dyakonov, D. D. Medina, T. Bein, *Chem. Sci.* **2020**, *11*, 12843–12853.

[74] M. Mbarek, M. Chemek, J. Wery, J. L. Duvail, K. Alimi, *J. Phys. Chem. Solids* **2014**, *75*, 752–758.

[75] C.-S. Choi, I. T. Kim, S. W. Lee, H. H. Lee, Y. N. Lee, K.-S. Jeon, K.-H. Lee, N.-D. Sung, M.-J. Kil, Y.-I. Lee, *Macromol. Res.* **2004**, *12*, 322–324.

[76] B. Ma, X. Lin, T. Zhu, X. Zheng, J. Zhu, *Colloids Surfaces B Biointerfaces* **2024**, *242*, 114101.

[77] W. Jiang, X. Ni, F. Liu, *Acc. Chem. Res.* **2021**, *54*, 416–426.

3.6. Appendix

3.6.1. Experimental section

Chemicals. All materials were purchased from Aldrich, Fluka, Acros, Activate Scientific, or TCI Europe in the common purities purum, puriss, or reagent grade. Materials were used as received without additional purification and handled in air unless noted otherwise. All used solvents were anhydrous and purged with inert gas.

Powder X-ray diffraction (PXRD) measurements. PXRD measurements were performed on a Bruker D8 Discover diffractometer using Ni-filtered Cu Kα radiation and a position sensitive LynxEye detector in Bragg-Brentano geometry.

Nitrogen sorption measurement. Nitrogen sorption isotherms were recorded on a Quantachrome Autosorb 1 at 77 K within a pressure range from p/p_0 = 0.001 to 0.98. Prior to the measurement of the sorption isotherms, the samples were heated for 24 h at 120 °C under turbo-pumped vacuum. For the evaluation of the surface area the BET model was applied

between 0.05 and 0.28 p/p_0. Pore size distributions were calculated using the NLDFT equilibrium model with a carbon kernel for slit/cylindrical pores.

The **structure models of the COFs** were constructed using the Accelrys Materials Studio software package. For W-A-H, P-3 symmetry and for W-A-Cl, W-A-Br and W-A-I COFs P-1 symmetry was applied. The structure models were optimized using the Forcite module with the Dreiding force-field. Further refinements using the Pawley method were carried out as implemented in the Reflex module of the Materials Studio software. Thompson-Cox-Hastings peak profiles were used, and peak asymmetry was corrected using the Berar-Baldinozzi method.

Liquid state ^{1}H and ^{13}C nuclear magnetic resonance (NMR) analysis. Liquid state NMR spectra were recorded on Bruker AV 400 and AV 400 TR spectrometers. Proton chemical shifts are expressed in parts per million (δ scale) and are calibrated using residual non-deuterated solvent peaks as internal reference (e.g. $CDCl_3$: 7.26 ppm in ^{1}H NMR and 77.0 ppm in ^{13}C NMR).

Solid state ^{13}C NMR analysis. The solid state ^{13}C cross-polarization magic angle spinning (CP/MAS) spectra were obtained on a Bruker Avance III-500 solid state NMR spectrometer with a 4 mm double resonance MAS probe and at a MAS rate of 10.0 kHz with a contact time of 2-5 ms and a pulse delay of 4 s.

Fourier-transform infrared (FT-IR) spectra. FT-IR measurements were performed with a Bruker Vertex 70 FTIR instrument by focusing light of a globar (silicon carbide) as MIR light source through a KBr beam splitter with integrated gold mirrors and an ATR sample stage with a Ge crystal. The spectra were recorded by an N_2-cooled MCT detector with a resolution of 2 cm^{-1} and averaged over 1000 scans.

Thermogravimetric analysis (TGA). TGA measurements were performed on a Netzsch Jupiter ST 449 C instrument equipped with a Netzsch TASC 414/4 controller. The samples were heated from room temperature to 900 °C under a synthetic air flow (25 mL min^{-1}) at a heating rate of 10 K min^{-1}.

Scanning electron microscopy (SEM) images. SEM images were recorded with an FEI Helios NanoLab G3 UC scanning electron microscope equipped with a field emission gun operated at 3 kV. Prior to the measurements, the samples were sputtered with carbon.

Transmission electron microscopy (TEM) images. TEM images were recorded with an FEI Titan Themis 60 - 300 equipped with a field emission gun operated at 300 kV.

Ultraviolet-Vis-infrared (UV-vis) absorption spectra. The UV-vis spectra were recorded on a Perkin-Elmer Lambda 1050 spectrometer equipped with a 150 mm integrating sphere with InGaAs detector. Diffuse reflectance spectra were collected with a Praying Mantis (Harrick) accessory and were referenced to barium sulfate powder as white standard. The specular reflection of the sample surface was removed from the signal using apertures that allow only light scattered at angles > 20° to pass.

Steady-state photoluminescence (PL) and time-correlated single-photon counting (TCSPC).

A home-built confocal laser scanning microscope (CLSM) setup was used for characterizing the photoluminescence of powder of W-A-X COFs (X = H, Cl, Br, I) and their linkers A-X-CHO (X = H, Cl, Br, I). The samples were measured in the epi-direction using an air objective (0.85 NA, Fluor 40, NIKON). A beamsplitter (MELLES GRIOT 03BTL005) and a 490 nm long-pass filter were utilized to separate the laser from the photoluminescence (PL) light. Excitation was provided by a sub-picosecond laser (iChrome TOPTICA) operating at 476 nm with repetition rate of 40 MHz. The detection system was divided into two components. The first part featured an avalanche photodiode (APD, type: MPD PDM, with a detector size of 50 × 50 μm), which was used in combination with time-correlated single-photon counting (TCSPC) electronics (BECKER UND HICKEL) to measure time-resolved PL transients. The second part comprised a spectrometer (ANDOR SHAMROCK SRi303) connected to a CCD camera (ANDOR NEWTON DU920) for capturing spectra. The data were recorded using a customized LABVIEW (National Instruments) program that integrated the manufacturers' software with our specific measurement requirements. Further data processing and analysis, including extracting PL spectra and TCSPC transients, were performed using MATLAB (MATHWORKS).

Density functional Theory (DFT). Theoretical calculations of structural and electronic properties of the four COFs and their fragments were performed with Vienna Ab initio Simulation Package (VASP),[1–4] utilizing the projector-augmented wave (PAW) method[5,6] in combination with the Perdew-Burke-Ernzerhof (PBE) exchange correlation functional[7] and periodic boundary conditions. For the gas-phase calculations for all building blocks and their extended fragments, a vacuum of at least 5 Å in each direction was applied. For the COF structures, we employed the Becke-Johnson damping variant of DFT-D3[8] to correct the van der Waals (vdW) dispersion. Geometry optimization of the atomic positions and the lattice parameters of the molecular structures were optimized in an alternating fashion with multiple steps, where an energy convergence value of 10^{-6} eV and a kinetic energy cutoff of 400 eV (for atom relaxation) and 520 eV (for lattice relaxation, only for 2D COFs) were used.

The electronic band structure was computed along the high symmetry paths in the Brillouin zone of the primitive hexagonal unit cell. Each segment along the high symmetry paths Γ – M – K – Γ – A was sampled by 10 points. To account for the opening of the band gap and to estimate the band gap at the Hybrid-DFT level (Heyd–Scuseria–Ernzerhof (HSE06) functional),[9] we employed a scissors shift[10] along the high symmetry path.

Time-Dependent Density Functional Theory (TD-DFT). For calculations of optical absorption data on the building blocks and the extended fragments, we used TD-DFT[11] with the HSE06 exchange correlation functional and a triple zeta basis set[12], as implemented in the Gaussian16 software package[13]. To account for spectral broadening, a Gaussian broadening with a finite width (σ = 0.2 eV) was applied. Since our focus lies on the relative, chemically induced shifts rather than absolute excitation energies, we did not apply any additional empirical offset, as is sometimes done.[14]

3.6.2. Linker synthesis

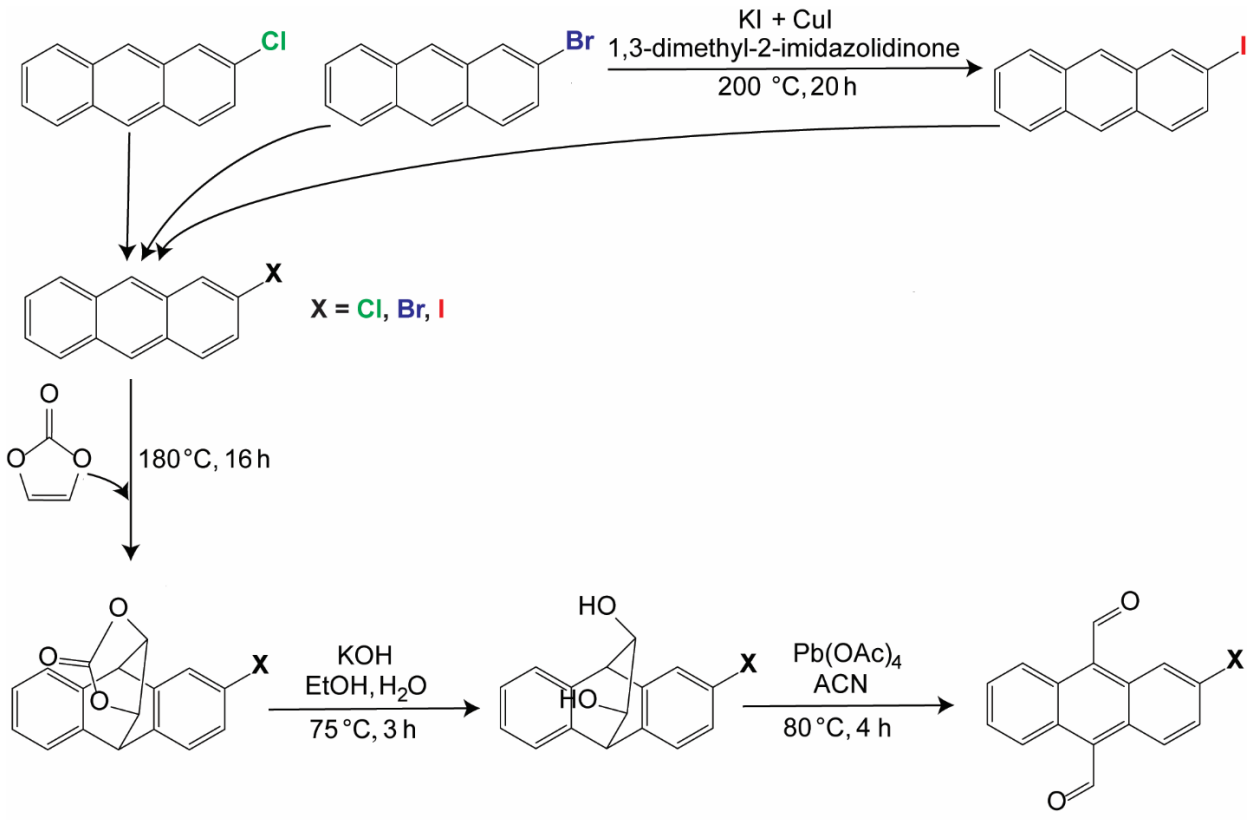

Scheme 3.1. Synthetic route to 2-halogen-9,10-anthracenedialdehyde (A-X-CHO, X = Cl, Br, I) linkers.

2-Chloro-9,10-dihydro-9,10-[4,5]epidioxoloanthracen-13-one (A-Cl-epO)

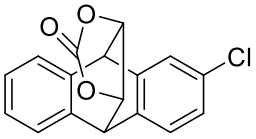

The following procedure was adapted from the previously published literature.[15] 2-Chloroanthracene (1.175 g, 5.541 mmol, 1 equiv.) and vinylene carbonate (3.484 g, 40.452 mmol, 7.3 equiv.) were heated under reflux with stirring for 18 hours, slowly forming a dark brown solution. The consumption of 2-chloroanthracene was monitored by thin-layer chromatography (CH_2Cl_2/hexane 1:49 , R=0.30). The mixture underwent rotary evaporation under high vacuum to remove the excess vinylene carbonate, providing 2-chloro-9,10-dihydro-

9,10-[4,5]epidioxoloanthracen-13-one (A-Cl-epO) as a light-brown solid (1.62 g, 5.43 mmol, 98.1 %). The product was used for the further reaction without additional purification.

^{1}H NMR (400 MHz, $CDCl_3$) δ 7.35 – 7.11 (m, 7H), 4.86 – 4.75 (m, 2H), 4.67 – 4.58 (m, 2H).

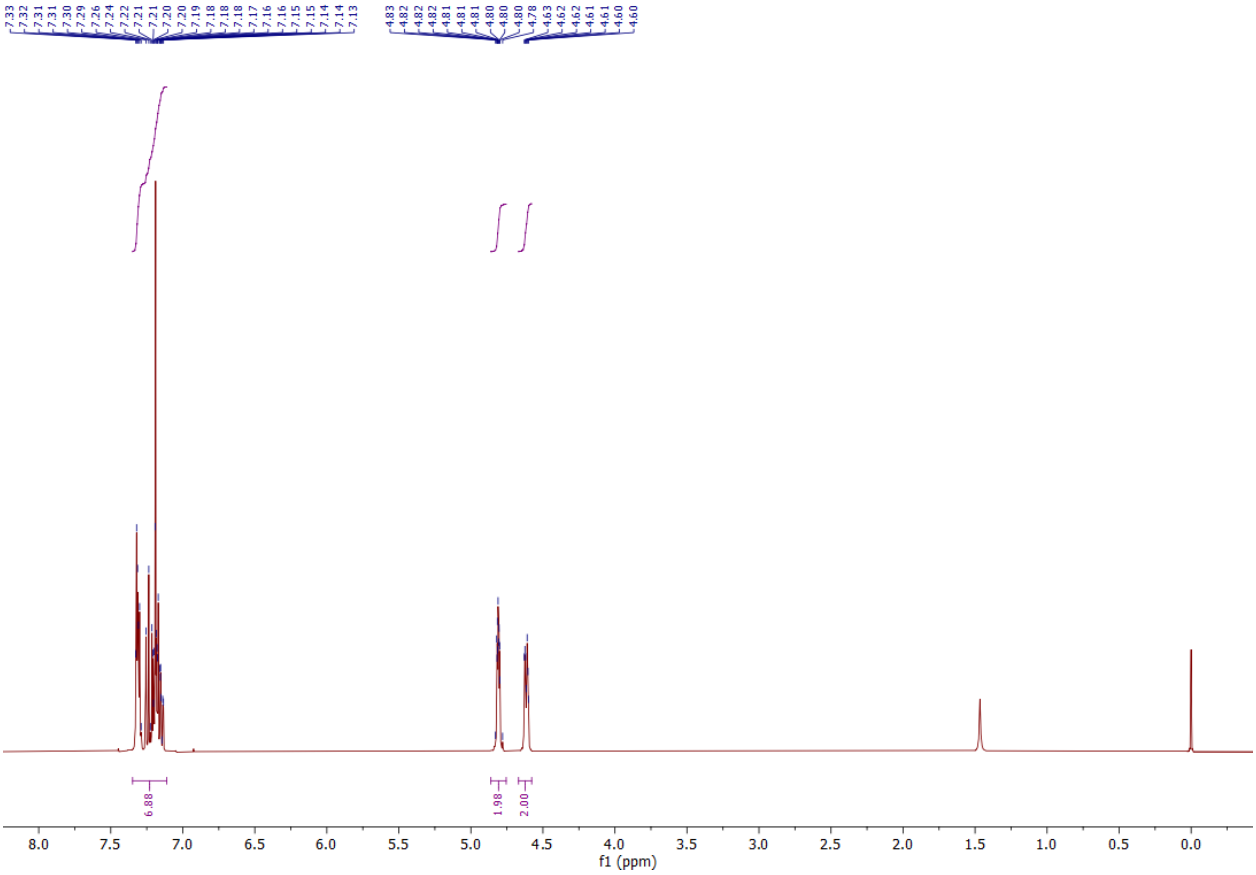

Figure 3.6. ^{1}H NMR spectra (400 MHz in $CDCl_3$) of A-Cl-epO.

2-Chloro-9,10-dihydro-9,10-ethanoanthracene-11,12-diol (A-Cl-(OH)$_2$)

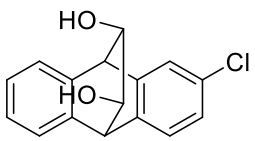

The following procedure was adapted from the previously published literature.[15] Solid potassium hydroxide (1.175 g, 5.225 mmol, 4 equiv.), deionized water (19.60 mL), and absolute ethanol (2.1 mL) were added to the A-Cl-epO (1.568 g, 5.225 mmol, 1 equiv.). The solution was stirred at 75° C for 3 hours. The consumption of the A-Cl-epO was monitored

through thin-layer chromatography (100% CH_2Cl_2, R=0.30). Afterwards, the solution underwent rotary evaporation under reduced pressure to remove the ethanol and roughly half of the water volume. Additional water (39.2 mL) was added to the solution and the solution was stirred at room temperature for one hour, resulting in the formation of a light-tan solid. The contents were vacuum-filtered and then washed with deionized water. The vacuum-filtration receiving flask was changed and the solid was washed with ethyl acetate through the filter paper. The ethyl acetate was removed through rotary evaporation, leaving a yellow solid residue. The product was purified through column chromatography (hexane/ethyl acetate 1:1, R=0.55 & R=0.50), providing two isomers of 2-chloro-9,10-dihydro-9,10-ethanoanthracene-11,12-diol (A-Cl-$(OH)_2$) as a white solid (1.006 g, 3.70 mmol, 70.8 %).

^{1}H NMR (400 MHz,$CHCl_3$) δ (ppm): 7.30 (d, *J* = 2.0 Hz, 1H), 7.27 – 7.19 (m, 3H), 7.15 – 7.07 (m, 3H), 4.36 – 4.29 (m, 2H), 4.04 – 3.97 (m, 2H)

^{1}H NMR (400 MHz,$CHCl_3$) δ (ppm): 7.30 (dd, *J* = 5.4, 3.3 Hz, 2H), 7.26 – 7.04 (m, 5H), 4.33 (dd, *J* = 7.3, 2.5 Hz, 2H), 4.03 – 3.95 (m, 2H)

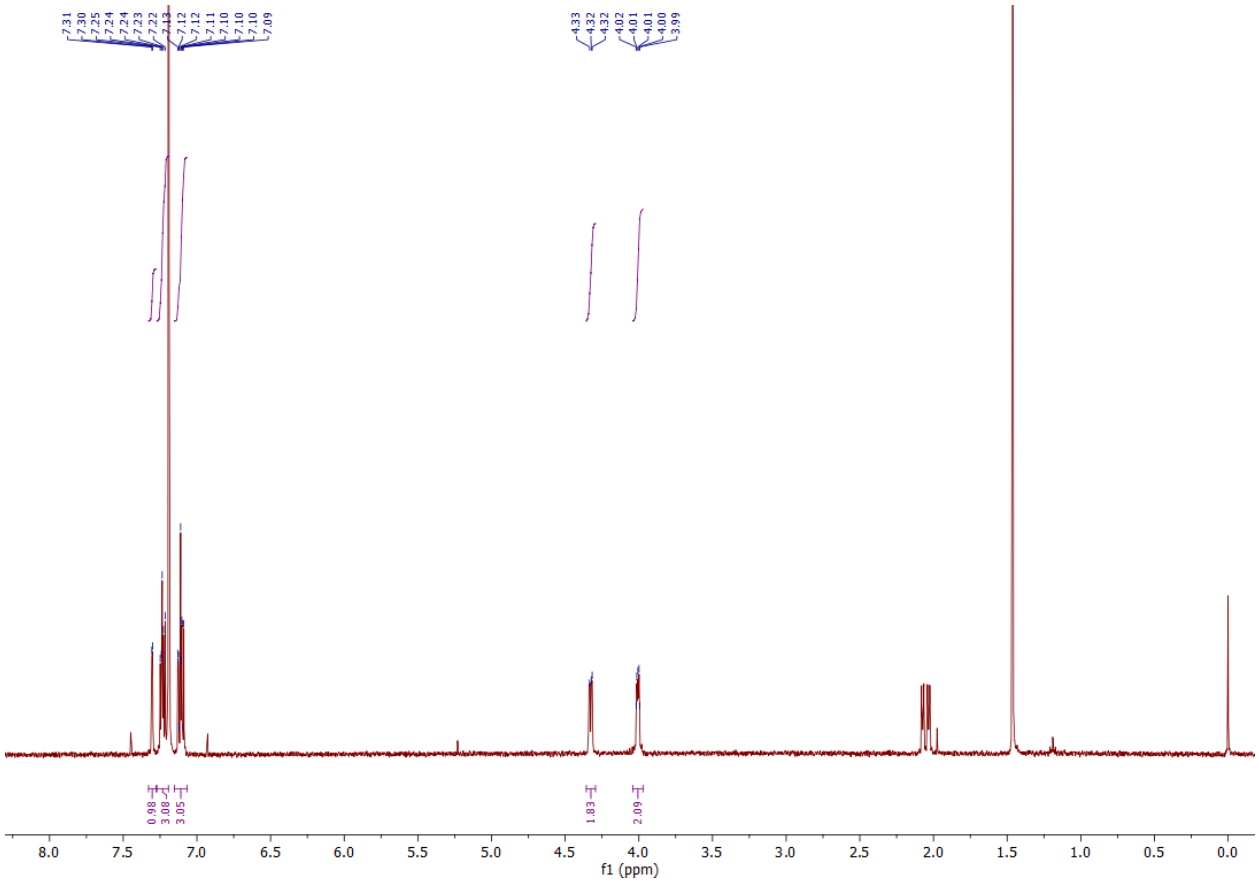

Figure 3.7. ^{1}H NMR spectra (400 MHz in $CDCl_3$) of A-Cl-$(OH)_2$ (isomer 1).

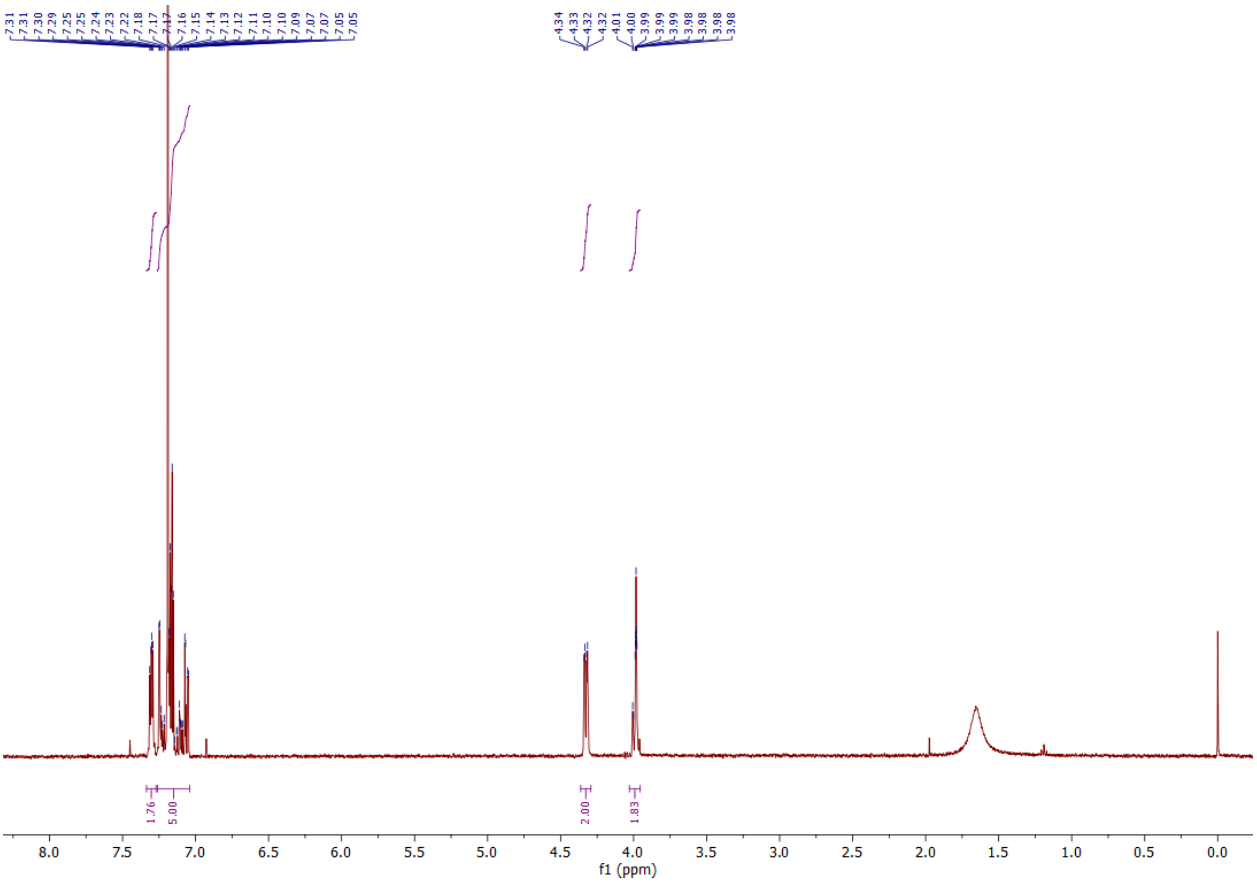

Figure 3.8. ^{1}H NMR spectra (400 MHz in $CDCl_3$) of A-Cl-$(OH)_2$ (isomer 2).

2-Chloroanthracene-9,10-dicarbaldehyde (A-Cl-CHO)

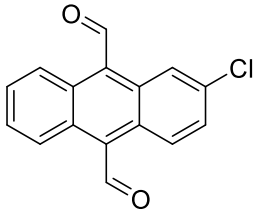

The following procedure was adapted from the previously published literature.[15] The A-Cl-$(OH)_2$ (0.995 g, 3,66 mmol, 1 equiv.) was dissolved in anhydrous acetonitrile (63 mL) and heated to reflux with stirring, forming a transparent, light-tan solution. Lead tetraacetate (3.243 g, 7.316 mmol, 2 equiv.) was added portion-wise to the solution over a period of 5 minutes, quickly turning the solution opaque and brown in color. The solution was then stirred at reflux for 4 hours, resulting in the formation of a dark-orange precipitate within the brown solution.

The consumption of the A-Cl-$(OH)_2$ was monitored through thin-layer chromatography (CH_2Cl_2/ethyl acetate 8:2, R=0.50 & R=0.33). After the reaction was complete, the reaction mixture was concentrated via rotary evaporation and gave a burgundy residue. 10% Aqueous sodium carbonate (70 mL) was added to the residue, allowing the residue to be suspended in the aqueous solution. The organic contents were extracted from the aqueous layer using dichloromethane. The opaque, yellow organic layer was dried over anhydrous sodium sulfate, filtered, and concentrated to give a yellow-orange solid residue. The residue was purified by column chromatography (hexane/CH_2Cl_2/ethyl acetate/hexane 10:1:1, R=0.3), providing 2-chloro-9,10-anthracenedialdehyde (A-Cl-CHO) as an orange solid (0.630 g, 2.350 mmol). Yield 64.26 %.

^{1}H NMR (400 MHz, $CDCl_3$) δ 11.39 (s, 1H), 11.37 (s, 1H), 8.80 (d, J = 2.1 Hz, 1H), 8.71 – 8.60 (m, 3H), 7.72 – 7.62 (m, 2H), 7.57 (dd, J = 9.5, 2.1 Hz, 1H).

^{13}C NMR (101 MHz, $CDCl_3$) δ 193.88, 193.40, 135.30, 133.05, 132.79, 131.33, 130.41, 129.62, 128.98, 128.55, 128.06, 126.13, 124.19, 123.94, 123.14.

Elemental analysis calculated: C (69.06 %), H (3.23 %), Cl (13.20 %). Theoretical: C (71.52 %), H (3.80 %), Cl (13.19 %).

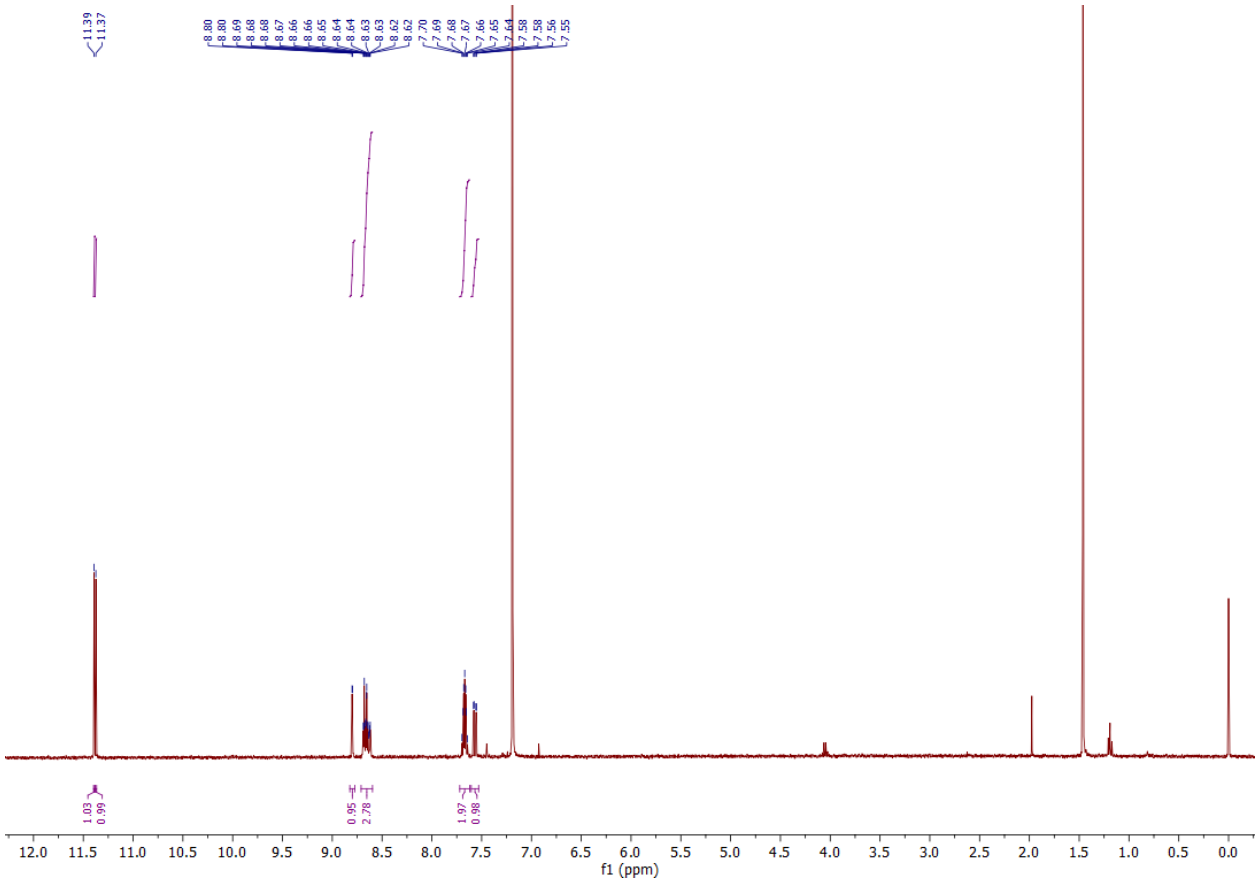

Figure 3.9. ^{1}H NMR spectra (400 MHz in $CDCl_3$) of A-Cl-CHO.

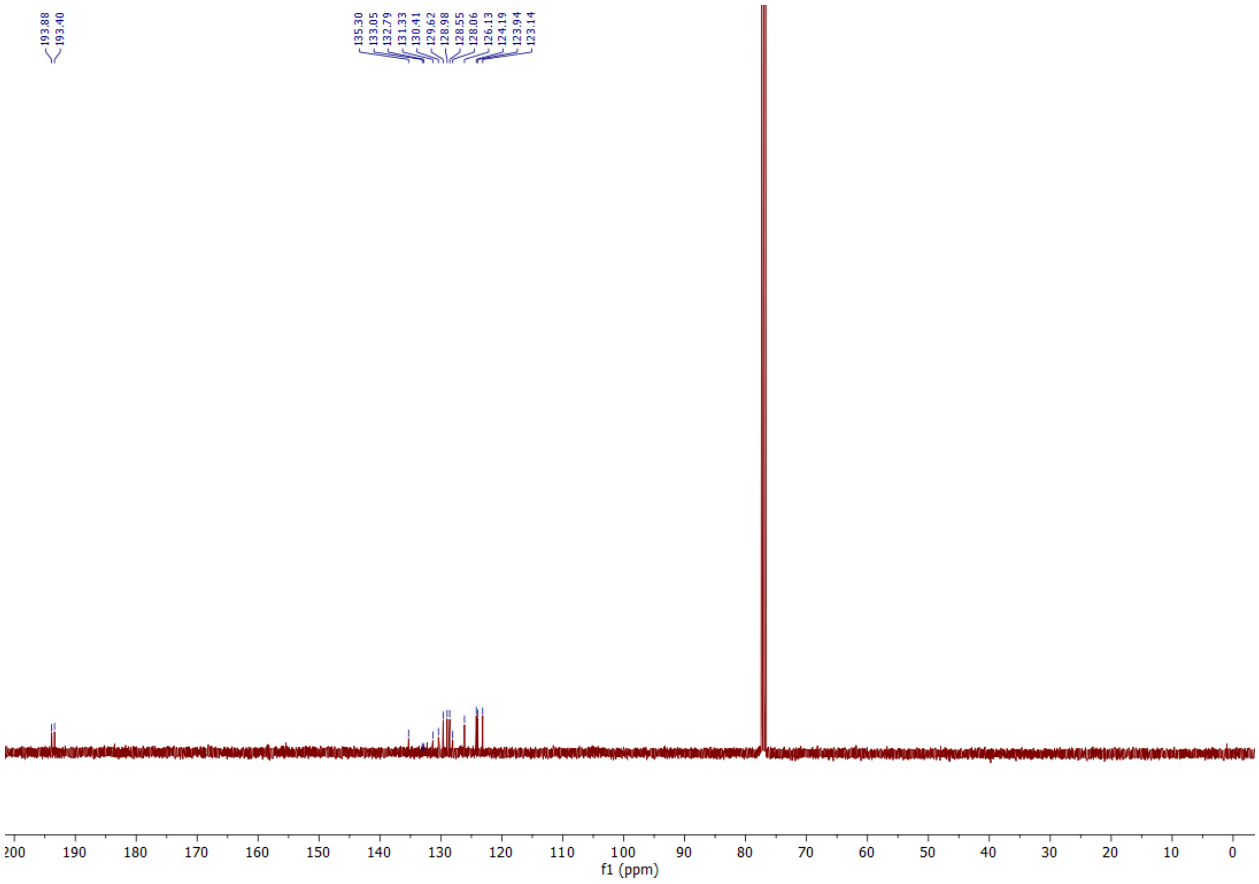

Figure 3.10. ^{13}C NMR spectra (101 MHz in $CDCl_3$) of A-Cl-CHO.

2-Bromo-9,10-dihydro-9,10-[4,5]epidioxoloanthracen-13-one (A-Br-epO)

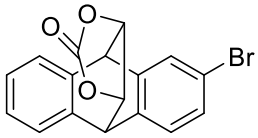

The following procedure was adapted from the previously published literature.[15] 2-Bromoanthracene (2.4 g, 9.39 mmol, 1 equiv.) and vinylene carbonate (5.9 g, 58.56 mmol, 7.3 equiv.) were heated under reflux with stirring for 18 hours, slowly forming a dark brown solution. The consumption of 2-bromoanthracene was monitored by thin-layer chromatography (CH_2Cl_2/hexane 1:49 , R=0.30). The mixture underwent rotary evaporation under high vacuum to remove the excess vinylene carbonate, providing the as 2-bromo-9,10-dihydro-9,10-[4,5]epidioxoloanthracen-13-one (A-Br-epO) light-brown solid (3.18 g, 9.30 mmol, 66.6%). The product was used for the further reaction without additional purification.

^{1}H NMR (400 MHz, $CDCl_3$) δ 7.46 (dd, J = 3.6, 1.9 Hz, 1H), 7.35 – 7.26 (m, 3H), 7.23 – 7.14 (m, 3H), 4.81 (dt, J = 3.7, 1.8 Hz, 2H), 4.61 (dq, J = 7.1, 1.6 Hz, 2H).

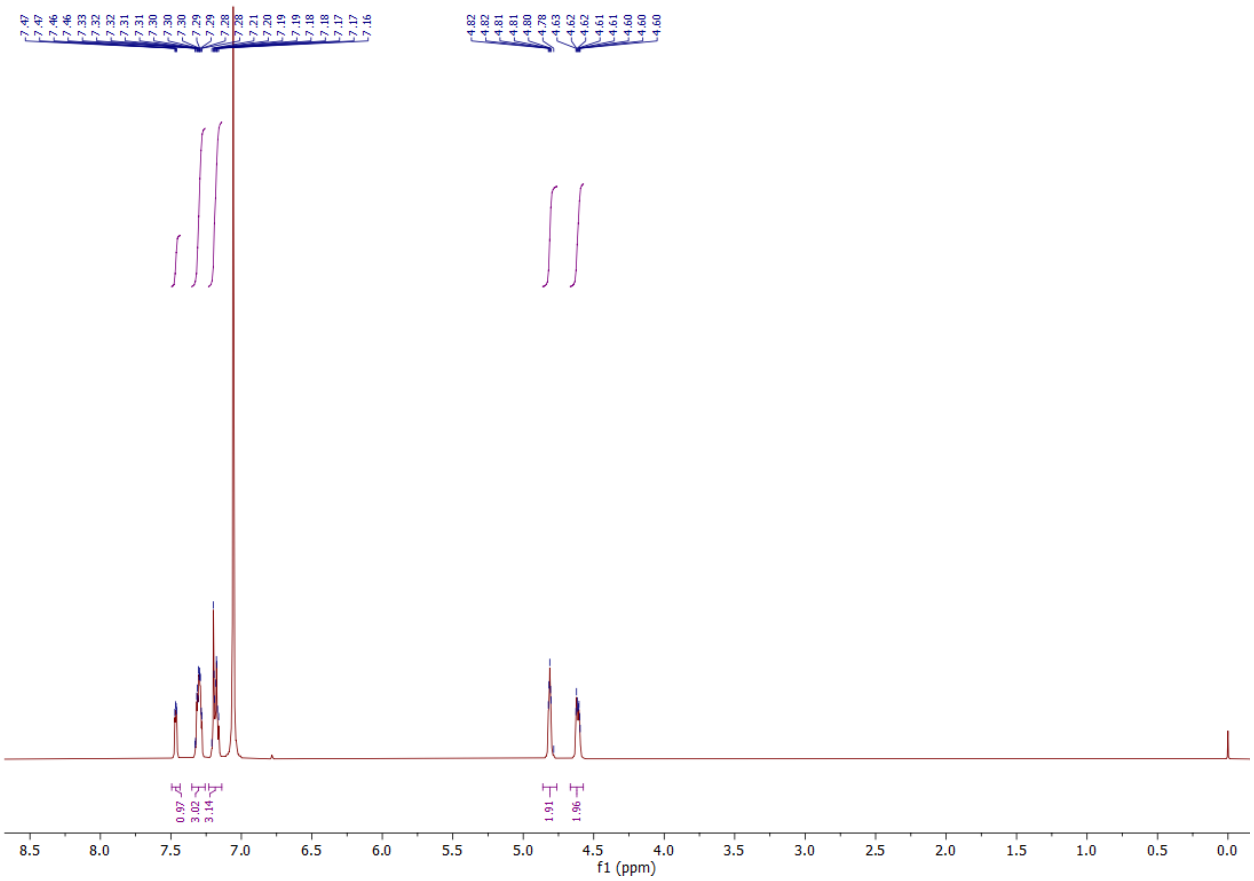

Figure 3.11. ^{1}H NMR spectra (400 MHz in $CDCl_3$) of A-Br-epO.

2-Bromo-9,10-dihydro-9,10-ethanoanthracene-11,12-diol (A-Br-(OH)$_2$)

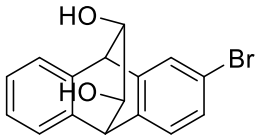

The following procedure was adapted from the previously published literature.[15] Solid potassium hydroxide (2.56 g, 45.59 mmol, 5.1 equiv.), deionized water (42.6 mL), and absolute ethanol (4.5 mL) were added to the A-Br-epO (3.06 g, 8.94 mmol, 1 equiv.). The solution was stirred at 75° C for 3 hours. The consumption of the A-Br-epO was monitored through thin-layer chromatography (100% CH_2Cl_2, R=0.30). Afterwards, the solution underwent rotary

evaporation under reduced pressure to remove the ethanol and roughly half of the water volume. Additional water (85 mL) was added to the solution and the solution was stirred at room temperature for one hour, resulting in the formation of a light-tan solid. The contents were vacuum-filtered and then washed with deionized water. The vacuum-filtration receiving flask was changed and the solid was washed with ethyl acetate through the filter paper. The ethyl acetate was removed through rotary evaporation, leaving a yellow solid residue. The product was purified through column chromatography (CH_2Cl_2/ethyl acetate 9:1, R=0.30 & R=0.15), providing two isomers of 2-bromo-9,10-dihydro-9,10-ethanoanthracene-11,12-diol (A-Br-$(OH)_2$) as a white solid (2.01 g, 79%).

^{1}H NMR (400 MHz, $CDCl_3$) δ 7.40 (d, J = 1.9 Hz, 1H), 7.34 – 7.06 (m, 6H), 4.32 (dd, J = 6.1, 2.4 Hz, 2H), 4.01 – 3.94 (m, 2H).

Elemental analysis calculated: C (60.59 %), H (4.07 %). Theoretical: C (60.59 %). H (4.13 %).

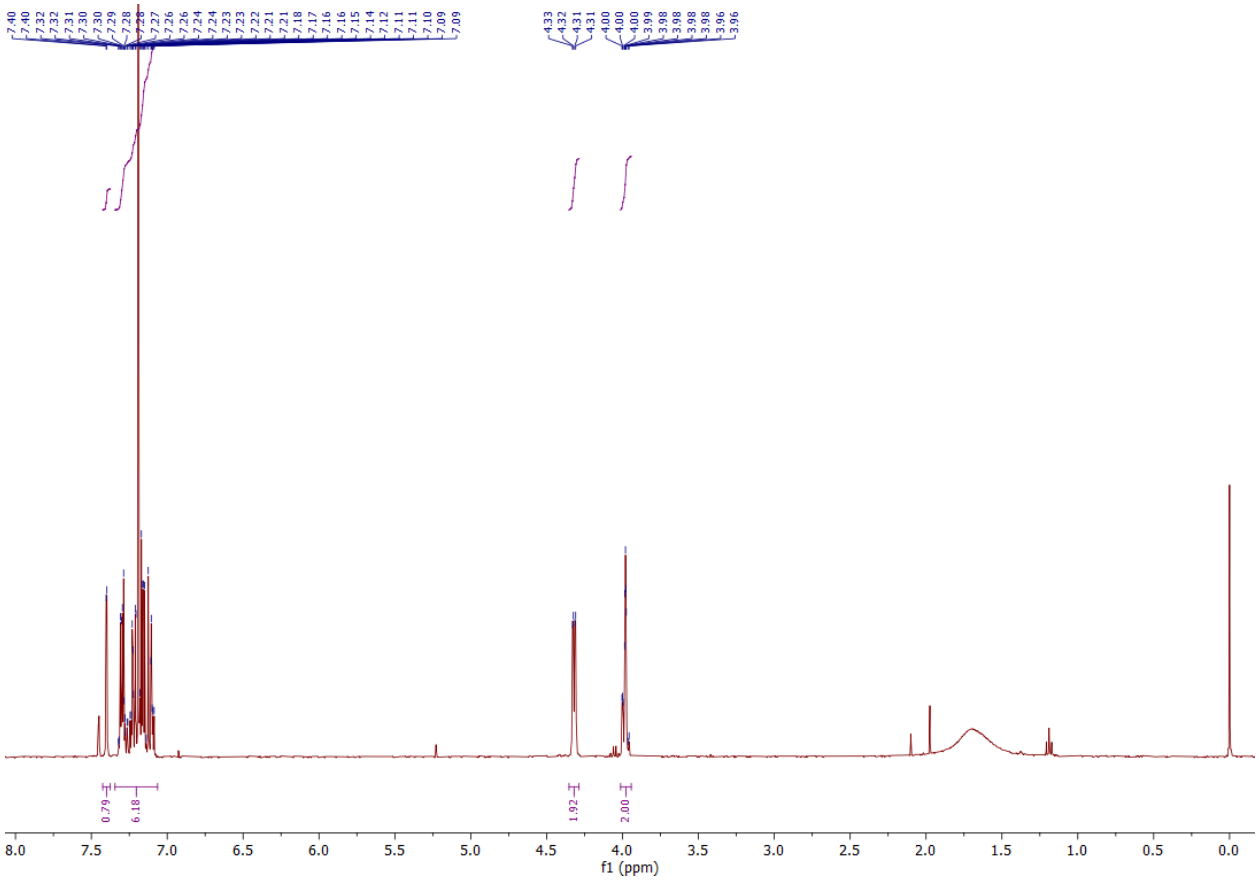

Figure 3.12. ^{1}H NMR spectra (400 MHz in $CDCl_3$) of A-Br-$(OH)_2$ (mixture of two isomers).

2-Bromoanthracene-9,10-dicarbaldehyde (A-Br-CHO)

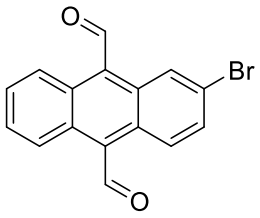

The following procedure was adapted from the previously published literature.[15] A-Br-$(OH)_2$ (2.00 g, mmol, 1 equiv.) was dissolved in anhydrous acetonitrile (127 mL) and heated to reflux with stirring, forming a transparent, light-tan solution. Lead tetraacetate (5.595 g, mmol, 2 equiv.) was added portion-wise to the solution over a period of 5 minutes, quickly turning the solution opaque and brown in color. The solution was then stirred at reflux for 4 hours, resulting in the formation of a dark-orange precipitate within the brown solution. The consumption of the A-Br-$(OH)_2$ was monitored through thin-layer chromatography (CH_2Cl_2/ethyl acetate 8:2, R=0.50 & R=0.33). After the reaction was complete, the reaction mixture was concentrated via rotary evaporation and gave a burgundy residue. 10% Aqueous sodium carbonate (130 mL) was added to the residue, allowing the residue to be suspended in the aqueous solution. The organic contents were extracted from the aqueous layer using dichloromethane. The opaque, yellow organic layer was dried over anhydrous sodium sulfate, filtered, and concentrated to give a yellow-orange solid residue. The residue was purified by column chromatography (ethyl acetate/hexane 2:8, R=0.3), providing 2-bromo-9,10-anthracenedialdehyde (A-Br-CHO) as an orange solid (1.71 g, 5.465 mmol). Yield 86.35 %.

^{1}H NMR (400 MHz, $CDCl_3$) δ 11.39 (s, 1H), 11.37 (s, 1H), 8.97 (dd, *J* = 1.9, 0.5 Hz, 1H), 8.71 – 8.55 (m, 3H), 7.73 – 7.63 (m, 3H).

^{13}C NMR (101 MHz, $CDCl_3$) δ 192.75, 192.40, 131.21, 130.92, 130.14, 129.63, 129.38, 129.23, 127.95, 127.57, 127.11, 125.50, 124.96, 123.15, 122.97, 122.87.

Elemental analysis calculated: C (60.44 %), H (2.98 %). Theoretical: C (61.37 %), H (2.90 %).

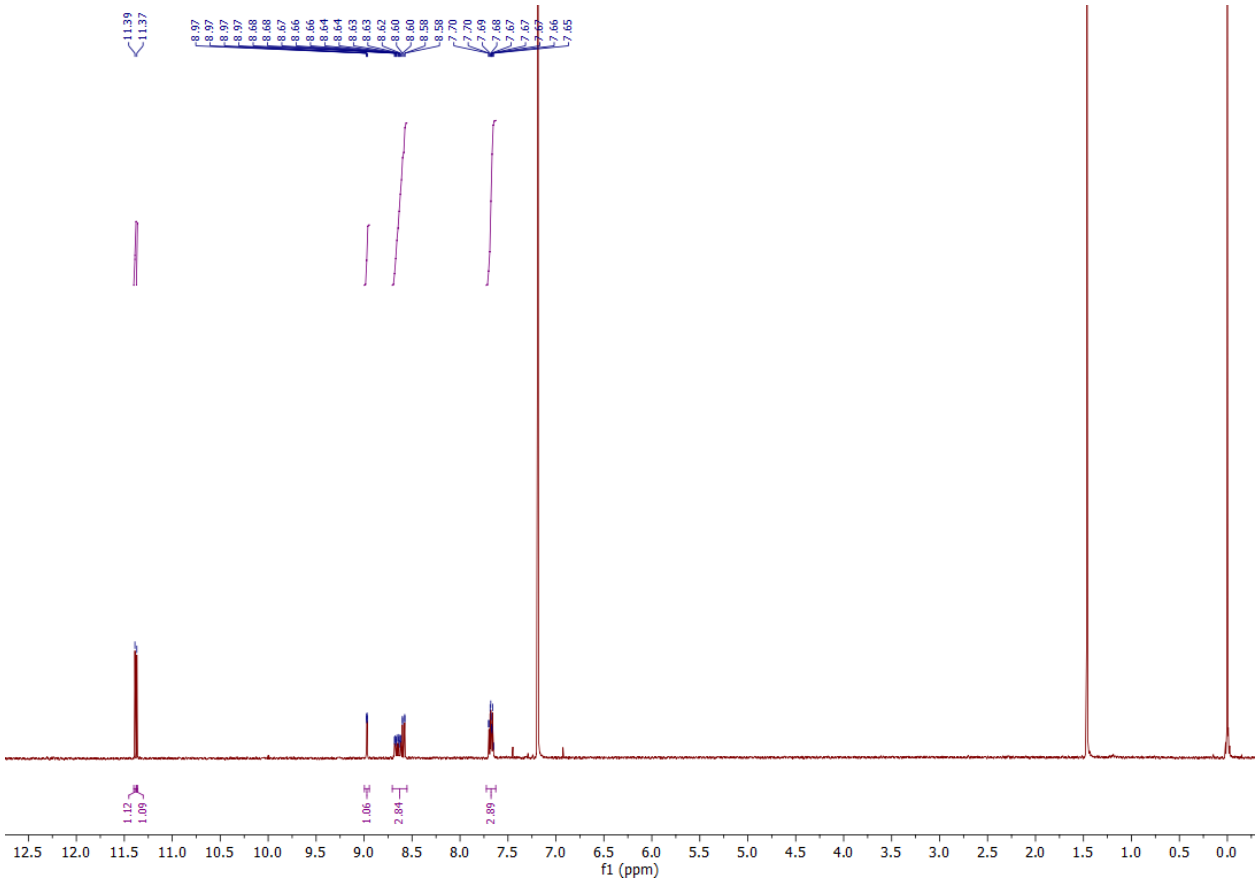

Figure 3.13. ^{1}H NMR spectra (400 MHz in $CDCl_3$) of A-Br-CHO.

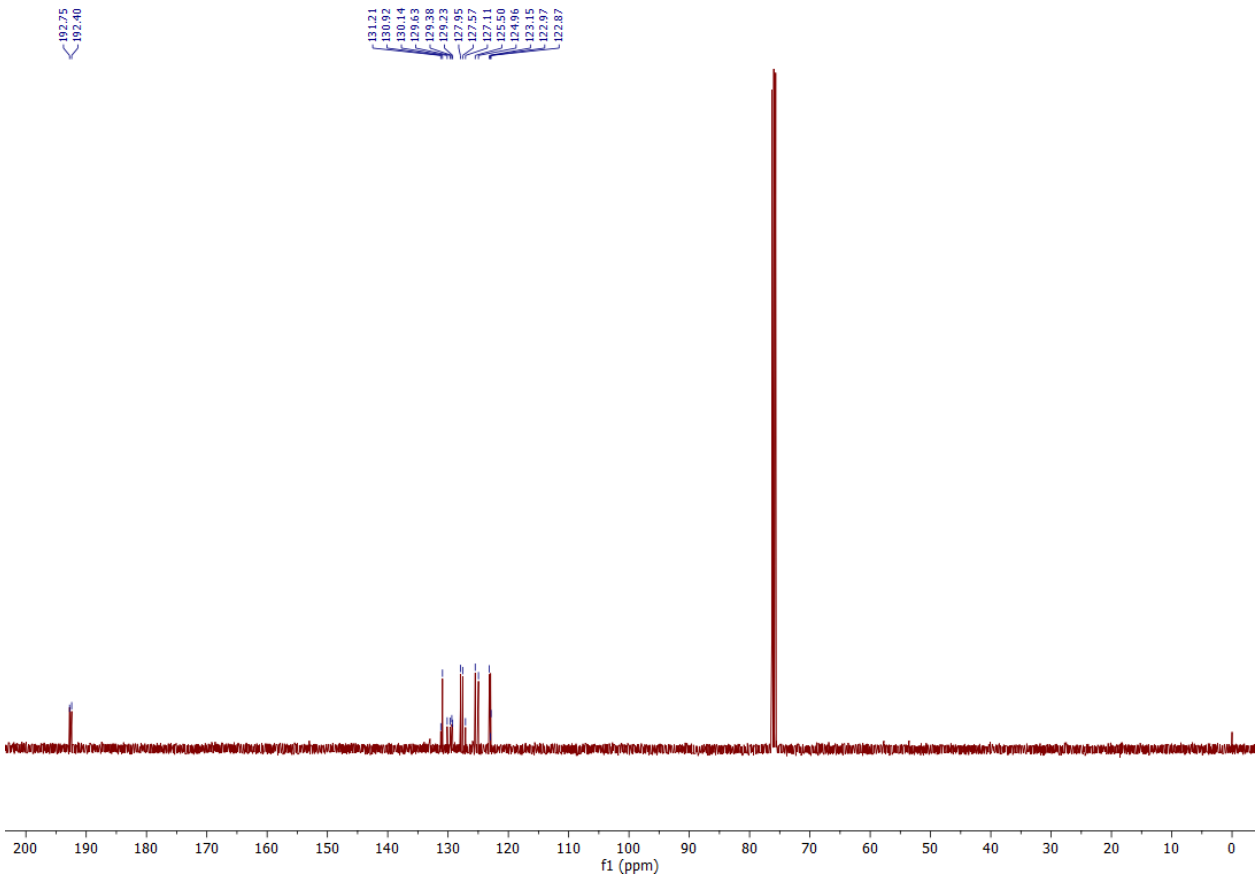

Figure 3.14. ^{13}C NMR spectra (101 MHz in $CDCl_3$) of A-Br-CHO.

2-Iodoantracene (A-I)

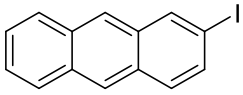

The following procedure was adapted from the previously published literature[16]. A mixture of 2-bromoanthracene (2.582 g, 10.09 mmol), KI (15.12 g, 91.09 mmol, 9.03 equiv.) and CuI (5.934 g, 31.16 mmol, 3.09 equiv.) in 38.7 ml 1,3-dimethyl-2-imidazolidinone was placed in 100 ml flask. The mixture was purged with N_2 and heated with vigorous stirring at 200 °C for 20 hours. After cooling to room temperature, brine and ice were added. The reaction vessel was placed in an ice bath for several hours, then precipitated inorganic salts were removed by filtration. The mixture underwent rotary evaporation under high vacuum to remove the excess of 1,3-dimethyl-2-imidazolidinone. The solid residue was extracted with DCM and the product

was purified through column chromatography (hexane/$CHCl_3$/ethyl acetate 5:3:1, R=0.9), providing 2-iodoanthracene (A-I) as a yellow solid (1.466 g, 4.82 mmol). Yield 47.8 %.

^{1}H NMR (400 MHz, $CDCl_3$) δ 8.36 (dt, *J* = 1.5, 0.8 Hz, 1H), 8.31 (s, 1H), 8.23 (s, 1H), 7.96 – 7.89 (m, 2H), 7.70 – 7.64 (m, 1H), 7.58 (dd, *J* = 9.0, 1.6 Hz, 1H), 7.47 – 7.38 (m, 2H).

^{13}C NMR (101 MHz, $CDCl_3$) δ 136.71, 133.49, 132.77, 131.79, 131.52, 129.76, 129.48, 128.07, 126.38, 126.04, 125.70, 125.17, 125.03, 91.03.

HRMS-EI: Calculated (*m*/*z*): 303.97, measured (*m*/*z*): 303.97

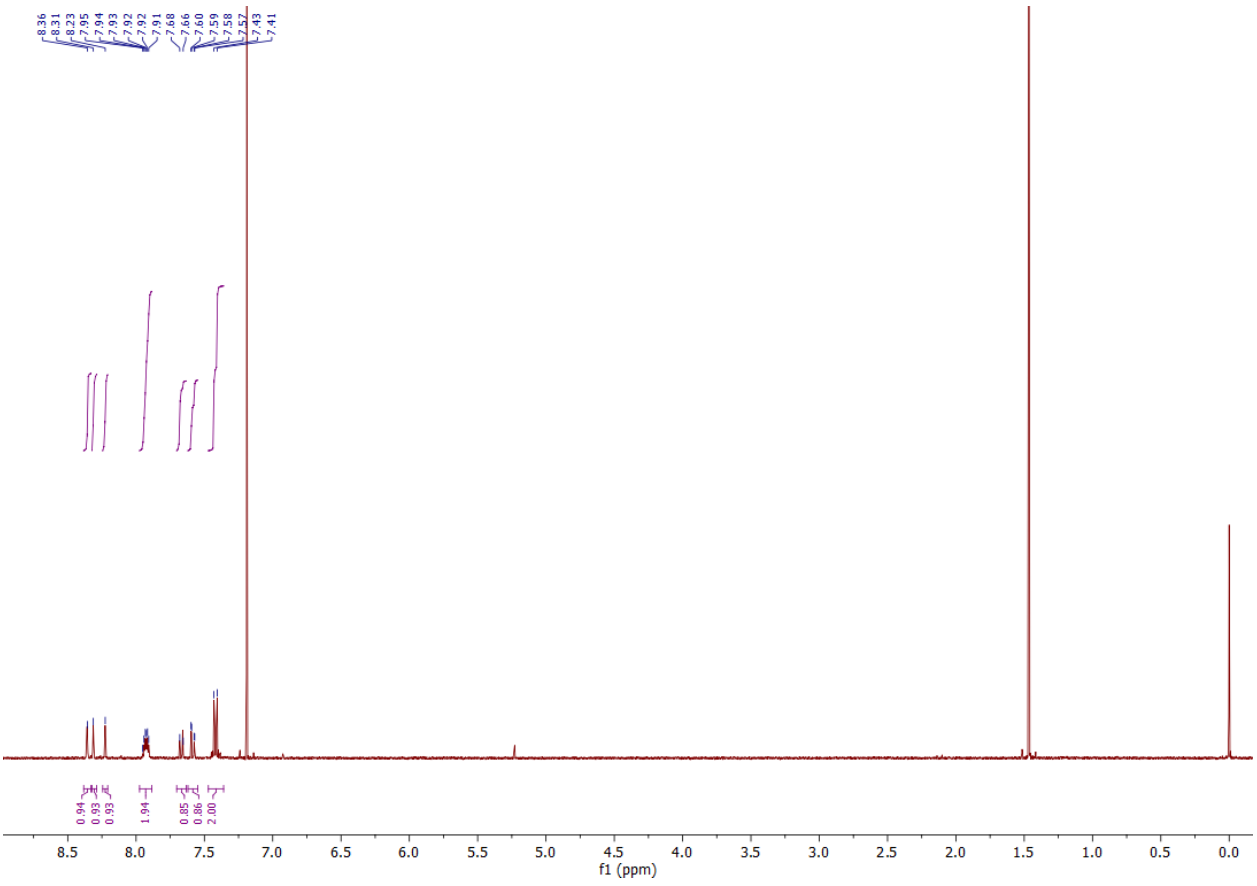

Figure 3.15. ^{1}H NMR spectra (400 MHz in $CDCl_3$) of A-I.

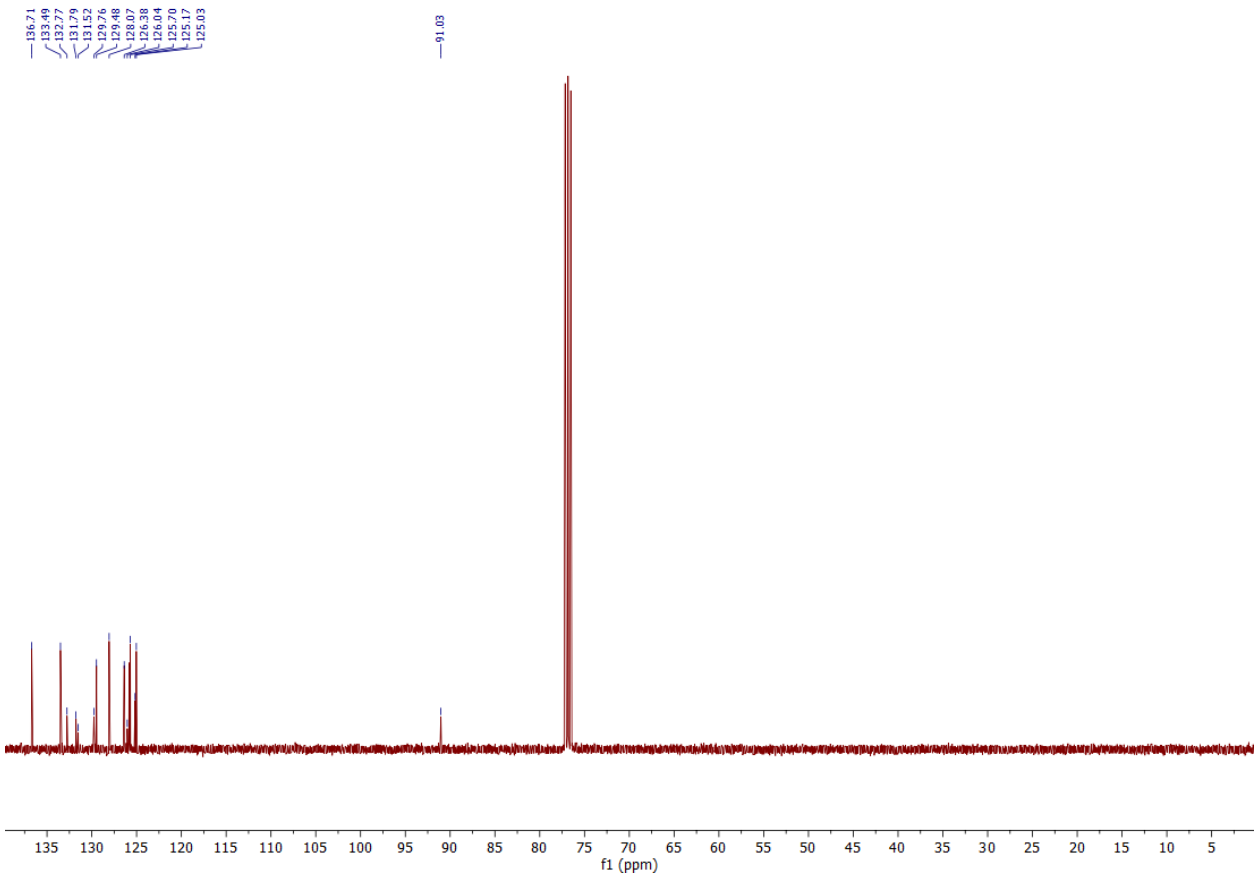

Figure 3.16. ^{13}C NMR spectra (101 MHz in $CDCl_3$) of A-I.

2-Iodo-9,10-dihydro-9,10-[4,5]epidioxoloanthracen-13-one (A-I-epO)

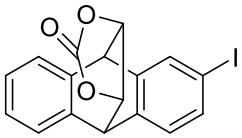

The following procedure was adapted from the previously published literature.[15] A-I (1.446 g, 4.76 mmol, 1 equiv.) and vinylene carbonate (2.99 g, 34.73 mmol, 7.3 equiv.) were heated under reflux with stirring for 18 hours, slowly forming a dark brown solution. The consumption of A-I was monitored by thin-layer chromatography (CH_2Cl_2/hexane 1:49 , R=0.30). The mixture underwent rotary evaporation under high vacuum to remove the excess vinylene carbonate, providing the 2-iodo-9,10-dihydro-9,10-[4,5]epidioxoloanthracen-13-one (A-I-epO) as a dark-brown solid (1.73 g, 92.8 %). The product was used for the further reaction without additional purification.

^{1}H NMR (400 MHz, $CDCl_3$) δ 7.64 (s, 1H), 7.54 – 7.41 (m, 1H), 7.34 – 7.23 (m, 2H), 7.16 (dd, *J* = 9.2, 4.0 Hz, 2H), 7.03 (dd, *J* = 7.7, 2.9 Hz, 1H), 4.83 – 4.70 (m, 2H), 4.56 (d, *J* = 9.4 Hz, 2H).

HRMS-EI: Calculated (*m*/*z*): 391.99, measured (*m*/*z*): 389.96

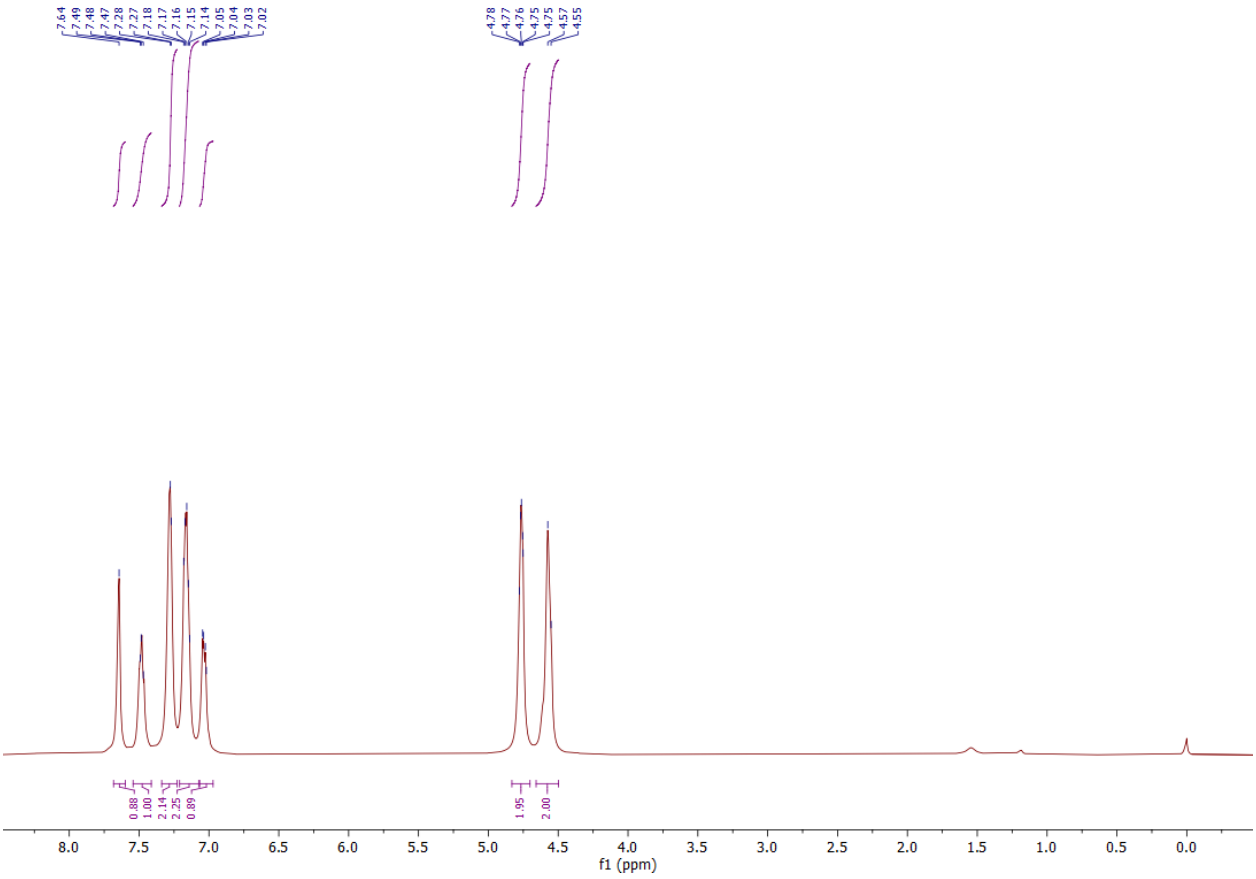

Figure 3.17. ^{1}H NMR spectra (400 MHz in $CDCl_3$) of A-I-epO.

2-Iodo-9,10-dihydro-9,10-ethanoanthracene-11,12-diol (A-I-(OH)$_2$)

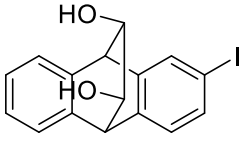

The following procedure was adapted from the previously published literature.[15] Solid potassium hydroxide (0.985 g, 17.6 mmol, 5.1 equiv.), deionized water (16.4 mL), and absolute

ethanol (1.75 mL) were added to the A-I-epO (1.72 g, 4.39 mmol, 1 equiv.). The solution was stirred at 75° C for 3 hours. The consumption of the A-I-epO intermediate was monitored through thin-layer chromatography (100% CH_2Cl_2, R=0.30). Afterwards, the solution underwent rotary evaporation under reduced pressure to remove the ethanol and roughly half of the water volume. Additional water (33 mL) was added to the solution and the solution was stirred at room temperature for one hour, resulting in the formation of light-tan solid. The contents were vacuum-filtered and then washed with deionized water. The vacuum-filtration receiving flask was changed and the solid was washed with ethyl acetate through the filter paper. The ethyl acetate was removed through rotary evaporation, leaving a yellow solid residue. The product was purified through column chromatography (CH_2Cl_2/ethyl acetate 8:1, R=0.30 & R=0.15), providing a mixture of two isomers of 2-iodo-9,10-dihydro-9,10-ethanoanthracene-11,12-diol (A-I-$(OH)_2$) as a white-yellowish solid (1.189 g, 3.25 mmol), Yield 74.0 %.

^{1}H NMR (400 MHz, $CDCl_3$) δ 7.65 (d, *J* = 1.7 Hz, 1H), 7.48 (dd, *J* = 7.8, 1.7 Hz, 1H), 7.23 (dd, *J* = 5.3, 3.3 Hz, 2H), 7.12 – 7.03 (m, 3H), 4.30 (dd, *J* = 7.3, 2.6 Hz, 2H), 4.07 – 3.96 (m, 2H).

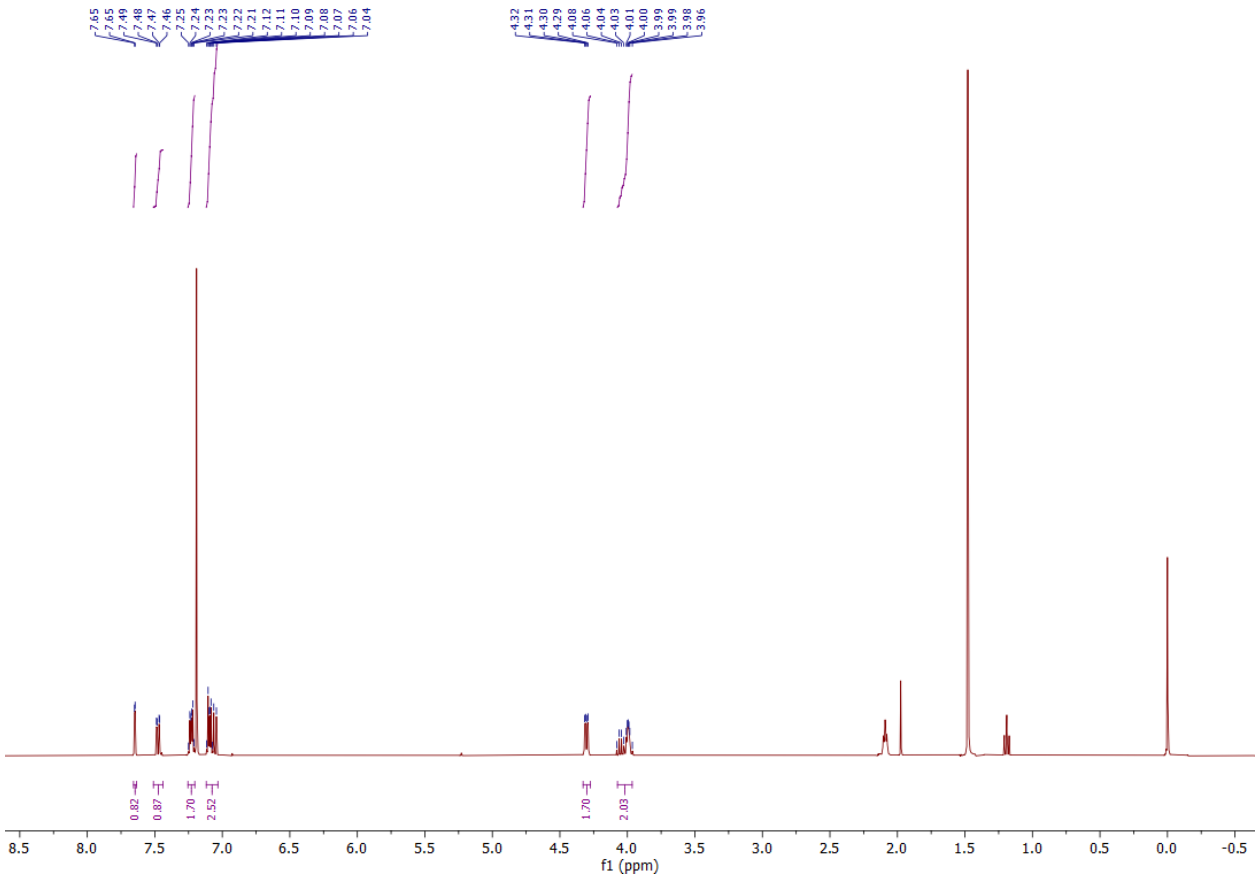

Figure 3.18. ^{1}H NMR spectra (400 MHz in $CDCl_3$) of A-I-$(OH)_2$.

2-Iodoanthracene-9,10-dicarbaldehyde (A-I-CHO)

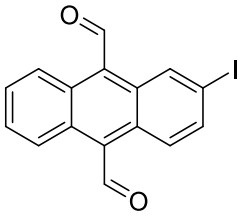

The following procedure was adapted from the previously published literature.[15] A-I-$(OH)_2$ (0.159 g, 0.43 mmol, 1 equiv.) was dissolved in anhydrous acetonitrile (10 mL) and heated to reflux with stirring, forming a transparent, light-tan solution. Lead tetraacetate (0.380 g, 0.86 mmol, 2 equiv.) was added portion-wise to the solution over a period of 5 minutes, quickly turning the solution opaque and brown in color. The solution was then stirred at reflux for 4 hours, resulting in the formation of a dark-orange precipitate within the brown solution. The

consumption of the diol intermediates were monitored through thin-layer chromatography (CH_2Cl_2/ethyl acetate 8:2, R=0.50 & R=0.33). After the reaction was complete, the reaction mixture was concentrated via rotary evaporation and gave a burgundy residue. 10% Aqueous sodium carbonate (30 mL) was added to the residue, allowing the residue to be suspended in the aqueous solution. The organic contents were extracted from the aqueous layer using dichloromethane. The opaque, yellow organic layer was dried over anhydrous sodium sulfate, filtered, and concentrated to give a yellow-orange solid residue. The residue was purified by column chromatography (ethyl acetate/hexane 2:8, R=0.3), providing 2-iodo-9,10-anthracenedialdehyde (A-I-CHO) as an orange solid (0.414 g, 1.15 mmol). Yield 36.0 %.

^{1}H NMR (400 MHz, $CDCl_3$) δ 11.35 (s, 1H), 11.33 (s, 1H), 9.13 (d, *J* = 1.7 Hz, 1H), 8.62 (ddt, *J* = 10.8, 7.1, 3.3 Hz, 2H), 8.39 (d, *J* = 9.4 Hz, 1H), 7.82 (dd, *J* = 9.4, 1.7 Hz, 1H), 7.68 – 7.62 (m, 2H).

^{13}C NMR (101 MHz, $CDCl_3$) δ 192.68, 192.52, 135.82, 132.31, 131.10, 129.88, 129.80, 129.47, 129.19, 127.90, 127.67, 127.35, 124.55, 123.13, 123.09, 95.10.

HRMS-EI: Calculated (*m*/*z*): 359.96, measured (*m*/*z*): 360.02

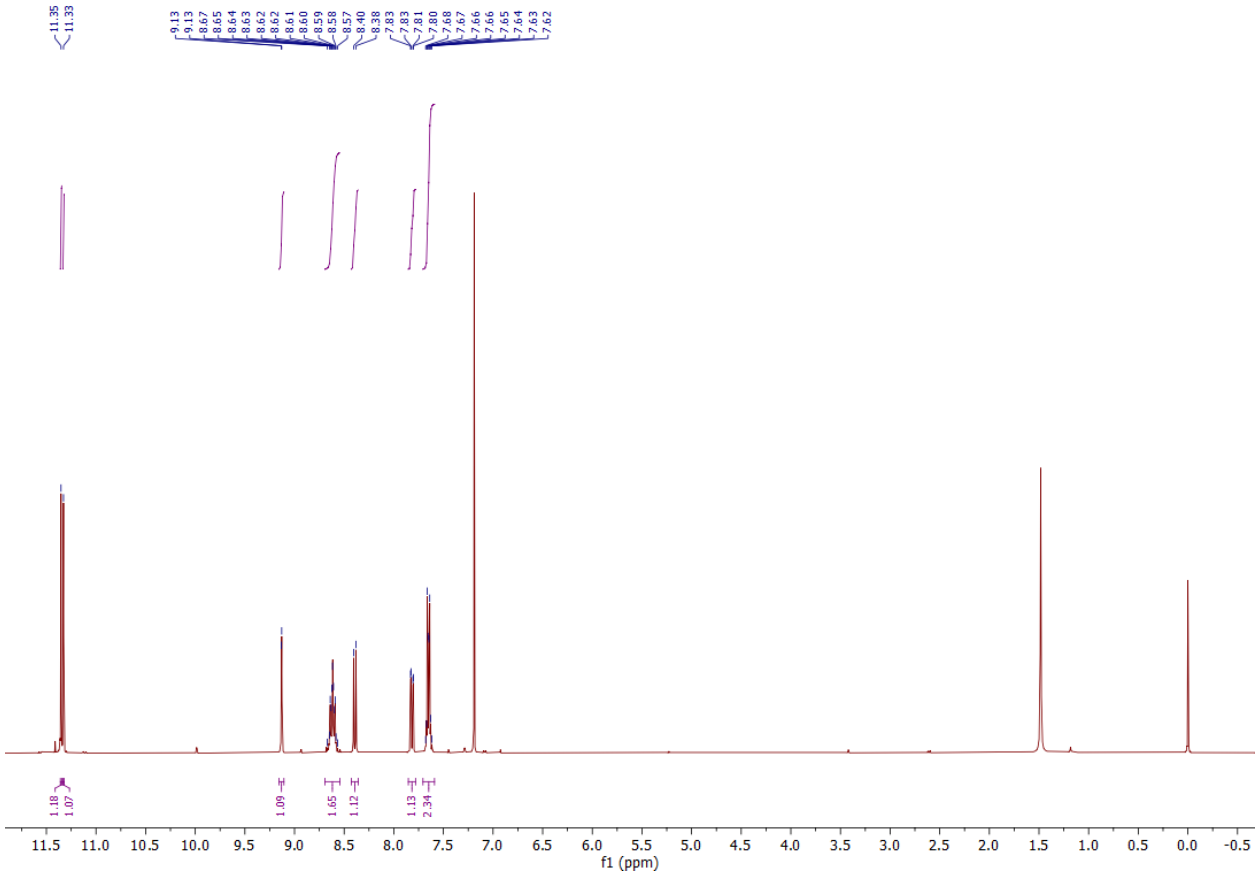

Figure 3.19. ^{1}H NMR spectra (400 MHz in $CDCl_3$) of A-I-CHO.

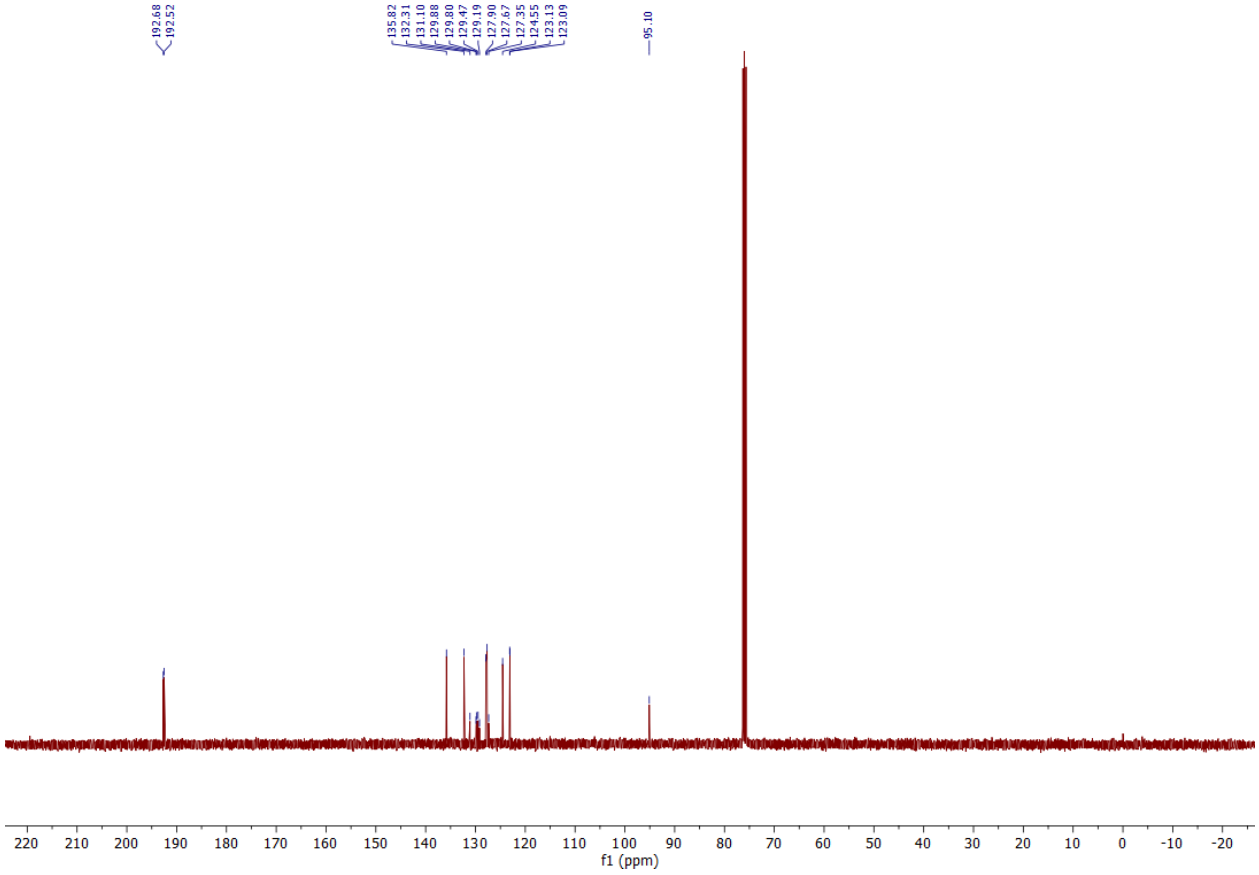

Figure 3.20. ^{13}C NMR spectra (101 MHz in $CDCl_3$) of A-I-CHO.

FT-IR analysis of linkers

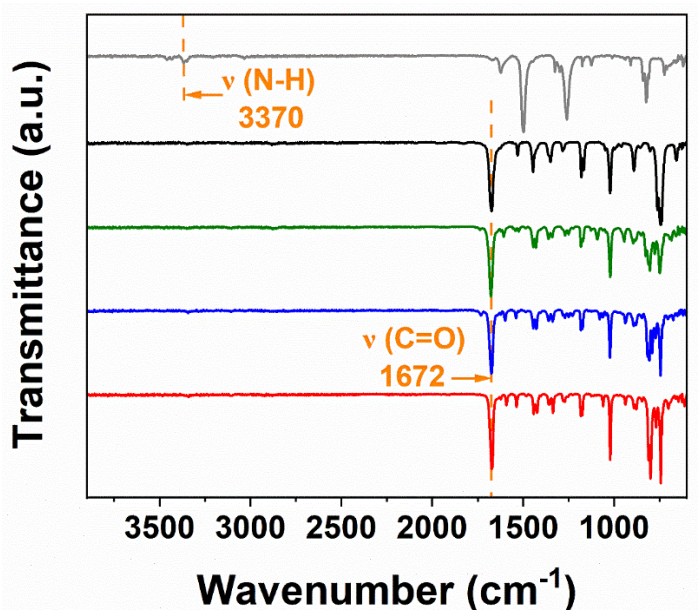

Figure 3.21. FT-IR spectra of N,N,N',N'-tetrakis(4-aminophenyl)-1,4-phenylenediamine (W-NH_2) (grey), anthracene-9,10-dicarbaldehyde (A-H-CHO) (black), A-Cl-CHO (green), A-Br-CHO (blue) and A-I-CHO (red). The vibration of the N–H group in the W–NH_2 moiety is visible at 3370 cm^{-1}.[17] The carbonyl stretch of the A–X–CHO linker appears at 1672 cm^{-1}.[18,19]

3.6.3. COF synthesis

W-A-H COF synthesis

W-NH_2 (9.22 mg, 19.52 µmol, 1.0 eq.) and A-H-CHO (9.14 mg, 39.05 µmol, 2.0 eq.) were filled into a 6 mL pyrex tube followed by the addition of chlorobenzene (400 µL), benzyl alcohol (BnOH) (400 µL), and 6 M acetic acid (100 µL). The tube was sealed and the reaction mixture was heated at 100 °C for 3 d. After cooling to room temperature, the resulting dark red precipitate was suction filtered, Soxhlet-extracted with dry THF, and dried under reduced pressure.

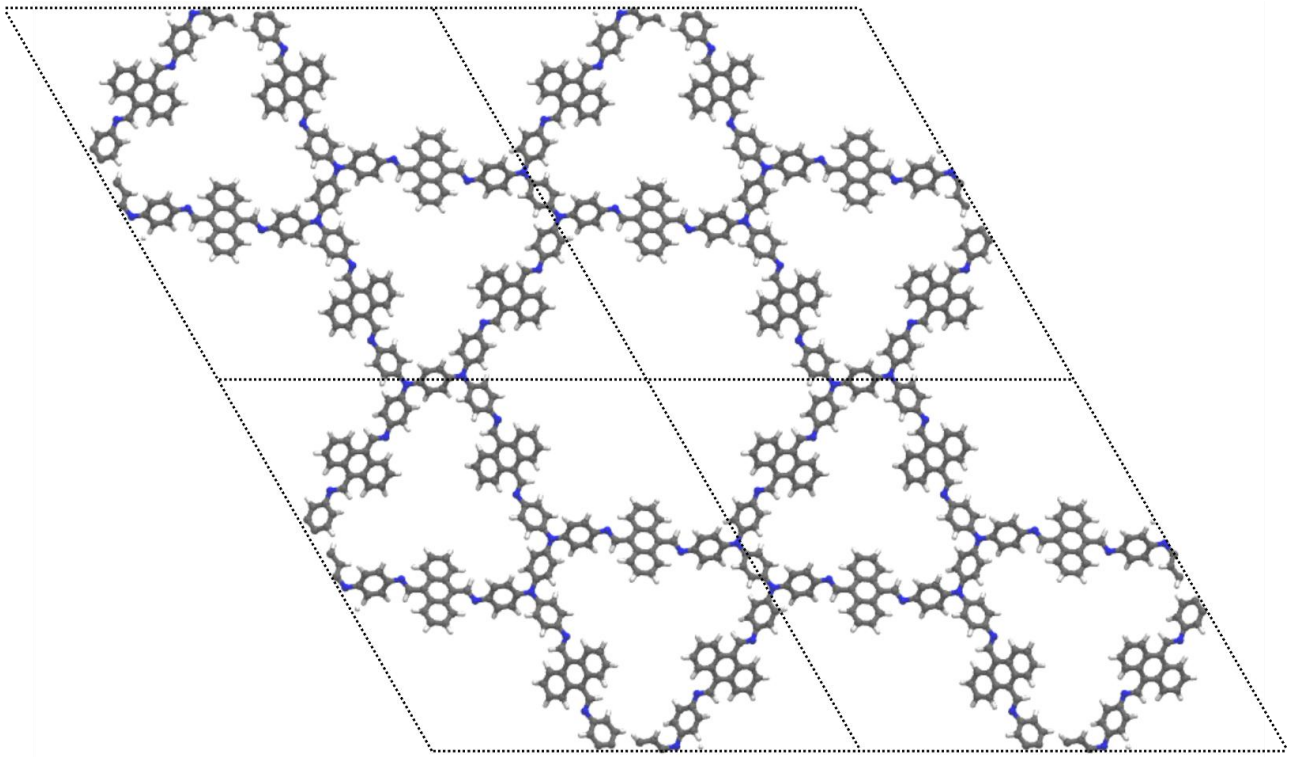

Figure 3.22. Simulated structure of W-A-H COF.

W-A-Cl COF synthesis

W-NH_2 (9.22 mg, 19.52 μmol, 1.0 eq.) and A-Cl-CHO (10.47 mg, 39.05 μmol, 2.0 eq.) were filled into a 6 ml pyrex tube, followed by the addition of $CHCl_3$ (400 μL), BnOH (400 μL), and 6 M acetic acid (100 μL). The tube was sealed and the reaction mixture was heated at 100 °C for 3 d. After cooling to room temperature, the resulting dark red precipitate was suction filtered, Soxhlet-extracted with dry THF, and dried under reduced pressure.

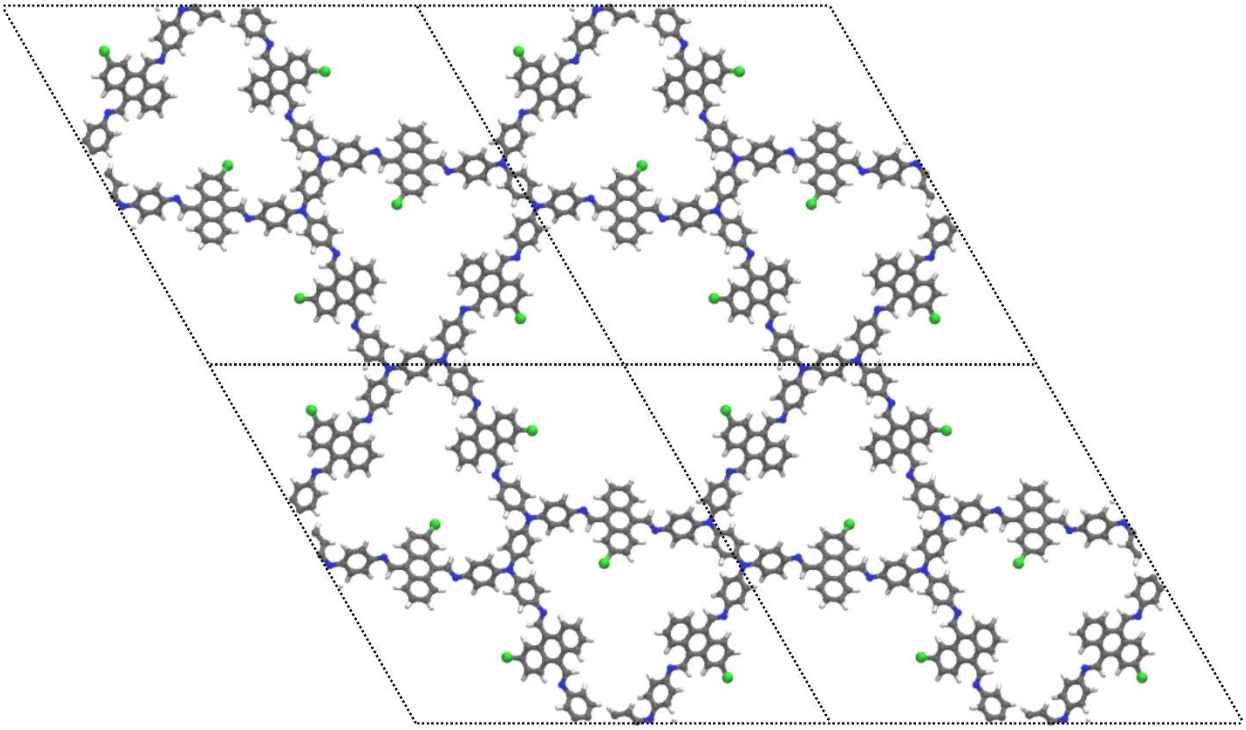

Figure 3.23. Simulated structure of W-A-Cl.

W-A-Br COF synthesis

W-NH_2 (9.22 mg, 19.52 μmol, 1.0 eq.) and A-Br-CHO (12.18 mg, 39.05 μmol, 2.0 eq.) were filled into a6 ml pyrex tube, followed by the addition of chlorobenzene (400 μL), BnOH (400 μL), and 6 M acetic acid (100 μL). The tube was sealed and the reaction mixture was heated at 100 °C for 3 d. After cooling to room temperature, the resulting dark red precipitate was suction filtered, Soxhlet-extracted with dry THF, and dried under reduced pressure.

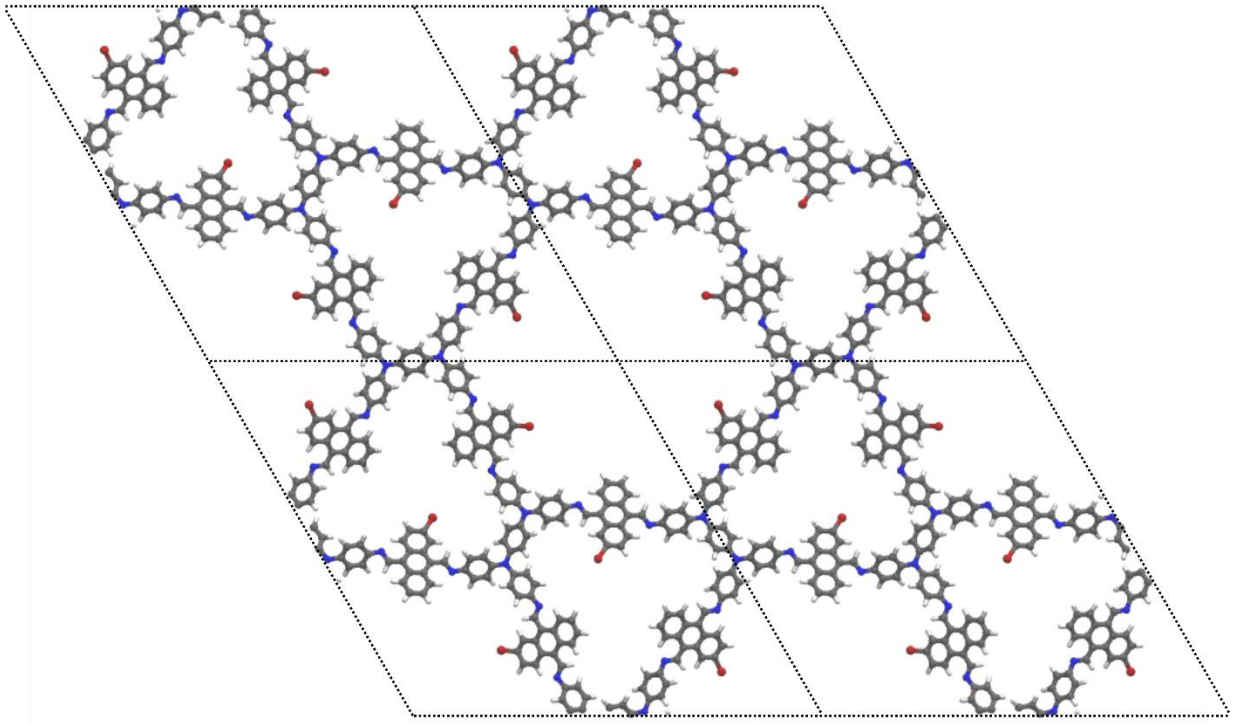

Figure 3.24. Simulated structure of W-A-Br COF.

W-A-I COF synthesis

W-NH_2 (9.22 mg, 19.52 μmol, 1.0 eq.) and A-I-CHO (14.40 mg, 39.05 μmol, 2.0 eq.) were filled into a 6 ml pyrex tube, followed by the addition of $CHCl_3$ (400 μL), BnOH (400 μL), and 6 M acetic acid (100 μL). The tube was sealed and the reaction mixture was heated at 100 °C for 3 d. After cooling to room temperature, the resulting dark red precipitate was suction filtered, Soxhlet-extracted with dry THF, and dried under reduced pressure.

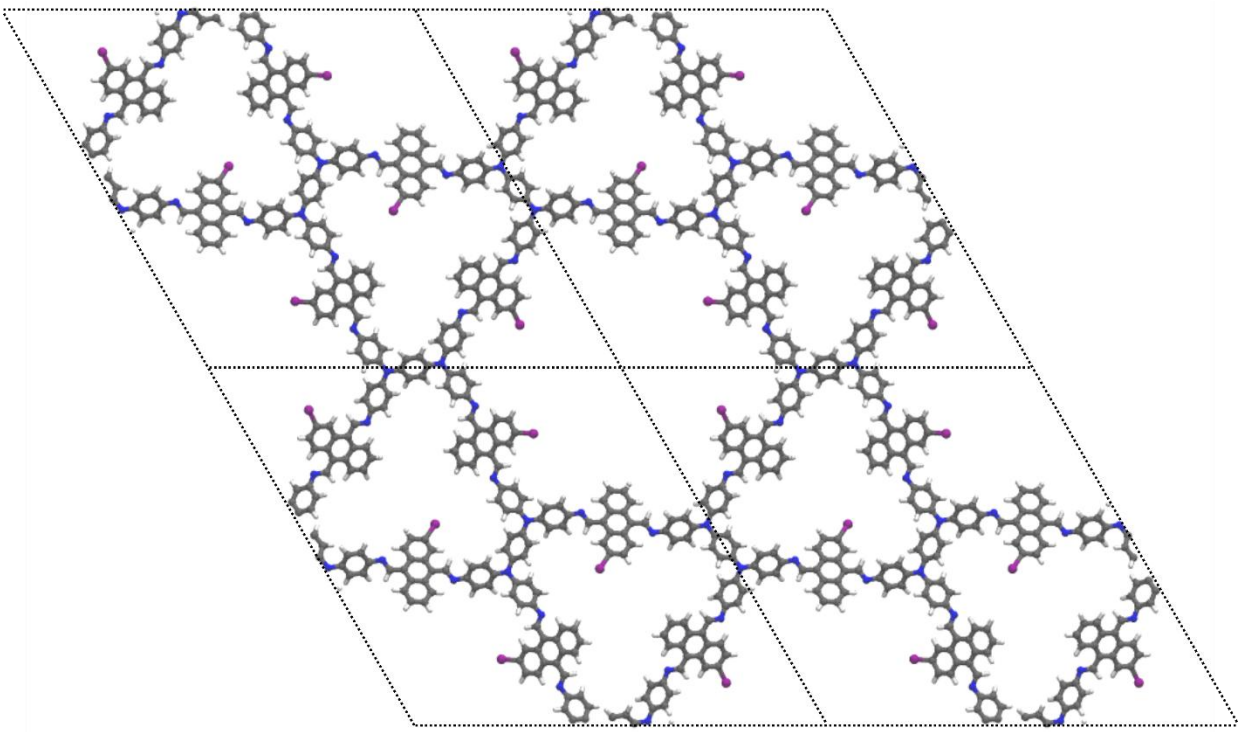

Figure 3.25. Simulated structure of W-A-I COF.

W-TA COF synthesis

The synthesis procedure for W-TA COF was adapted from the literature.[20] W-NH_2 (18.00 mg, 40.00 µmol, 1.0 eq.) and terephthalaldehyde (TA) (10.20 mg, 80.00 µmol, 2.0 eq.) were filled into a 6 ml pyrex tube, followed by the addition of mesitylene (1500 µL), BnOH (1500 µL), and 6 M acetic acid (150 µL). The tube was sealed and the reaction mixture was heated at 100 °C for 3 d. After cooling to room temperature, the resulting dark red precipitate was suction filtered, Soxhlet-extracted with dry THF, and dried under reduced pressure.

3.6.4. Structural analysis

W-A-H COF unit cell

$a = b = 4.236$ nm, $c = 0.411$ nm

$\alpha = \beta = 90.00°$, $\gamma = 120°$

Table 3.1. Fractional coordinates of W-A-H with symmetry P-3.

C1	0.70734	0.56751	0.60940
C2	0.52990	0.53593	0.50241
C3	0.53125	0.50786	0.67043
C4	0.49792	0.52722	0.33204
C5	0.59545	0.57758	0.51776
C6	0.60421	0.55308	0.37057
C7	0.63887	0.55808	0.39287
C8	0.66658	0.58820	0.56048
C9	0.65819	0.61366	0.69219
C10	0.62337	0.60823	0.67529
C11	0.95223	0.55381	0.50720
C12	0.94484	0.57836	0.67222
C13	0.91017	0.57340	0.68044
C14	0.88109	0.54336	0.52481
C15	0.88826	0.51799	0.37159
C16	0.92312	0.52334	0.35874
C17	0.84118	0.56510	0.52090
C18	0.80702	0.56468	0.54597
C19	0.77596	0.53626	0.70500
C20	0.74362	0.53883	0.73748
C21	0.74221	0.56919	0.60540
C22	0.77359	0.59808	0.45408
C23	0.80592	0.59547	0.42049
C24	0.77629	0.50581	0.84592
C25	0.74663	0.47906	0.00730
C26	0.71502	0.48163	0.04268
C27	0.71387	0.51088	0.91449
C28	0.77356	0.62899	0.32065
C29	0.80341	0.65610	0.16437

C30	0.83491	0.65340	0.12595
C31	0.83579	0.62376	0.24725
H1	0.68372	0.53991	0.62531
H2	0.55546	0.51377	0.80818
H3	0.49613	0.54824	0.19620
H4	0.58347	0.52995	0.23539
H5	0.64517	0.53934	0.26614
H6	0.67954	0.63722	0.81915
H7	0.61749	0.62806	0.78314
H8	0.96684	0.60149	0.79646
H9	0.90505	0.59211	0.82215
H10	0.86592	0.49463	0.25129
H11	0.92802	0.50371	0.23224
H12	0.86523	0.59228	0.49733
H13	0.80086	0.50421	0.82365
H14	0.74796	0.45641	0.11737
H15	0.69198	0.46111	0.18171
H16	0.68991	0.51313	0.96071
H17	0.74905	0.63066	0.34629
H18	0.80235	0.67921	0.06184
H19	0.85816	0.67424	0.99131
H20	0.85983	0.62169	0.19996
N1	0.55972	0.57173	0.50399
N2	0.70180	0.59478	0.59326
N3	0.84581	0.53720	0.52106

W-A-Cl COF unit cell

$a = b = 4.265$ nm, $c = 0.408$ nm

$\alpha = \beta = 90.00°$, $\gamma = 120°$

Table 3.2. Fractional coordinates of W-A-Cl with symmetry P-1.

C1	0.43306	0.14027	0.59845
C2	0.85976	0.29280	0.59807
C3	0.70704	0.56673	0.59648
C4	0.47008	0.46413	0.49627
C6	0.53587	0.00592	0.49643
C8	0.99405	0.52993	0.49670
C10	0.53118	0.50771	0.67036
C11	0.49231	0.02349	0.67014
C12	0.97655	0.46881	0.67023
C13	0.50199	0.47269	0.66659
C14	0.52732	0.02928	0.66658
C15	0.97073	0.49801	0.66692
C16	0.59543	0.57729	0.51861
C17	0.42270	0.01820	0.51835
C18	0.98187	0.40453	0.51781
C19	0.60395	0.55273	0.36941
C20	0.44718	0.05126	0.36863
C21	0.94879	0.39595	0.36854
C22	0.63851	0.55757	0.38892
C23	0.44227	0.08095	0.38802
C24	0.91909	0.36135	0.38801
C25	0.66639	0.58758	0.55566
C26	0.41227	0.07879	0.55496
C27	0.92125	0.33350	0.55468
C28	0.65824	0.61307	0.68999
C29	0.38686	0.04516	0.68992
C30	0.95490	0.34171	0.68915
C31	0.62348	0.60780	0.67596
C32	0.39221	0.01573	0.67621

C33	0.98435	0.37650	0.67522
C34	0.44599	0.39847	0.50353
C35	0.60153	0.04745	0.50377
C36	0.95248	0.55401	0.50476
C37	0.42136	0.36650	0.66712
C38	0.63353	0.05478	0.66696
C39	0.94512	0.57860	0.66890
C40	0.42625	0.33678	0.67442
C41	0.66327	0.08938	0.67409
C42	0.91048	0.57367	0.67677
C43	0.45632	0.33777	0.51964
C44	0.66229	0.11848	0.51949
C45	0.88140	0.54362	0.52196
C46	0.48175	0.37033	0.36781
C47	0.62972	0.11136	0.36781
C48	0.88855	0.51824	0.36946
C49	0.47646	0.39984	0.35563
C50	0.60019	0.07656	0.35585
C51	0.92337	0.52356	0.35673
C52	0.43469	0.27616	0.51592
C53	0.72392	0.15849	0.51605
C54	0.84140	0.56525	0.51712
C55	0.43533	0.24256	0.53961
C56	0.75750	0.19274	0.53954
C57	0.80715	0.56462	0.53963
C58	0.46392	0.24001	0.69571
C59	0.76004	0.22387	0.69574
C60	0.77605	0.53604	0.69510
C61	0.46161	0.20522	0.72628
C62	0.79481	0.25637	0.72597

C63	0.74344	0.53813	0.72245
C64	0.43136	0.17343	0.59383
C65	0.82661	0.25794	0.59335
C66	0.74191	0.56847	0.59195
C67	0.40241	0.17582	0.44448
C68	0.82424	0.22662	0.44382
C69	0.77333	0.59751	0.44324
C70	0.40459	0.21056	0.41515
C71	0.78951	0.19403	0.41472
C72	0.80585	0.59524	0.41267
C73	0.49431	0.27082	0.83616
C74	0.72924	0.22341	0.83683
C75	0.77642	0.50568	0.83693
C76	0.52120	0.26805	0.99596
C77	0.73199	0.25305	0.99664
C78	0.74663	0.47827	0.98988
C79	0.51884	0.23399	0.02985
C80	0.76603	0.28481	0.02989
C81	0.71476	0.48048	0.01316
C82	0.48968	0.20356	0.90162
C83	0.79645	0.28610	0.90123
C84	0.71333	0.50971	0.89017
C85	0.37161	0.14490	0.30980
C86	0.85514	0.22677	0.30859
C87	0.77313	0.62826	0.30885
C88	0.34396	0.14715	0.16048
C89	0.85291	0.19689	0.15906
C90	0.80297	0.65551	0.15429
C91	0.34639	0.18129	0.13275
C92	0.81879	0.16515	0.13168

C93	0.83465	0.65314	0.11899
C94	0.37593	0.21206	0.24990
C95	0.78802	0.16389	0.24930
C96	0.83572	0.62366	0.24143
Cl1	0.67712	0.44583	0.20520
Cl2	0.31157	0.18418	0.94356
Cl3	0.81592	0.12746	0.94238
H1	0.46064	0.14425	0.61416
H2	0.85579	0.31640	0.61371
H3	0.68343	0.53914	0.60877
H4	0.55533	0.51348	0.80786
H5	0.48655	0.04189	0.80754
H6	0.95817	0.44465	0.80773
H7	0.50372	0.45159	0.80120
H8	0.54842	0.05210	0.80132
H9	0.94791	0.49628	0.80191
H10	0.58307	0.52971	0.23475
H11	0.47019	0.05342	0.23358
H12	0.94660	0.41681	0.23383
H13	0.64457	0.53876	0.26083
H14	0.46098	0.10582	0.25924
H15	0.89421	0.35521	0.25954
H16	0.67970	0.63654	0.81646
H17	0.36338	0.04312	0.81656
H18	0.95694	0.32027	0.81580
H19	0.61779	0.62764	0.78603
H20	0.37243	0.99020	0.78683
H21	0.00989	0.38224	0.78546
H22	0.39821	0.36532	0.79098
H23	0.63472	0.03281	0.79055

H24	0.96709	0.60173	0.79281
H25	0.40740	0.31290	0.81440
H26	0.68716	0.09439	0.81377
H27	0.90541	0.59245	0.81753
H28	0.50516	0.37140	0.24861
H29	0.62869	0.13370	0.24821
H30	0.86622	0.49487	0.24975
H31	0.49617	0.42441	0.23052
H32	0.57562	0.07171	0.23071
H33	0.92824	0.50389	0.23090
H34	0.40749	0.27294	0.49376
H35	0.72716	0.13451	0.49435
H36	0.86537	0.59246	0.49398
H37	0.49576	0.29691	0.81482
H38	0.70317	0.19873	0.81605
H39	0.80120	0.50440	0.82049
H40	0.54381	0.29206	0.10534
H41	0.70799	0.25162	0.10677
H42	0.74754	0.45542	0.09888
H43	0.53949	0.23158	0.16737
H44	0.76843	0.30786	0.16726
H45	0.48764	0.17743	0.94622
H46	0.82257	0.31022	0.94540
H47	0.68869	0.51082	0.92831
H48	0.37020	0.11881	0.33065
H49	0.88122	0.25147	0.32911
H50	0.74850	0.62971	0.33229
H51	0.32068	0.12320	0.05880
H52	0.87685	0.19759	0.05682
H53	0.80179	0.67850	0.05109

H54	0.85792	0.67412	0.98623
H55	0.37694	0.23774	0.20976
H56	0.76234	0.13920	0.20938
H57	0.85994	0.62187	0.19684
N1	0.44021	0.42839	0.49344
N3	0.57160	0.01177	0.49375
N5	0.98818	0.55980	0.49420
N7	0.70156	0.59403	0.58582
N8	0.40578	0.10751	0.58453
N9	0.89254	0.29829	0.58436
N10	0.46251	0.30870	0.51550
N11	0.69137	0.15374	0.51519
N12	0.84612	0.53743	0.51799

W-A-Br COF unit cell

$a = b = 4.263$ nm, $c = 0.409$ nm

$\alpha = \beta = 90.00°$, $\gamma = 120°$

Table 3.3. Fractional coordinates of W-A-Br with symmetry P-1.

Br1	0.67315	0.44214	0.21732
Br2	0.30794	0.18448	0.93193
Br3	0.81566	0.12360	0.93048
C1	0.43303	0.14022	0.60062
C2	0.85982	0.29285	0.60076
C3	0.70711	0.56692	0.59855
C4	0.47009	0.46412	0.49630
C6	0.53589	0.00595	0.49637
C8	0.99402	0.52992	0.49652
C10	0.53119	0.50773	0.67069
C11	0.49228	0.02347	0.67052

C12	0.97656	0.46881	0.67063
C13	0.50199	0.47269	0.66696
C14	0.52731	0.02929	0.66691
C15	0.97071	0.49800	0.66714
C16	0.59543	0.57735	0.51898
C17	0.42265	0.01815	0.51872
C18	0.98192	0.40454	0.51838
C19	0.60400	0.55279	0.37018
C20	0.44715	0.05124	0.36927
C21	0.94881	0.39595	0.36937
C22	0.63859	0.55767	0.39009
C23	0.44223	0.08093	0.38904
C24	0.91910	0.36133	0.38932
C25	0.66644	0.58774	0.55683
C26	0.41219	0.07873	0.55607
C27	0.92131	0.33350	0.55621
C28	0.65824	0.61323	0.69074
C29	0.38676	0.04507	0.69065
C30	0.95499	0.34172	0.69030
C31	0.62346	0.60791	0.67631
C32	0.39213	0.01563	0.67658
C33	0.98444	0.37652	0.67589
C34	0.44604	0.39846	0.50396
C35	0.60155	0.04751	0.50403
C36	0.95242	0.55398	0.50483
C37	0.42139	0.36649	0.66771
C38	0.63355	0.05483	0.66728
C39	0.94509	0.57859	0.66910
C40	0.42631	0.33677	0.67555
C41	0.66329	0.08945	0.67487

C42	0.91045	0.57367	0.67732
C43	0.45642	0.33779	0.52107
C44	0.66228	0.11856	0.52059
C45	0.88134	0.54360	0.52270
C46	0.48187	0.37035	0.36908
C47	0.62971	0.11145	0.36884
C48	0.88846	0.51818	0.37010
C49	0.47655	0.39986	0.35640
C50	0.60018	0.07664	0.35645
C51	0.92328	0.52350	0.35706
C52	0.43476	0.27617	0.51763
C53	0.72391	0.15856	0.51752
C54	0.84144	0.56534	0.51798
C55	0.43537	0.24256	0.54142
C56	0.75751	0.19281	0.54120
C57	0.80723	0.56479	0.54157
C58	0.46396	0.24000	0.69789
C59	0.76004	0.22393	0.69793
C60	0.77614	0.53622	0.69774
C61	0.46162	0.20519	0.72860
C62	0.79484	0.25643	0.72852
C63	0.74353	0.53833	0.72501
C64	0.43135	0.17340	0.59597
C65	0.82664	0.25799	0.59581
C66	0.74200	0.56868	0.59448
C67	0.40239	0.17578	0.44632
C68	0.82427	0.22667	0.44578
C69	0.77344	0.59774	0.44566
C70	0.40462	0.21055	0.41687
C71	0.78952	0.19411	0.41625

C72	0.80594	0.59543	0.41463
C73	0.49436	0.27082	0.83851
C74	0.72923	0.22346	0.83912
C75	0.77652	0.50585	0.83964
C76	0.52124	0.26803	0.99856
C77	0.73198	0.25311	0.99926
C78	0.74666	0.47832	0.99155
C79	0.51886	0.23394	0.03260
C80	0.76605	0.28486	0.03281
C81	0.71482	0.48057	0.01315
C82	0.48968	0.20351	0.90425
C83	0.79649	0.28616	0.90416
C84	0.71334	0.50982	0.89185
C85	0.37156	0.14486	0.31184
C86	0.85520	0.22681	0.31082
C87	0.77324	0.62851	0.31138
C88	0.34385	0.14709	0.16269
C89	0.85299	0.19689	0.16131
C90	0.80307	0.65575	0.15632
C91	0.34639	0.18127	0.13565
C92	0.81883	0.16523	0.13432
C93	0.83473	0.65334	0.12041
C94	0.37592	0.21209	0.25178
C95	0.78800	0.16391	0.25073
C96	0.83580	0.62384	0.24285
H1	0.46060	0.14416	0.61681
H2	0.85588	0.31647	0.61698
H3	0.68349	0.53931	0.61051
H4	0.55535	0.51353	0.80847
H5	0.48650	0.04185	0.80823

H6	0.95821	0.44464	0.80842
H7	0.50372	0.45159	0.80184
H8	0.54842	0.05210	0.80191
H9	0.94790	0.49627	0.80230
H10	0.58313	0.52972	0.23559
H11	0.47018	0.05342	0.23418
H12	0.94661	0.41680	0.23452
H13	0.64468	0.53885	0.26247
H14	0.46095	0.10584	0.26053
H15	0.89419	0.35516	0.26113
H16	0.67970	0.63673	0.81724
H17	0.36326	0.04300	0.81731
H18	0.95705	0.32029	0.81706
H19	0.61772	0.62775	0.78597
H20	0.37233	0.99007	0.78684
H21	0.01002	0.38229	0.78577
H22	0.39820	0.36530	0.79114
H23	0.63475	0.03283	0.79046
H24	0.96710	0.60174	0.79274
H25	0.40744	0.31288	0.81553
H26	0.68719	0.09446	0.81448
H27	0.90539	0.59246	0.81817
H28	0.50530	0.37142	0.25012
H29	0.62867	0.13382	0.24948
H30	0.86610	0.49479	0.25055
H31	0.49627	0.42444	0.23119
H32	0.57560	0.07179	0.23127
H33	0.92814	0.50381	0.23118
H34	0.40756	0.27298	0.49559
H35	0.72714	0.13456	0.49599

H36	0.86545	0.59252	0.49368
H37	0.49583	0.29693	0.81703
H38	0.70314	0.19878	0.81810
H39	0.80132	0.50459	0.82372
H40	0.54387	0.29205	0.10804
H41	0.70798	0.25168	0.10939
H42	0.74763	0.45545	0.09950
H43	0.53950	0.23152	0.17037
H44	0.76845	0.30792	0.17045
H45	0.48762	0.17736	0.94899
H46	0.82262	0.31027	0.94864
H47	0.68868	0.51097	0.92854
H48	0.37011	0.11874	0.33288
H49	0.88130	0.25150	0.33173
H50	0.74861	0.62998	0.33529
H51	0.32054	0.12306	0.06204
H52	0.87702	0.19766	0.06016
H53	0.80189	0.67875	0.05320
H54	0.85800	0.67430	0.98718
H55	0.37701	0.23783	0.21283
H56	0.76227	0.13926	0.21168
H57	0.86001	0.62202	0.19782
N1	0.44023	0.42837	0.49346
N3	0.57163	0.01182	0.49365
N5	0.98813	0.55978	0.49391
N7	0.70163	0.59422	0.58760
N8	0.40571	0.10745	0.58606
N9	0.89259	0.29830	0.58637
N10	0.46261	0.30871	0.51708
N11	0.69136	0.15384	0.51643

N12	0.84608	0.53746	0.51917

W-A-I COF unit cell

$a = b = 4.263$ nm, $c = 0.408$ nm

$\alpha = \beta = 90.00°$, $\gamma = 120°$

Table 3.4. Fractional coordinates of W-A-I with symmetry P-1.

C1	0.43346	0.14046	0.59726
C2	0.85957	0.29298	0.59642
C3	0.70711	0.56680	0.59298
C4	0.47008	0.46414	0.49659
C6	0.53586	0.00592	0.49644
C8	0.99406	0.52993	0.49648
C10	0.53119	0.50771	0.67007
C11	0.49231	0.02348	0.67021
C12	0.97654	0.46883	0.67019
C13	0.50200	0.47270	0.66663
C14	0.52731	0.02927	0.66666
C15	0.97072	0.49803	0.66667
C16	0.59542	0.57726	0.51772
C17	0.42278	0.01825	0.51808
C18	0.98178	0.40454	0.51772
C19	0.60393	0.55270	0.36842
C20	0.44730	0.05128	0.36821
C21	0.94874	0.39604	0.36804
C22	0.63849	0.55755	0.38731
C23	0.44248	0.08102	0.38751
C24	0.91900	0.36147	0.38712
C25	0.66639	0.58758	0.55354
C26	0.41253	0.07895	0.55447

C27	0.92108	0.33358	0.55375
C28	0.65824	0.61305	0.68830
C29	0.38707	0.04535	0.68960
C30	0.95468	0.34171	0.68874
C31	0.62349	0.60777	0.67490
C32	0.39233	0.01586	0.67600
C33	0.98417	0.37647	0.67524
C34	0.44599	0.39849	0.50382
C35	0.60152	0.04741	0.50373
C36	0.95256	0.55410	0.50446
C37	0.42136	0.36651	0.66717
C38	0.63352	0.05475	0.66670
C39	0.94526	0.57873	0.66839
C40	0.42628	0.33680	0.67432
C41	0.66324	0.08936	0.67401
C42	0.91065	0.57387	0.67624
C43	0.45637	0.33784	0.51966
C44	0.66222	0.11845	0.51979
C45	0.88153	0.54384	0.52179
C46	0.48178	0.37041	0.36792
C47	0.62966	0.11130	0.36807
C48	0.88863	0.51842	0.36934
C49	0.47646	0.39990	0.35585
C50	0.60015	0.07651	0.35594
C51	0.92342	0.52368	0.35653
C52	0.43487	0.27625	0.51650
C53	0.72382	0.15855	0.51701
C54	0.84158	0.56551	0.51683
C55	0.43564	0.24271	0.53870
C56	0.75735	0.19287	0.53894

C57	0.80733	0.56488	0.53928
C58	0.46426	0.24020	0.69443
C59	0.75986	0.22400	0.69469
C60	0.77623	0.53631	0.69488
C61	0.46200	0.20543	0.72460
C62	0.79462	0.25654	0.72430
C63	0.74361	0.53837	0.72109
C64	0.43179	0.17363	0.59193
C65	0.82641	0.25814	0.59123
C66	0.74202	0.56863	0.58974
C67	0.40285	0.17599	0.44214
C68	0.82405	0.22684	0.44137
C69	0.77344	0.59767	0.44116
C70	0.40498	0.21070	0.41363
C71	0.78935	0.19424	0.41334
C72	0.80598	0.59544	0.41150
C73	0.49460	0.27102	0.83521
C74	0.72906	0.22350	0.83616
C75	0.77657	0.50597	0.83731
C76	0.52150	0.26828	0.99501
C77	0.73180	0.25313	0.99587
C78	0.74667	0.47842	0.98848
C79	0.51919	0.23424	0.02860
C80	0.76582	0.28491	0.02867
C81	0.71471	0.48051	0.00951
C82	0.49008	0.20381	0.90002
C83	0.79624	0.28624	0.89959
C84	0.71340	0.50985	0.88738
C85	0.37210	0.14511	0.30680
C86	0.85491	0.22700	0.30537

C87	0.77318	0.62835	0.30579
C88	0.34431	0.14728	0.15887
C89	0.85273	0.19704	0.15734
C90	0.80300	0.65558	0.15106
C91	0.34659	0.18138	0.13323
C92	0.81865	0.16519	0.13228
C93	0.83471	0.65326	0.11664
C94	0.37620	0.21217	0.24968
C95	0.78787	0.16400	0.24931
C96	0.83583	0.62386	0.24008
H1	0.46100	0.14438	0.61338
H2	0.85564	0.31660	0.61253
H3	0.68353	0.53918	0.60332
H4	0.55536	0.51348	0.80728
H5	0.48655	0.04188	0.80761
H6	0.95815	0.44467	0.80759
H7	0.50375	0.45161	0.80122
H8	0.54841	0.05208	0.80145
H9	0.94791	0.49630	0.80148
H10	0.58303	0.52965	0.23424
H11	0.47028	0.05337	0.23317
H12	0.94664	0.41694	0.23336
H13	0.64450	0.53869	0.25940
H14	0.46123	0.10586	0.25863
H15	0.89416	0.35540	0.25838
H16	0.67972	0.63651	0.81462
H17	0.36363	0.04338	0.81628
H18	0.95664	0.32024	0.81544
H19	0.61781	0.62760	0.78537
H20	0.37252	0.99037	0.78683

H21	0.00967	0.38215	0.78595
H22	0.39820	0.36529	0.79097
H23	0.63474	0.03278	0.79003
H24	0.96725	0.60185	0.79218
H25	0.40741	0.31290	0.81387
H26	0.68714	0.09436	0.81331
H27	0.90563	0.59269	0.81678
H28	0.50519	0.37150	0.24870
H29	0.62861	0.13364	0.24861
H30	0.86628	0.49506	0.24975
H31	0.49616	0.42447	0.23085
H32	0.57558	0.07165	0.23084
H33	0.92824	0.50398	0.23073
H34	0.40762	0.27294	0.49654
H35	0.72714	0.13461	0.49729
H36	0.86554	0.59271	0.49299
H37	0.49599	0.29708	0.81406
H38	0.70302	0.19880	0.81572
H39	0.80136	0.50472	0.82220
H40	0.54408	0.29229	0.10464
H41	0.70781	0.25168	0.10624
H42	0.74781	0.45562	0.09579
H43	0.53985	0.23185	0.16612
H44	0.76820	0.30796	0.16598
H45	0.48808	0.17770	0.94436
H46	0.82234	0.31038	0.94338
H47	0.68881	0.51116	0.92188
H48	0.37073	0.11903	0.32647
H49	0.88098	0.25173	0.32453
H50	0.74852	0.62974	0.32857

H51	0.32112	0.12315	0.05858
H52	0.87685	0.19800	0.05643
H53	0.80177	0.67851	0.04701
H54	0.85796	0.67423	0.98371
H55	0.37739	0.23797	0.21297
H56	0.76208	0.13937	0.21301
H57	0.86008	0.62211	0.19612
I1	0.66838	0.43786	0.22862
I2	0.30377	0.18485	0.91586
I3	0.81519	0.11890	0.91510
N1	0.44021	0.42841	0.49403
N3	0.57158	0.01174	0.49382
N5	0.98823	0.55982	0.49392
N7	0.70158	0.59407	0.58353
N8	0.40613	0.10772	0.58366
N9	0.89231	0.29840	0.58286
N10	0.46263	0.30881	0.51502
N11	0.69125	0.15373	0.51526
N12	0.84628	0.53769	0.51821

3.6.5. Simulations of different halogen positions

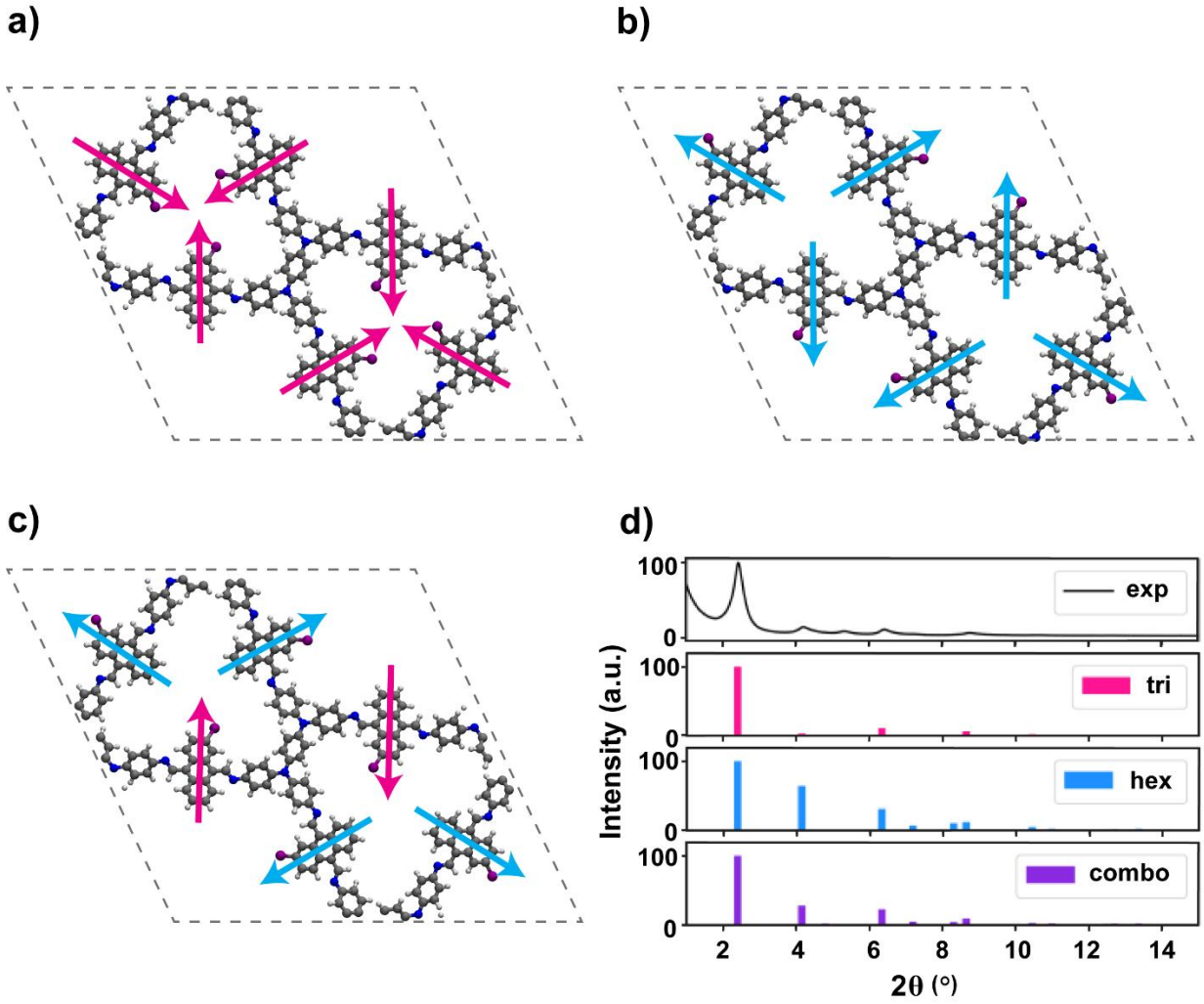

Figure 3.26. Simulated structures of W-A-Br COF when halogens atoms are facing (a) exclusively into the trigonal pore (pink arrows), (b) facing exclusively into the hexagonal pore (blue arrows) and (c) with a combination of two halogens facing trigonal pores and four halogens facing the hexagonal pores per unit cell. (d) Experimental PXRD pattern for W-A-Br COF (black) and simulated PXRD patterns for simulated structures of all halogens facing into the trigonal pores (pink) and into the hexagonal pores (blue), as well as the simulated PXRD pattern for the combinational structure with halogens facing both types of pores (purple).

3.6.6. TEM images

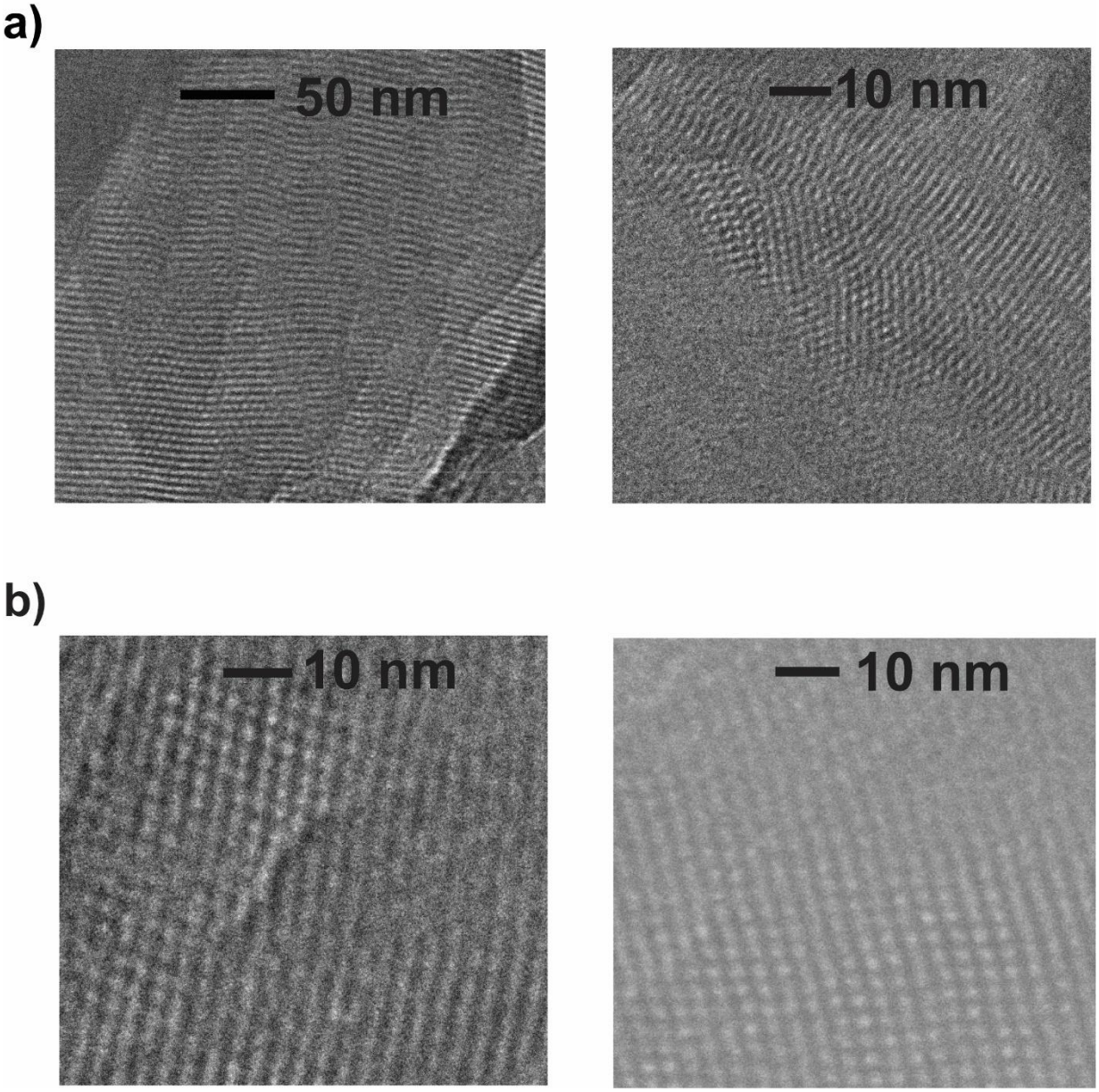

Figure 3.27. TEM images of W-A-Br COF showing (a) dominant Kagome structure with 120° angle and (b) distorted crystalline structure and revealing a lattice angles of approximately 100°.

3.6.7. ESP calculations

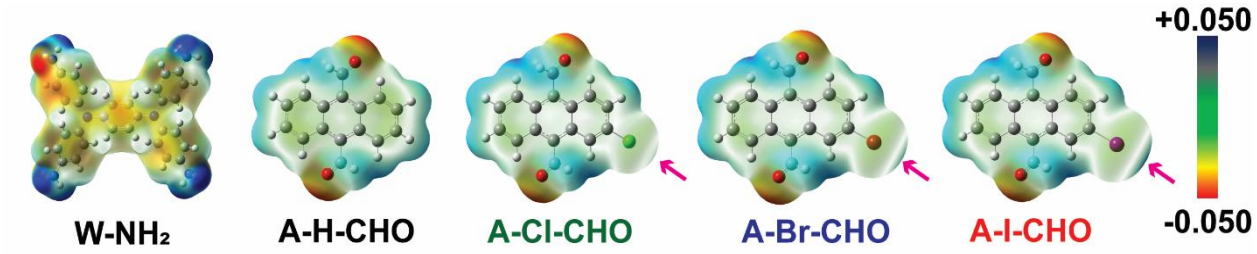

Figure 3.28. ESP maps superimposed on the M06-2X/def2-SVPP optimized geometry of W-NH_2 and anthracene-based linkers A-X-CHO (X = H, Cl, Br, I). The ESP values in atomic units (a.u.) are mapped onto the total electron density surface with an isovalue of 0.001 highlighting electron-rich (red) and electron-deficient (blue) regions. Introduction of Cl, Br, and I induces progressively larger σ-holes (positive ESP regions) opposite the C-X bonds (highlighted with pink arrows).

3.6.8. SEM images

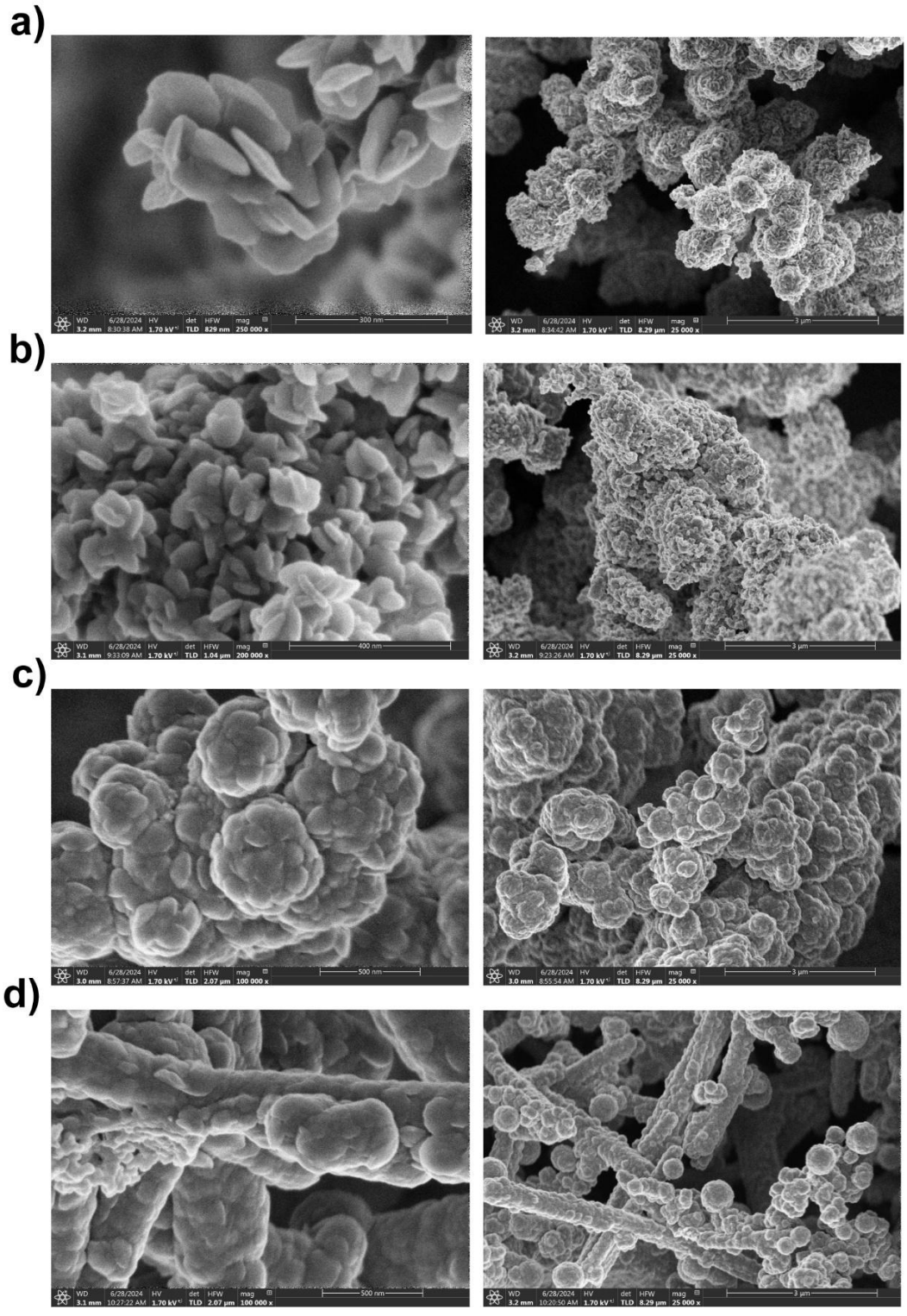

Figure 3.29. SEM images of (a) W-A-H, (b) W-A-Cl, (c) W-A-Br, (d) W-A-I.

3.6.9. Sorption and porosity parameters

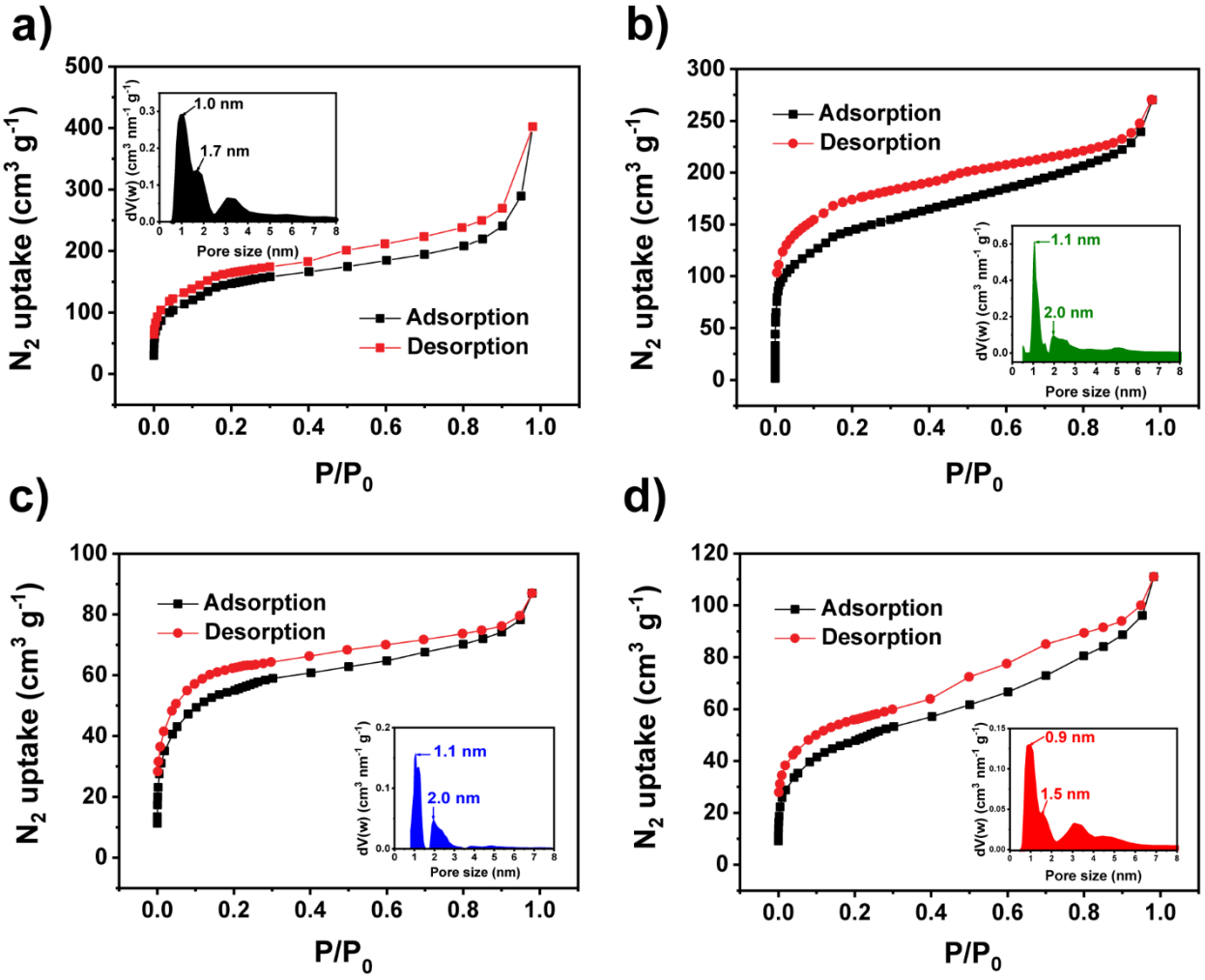

Figure 3.30. Nitrogen sorption isotherms and pore size distributions (insets) of the COFs (a) W-A-H, (b) W-A-Cl, (c) W-A-Br, (d) W-A-I.

Table 3.5. Theoretical (*Zeo++[21] and **PoreBlazer v4.0[22]) and experimental geometric porosity parameters of the COFs (probe radius corresponds to N_2; 0.18 nm). *** Experimental pore volume was calculated based on the average uptake from the desorption branch in the relative pressure range P/P_0 = 0.60-0.80.

COF	Pore	*Maximum pore diameter (m_{pd}) (nm)	*Pore window size (p_{ws}) (nm)	**Theoretical pore volume (V_{pt})	Experimental pore volume*** (V_{et}) ($cm^3\ g^{-1}$)	*Unit cell density ($g\ cm^{-3}$)	Experimental BET surface area ($m^2\ g^{-1}$)	Theoretical network-accessible surface

				(cm^3 g^{-1})				area (m^2 g^{-1})
W-A-H	Trigonal	0.73	0.70	0.364	0.35	0.67	548	897
	Hexagonal	2.08	2.07					
W-A-Cl	Trigonal	0.68	0.62	0.317	0.33	0.74	490	806
	Hexagonal	1.88	1.86					
W-A-Br	Trigonal	0.69	0.63	0.293	0.11	0.81	187	674
	Hexagonal	1.87	1.84					
W-A-I	Trigonal	0.66	0.61	0.260	0.13	0.90	170	653
	Hexagonal	1.84	1.80					

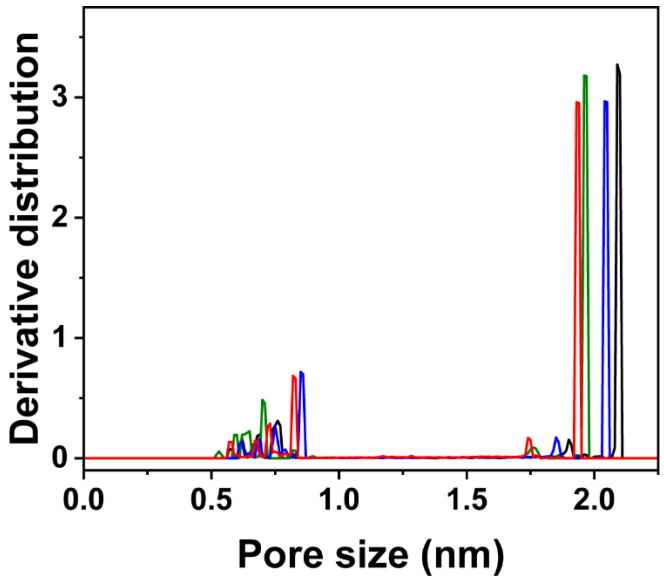

Figure 3.31. Simulated pore size distribution of the COFs W-A-H (black), W-A-Cl (green), W-A-Br (blue) and W-A-I (red) using Zeo++.[21]

3.6.10. FT-IR analysis of COFs

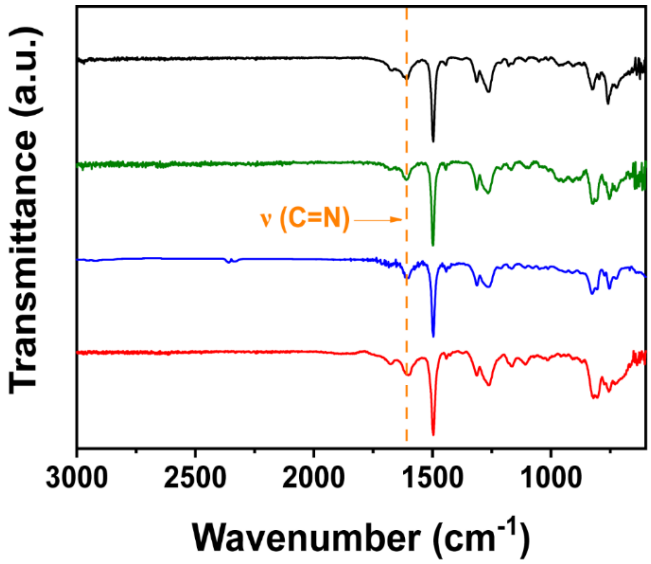

Figure 3.32. FT-IR spectra of the COFs W-A-H (black), W-A-Cl (green), W-A-Br (blue) and W-A-I (red).

3.6.11. Solid-state ^{13}C NMR of COFs

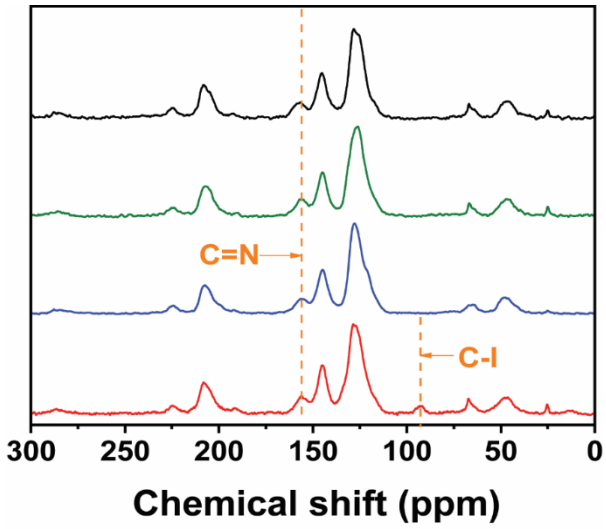

Figure 3.33. ^{13}C NMR spectra of the COFs W-A-H (black), W-A-Cl (green), W-A-Br (blue) and W-A-I (red).

3.6.12. TGA analysis

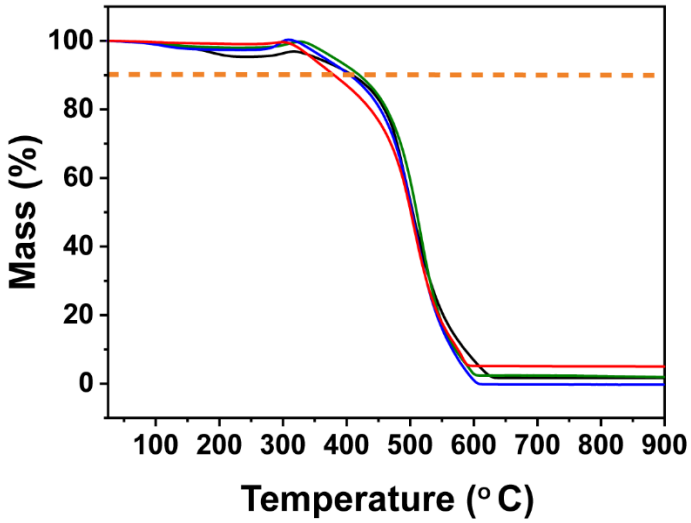

Figure 3.34. TGA analysis of the COFs W-A-H (black), W-A-Cl (green), W-A-Br (blue) and W-A-I (red).

3.6.13. Experimental optical properties

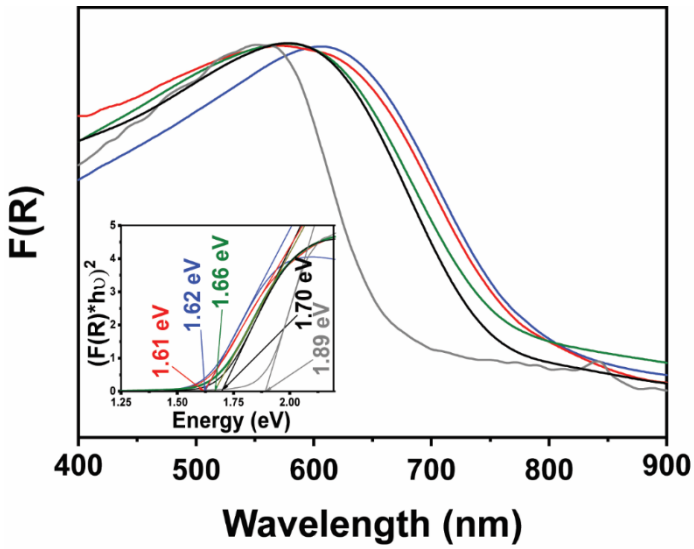

Figure 3.35. Optical absorption spectra (Kubelka Munk function F(R)) and Tauc plots of the COFs W-TA (grey), W-A-H (black), W-A-Cl (green), W-A-Br (blue), W-A-I (red).

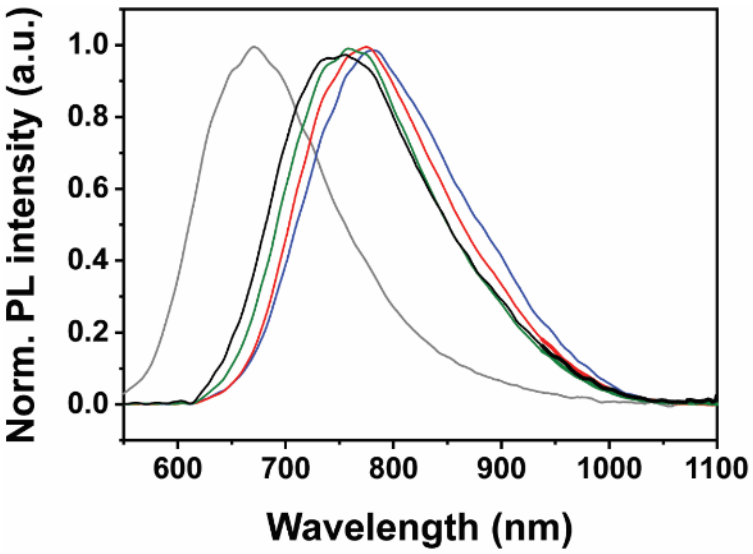

Figure 3.36. PL of the COFs W-TA (grey), W-A-H (black), W-A-Cl (green), W-A-Br (blue), W-A-I (red).

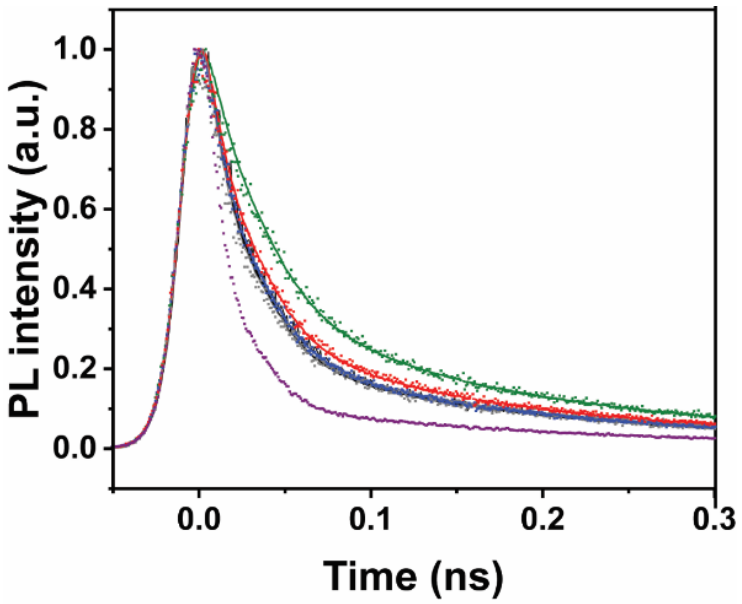

Figure 3.37. Time-resolved PL lifetime measurements of the COFs W-TA (grey), W-A-H (black), W-A-Cl (green), W-A-Br (blue), W-A-I (red). The purple curve represents the instrument response function (IRF).

3.6.14. Calculated optical properties

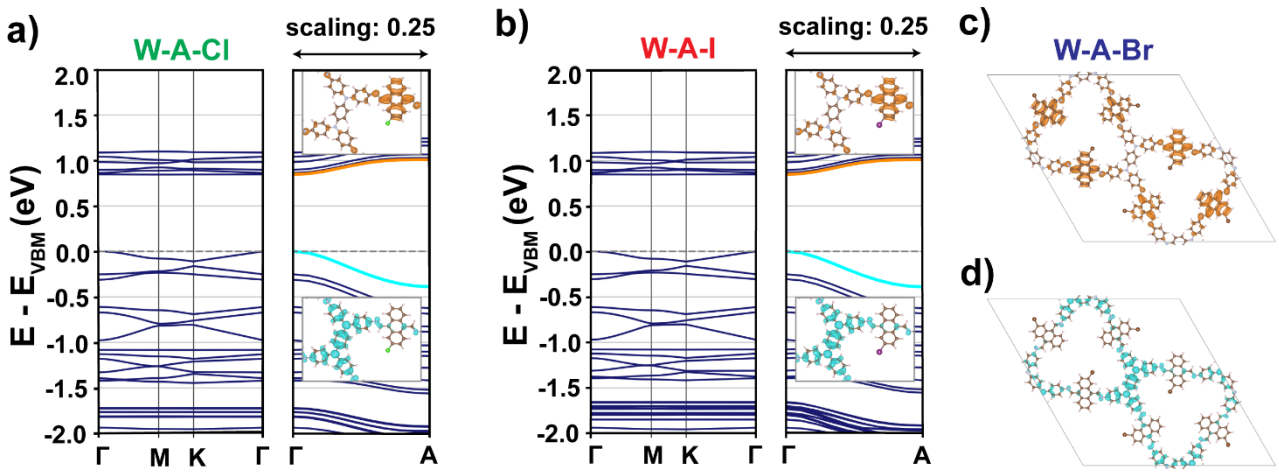

Figure 3.38. Electronic band structures of (a) W-A-Cl and (b) W-A-I COFs with insets of the partial charge densities of LUMO (orange) and HOMO (blue) bands. Partial charge densities of (c) LUMO band and (d) HOMO band of W-A-Br.

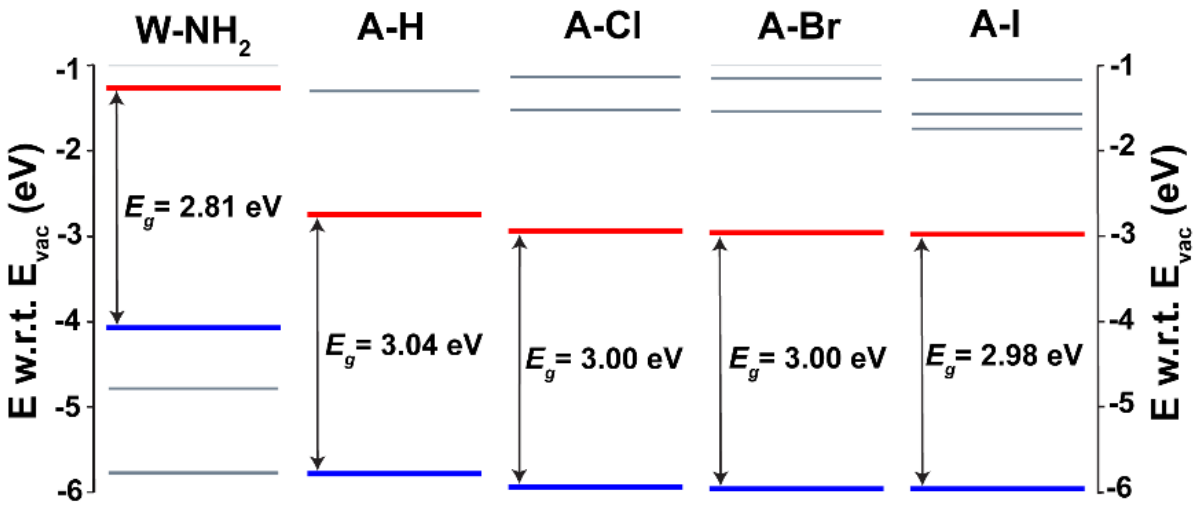

Figure 3.39. Kohn-Sham eigenvalues of W-NH_2, and (non-)halogenated anthracene (A-X, X = H, Cl, Br, I) building blocks with highlighted HOMO (blue) and LUMO (red).

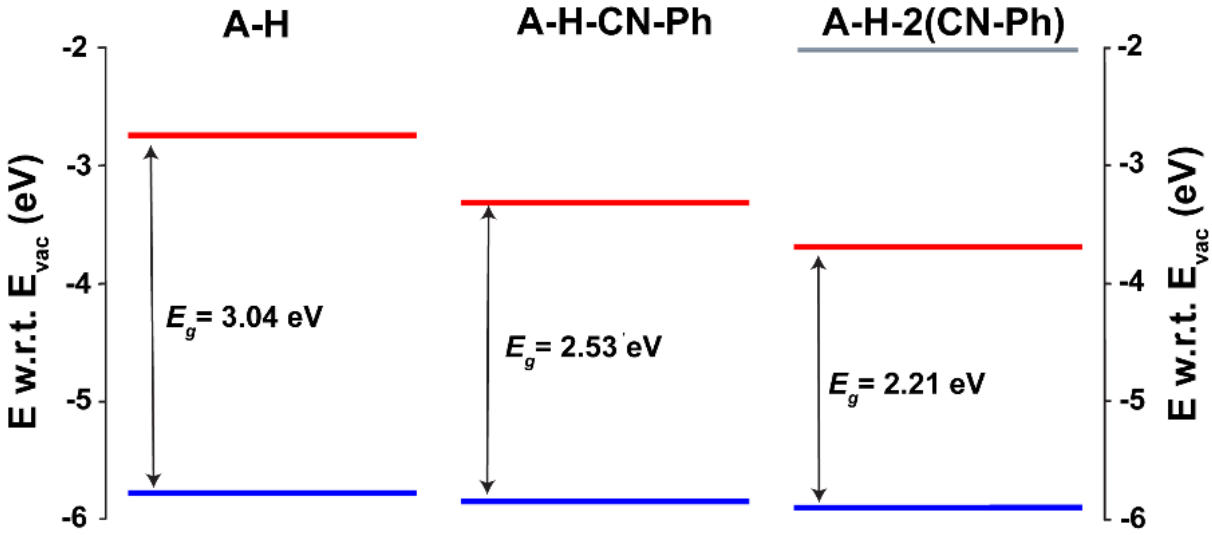

Figure 3.40. Kohn-Sham eigenvalues of the systematic extension of anthracene (A-H) toward a combined anthracene-Wurster fragment of W-A-H (A-H-2(CN-Ph)).

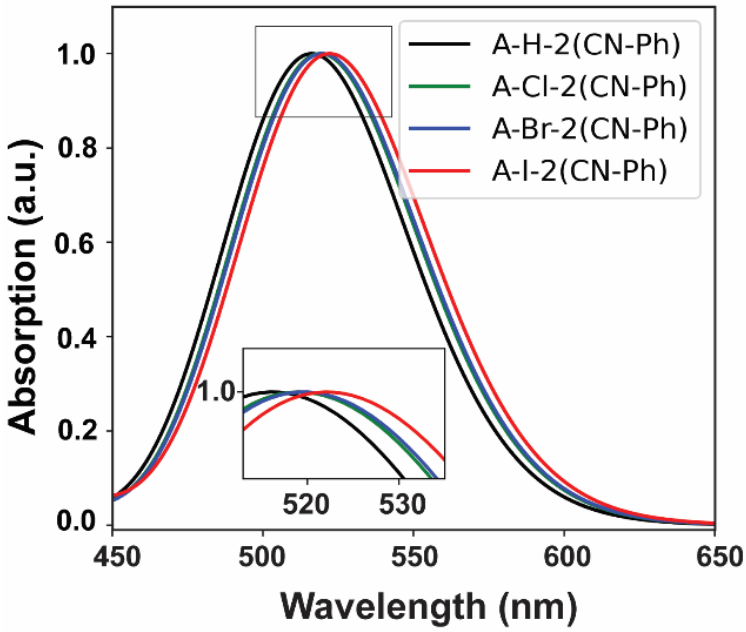

Figure 3.41. Theoretical absorption spectrum of (non-)halogenated extensions of anthracene towards a combined Wurster-anthracene fragment; inset shows close-up of the absorption maxima.

3.6.15. References

[1] G. Kresse, J. Hafner, *Phys. Rev. B* **1994**, *49*, 14251–14269.

[2] G. Kresse, J. Hafner, *Phys. Rev. B* **1993**, *47*, 558–561.

[3] G. Kresse, J. Furthmüller, *Phys. Rev. B* **1996**, *54*, 11169–11186.

[4] G. Kresse, J. Furthmüller, *Comput. Mater. Sci.* **1996**, *6*, 15–50.

[5] G. Kresse, D. Joubert, *Phys. Rev. B* **1999**, *59*, 1758–1775.

[6] P. E. Blöchl, *Phys. Rev. B* **1994**, *50*, 17953–17979.

[7] J. P. Perdew, K. Burke, M. Ernzerhof, *Phys. Rev. Lett.* **1996**, *77*, 3865–3868.

[8] S. Grimme, S. Ehrlich, L. Goerigk, *J. Comput. Chem.* **2011**, *32*, 1456–1465.

[9] A. V. Krukau, O. A. Vydrov, A. F. Izmaylov, G. E. Scuseria, *J. Chem. Phys.* **2006**, *125*, 224106.

[10] F. Bechstedt, *Many-Body Approach to Electronic Excitations*, Springer Berlin Heidelberg, Berlin, Heidelberg, **2015**.

[11] R. E. Stratmann, G. E. Scuseria, M. J. Frisch, *J. Chem. Phys.* **1998**, *109*, 8218–8224.

[12] F. Weigend, *Phys. Chem. Chem. Phys.* **2006**, *8*, 1057.

[13] D. J. F. M. J. Frisch, G. W. Trucks, H. B. Schlegel, G. E. Scuseria, M. A. Robb, J. R. Cheeseman, G. Scalmani, V. Barone, G. A. Petersson, H. Nakatsuji, X. Li, M. Caricato, A. V. Marenich, J. Bloino, B. G. Janesko, R. Gomperts, B. Mennucci, H. P. Hratchian, J. V., **2016**.

[14] B. B. Rath, L. Fuchs, F. Stemmler, A. Rodríguez-Camargo, Y. Wang, M. F. X. Dorfner, J. Olbrich, J. van Slageren, F. Ortmann, B. V. Lotsch, *J. Am. Chem. Soc.* **2025**, *147*, 18492–18503.

[15] Otto Phanstiel, *Fluorescent Cytotoxic Compounds Specific for the Cellular Polyamine Transport System*, **2001**.

[16] K. I. Yamashita, M. Tsuboi, M. S. Asano, K. I. Sugiura, *Synth. Commun.* **2012**, *42*, 170–175.

[17] K. Kawamata, P. K. Chowdhury, F. Ito, K. Sugawara, T. Nakanaga, *J. Phys. Chem. A* **1998**, *102*, 4788–4793.

[18] J. Jebasingh Kores, I. Antony Danish, T. Sasitha, J. Gershom Stuart, E. Jimla Pushpam, J. Winfred Jebaraj, *Heliyon* **2021**, *7*, e08377.

[19] A. Bree, R. A. Kydd, *J. Chem. Phys.* **1969**, *51*, 989–995.

[20] J. M. Rotter, R. Guntermann, M. Auth, A. Mähringer, A. Sperlich, V. Dyakonov, D. D. Medina, T. Bein, *Chem. Sci.* **2020**, *11*, 12843–12853.

[21] T. F. Willems, C. H. Rycroft, M. Kazi, J. C. Meza, M. Haranczyk, *Microporous Mesoporous Mater.* **2012**, *149*, 134–141.

[22] L. Sarkisov, R. Bueno-Perez, M. Sutharson, D. Fairen-Jimenez, *Chem. Mater.* **2020**, *32*, 9849–9867.

4. Pre-synthetic modification of Wurster-Anthracene COF: tuning the intermolecular interactions

This chapter is based on the following article:

Single-Atom Halogen Substitution in Covalent Organic Frameworks Enables *σ*-Hole–Driven CO_2 Adsorption

Submitted to "Chemistry of Materials"

Klaudija Paliušytė, Kuangjie Liu, Kornel Roztocki, Shuo Sun, Hendrik Zipse, and Jenny Schneider*

Department of Chemistry and Center for NanoScience (CeNS), University of Munich (LMU), Munich 81377, Germany

Faculty of Chemistry, Adam Mickiewicz University, 61-614 Poznań, Poland

*Corresponding authors

4.1. Abstract

Covalent organic frameworks (COFs) are promising materials for CO_2 adsorption owing to their tunable porosity and modular functionality. Yet, the atomic-level origins of adsorption enhancement remain unclear. Here, we report a systematic study on halogenated N,N,N′,N′-tetraphenyl-1,4-phenylenediamine (Wurster, W)-anthracene (A) COFs (W-A-X, X = H, Cl, Br, I) designed to isolate the effect of halogen atoms on CO_2 sorption behavior. All halogen-

functionalized COFs exhibit significantly higher CO_2 uptake and increased isosteric heats of adsorption compared to the W-A-H COF. To elucidate the origin of this enhanced affinity, density functional theory (DFT) calculations were performed on molecular fragments and, for the first time, on extended COF frameworks, enabling direct insight into host-guest interactions within the lattice. In W-A-H, CO_2 binds primarily via $N(\delta^-)\cdots C(\delta^+)$ interactions at the imine linkage, whereas halogenated derivatives introduce additional adsorption sites through σ-holes, localized regions of positive electrostatic potential on halogen atoms, allowing $X–\sigma(\delta^+)\cdots O(\delta^-)$ interactions with CO_2. The interaction strength follows the trend I > Br > Cl, consistent with halogen polarizability. These findings demonstrate *σ*-hole–mediated adsorption in COFs and establish halogenation as a powerful molecular design strategy to tune host-guest electrostatics for enhanced CO_2 uptake.

4.2. Introduction

Carbon dioxide is an essential greenhouse gas driving global warming.[1] To mitigate its rise, carbon capture and storage (CCS) technologies is critical to mitigate its rise.[2,3] Covalent organic frameworks (COFs) have emerged as promising materials for CO_2 sorption and storage due to their high surface areas, tunable porosity, and ability to incorporate functional groups.[4,5] Functionalizing COFs with additional functional groups or heteroatoms is a well-established strategy to enhance gas sorption performance. Polar moieties such as $-SO_3H$, $-NO_2$, and -OH increase framework polarity and dipole moment, thereby strengthening electrostatic interactions with CO_2, raising the heat of adsorption, and improving both capacity and selectivity.[6–8] However, these bulky functional groups can reduce pore volume and sometimes compromise framework stability, particularly under humid conditions. Hydrophobic modifications, by contrast, can preserve structural integrity by repelling water.[9]

Among these, halogen atoms offer a unique balance between hydrophobicity and enhanced sorption properties.[4,8] Various studies have investigated the interactions between different halogen atoms and CO_2 molecules within diverse porous materials during the adsorption process.[10–13] Although COFs are typically composed of light elements (C, H, N, O, S), the incorporation of heavier and electronegative atoms such as halogens can significantly alter the framework's electronic environment, polarizability, surface charge, and chemical reactivity.[13–

[19] For example, Li *et al.* reported the incorporation of electronegative fluorine atoms into the COF structure, which introduced additional binding sites through $F(\delta^-)\cdots C(\delta^+)$ interactions with CO_2 molecules, resulting in a higher CO_2 uptake compared to the non-functionalized COF.[20] Further advantage of halogens over conventional polar groups is their ability to form σ-holes, electron-deficient regions that act as Lewis acids, enabling strong halogen bonding interactions with electronegative atoms in gas molecules like CO_2.[21] The role of the σ-hole, a localized positive potential on halogen atoms that drives directional noncovalent interactions, has been well characterized in supramolecular systems.[22] However, σ-hole effect on host-guest interactions in halogen-functionalized COFs remains unexplored, representing a novel opportunity for rational framework design.

Most reported halogenated COFs have been constructed from small building blocks consisting of single benzene rings functionalized with halogens,[14,16,18,20,23] whereas studies employing larger, π-extended halogen-containing units remain rare. In our previous work,[24] we demonstrated the successful synthesis of halogen-containing anthracene building blocks for the further construction of halogenated COFs. Anthracene serves a dual purpose: its extended aromatic side rings shape the pore architecture and enhance gas-wall interactions, particularly at low pressures,[25] while its peripheral positions offer precise sites for halogen substitution. The central ring retains aldehyde groups essential for COF formation, allowing halogen atoms to be positioned directly at the pore periphery, where they can interact specifically with gas molecules through halogen bonding.

In this study, we investigate CO_2 sorption in four COFs constructed from N,N,N′,N′-tetraphenyl-1,4-phenylenediamine (Wurster) and halogenated anthracene-based dialdehydes.[24] A significant increase in CO_2 uptake and heat of adsorption in COFs is observed for the first time upon single-atom substitution in the anthracene building block. To uncover the observed higher affinity of the halogenated COFs towards CO_2 adsorption in comparison to non-functionalized COF, we have performed density functional theory (DFT) -based computational modeling[26] of CO_2 interaction with molecular fragments and extended COF structure. Using cluster models that adsorption the local framework environment without periodic boundary conditions, we identified the key interaction mechanisms at specific binding sites. We further employ real-space interaction analysis[27–29] to visualize and analyze non-covalent interactions

with CO_2, enabling us to assess not only the local effects of halogen substitution but also how adsorption affinity is distributed across the extended COF structure. This dual experimental-computational strategy reveals how subtle single-atom modifications is sufficient to reprogram local electrostatics in COFs, establishing σ-hole interactions as a promising design parameter to tailor host-guest chemistry, opening exciting opportunities for the rational design of functional porous materials.

4.3. Results and discussion

The four previously established Wurster-anthracene-based COFs (W-A-X), functionalized with different substituents (X = H, Cl, Br, I), were selected to explore how the substitution of a single atom can influence the COFs affinity for CO_2 adsorption. Anthracene-based 2-halogen-9,10-anthracenedialdehyde linkers (A-X-CHO; X = Cl, Br, I) were prepared via a general synthetic pathway[30,31] as depicted in **Scheme 4.1** (see Appendix). Schiff-base condensation reaction between A-X-CHO and N,N,N′,N′-tetrakis(4-aminophenyl)-1,4-phenylenediamine (W-NH_2) yielded four distinct COFs.

Figure 4.1a illustrates the dual-pore Kagome structure of W-A-X COF functionalized with halogens. The four COFs were fully characterized by scattering and electron spectroscopy in our previous study.[24] Here, we present the Powder X-ray diffraction (PXRD) data to confirm the crystalline structure of all four synthesized W-A-X COFs (

Figure 4.1b). Sharp diffraction peaks observed for W-A-H, W-A-Cl, and W-A-Br indicate a high degree of crystallinity, whereas W-A-I exhibits a moderate level of crystallinity. The PXRD data were simulated using a previously established energetically most stable structural model featuring two halogens oriented toward the trigonal pores and four halogens facing the hexagonal pores per unit cell. The simulated PXRD data aligned perfectly with the experimental pattern.

The porosity of the COFs was confirmed by nitrogen sorption isotherms. The Brunauer-Emmett-Teller (BET) surface areas and pore volumes of W-A-H and W-A-Cl were comparable, measuring 548.2 $m^2\ g^{-1}$ (0.35 $cm^3\ g^{-1}$) and 489.7 $m^2\ g^{-1}$ (0.33 $cm^3\ g^{-1}$), respectively (**Figure 4.4**, see Appendix). The substitution with larger halogens led to a marked decrease in

porosity, with W-A-Br and W-A-I exhibiting surface areas and pore volumes of 187.1 m^2 g^{-1} (0.11 cm^3 g^{-1}) and 170.1 m^2 g^{-1} (0.13 cm^3 g^{-1}). The average pore size of hexagonal and trigonal pores (calculated using non-local density functional theory (NLDFT))[32] for slit and cylindrical pores) remains consistent across the COF series: 1.1 nm and 1.7 nm for W-A-H, and 1.1 nm and 2.0 nm for W-A-Cl and W-A-Br, and 1.1 nm and 1.5 nm for W-A-I. These values confirm that all materials remain in the microporous regime. However, the reduction in BET surface area and pore volume upon substitution with Br and I can be attributed not only to steric effects, consistent with previous reports on halogenated porous networks,[12,15,33] but also to possible presence of unreacted oligomers within the pores.[34,35]

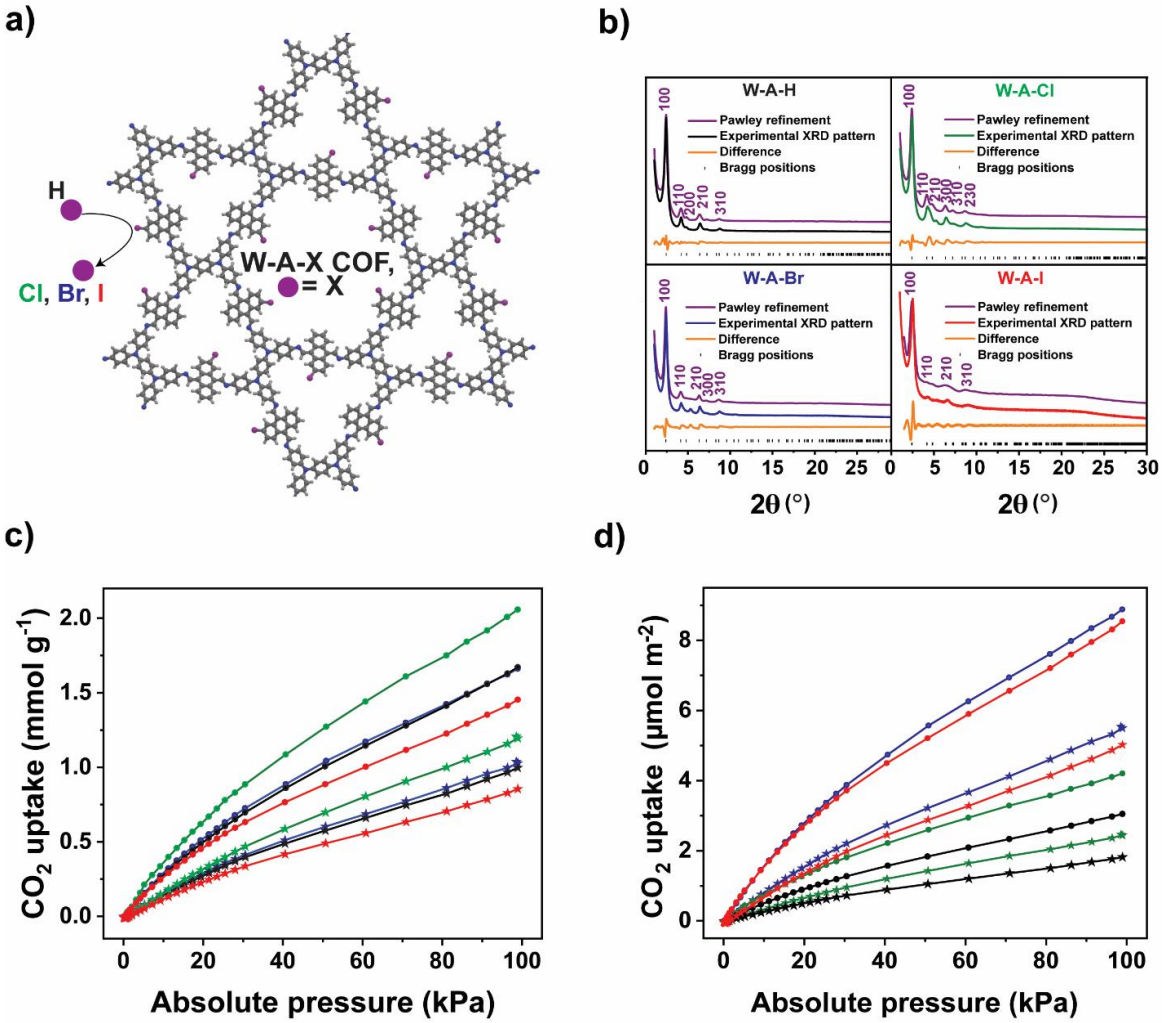

Figure 4.1. (a) Dual-pore Kagome structure of W-A-X COFs, functionalized with different substituents X (H, Cl, Br, I). (b) Simulated and experimental PXRD patterns of W-A-H, W-A-Cl, W-A-Br and W-A-I. CO_2 gas uptake for W-A-H (black), W-A-Cl (green), W-A-Br (blue)

and W-A-I (red) measured at 273K (filled circles) and 298 K (stars), presented as (c) mmol g^{-1} (raw data) and as (d) μmol m^{-2} (normalized to the BET surface area).

4.3.1. CO_2 adsorption in Wurster-Anthracene-Based COFs

All four W-A-X COFs were tested for CO_2 gas sorption at 273 and 298 K under pressures of up to 100 kPa (**Figure 4.1**c). Among the COFs series, W-A-Cl exhibits the highest sorption capacity of 2.1 mmol g^{-1} (273 K) and 1.2 mmol g^{-1} (298 K), under low CO_2 pressure of 100 kPa. This is followed by W-A-Br (1.7 and 1.0 mmol g^{-1}),W-A-H (1.7 and 1.0 mmol g^{-1})), and W-A-I (1.5 and 0.9 mmol g^{-1}).

To rationalize the differing adsorption performance of the four COFs, both the BET surface area and the adsorbent–adsorbate affinity must be considered. The former reflects the total number of available adsorption sites,[36–39] particularly relevant in the low-pressure region where monolayer formation dominates, while the latter describes the strength of interaction between the adsorbent and the CO_2 molecules.[40,41]

Although W-A-Cl has similar porosity to W-A-H, it outperforms it in CO_2 sorption. In contrast, substitution with Br and I results in a drastic reduction in porosity, indicating fewer available adsorption sites, yet both materials still display notable CO_2 sorption performance. To account for the BET surface effect, the gas uptake values were normalized to the BET surface area of the COFs, following previously reported approach[42,43] (**Figure 4.1**d). Among the studied materials, W-A-Br shows the highest sorption capacity at both temperatures, with values of 8.9 μmol m^{-2} at 273 K and 5.5 μmol m^{-2} at 298 K. This is followed by W-A-I (8.5 μmol m^{-2} and 5.0 μmol m^{-2}), W-A-Cl (4.2 μmol m^{-2} and 2.5 μmol m^{-2}), and W-A-H (3.0 μmol m^{-2} and 1.9 μmol m^{-2}). The higher CO_2 uptake observed for the halogenated COFs compared to W-A-H indicates that halogen substitution enhances the affinity toward CO_2. This trend is consistent with previous reports on porous networks showing that halogen functionalization can significantly increase adsorption affinity by introducing additional binding sites and enabling stronger interactions with polarizable gas molecules such as CO_2.[20,44–46] To further evaluate this effect, the isosteric heats of adsorption (Q_{st}) were determined for all COFs (**Figure 4.5**). The halogenated frameworks exhibited markedly stronger adsorption enthalpies, with Q_{st} values of -34.3 ± 0.3 kJ mol^{-1} for W-A-Cl, -39.6 ± 1.1 kJ mol^{-1} for W-A-Br, and -38.6 ± 5.2 kJ mol^{-1} for

W-A-I, significantly exceeding that of W-A-H (-23.0 ± 0.3 kJ mol^{-1}). Detailed isosteric heat calculations are provided in Appendix. These results unambiguously demonstrate that single-atom halogen substitution strengthens CO_2 adsorption interactions, thereby enhancing both affinity and adsorption capacity across the COF series.

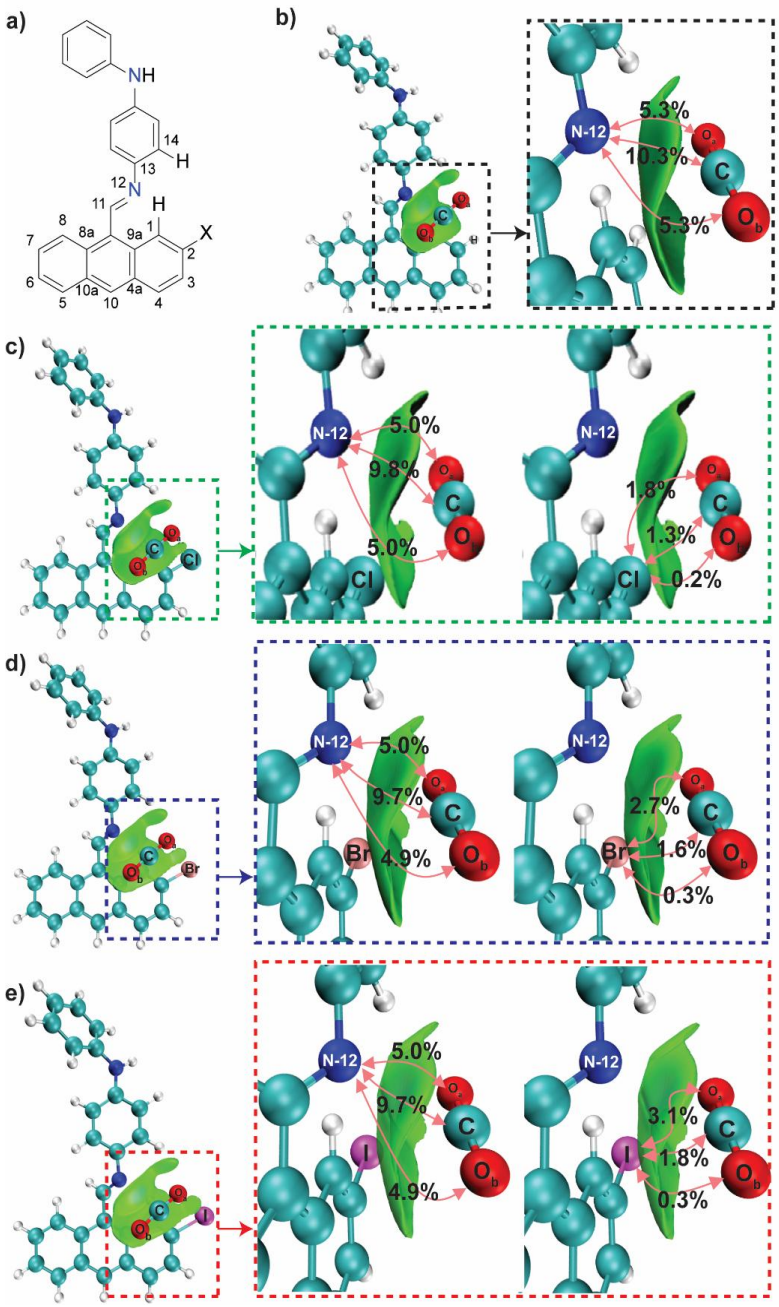

Figure 4.2. (a) W-A-X adsorption unit. Visualization of iso-surface with δg^{inter} = 0.004 a.u. from IGMH analysis, prominent non-covalent interactions and atom-wise contribution for adsorption units of (b) W-A-H, (c) W-A-Cl, (d) W-A-Br and (e) W-A-I.

4.3.2. DFT modeling on CO_2 interaction with molecular fragments

Density Functional Theory (DFT)[47–49] calculations are widely used to evaluate adsorption geometries, energetics, and interaction strengths, enabling quantification of CO_2 interactions with various functional groups. In order to understand the mechanism by which the halogen atoms enhance the adsorbent–adsorbate affinity of the COF, we carried out computational studies, beginning with an investigation of how the incorporation of halogen elements alters both the electronic structure and local charge distribution of anthracene molecules. To assess this effect, we performed surface electrostatic potential (ESP) analysis (**Figure 4.6**) using DFT calculations at the M06-2X/def2-SVPP level of theory. Additionally, we carried out a comparative partial charge analysis of the anthracene molecules (**Table 4.1**) using five different population analysis methods,[50–57] with detailed information about the computational methods being provided in Appendix. A comparison of partial charges in anthracene (A-H) with its halogen-substituted analogues 2-X-anthracene (A-X, where X = Cl, Br, I) reveals several key trends. Across all methods, halogen atoms disrupt the symmetrical charge distribution of the unsubstituted ring. Carbons adjacent to the halogen acquire more positive charge, consistent with the halogen electronegativity values. The atomic polar tensor (APT) charge at the C-2 position shifts from −0.048 in A-H to +0.474 in A-Cl. Meanwhile, the halogens themselves exhibit varying partial charges: Most of the methods often register them as negative, whereas the natural bond orbital (NBO) method can assign positive charges for heavier halogens such as Br with +0.065 and I with +0.155. Crucially, the hydrogens near the substitution site, H-1 and H-3, also become more electropositive. The pronounced electronic effects observed in small anthracene molecules underscore the sensitivity of such systems to halogen substitution. Given the extent of charge redistribution and asymmetry induced by halogen atoms in these simple aromatic molecules, it is reasonable to expect similar, but likely less pronounced, electronic perturbations in larger, more delocalized systems such as polymeric COFs. While the extended conjugation and structural rigidity of COFs may reduce the localized effects seen in anthracene, notable changes in electronic distribution are still anticipated upon halogenation.

To better understand the difference in affinity of W-A-X COFs with CO_2, interaction energies of single CO_2 molecules with representative models of the W-A-X adsorption units were determined using quantum chemical calculations. The models include the anthracene-X moiety,

imine linkage and aromatic rings of Wurster moiety (**Figure 4.2**a), and the cut bonds were capped with hydrogen atoms ensuring chemical consistency and structural integrity. Across all four derivatives of the W-A-X COFs, conformational searches consistently revealed a preferred binding site for CO_2 near the nitrogen atom of the imine bond. Once the optimal conformers were identified (see **Figure 4.7** - **Figure 4.10**, **Table 4.2** - **Table 4.5**), the adsorption enthalpies (ΔH_{ads}) were calculated (see **Table 4.6**). Among the derivatives, W-A-H exhibited the most exothermic ΔH_{ads} value of -19.3 kJ mol^{-1}, indicating a stronger local interaction with CO_2 compared to its halogen-substituted counterparts: -18.3 kJ mol^{-1} for W-A-Cl, -18.4 kJ mol^{-1} for W-A-Br, and -18.8 kJ mol^{-1} for W-A-I. This interaction occurs between the electron-deficient carbon C(δ^+) of the CO_2 molecule and the electron-rich nitrogen N(δ^-) of the imine bond. The presence of halogen substituents on the anthracene rings influences this interaction through their electron-withdrawing effects, which reduce the basicity (and electron density) of the imine nitrogen. As the electronegativity of the halogen increases (I < Br < Cl), the nitrogen becomes less Lewis basic, weakening its interaction with CO_2. To further probe the impact of halogen substitution on the basicity of the imine linkage, we designed an isodesmic proton transfer reaction (**Scheme 4.2**) between the adsorption unit of the W-A-X COFs and protonated *N*-benzylideneaniline (BA-H^+). BA was selected for its well-studied behavior[58,59] and structural similarity to the imine unit in our COFs, ensuring a meaningful comparison. The local proton affinity of each adsorption unit (X = H, Cl, Br, I) was evaluated through the reaction free energy (ΔG_P) (detailed calculations provided in **Table 4.7**). The results show that the unsubstituted W-A-H has the most negative ΔG_P at -49.6 kJ mol^{-1}, indicating the highest proton affinity and strongest driving force for proton transfer. In contrast, the halogen-substituted analogues exhibit less negative values: W-A-Cl (-40.7 kJ mol^{-1}), W-A-Br (-41.3 kJ mol^{-1}), and W-A-I (-41.7 kJ mol^{-1}). This trend reflects the reduced basicity of the imine nitrogen upon halogenation, consistent with the electronegativity values of these substituents. Notably, W-A-Cl shows the weakest proton affinity among the halogenated series. The slightly more negative ΔG_P values for W-A-Br and W-A-I may be attributed to their lower electronegativity and greater polarizability compared to chlorine. In summary, the trend in proton affinity among these COFs follows the order: W-A-H >> W-A-I > W-A-Br > W-A-Cl. The surface charge distribution of the W-A-X adsorption units can be analyzed through inspection of the respective ESP surface maps (**Figure 4.11**). The results show that the most negatively charged regions are

located around the imine bonds. Notably, these regions become slightly less negative, reflected by a shift in color, when hydrogen atoms at C2 position are replaced by halogen substituents.

In addition, we used the Independent gradient model based on Hirshfeld partition (IGMH)[27] method to visualize and analyze the non-covalent interactions between CO_2 and the W-A-X adsorption unit as separate fragments. For this purpose we selected the previously mentioned energetically most favorable conformer, in which the CO_2 molecule is located near the imine bond of a COF. The IGMH method derives atomic densities from the Hirshfeld scheme and calculates the sign(λ_2)ρ function using the actual electron density, thereby revealing both the location and type of interactions. λ_2 is the second-largest eigenvalue of the electron density Hessian, while sign(λ_2) extracts the sign of λ_2, with a positive value being repulsive and a negative value being attractive. ρ is the electron density at each point reflecting the strength of interaction. By multiplying sign(λ_2) and ρ to get sign(λ_2)ρ, IGMH distinguishes different interaction regimes, which are projected as a color scale on the iso-surface (**Figure 4.12**). For all four W-A-X COFs, the IGMH analysis revealed a green iso-surface localized between the CO_2 molecule and imine bond of the COFs as well as part of anthracene unit (**Figure 4.13**). The uniform green coloring indicates the presence of weak, non-directional van der Waals interactions, which are characteristic of physisorption. Additionally, to highlight bonding interactions between atoms, we calculated bond critical points (BCPs) between atoms with bonding interactions.[60] In all four COFs, the primary interaction was observed between the carbon atom of the CO_2 molecule and the nitrogen atom of the COF's imine bond. Interestingly, in the case of W-A-I COF, an additional BCP was found between the iodine atom and the O(δ^-) of the CO_2 molecule. For W-A-Cl and W-A-Br, new iso-surfaces were observed between the halogen atoms (Cl, Br) and the O(δ^-) of CO_2; however, no additional BCPs were detected in these cases.

To identify the atoms involved in stabilizing CO_2 via non-covalent interactions, we generated atom-wise contributions between CO_2 and our COF fragment model (δg^{atom} (%)) using Multiwfn[28,29,61] (full set of non-covalent interactions is provided in **Figure 4.14**). For the W-A-H COF, the main atom-wise contributions (**Figure 4.2**b-e) to the interaction with CO_2 were observed between the C(δ^+) of CO_2 and the N(δ^-) of the COF (10.3%), as well as between the two O(δ^-) of CO_2 and the same N(δ^-) (10.6%). For all halogenated COFs, the atom-wise

contribution values remained comparable to those observed in W-A-H; however, additional interactions were detected between all atoms of the CO_2 molecule and the halogen atoms of the frameworks. Specifically, the halogen contributions were 3.3% for Cl in W-A-Cl, 4.6% for Br in W-A-Br, and 5.2% for I in W-A-I. These results indicate that halogen atoms indeed participate in the CO_2 adsorption process. Therefore, we further proceed with a more in-depth analysis to evaluate how halogens interact with the CO_2 molecule in a broader structural context - beyond the isolated W-A-X adsorption unit.

4.3.3. DFT modeling of CO_2 interaction with extended COF structure

To investigate the influence of framework connectivity on CO_2 adsorption beyond the isolated adsorption unit, we selected a triangular subunit (W-A-X triangle) as a larger representative fragment of the full polymeric COF structure (**Figure 4.3**). Despite a higher computational demand, this unit reflects the connectivity of the extended framework more comprehensively than our initial model. This fragment also allows for the assessment of CO_2 interactions when the molecule is positioned within the pore, where it can simultaneously interact with multiple parts of the framework from several sides. We thus compared the difference of adsorption behavior when CO_2 is sitting in these two energetically most favorable regions - the previously discussed imine bond (**Figure 4.3**a-d) and the space inside the trigonal pore between two anthracene units (**Figure 4.3**e-h).

The calculations revealed differences in absorption energies in these two regions within the larger COF unit (triangle). In both cases, the generated iso-surface becomes larger as the atomic size of X increases, with hydrogen being the smallest and iodine the largest. Inside the trigonal pore, an interesting phenomenon is observed - the CO_2 molecule adopts a different orientation for X = H as compared to the halogenated structures where X is chlorine, bromine, or iodine. This difference arises from variations in the interatomic non-covalent interactions between the CO_2 molecule and the halogenated moieties, as further discussed in the following sections.

In the W-A-H system (**Figure 4.3**e), only one iso-surface appears between the O(δ^-) of the CO_2 molecule and the hydrogens of the anthracene unit, suggesting weak van der Waals interactions. In contrast, for the halogenated systems (**Figure 4.3**f-h), iso-surfaces are visible on both sides of the CO_2 molecule. On the upper side, interactions occur between the C(δ^+) and

O(δ^-) of the CO_2 molecule and the hydrogen and carbon atoms of the COF. On the opposite side, the distance between the halogen and oxygen atoms increases with the size of the halogen: 3.126 Å for W-A-Cl, 3.250 Å for W-A-Br, and 3.302 Å for W-A-I. This can be attributed to the larger spatial demand of the heavier halogen atoms, which pushes the oxygen atom closer to the upper anthracene unit. The iso-surface between the halogen atom on the lower anthracene unit and the CO_2 molecule becomes more pronounced as the atomic size of the halogen increases, following the trend iodine > bromine > chlorine. This indicates progressively stronger non-covalent interactions during the adsorption process (I > Br > Cl). This phenomenon can be explained by the concept of the *σ*-hole, a region of positive partial charge that appears opposite the covalent bond axis (C–X) on a halogen atom engaged in bonding.[62] This arises as electron density is polarized toward the bonding region, leaving a positively charged region on the surface of the halogen atom adjacent to the bond. *σ*-holes are crucial for understanding non-covalent interactions and the relative bonding strengths in molecular systems, particularly those involving halogen atoms. These regions can attractively interact with negatively charged sites such as lone pairs on Lewis bases or partial negative charges like the oxygen atoms in CO_2,[63] thereby facilitating the formation of non-covalent complexes.[64]

The *σ*-holes for small halogenated anthracene molecules and W-A-X adsorption units are clearly visible in **Figure 4.6** and **Figure 4.11** appearing as regions of positive ESP (shown in blue). To examine how this effect translates to the larger polymeric systems, we calculated the ESP for the four triangle units of W-A-X COFs (**Figure 4.3**i-l). The results revealed a distinct region of positive potential (shown in blue) for the halogenated structures (marked with arrows), indicating that the *σ*-hole effect persists within the extended framework. The size of this region increases with the halogen's atomic size, being most pronounced for iodine, followed by bromine and then chlorine. This trend can be attributed to iodine's higher atomic mass and its stronger polarization effects. The polarizability of the halogen atoms increases as they become heavier, resulting in a larger and more positive *σ*-hole. This enhanced positive region makes iodine a more favorable site for non-covalent bonding interactions compared to the lighter halogens.[65]

To quantify the difference of these two adsorption spots, next to imine or halogen, among our novel COFs, we compared adsorption enthalpies of these two CO_2 bonding positions (**Table**

4.8). For the imine bond, the calculated adsorption enthalpies at M06-2X/def2-SVPP level of theory are as follows: -27.0 kJ mol^{-1} for W-A-H, -25.9 kJ mol^{-1} for W-A-Cl, -26.1 kJ mol^{-1} for W-A-Br, and -26.2 kJ mol^{-1} for W-A-I, showing a similar trend to the results we previously discussed with the smaller adsorption unit (**Figure 4.2**). This indicates that the COFs follow the trend in binding affinity: W-A-H > W-A-I > W-A-Br > W-A-Cl. These results are consistent with previous proton affinity calculations, which showed that W-A-H exhibits the highest imine basicity. This can be attributed to the absence of electronegative halogen atoms, which in the halogenated COFs withdraw electron density from the imine bond and reduce its basicity. Among the halogenated COFs, W-A-Cl displays the lowest basicity due to the strong electron-withdrawing effect of chlorine.

In contrast, the adsorption enthalpies for CO_2 binding within the trigonal pore formed between two anthracene units follow a different trend: -10.7 kJ mol^{-1} for W-A-H, -12.1 kJ mol^{-1} for W-A-Cl, -13.5 kJ mol^{-1} for W-A-Br, and -16.1 kJ mol^{-1} for W-A-I. In this case, the binding affinity in this scenario increases in the order: W-A-I > W-A-Br > W-A-Cl > W-A-H. As previously discussed, larger halogen atoms possess more pronounced σ-holes which facilitate stronger interactions with the partially negative oxygen atom of the CO_2 molecule. Therefore, the observed trend in CO_2 affinity within the trigonal pore is primarily governed by the nature of the halogen substituent and its ability to enhance electrostatic interactions through the formation of a σ-hole.

To summarize all computational findings, two main factors influence the CO_2 adsorption affinity of W-A-X COFs: the basicity of the imine bond and the nature of the halogen substituent. Overall CO_2 adsorption affinities arise from a complex interplay of these two factors, which cannot be fully disentangled or quantitatively assessed in terms of their individual contributions. From the perspective of basicity, W-A-H is favored, whereas in terms of σ-hole-driven interactions, W-A-I is superior.

These computational findings provide a rationale for the experimentally observed CO_2 adsorption behavior (see **Figure 4.1**d). Among the four COFs, W-A-Br exhibits the highest CO_2 uptake, closely followed by W-A-I, then W-A-Cl, and finally W-A-H. The slightly lower

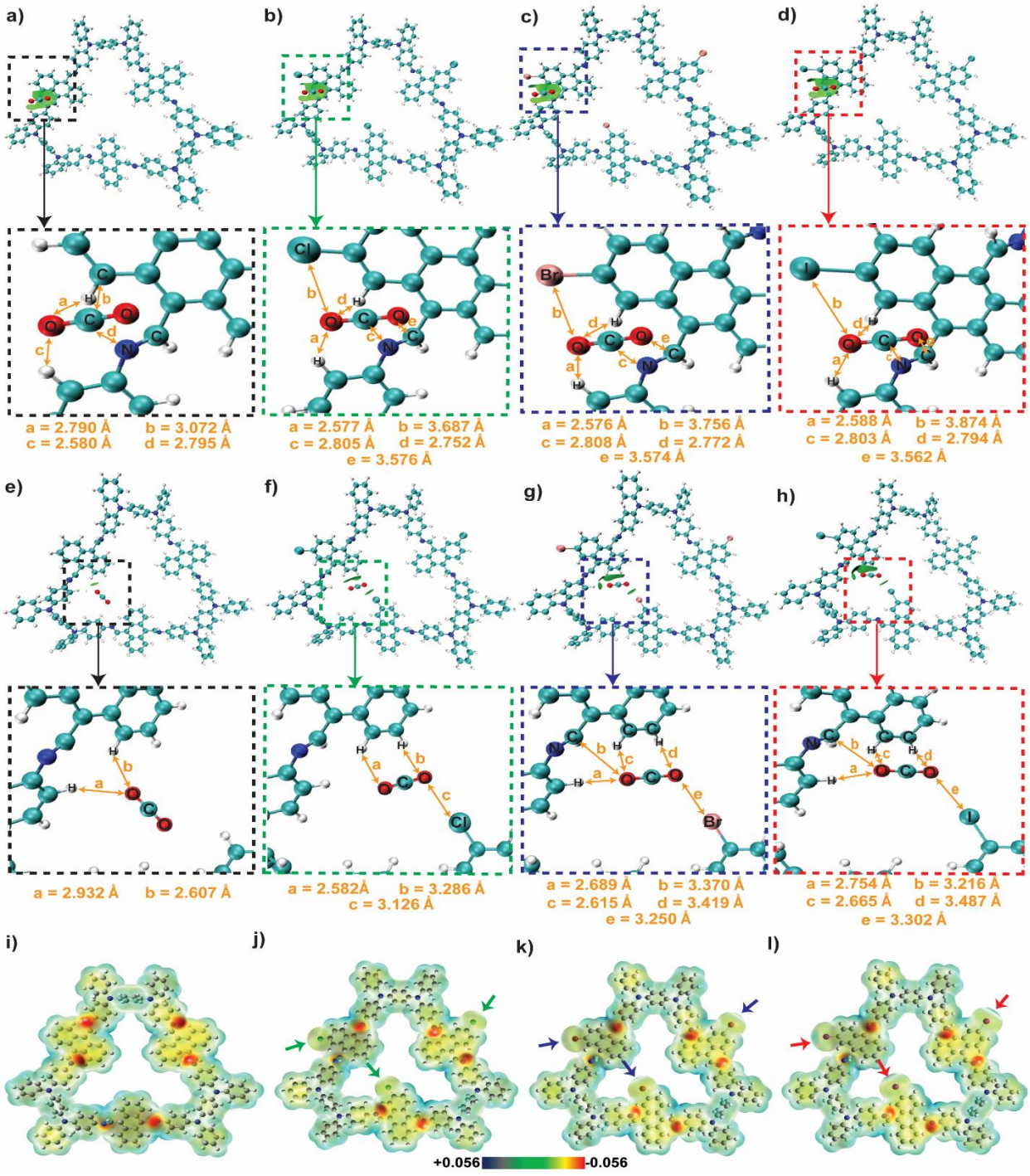

Figure 4.3. Visualization of the iso-surfaces and interatomic distances relevant to CO_2 binding in W-A-X triangle near the imine bond for (a) W-A-H, (b) W-A-Cl, (c) W-A-Br, and (d) W-A-I; inside the trigonal pore for (e) W-A-H, (f) W-A-Cl, (g) W-A-Br, and (h) W-A-I. ESP maps superimposed on the M06-2X/def2-SVPP optimized geometry of W-A-X triangle: (i) W-A-H, (j) W-A-Cl, (k) W-A-Br and (l) W-A-I. Introduction of Cl, Br, and I induces progressively larger σ-holes (positive ESP regions) opposite the C-X bonds (highlighted with arrows).

performance of W-A-I compared to W-A-Br can be attributed to its moderate crystallinity, whereas W-A-Br, W-A-Cl, and W-A-H all display similarly high crystallinity. Excluding W-A-I, the remaining COFs follow the expected trend based on the second key factor - the σ-hole effect. With the second-largest σ-hole and high crystallinity, W-A-Br outperforms W-A-Cl, which, despite also having high crystallinity, features a smaller σ-hole. W-A-H, which lacks a halogen and thus has no σ-hole, shows the lowest CO2 affinity among the high-crystallinity COFs.

In conclusion, the addition of halogen elements into the anthracene segments exerts a dual, somewhat contradictory effect on CO_2 adsorption: it diminishes the interaction between the imine linkage and the CO_2 molecule, yet concurrently introduces an extra adsorption site in the proximity of the halogen element. A comparison among four COFs with varying substituents (H, Cl, Br, I) demonstrates that, for CO_2 binding at the imine linkage, the weakest and strongest interactions are noted in W-A-Cl and W-A-H, respectively, with a disparity in adsorption enthalpy of 1.1 kJ mol^{-1}. Conversely, for CO_2 binding within the trigonal pore, the strongest interaction is recorded for W-A-I and the weakest for W-A-H, resulting in a more significant, roughly five-fold, enthalpy difference of 5.4 kJ mol^{-1}. Analysis reveals that even though the introduction of halogens reduces the CO_2 binding strength at the imine position, the cumulative adsorption capability is improved thanks to the emergence of more energetically advantageous binding sites introduced by halogen atoms, thereby producing a net gain in CO_2 attraction.

Taken together with our previous findings on the optical properties of W-A-X COFs, these results underscore the multifaceted role of halogenation in tuning both electrostatics and host-guest interactions through *σ*-hole effects, while simultaneously enabling bandgap modulation via local electronic transitions. This combined control over sorption energetics and optoelectronic characteristics highlights halogenation as a versatile design strategy for functional COFs, particularly in applications such as photocatalysis, where the synergy of tunable bandgaps and tailored electrostatic interactions[66,67] is of central importance.

4.4. Conclusions

This study provides the first systematic evidence that single-atom halogen substitution in COFs can be used to deliberately tune CO_2 adsorption via *σ*-hole interactions. While halogenation decreases porosity and weakens adsorption at traditional imine binding sites, it simultaneously introduces a new, more energetically favorable adsorption site near the halogen atom. DFT calculations reveal that CO_2 binding in non-halogenated W-A-H occurs solely at the imine linkage, whereas halogenated analogues additionally stabilize CO_2 through X–σ(δ^+)···O(δ^-) interactions within the trigonal pore. This work underscores the importance of employing structurally representative COF models in computational studies to accurately capture adsorption phenomena within extended frameworks. The strength of this *σ*-hole-driven interaction follows the trend I > Br > Cl, consistent with increasing halogen polarizability. Experimentally, this manifests as significantly enhanced CO_2 uptake and higher isosteric heats of adsorption in all halogenated COFs compared to W-A-H. Among the series, W-A-Br achieves the best balance between strong *σ*-hole interactions and high crystallinity, leading to the highest low-pressure CO_2 adsorption performance. These findings demonstrate that halogenation, through *σ*-hole engineering, can precisely program intermolecular electrostatic interactions in porous networks, providing a versatile strategy for advanced COFs design, controlled CO_2 sorption and beyond. The combined strategy of experimental sorption experiments and computational analysis of individual interaction sites established in this work is, of course, quite general and therefore applicable to functional materials beyond COFs.

4.5. References

[1] K. Abbass, M. Z. Qasim, H. Song, M. Murshed, H. Mahmood, I. Younis, *Environ. Sci. Pollut. Res.* **2022**, *29*, 42539–42559.

[2] L. J. R. Nunes, *Environments* **2023**, *10*, 66.

[3] A. S. Ahmed, M. R. Rahman, M. K. Bin Bakri, *J. Appl. Sci. Process Eng.* **2021**, *8*, 722–737.

[4] J. Ozdemir, I. Mosleh, M. Abolhassani, L. F. Greenlee, R. R. Beitle, M. H. Beyzavi, *Front. Energy Res.* **2019**, *7*, 77.

[5] Z. Zhou, T. Ma, H. Zhang, S. Chheda, H. Li, K. Wang, S. Ehrling, R. Giovine, C. Li, A. H. Alawadhi, M. M. Abduljawad, M. O. Alawad, L. Gagliardi, J. Sauer, O. M. Yaghi, *Nature* **2024**, *635*, 96–101.

[6] S. Wei, H. Xin, M. Wang, S. Xu, W. Zhai, S. Liu, L. Wang, S. Liu, Z. Wang, X. Lu, *Adv. Theory Simulations* **2022**, *5*, 2200588.

[7] G. Lee, I. Ahmed, S. H. Jhung, *Chem. Eng. J.* **2024**, *481*, 148440.

[8] F. Yuan, Z. Yang, X. Zhang, C. Tong, G. Gahungu, W. Li, J. Zhang, *J. Comput. Chem.* **2021**, *42*, 888–896.

[9] A. Torrisi, R. G. Bell, C. Mellot-Draznieks, *Cryst. Growth Des.* **2010**, *10*, 2839–2841.

[10] H. Li, Y. Lu, X. Zhu, C. Peng, J. Hu, H. Liu, Y. Hu, *Sci. China Chem.* **2012**, *55*, 1566–1572.

[11] A. Karmakar, A. A. C. D. Santos, N. Pagliaricci, J. Pires, M. Batista, E. C. B. A. Alegria, A. Martin-Calvo, J. J. Gutiérrez-Sevillano, S. Calero, M. F. C. Guedes da Silva, R. Pettinari, A. J. L. Pombeiro, *ACS Appl. Mater. Interfaces* **2024**, *16*, 20626–20641.

[12] D. M. Franz, M. Djulbegovic, T. Pham, B. Space, *AIMS Mater. Sci.* **2018**, *5*, 226–245.

[13] G. O. Aksu, S. Keskin, *ACS Appl. Mater. Interfaces* **2024**, *16*, 19806–19818.

[14] D. Cao, J. Guan, J. Du, Q. Sun, J. Ma, J. Li, J. Liu, G. Sheng, *J. Hazard. Mater.* **2024**, *476*, 134956.

[15] K. Zhao, H. Qiao, S. Wang, X. Xu, C. Wang, M. Jiao, L. Yang, X. Kong, Z. Zhu, N. Qin, L. Zhai, *ACS Mater. Lett.* **2024**, *6*, 212–221.

[16] H. Hou, Y. Wu, J. Wan, R. Luo, L. Wu, Y. Zhao, X. Wu, J. Lei, *Angew. Chemie Int. Ed.* **2025**, *64*, e202506309.

[17] W. Chen, L. Wang, D. Mo, F. He, Z. Wen, X. Wu, H. Xu, L. Chen, *Angew. Chemie - Int. Ed.* **2020**, *59*, 16902–16909.

[18] S. Liu, C. Hao, C. Meng, S. Liu, W. Zhai, Q. Zhu, W. Li, S. Wei, Z. Wang, X. Lu, *ACS Appl. Nano Mater.* **2023**, *6*, 12124–12131.

[19] J. Hu, J. Zhao, T. Yan, *J. Phys. Chem. C* **2015**, *119*, 2010–2014.

[20] Q. Li, Y. Xu, Z. Lin, Z. Sun, Y. Liu, *Sep. Purif. Technol.* **2025**, *367*, 132992.

[21] T. Lang, X. Zhang, L. Meng, Y. Zeng, *Struct. Chem.* **2016**, *27*, 927–937.

[22] R. Siddiqui, J. Rani, H. M. Titi, R. Patra, *Coord. Chem. Rev.* **2024**, *517*, 215994.

[23] K. Zhao, H. Qiao, S. Wang, X. Xu, C. Wang, M. Jiao, L. Yang, X. Kong, Z. Zhu, N. Qin, L. Zhai, *ACS Mater. Lett.* **2024**, *6*, 212–221.

[24] K. Paliušytė, L. Fuchs, Z. Xu, K. Liu, K. Roztocki, S. Sun, H. Zipse, A. Hartschuh, F. Ortmann, J. Schneider, *J. Mater. Chem. A* **n.d.**

[25] M. Yoshizawa, J. K. Klosterman, *Chem. Soc. Rev.* **2014**, *43*, 1885–1898.

[26] R. Poloni, B. Smit, J. B. Neaton, *J. Phys. Chem. A* **2012**, *116*, 4957–4964.

[27] T. Lu, Q. Chen, *J. Comput. Chem.* **2022**, *43*, 539–555.

[28] T. Lu, *J. Chem. Phys.* **2024**, *161*, 082503.

[29] T. Lu, F. Chen, *J. Comput. Chem.* **2012**, *33*, 580–592.

[30] Otto Phanstiel, *Fluorescent Cytotoxic Compounds Specific for the Cellular Polyamine Transport System*, **2013**.

[31] K. I. Yamashita, M. Tsuboi, M. S. Asano, K. I. Sugiura, *Synth. Commun.* **2012**, *42*, 170–175.

[32] G. Kupgan, T. P. Liyana-Arachchi, C. M. Colina, *Langmuir* **2017**, *33*, 11138–11145.

[33] B. Song, R. E. Sikma, C. McKeown, K. Leung, D. F. Sava Gallis, A. G. Ilgen, *ACS Appl. Nano Mater.* **2025**, *8*, 15791–15798.

[34] T. Xue, O. A. Syzgantseva, L. Peng, M. A. Syzgantseva, R. Li, G. Xu, D. T. Sun, R. Qiu, C. Liu, S. Zhang, T. Su, P. Su, S. Yang, J. Li, B. Han, *Chem. Mater.* **2022**, *34*, 10584–10593.

[35] A. Della Martina, L. Garamszegi, J. G. Hilborn, *J. Polym. Sci. Part A Polym. Chem.* **2003**, *41*, 2036–2046.

[36] Y. Zheng, X. Xu, X. Zhang, L. Qin, Y. Lu, G. Zhang, *IOP Conf. Ser. Earth Environ. Sci.* **2018**, *170*, 032073.

[37] S. Gu, J. He, Y. Zhu, Z. Wang, D. Chen, G. Yu, C. Pan, J. Guan, K. Tao, *ACS Appl. Mater. Interfaces* **2016**, *8*, 18383–18392.

[38] E. Dautzenberg, G. Li, L. C. P. M. de Smet, *ACS Appl. Mater. Interfaces* **2023**, *15*, 5118–5127.

[39] Y. Zeng, R. Zou, Y. Zhao, *Adv. Mater.* **2016**, *28*, 3032–3032.

[40] Q. Sun, B. Aguila, L. D. Earl, C. W. Abney, L. Wojtas, P. K. Thallapally, S. Ma, *Adv. Mater.* **2018**, *30*, 1705479.

[41] N. Huang, R. Krishna, D. Jiang, *J. Am. Chem. Soc.* **2015**, *137*, 7079–7082.

[42] R. L. S. Canevesi, S. Schaefer, M. T. Izquierdo, A. Celzard, V. Fierro, *ACS Appl. Nano Mater.* **2022**, *5*, 3843–3854.

[43] K. Paliušytė, L. Leão Nascimento, H. Illner, M. Wiedmaier, R. Guntermann, M. Döblinger, T. Bein, A. O. T. Patrocinio, J. Schneider, *Small* **2025**, *21*, 2500870.

[44] D. B. Shinde, M. Ostwal, X. Wang, A. M. Hengne, Y. Liu, G. Sheng, K.-W. Huang, Z. Lai, *CrystEngComm* **2018**, *20*, 7621–7625.

[45] Y. Han, K. H. Cho, S.-K. Lee, J. W. Yoon, Y.-S. Bae, D. Jo, U.-H. Lee, *Microporous Mesoporous Mater.* **2024**, *366*, 112958.

[46] T. J. Matemb Ma Ntep, W. Wu, H. Breitzke, C. Schlüsener, B. Moll, L. Schmolke, G. Buntkowsky, C. Janiak, *Aust. J. Chem.* **2019**, *72*, 835.

[47] M. Alharbi, R. Aljohani, R. Alzahrani, Y. Alsufyani, N. Alsumani, *Comput. Chem.* **2023**, *11*, 53–66.

[48] B. Dash, *J. Mol. Model.* **2018**, *24*, 120.

[49] K. A. Othman, Y. H. Azeez, R. A. Omer, R. O. Kareem, *Kondens. sredy i mezhfaznye granitsy = Condens. Matter Interphases* **2024**, *26*, 280–294.

[50] R. S. Mulliken, *J. Chem. Phys.* **1955**, *23*, 1833–1840.

[51] J. Cioslowski, *J. Am. Chem. Soc.* **1989**, *111*, 8333–8336.

[52] A. E. Reed, R. B. Weinstock, F. Weinhold, *J. Chem. Phys.* **1985**, *83*, 735–746.

[53] F. L. Hirshfeld, *Theor. Chim. Acta* **1977**, *44*, 129–138.

[54] C. M. Breneman, K. B. Wiberg, *J. Comput. Chem.* **1990**, *11*, 361–373.

[55] B. H. Besler, K. M. Merz, P. A. Kollman, *J. Comput. Chem.* **1990**, *11*, 431–439.

[56] T. Lu, F. Chen, *J. Theor. Comput. Chem.* **2012**, *11*, 163–183.

[57] L. Tian, C. Fei-Wu, *Acta Physico-Chimica Sin.* **2012**, *28*, 1–18.

[58] J. Bernstein, Y. M. Engel, A. T. Hagler, *J. Chem. Phys.* **1981**, *75*, 2346–2353.

[59] C. H. Warren, G. Wettermark, K. Weiss, *J. Am. Chem. Soc.* **1971**, *93*, 4658–4663.

[60] I. Alkorta, I. Rozas, J. Elguero, *J. Mol. Struct. THEOCHEM* **1998**, *452*, 227–232.

[61] J. Zhang, T. Lu, *Phys. Chem. Chem. Phys.* **2021**, *23*, 20323–20328.

[62] A. Mehmood, B. G. Janesko, *Phys. Chem. Chem. Phys.* **2025**, *27*, 861–867.

[63] X. Yang, C. Yan, F. Yang, D. Zhou, P. Zhou, S. Liu, *ChemistrySelect* **2017**, *2*, 2687–2699.

[64] M. H. Kolář, P. Carloni, P. Hobza, *Phys. Chem. Chem. Phys.* **2014**, *16*, 19111–19114.

[65] N. Robinson, N. Pham, K. J. Donald, *J. Phys. Chem. A* **2025**, *129*, 955–966.

[66] J. Feng, W. Zhang, Z. Gu, *Chempluschem* **2024**, *89*, e202400069.

[67] M. Yu, W. Chen, Q. Lin, L. Li, Z. Liu, J. Bi, Y. Yu, *Angew. Chemie Int. Ed.* **2025**, *64*, e202418422.

4.6. Appendix

4.6.1. Experimental section

Chemicals. All materials were purchased from Aldrich, Fluka, Acros, Activate Scientific, or TCI Europe in the common purities purum, puriss, or reagent grade. Materials were used as received without additional purification and handled under air unless noted otherwise. All used solvents were anhydrous and purged with inert gas.

Powder X-ray diffraction (PXRD) measurements. Powder X-ray diffraction measurements were performed on a Bruker D8 Discover diffractometer using Ni-filtered Cu Kα radiation and a position sensitive LynxEye detector in Bragg-Brentano geometry.

Nitrogen sorption measurement. Nitrogen sorption isotherms were recorded on a Quantachrome Autosorb 1 at 77 K within a pressure range from P/P0 = 0.001 to 0.98. Prior to the measurement of the sorption isotherms, the samples were heated for 24 h at 393 K under turbo-pumped vacuum. For the evaluation of the surface area the Brunauer–Emmett–Teller (BET) model was applied between 0.05 and 0.28 P/P_0, considering an experimentally determined standard deviation of 8%. Pore size distributions were calculated using the NLDFT equilibrium model with a carbon kernel for slit/cylindrical pores.[1]

Low-pressure carbon dioxide sorption measurement. Carbon dioxide sorption isotherms were recorded on a Quantachrome Autosorb 1 at at 273 and 298 K within a pressure range from P/P0 = 0.001 to 0.98. Prior to the measurement of the sorption isotherms, the samples were heated for 24 h at 393 K under turbo-pumped vacuum.

High-pressure carbon dioxide sorption measurement. Volumetric high-pressure single-gas adsorption experiments were conducted using the BELSORP-VC (Microtrac MRB) instrument. Helium gas (99.999% purity, Praxair) was used for the dead volume measurement. Carbon dioxide (99.999% purity, Praxair) was used in adsorption experiments. The samples were degassed in dynamic vacuum over 6 h at 373 K in the measurement cell. Single-gas adsorption isotherms were measured at 280 K, 290 K and 298 K in a pressure range of 0.5−4207 kPa and 0.1% of pressure change within 300 s was set as adsorption equilibrium conditions. The

isotherm was corrected for non-linear pressure / molar volume dependence using the coefficients from the virial equation for CO_2.

Computational methods. Structure simulations and solutions were performed using Materials Studio. PXRD data were refined through Pawley method, with the experimental and simulated PXRD patterns well-fitted using the X-cell program. The unit cell parameters were confirmed under the P-3 and P-1 space groups. Simulated unit cells were optimized and verified for accuracy by ensuring the absence of imaginary frequencies. To investigate interactions between the COF and gas molecules, a representative COF fragment was selected. Constrained sampling was performed using CREST 2.12[2,3] at the GFN2 level in the gas phase, where the COF fragment was fixed with a force constant of 0.5, and gas molecules were allowed to move freely. Prior to sampling, pre-optimization was conducted to ensure reliable topology. Conformers within a 6 kcal/mol energy window were further optimized with Density Functional Theory (DFT) calculations in Gaussian 09[4] at the M06-2X[5]/def2-SVPP[6] level of theory in the gas phase, followed by single point calculation at the M06-2X/def2-TZVPP[6] level of theory in the gas phase. Visualizations of the optimized structures were created and exported using GaussView 6.0.16. Atomic charge analysis was done with Gaussian 09 and Multiwfn[7–9]. Independent gradient model based on Hirshfeld partition (IGMH) and Atoms in molecule (AIM) analysis were done with Multiwfn and the results were visualized with VMD 1.9.4a53[10]. Scatter maps of sign(λ2)ρ against δginter were plotted with Gnuplot. To obtain a comprehensive picture of how electron density is distributed in anthracene and its halogen-doped analogues, five different population analysis methods were chosen: Mulliken[11], atomic polar tensor (APT)[12], natural population analysis (NPA)[13], Hirshfeld[14], Charges from Electrostatic Potentials using a Grid-based method (CHELPG)[15], Merz-Kollmann (MK)[16], and atomic dipole-moment corrected Hirshfeld (ADCH) atomic charges[17,18]. Various methods for partitioning electron density offer distinct theoretical frameworks and strengths. Mulliken analysis is one of the earliest approaches, known for its conceptual simplicity and computational efficiency. However, it is highly sensitive to the choice of basis set due to its reliance on orbital overlap. APT, on the other hand, is particularly suited for interpreting vibrational and polarizability data derived from the molecular Hessian. APT charges are generally less sensitive to basis set choice and are widely applied in vibrational spectroscopy studies. NPA identifies "natural" localized orbitals and provides insight into covalent bonding

and electron donation. This method often yields larger partial charge magnitudes due to its emphasis on bonding interactions. Hirshfeld population analysis is computationally efficient and qualitatively consistent with electronegativity based on deformation density partitioning. However, Hirshfeld charges tend to be too small and exhibit poor reproducibility for properties such as molecular dipole moments and electrostatic potential (ESP), as the method neglects atomic dipole moments. To address this, atomic dipole-moment corrected Hirshfeld (ADCH) atomic charge introduces atomic dipole moment corrections, which improves the reproducibility of molecular dipole moments and ESP. CHELPG and MK charges are derived from fitting the molecular ESP. While CHELPG places grid points around the molecule, MK uses concentric layers following the van der Waals surface. These methods are widely used in force field parameterization and ESP-related analyses due to their ability to reproduce the molecular ESP accurately. Both approaches are computationally practical and effective in capturing localized charge distributions for molecular systems.

4.6.2. Syntheses of halogenated anthracene building blocks

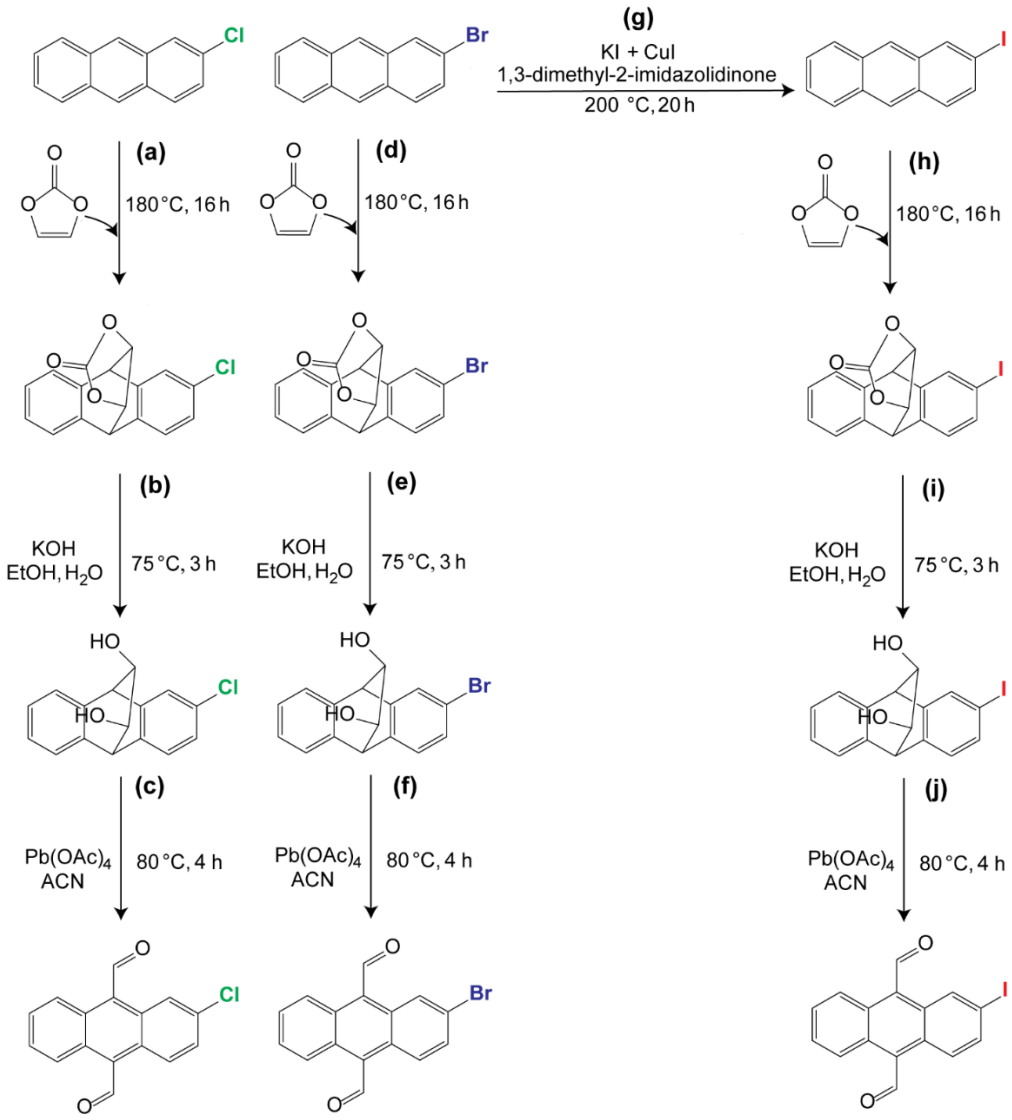

Scheme 4.1. Synthetic route to 2-halogen-9,10-anthracenedialdehyde (A-X-CHO; X = Cl, Br, I) linkers.

Synthesis of 2-chloro-9,10-dihydro-9,10-[4,5]epidioxoloanthracen-13-one (a)

The synthesis procedure was adapted from the previously published literature.[19] 2-Chloroanthracene (1.175 g, 5.541 mmol, 1 equiv.) and vinylene carbonate (3.484 g, 40.452 mmol, 7.3 equiv.) were refluxed with stirring for 18 hours, during which a dark brown solution gradually formed. The progress of the reaction was monitored by thin-layer chromatography (CH_2Cl_2/hexane 1:49, R = 0.30). After completion, the reaction mixture was concentrated under high vacuum using rotary evaporation to remove excess vinylene carbonate, yielding the cyclic

carbonate intermediate as a light brown solid (1.62 g, 5.43 mmol, 98.1 % yield). The product was used in subsequent reactions without further purification.

^{1}H NMR (400 MHz, $CDCl_3$) δ 7.35 – 7.11 (m, 7H), 4.86 – 4.75 (m, 2H), 4.67 – 4.58 (m, 2H).

Synthesis of 2-chloro-9,10-dihydro-9,10-ethanoanthracene-11,12-diol (b)

The synthesis procedure was adapted from the previously published literature.[19] Solid potassium hydroxide (1.175 g, 5.225 mmol, 4 equiv.), deionized water (19.60 mL), and absolute ethanol (2.1 mL) were added to the dark brown cyclic carbonate intermediate (a) (1.568 g, 5.225 mmol, 1 equiv.). The mixture was stirred at 75 °C for 3 hours, and the reaction progress was monitored by thin-layer chromatography (100% CH_2Cl_2, R = 0.30). After completion, the ethanol and approximately half of the water were removed by rotary evaporation under reduced pressure. Additional deionized water (39.2 mL) was then added, and the mixture was stirred at room temperature for 1 hour, resulting in the formation of a light tan solid. The solid was collected by vacuum filtration, washed with deionized water, and then with ethyl acetate on the filter. The ethyl acetate washings were concentrated by rotary evaporation, leaving a yellow solid residue. The crude product was purified by column chromatography (hexane/ethyl acetate 1:1, R = 0.55 and 0.50), affording two diol isomers as a white solid (1.006 g, 3.70 mmol, 70.8% yield).

^{1}H NMR (400 MHz,$CHCl_3$) δ (ppm): 7.30 (d, *J* = 2.0 Hz, 1H), 7.27 – 7.19 (m, 3H), 7.15 – 7.07 (m, 3H), 4.36 – 4.29 (m, 2H), 4.04 – 3.97 (m, 2H)

^{1}H NMR (400 MHz,$CHCl_3$) δ (ppm): 7.30 (dd, *J* = 5.4, 3.3 Hz, 2H), 7.26 – 7.04 (m, 5H), 4.33 (dd, *J* = 7.3, 2.5 Hz, 2H), 4.03 – 3.95 (m, 2H)

Synthesis of 2-chloroanthracene-9,10-dicarbaldehyde (c)

The synthesis procedure was adapted from the previously published literature.[19] The diol intermediate (b) (0.995 g, 3.66 mmol, 1 equiv.) was dissolved in anhydrous acetonitrile (63 mL) and heated to reflux with stirring, forming a transparent light tan solution. Lead tetraacetate (3.243 g, 7.316 mmol, 2 equiv.) was added portionwise over 5 minutes, during which the solution quickly turned opaque and brown. The mixture was stirred at reflux for 4 hours, resulting in the formation of a dark orange precipitate within the brown solution. The progress of the reaction was monitored by thin-layer chromatography (CH_2Cl_2/ethyl acetate

8:2, R = 0.50 and 0.33). Upon completion, the reaction mixture was concentrated by rotary evaporation, yielding a burgundy residue. The residue was suspended in 10% aqueous sodium carbonate (70 mL), and the organic components were extracted with dichloromethane. The opaque yellow organic layer was dried over anhydrous sodium sulfate, filtered, and concentrated to afford a yellow–orange solid. Purification by column chromatography (hexane/CH_2Cl_2/ethyl acetate 10:1:1, R = 0.3) gave 2-chloro-9,10-anthracenedialdehyde (A-Cl-CHO) as an orange solid (0.630 g, 2.350 mmol, 64.26% yield).

^{1}H NMR (400 MHz, $CDCl_3$) δ 11.39 (s, 1H), 11.37 (s, 1H), 8.80 (d, J = 2.1 Hz, 1H), 8.71 – 8.60 (m, 3H), 7.72 – 7.62 (m, 2H), 7.57 (dd, J = 9.5, 2.1 Hz, 1H).

^{13}C NMR (101 MHz, $CDCl_3$) δ 193.88, 193.40, 135.30, 133.05, 132.79, 131.33, 130.41, 129.62, 128.98, 128.55, 128.06, 126.13, 124.19, 123.94, 123.14.

Elemental analysis (CHNSCl): C (69.06 %), H (3.23 %), Cl (13.20 %). Theoretical: C (71.52 %), H (3.80 %), Cl (13.19 %).

Synthesis of 2-bromo-9,10-dihydro-9,10-[4,5]epidioxoloanthracen-13-one (d)

The synthesis procedure was adapted from the previously published literature.[19] 2-Bromoanthracene (2.4 g, 9.39 mmol, 1 equiv.) and vinylene carbonate (5.9 g, 58.56 mmol, 7.3 equiv.) were refluxed with stirring for 18 hours, during which a dark brown solution gradually formed. The progress of the reaction was monitored by thin-layer chromatography (CH_2Cl_2/hexane 1:49, R = 0.30). After completion, the reaction mixture was concentrated under high vacuum using rotary evaporation to remove excess vinylene carbonate, yielding the cyclic carbonate intermediate as a light brown solid (3.18 g, 9.30 mmol, 66.6% yield). The product was used in subsequent reactions without further purification.

^{1}H NMR (400 MHz, $CDCl_3$) δ 7.46 (dd, J = 3.6, 1.9 Hz, 1H), 7.35 – 7.26 (m, 3H), 7.23 – 7.14 (m, 3H), 4.81 (dt, J = 3.7, 1.8 Hz, 2H), 4.61 (dq, J = 7.1, 1.6 Hz, 2H).

Synthesis of 2-bromo-9,10-dihydro-9,10-ethanoanthracene-11,12-diol (e)

The synthesis procedure was adapted from the previously published literature.[19] Solid potassium hydroxide (2.56 g, 45.59 mmol, 5.1 equiv.), deionized water (42.6 mL), and absolute ethanol (4.5 mL) were added to the dark brown cyclic carbonate intermediate (d) (3.06 g, 8.94 mmol, 1 equiv.). The mixture was stirred at 75 °C for 3 hours, and the reaction progress was

monitored by thin-layer chromatography (100% CH_2Cl_2, R = 0.30). After completion, the ethanol and approximately half of the water were removed by rotary evaporation under reduced pressure. Additional deionized water (85 mL) was then added, and the mixture was stirred at room temperature for 1 hour, resulting in the formation of a light tan solid. The solid was collected by vacuum filtration, washed with deionized water, and then with ethyl acetate on the filter. The ethyl acetate washings were concentrated by rotary evaporation, leaving a yellow solid residue. The crude product was purified by column chromatography (CH_2Cl_2/ethyl acetate 9:1, R = 0.30 and 0.15), affording two diol isomers as a white solid (2.01 g, 79% yield).

^{1}H NMR (400 MHz, $CDCl_3$) δ 7.40 (d, *J* = 1.9 Hz, 1H), 7.34 – 7.06 (m, 6H), 4.32 (dd, *J* = 6.1, 2.4 Hz, 2H), 4.01 – 3.94 (m, 2H).

Elemental analysis (CHNSCl): C (60.59 %), H (4.07 %). Theoretical: C (60.59 %). H (4.13 %).

Synthesis of 2-bromoanthracene-9,10-dicarbaldehyde (f)

The synthesis procedure was adapted from the previously published literature.[19] The diol intermediate (e) (2.00 g, mmol, 1 equiv.) was dissolved in anhydrous acetonitrile (127 mL) and heated to reflux with stirring, forming a transparent light tan solution. Lead tetraacetate (5.595 g, mmol, 2 equiv.) was added portionwise over 5 minutes, during which the solution quickly turned opaque and brown. The mixture was stirred at reflux for 4 hours, resulting in the formation of a dark orange precipitate within the brown solution. The progress of the reaction was monitored by thin-layer chromatography (CH_2Cl_2/ethyl acetate 8:2, R = 0.50 and 0.33). Upon completion, the reaction mixture was concentrated by rotary evaporation, yielding a burgundy residue. The residue was suspended in 10% aqueous sodium carbonate (130 mL), and the organic components were extracted with dichloromethane. The opaque yellow organic layer was dried over anhydrous sodium sulfate, filtered, and concentrated to afford a yellow-orange solid. Purification by column chromatography (ethyl acetate/hexane 2:8, R = 0.3) gave 2-bromo-9,10-anthracenedialdehyde (A-Br-CHO) as an orange solid (1.71 g, 5.465 mmol, 86.35% yield).

^{1}H NMR (400 MHz, $CDCl_3$) δ 11.39 (s, 1H), 11.37 (s, 1H), 8.97 (dd, *J* = 1.9, 0.5 Hz, 1H), 8.71 – 8.55 (m, 3H), 7.73 – 7.63 (m, 3H).

^{13}C NMR (101 MHz, $CDCl_3$) δ 192.75, 192.40, 131.21, 130.92, 130.14, 129.63, 129.38, 129.23, 127.95, 127.57, 127.11, 125.50, 124.96, 123.15, 122.97, 122.87.

Elemental analysis (CHNSCl): C (60.44 %), H (2.98 %). Theoretical: C (61.37 %), H (2.90 %).

Synthesis of 2-Iodoanthracene (g)

The synthesis procedure was adapted from the previously published literature[20]. A mixture of 2-bromoanthracene (2.582 g, 10.09 mmol, 1 equiv.), KI (15.12 g, 91.09 mmol, 9.03 equiv.), and CuI (5.934 g, 31.16 mmol, 3.09 equiv.) was placed in a 100 mL round-bottom flask with 1,3-dimethyl-2-imidazolidinone (38.7 mL). The reaction mixture was purged with nitrogen and heated with vigorous stirring at 200 °C for 20 hours. After cooling to room temperature, brine and ice were added, and the vessel was placed in an ice bath for several hours. The precipitated inorganic salts were removed by filtration, and the filtrate was concentrated under high vacuum to remove excess 1,3-dimethyl-2-imidazolidinone. The solid residue was extracted with dichloromethane, and the crude product was purified by column chromatography (hexane/$CHCl_3$/ethyl acetate 5:3:1, R = 0.9) to afford 2-iodoanthracene as a yellow solid (1.466 g, 4.82 mmol, 47.8% yield).

^{1}H NMR (400 MHz, $CDCl_3$) δ 8.36 (dt, *J* = 1.5, 0.8 Hz, 1H), 8.31 (s, 1H), 8.23 (s, 1H), 7.96 – 7.89 (m, 2H), 7.70 – 7.64 (m, 1H), 7.58 (dd, *J* = 9.0, 1.6 Hz, 1H), 7.47 – 7.38 (m, 2H).

^{13}C NMR (101 MHz, $CDCl_3$) δ 136.71, 133.49, 132.77, 131.79, 131.52, 129.76, 129.48, 128.07, 126.38, 126.04, 125.70, 125.17, 125.03, 91.03.

HRMS-EI: Calculated (*m*/*z*): 303.97, measured (*m*/*z*): 303.97

Synthesis of 2-iodo-9,10-dihydro-9,10-[4,5]epidioxoloanthracen-13-one (h)

The synthesis procedure was adapted from the previously published literature.[19] 2-Iodoanthracene (g) (1.446 g, 4.76 mmol, 1 equiv.) and vinylene carbonate (2.99 g, 34.73 mmol, 7.3 equiv.) were refluxed with stirring for 18 hours, during which a dark brown solution gradually formed. The progress of the reaction was monitored by thin-layer chromatography (CH_2Cl_2/hexane 1:49, R = 0.30). After completion, the reaction mixture was concentrated under high vacuum using rotary evaporation to remove excess vinylene carbonate, yielding the cyclic

carbonate intermediate as a dark brown solid (1.73 g, 92.8% yield). The product was used in subsequent reactions without further purification.

^{1}H NMR (400 MHz, $CDCl_3$) δ 7.64 (s, 1H), 7.54 – 7.41 (m, 1H), 7.34 – 7.23 (m, 2H), 7.16 (dd, *J* = 9.2, 4.0 Hz, 2H), 7.03 (dd, *J* = 7.7, 2.9 Hz, 1H), 4.83 – 4.70 (m, 2H), 4.56 (d, *J* = 9.4 Hz, 2H).

HRMS-EI: Calculated (*m*/*z*): 391.99, measured (*m*/*z*): 389.96

Synthesis of 2-iodo-9,10-dihydro-9,10-ethanoanthracene-11,12-diol (i)

The synthesis procedure was adapted from the previously published literature.[19] Solid potassium hydroxide (0.985 g, 17.6 mmol, 5.1 equiv.), deionized water (16.4 mL), and absolute ethanol (1.75 mL) were added to the dark brown cyclic carbonate intermediate (h) (1.72 g, 4.39 mmol, 1 equiv.). The mixture was stirred at 75 °C for 3 hours, and the reaction progress was monitored by thin-layer chromatography (100% CH_2Cl_2, R = 0.30). After completion, the ethanol and approximately half of the water were removed by rotary evaporation under reduced pressure. Additional deionized water (33 mL) was then added, and the mixture was stirred at room temperature for 1 hour, resulting in the formation of a light tan solid. The solid was collected by vacuum filtration, washed with deionized water, and then with ethyl acetate on the filter. The ethyl acetate washings were concentrated by rotary evaporation, leaving a yellow solid residue. The crude product was purified by column chromatography (CH_2Cl_2/ethyl acetate 8:1, Rf = 0.30 and 0.15), affording a mixture of two diol isomers as a white–yellowish solid (1.189 g, 3.25 mmol, 74.0% yield).

^{1}H NMR (400 MHz, $CDCl_3$) δ 7.65 (d, *J* = 1.7 Hz, 1H), 7.48 (dd, *J* = 7.8, 1.7 Hz, 1H), 7.23 (dd, *J* = 5.3, 3.3 Hz, 2H), 7.12 – 7.03 (m, 3H), 4.30 (dd, *J* = 7.3, 2.6 Hz, 2H), 4.07 – 3.96 (m, 2H).

Synthesis of 2-iodoanthracene-9,10-dicarbaldehyde (j)

The synthesis procedure was adapted from the previously published literature.[19] The diol intermediate (i) (0.159 g, 0.43 mmol, 1 equiv.) was dissolved in anhydrous acetonitrile (10 mL) and heated to reflux with stirring, forming a transparent light tan solution. Lead tetraacetate (0.380 g, 0.86 mmol, 2 equiv.) was added portionwise over 5 minutes, during which the solution quickly turned opaque and brown. The mixture was stirred at reflux for 4 hours,

resulting in the formation of a dark orange precipitate within the brown solution. The progress of the reaction was monitored by thin-layer chromatography (CH_2Cl_2/ethyl acetate 8:2, R = 0.50 and 0.33). Upon completion, the reaction mixture was concentrated by rotary evaporation, yielding a burgundy residue. The residue was suspended in 10% aqueous sodium carbonate (30 mL), and the organic components were extracted with dichloromethane. The opaque yellow organic layer was dried over anhydrous sodium sulfate, filtered, and concentrated to afford a yellow–orange solid. Purification by column chromatography (ethyl acetate/hexane 2:8, R = 0.3) gave 2-iodo-9,10-anthracenedialdehyde (A-I-CHO) as an orange solid (0.414 g, 1.15 mmol, 36.0% yield).

^{1}H NMR (400 MHz, $CDCl_3$) δ 11.35 (s, 1H), 11.33 (s, 1H), 9.13 (d, *J* = 1.7 Hz, 1H), 8.62 (ddt, *J* = 10.8, 7.1, 3.3 Hz, 2H), 8.39 (d, *J* = 9.4 Hz, 1H), 7.82 (dd, *J* = 9.4, 1.7 Hz, 1H), 7.68 – 7.62 (m, 2H).

^{13}C NMR (101 MHz, $CDCl_3$) δ 192.68, 192.52, 135.82, 132.31, 131.10, 129.88, 129.80, 129.47, 129.19, 127.90, 127.67, 127.35, 124.55, 123.13, 123.09, 95.10.

HRMS-EI: Calculated (*m*/*z*): 359.96, measured (*m*/*z*): 360.02

4.6.3. Syntheses of COFs

Synthesis of W-A-H COF

N,N,N',N'-Tetrakis(4-aminophenyl)-1,4-phenylenediamine (W-NH_2) (9.22 mg, 19.52 μmol, 1.0 eq.) and anthracene-9,10-dicarbaldehyde (A-H-CHO) (9.14 mg, 39.05 μmol, 2.0 eq.) were combined in a reaction tube. Chlorobenzene (400 μL), benzyl alcohol (400 μL), and 6 M acetic acid (100 μL) were added subsequently. The tube was sealed and the reaction mixture was heated at 100 °C for 3 days. After cooling to room temperature, the resulting dark red precipitate was collected by suction filtration, subjected to Soxhlet extraction with dry THF, and dried under reduced pressure.

Synthesis of W-A-Cl COF

W-NH_2 (9.22 mg, 19.52 μmol, 1.0 eq.) and A-Cl-CHO (10.47 mg, 39.05 μmol, 2.0 eq.) were combined in a reaction tube. Chloroform (400 μL), benzyl alcohol (400 μL), and 6 M acetic acid (100 μL) were added subsequently. The tube was sealed and the reaction mixture was

heated at 100 °C for 3 days. After cooling to room temperature, the resulting dark red precipitate was collected by suction filtration, subjected to Soxhlet extraction with dry THF, and dried under reduced pressure.

Synthesis of W-A-Br COF

W-NH_2 (9.22 mg, 19.52 μmol, 1.0 eq.) and A-Br-CHO (12.18 mg, 39.05 μmol, 2.0 eq.) were combined in a reaction tube. Chlorobenzene (400 μL), benzyl alcohol (4.00 μL), and 6 M acetic acid (100 μL) were added subsequently. The tube was sealed and the reaction mixture was heated at 100 °C for 3 days. After cooling to room temperature, the resulting dark red precipitate was collected by suction filtration, subjected to Soxhlet extraction with dry THF, and dried under reduced pressure.

Synthesis of W-A-I COF

W-NH_2 (9.22 mg, 19.52 μmol, 1.0 eq.) and A-Br-CHO (14.40 mg, 39.05 μmol, 2.0 eq.) were combined in a reaction tube. Chloroform (400 μL), benzyl alcohol (4.00 μL), and 6 M acetic acid (100 μL) were added subsequently. The tube was sealed and the reaction mixture was heated at 100 °C for 3 days. After cooling to room temperature, the resulting dark red precipitate was collected by suction filtration, subjected to Soxhlet extraction with dry THF, and dried under reduced pressure.

4.6.4. BET surface areas

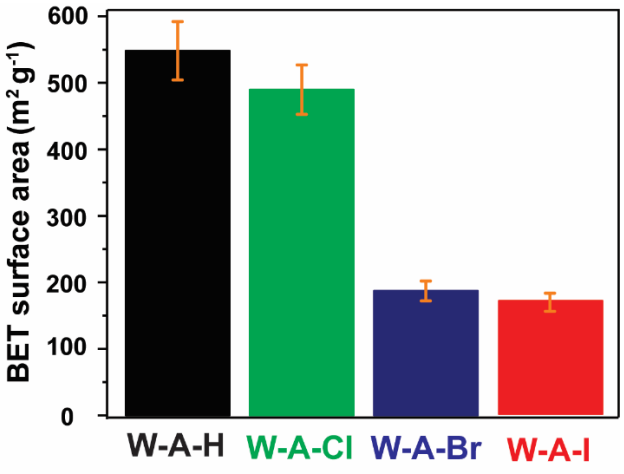

Figure 4.4. BET surface areas of W-A-H, W-A-Cl, W-A-Br and W-A-I (error bars highlighted in orange).

4.6.5. Isosteric heat calculations

The isosteric heat for W-A-X COFs was determined as follows. First, it was necessary to identify data points at three different temperatures where the same CO_2 uptake was observed at corresponding pressures. The equilibrium pressure values of the adsorbed gas at various temperatures were extrapolated from experimental sorption isotherms for a fixed adsorption capacity, ranging from 10 to 100 $cm^3\ g^{-1}$ (0.70 to 1.56 mmol g^{-1}) in increments of 5 $cm^3\ g^{-1}$ (0.22 mmol g^{-1}). Since the isosteric heat is most accurately determined from the lower pressure range, five extrapolated equilibrium pressure values for each COF were selected for the calculations. The natural logarithm of these extrapolated pressure values (lnP) was plotted against the reciprocal of temperature (T^{-1}). The slope of the resulting straight-line equation (**Figure 4.5**) was then used to calculate the isosteric heat of adsorption (Q_{st}) using Clausius-Clapeyron equation:[21]

q_{st}= slope × R

where R is the universal gas constant (8.314 J mol^{-1} K^{-1}).

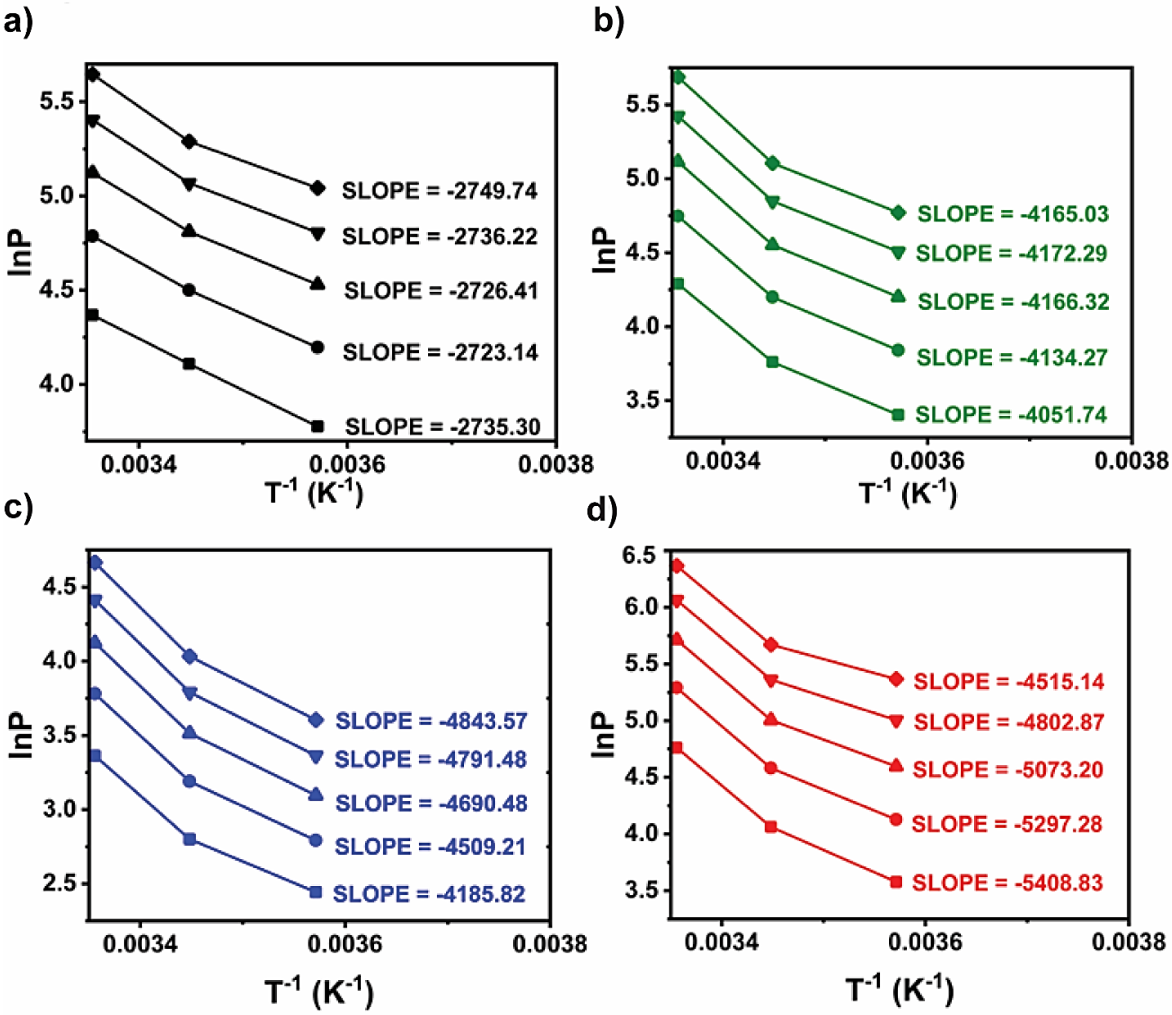

Figure 4.5. Calculated slope values for the linear expression of lnP versus T^{-1} at CO_2 uptake levels of (■) 15 cm^3 g^{-1}, (●) 20 cm^3 g^{-1}, (▲) 25 cm^3 g^{-1}, (▼) 30 cm^3 g^{-1}, and (◆) 35 cm^3 g^{-1} for (a) W-A-H, (b) W-A-Cl, (c) W-A-Br, (d) W-A-I.

4.6.6. ESP of 2-X-anthracene (X = H, Cl, Br, I)

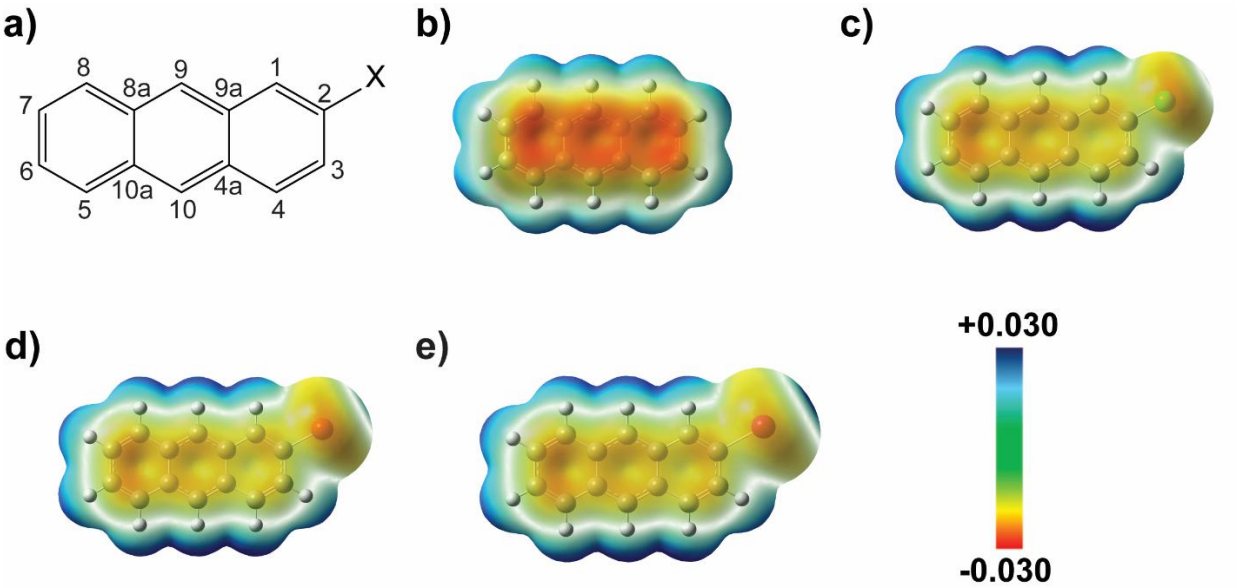

Figure 4.6. (a) Chemical structure of anthracene and 2-X-anthracene (X = H, Cl, Br, I). Electrostatic Potential (ESP) maps superimposed on the M06-2X/def2-SVPP optimized geometry of: (b) anthracene (A-H), (c) 2-chloroanthracene (A-Cl), (d) 2-bromoanthracene (A-Br), (e) 2-iodoanthracene (A-I). ESP values in atomic units (a.u.) are mapped onto the total electron density surface with an isovalue of 0.001 highlighting electron-rich (red) and electron-deficient (blue) regions.

Table 4.1. Comparative charge analysis of gas-phase optimized A-X (X = H, Cl, Br, I) at the M06-2X/def2-SVPP level of theory. The columns display atomic partial charges at different positions based on different methods.

	M06-2X/def2-SVPP								
A-H	**C-1**	**C-2**	**C-3**	**C-4**	**C-9a**	**1-H**	**2-H**	**3-H**	**4-H**
Mulliken	-0.120	-0.089	-0.089	-0.119	0.100	0.086	0.097	0.097	0.086
APT	-0.011	-0.048	-0.048	-0.011	-0.022	0.034	0.036	0.036	0.034
NBO	-0.189	-0.220	-0.220	-0.189	-0.067	0.222	0.224	0.224	0.222
Hirshfeld	-0.038	-0.041	-0.041	-0.038	-0.006	0.041	0.042	0.042	0.041
CHELPG	-0.200	-0.076	-0.076	-0.200	0.206	0.112	0.092	0.092	0.112
MK	-0.215	-0.118	-0.118	-0.215	0.173	0.135	0.127	0.127	0.135
ADCH	-0.118	-0.122	-0.122	-0.118	-0.016	0.123	0.127	0.127	0.123
A-Cl	**C-1**	**C-2**	**C-3**	**C-4**	**C-9a**	**1-H**	**2-Cl**	**3-H**	**4-H**
Mulliken	-0.146	0.084	-0.081	-0.124	0.101	0.089	-0.100	0.099	0.094
APT	-0.143	0.474	-0.142	0.043	0.031	0.059	-0.394	0.066	0.037
NBO	-0.206	-0.032	-0.232	-0.173	-0.058	0.239	-0.014	0.240	0.228

Hirshfeld	-0.046	0.024	-0.045	-0.030	-0.003	0.047	-0.058	0.047	0.046
CHELPG	-0.187	0.095	-0.067	-0.214	0.126	0.123	-0.129	0.102	0.127
MK	-0.192	0.064	-0.110	-0.222	0.135	0.140	-0.103	0.133	0.151
ADCH	-0.122	0.009	-0.129	-0.102	-0.007	0.128	-0.055	0.132	0.130
A-Br	**C-1**	**C-2**	**C-3**	**C-4**	**C-9a**	**1-H**	**2-Br**	**3-H**	**4-H**
Mulliken	-0.142	0.000	-0.083	-0.119	0.102	0.094	-0.039	0.104	0.094
APT	-0.146	0.408	-0.166	0.041	0.026	0.060	-0.298	0.069	0.034
NBO	-0.200	-0.126	-0.229	-0.173	-0.058	0.239	0.065	0.241	0.228
Hirshfeld	-0.043	0.000	-0.045	-0.030	-0.003	0.046	-0.039	0.045	0.046
CHELPG	-0.171	0.065	-0.060	-0.202	0.143	0.097	-0.087	0.078	0.131
MK	-0.097	-0.063	-0.023	-0.261	0.106	0.117	-0.075	0.110	0.156
ADCH	-0.116	-0.021	-0.126	-0.098	-0.004	0.125	-0.041	0.129	0.131
A-I	**C-1**	**C-2**	**C-3**	**C-4**	**C-9a**	**1-H**	**2-I**	**3-H**	**4-H**
Mulliken	-0.133	-0.123	-0.085	-0.115	0.104	0.098	0.064	0.108	0.094
APT	-0.161	0.343	-0.200	0.038	0.020	0.057	-0.161	0.066	0.027
NBO	-0.199	-0.214	-0.230	-0.173	-0.059	0.238	0.155	0.239	0.228
Hirshfeld	-0.041	-0.013	-0.044	-0.030	-0.003	0.044	-0.027	0.043	0.046
CHELPG	-0.125	0.008	-0.029	-0.206	0.135	0.073	-0.045	0.057	0.129
MK	-0.010	-0.179	0.053	-0.302	0.068	0.093	-0.037	0.089	0.161
ADCH	-0.112	-0.049	-0.125	-0.098	-0.003	0.122	-0.016	0.126	0.130

4.6.7. Representative conformers for W-A-X-CO_2 complexes

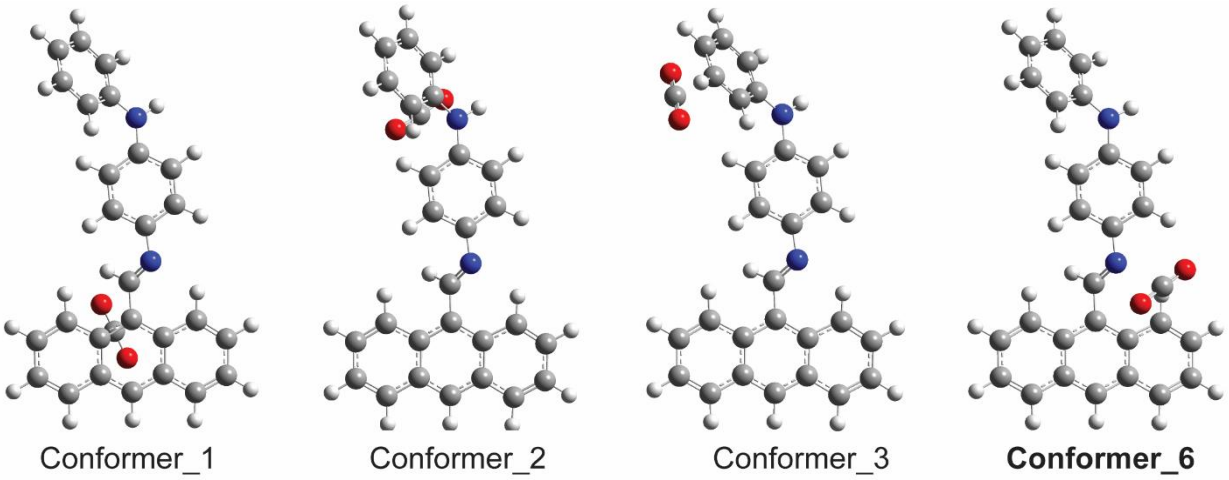

Figure 4.7. M06-2X/def2-SVPP optimized geometries of representative conformers for the W-A-H-CO_2 complex with the optimum marked bold.

Table 4.2. Conformers of gas phase optimized W-A-H-CO2 at the M06-2X/def2-SVPP level of theory followed by single point calculation at the M06-2X/def2 TZVPP level of theory. The columns display total energy (E_{Tot}), thermal correction to enthalpy (δH), Gibbs free (δG), and total energy calculated at the M06-2X/def2-TZVPP level of theory ($E_{Tot,TZ}$), along with their corrected enthalpy (H_{298}), and Gibbs free energy (G_{298}). ΔE, ΔH_{298}, and ΔG_{298} representing the respective energy difference to the lowest structure. Only conformers within the 24 kJ/mol (6 kcal/mol) energy window above the lowest in CREST are included in initial conformer sampling. Duplicates of the same structure are excluded. The overall optimum is marked bold.

	M06-2X/def2-SVPP			M06-2X/def2-TZVPP[a]					
W-A-H-CO_2	**E_{Tot}**	**δH**	**δG**	**$E_{Tot,TZ}$**	**H_{298}**	**G_{298}**	**ΔE**	**ΔH_{298}**	**ΔG_{298}**
No.	(Hartree)	(Hartree)	(Hartree)	(Hartree)	(Hartree)	(Hartree)	(kJ/mol)	(kJ/mol)	(kJ/mol)
conformer_1	-1337.441059	0.438734	0.349306	-1338.964323	-1338.525589	-1338.615017	8.9	8.9	6.1
conformer_2	-1337.441759	0.438867	0.349973	-1338.965166	-1338.526299	-1338.615193	6.6	7.1	5.6
conformer_3	-1337.440616	0.438663	0.347478	-1338.964047	-1338.525384	-1338.616569	9.6	9.5	2.0
conformer_4	-1337.443940	0.438980	0.350899	-1338.966243	-1338.527263	-1338.615344	3.8	4.5	5.2
conformer_5	-1337.434682	0.438785	0.342490	-1338.959489	-1338.520704	-1338.616999	21.6	21.7	0.9
conformer_6	**-1337.444625**	**0.438710**	**0.351089**	**-1338.967696**	**-1338.528986**	**-1338.616607**	**0**	**0**	**1.9**

conformer_7	-1337.434599	0.438815	0.342071	-1338.959411	-1338.520596	-1338.617340	21.8	22.0	0
[a]: Single-point calculation in the gas phase.									

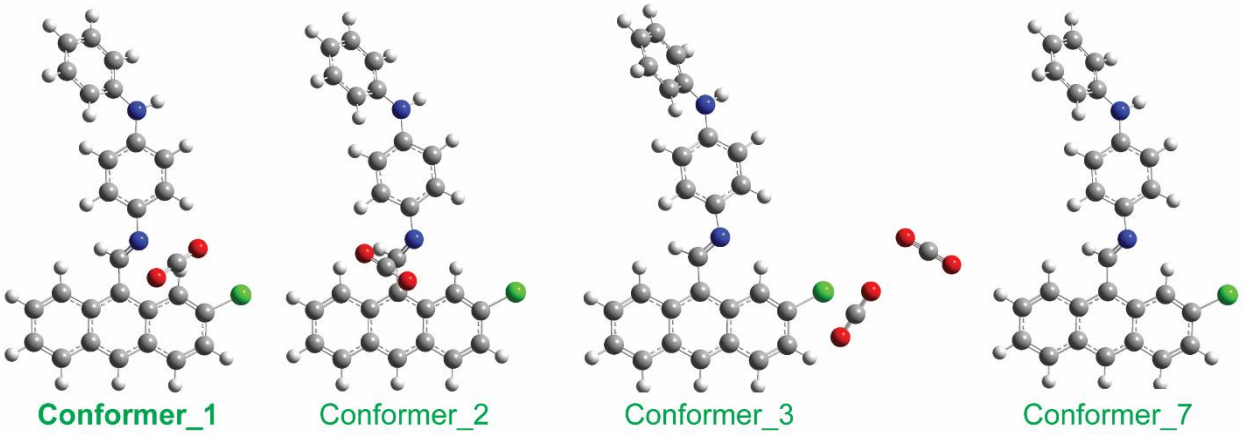

Figure 4.8. M06-2X/def2-SVPP optimized geometries of representative conformers for the W-A-Cl-CO_2 complex with the optimum marked bold.

Table 4.3. Conformers of gas-phase optimized W-A-Cl-CO_2 at the M06-2X/def2-SVPP level of theory followed by single-point calculation at the M06-2X/def2-TZVPP level of theory. The columns display total energy (E_{Tot}), thermal correction to enthalpy (δH), Gibbs free energy (δG), and total energy calculated at the M06-2X/def2-TZVPP level of theory ($E_{Tot,TZ}$), along with their corrected enthalpy (H_{298}), and Gibbs free energy (G_{298}). ΔE, ΔH_{298}, and ΔG_{298} representing the respective energy difference to the lowest structure. Only conformers within the 24 kJ/mol (6 kcal/mol) energy window above the lowest in CREST are included in initial conformer sampling. Duplicates of the same structure are excluded. The overall optimum is marked bold.

	M06-2X/def2-SVPP			**M06-2X/def2-TZVPP[a]**					
W-A-Cl-CO_2	**E_{Tot}**	**δH**	**δG**	**$E_{Tot,TZ}$**	**H_{298}**	**G_{298}**	**ΔE**	**ΔH_{298}**	**ΔG_{298}**
No.	(Hartree)	(Hartree)	(Hartree)	(Hartree)	(Hartree)	(Hartree)	(kJ/mol)	(kJ/mol)	(kJ/mol)
conformer_1	**-1796.894722**	**0.430258**	**0.339349**	**-1798.571835**	**-1798.141577**	**-1798.232486**	**0**	**0**	**2.8**
conformer_2	-1796.892788	0.430210	0.337129	-1798.570267	-1798.140057	-1798.233138	4.1	4.0	1.0
conformer_3	-1796.888849	0.430299	0.335444	-1798.566442	-1798.136143	-1798.230998	14.2	14.3	6.7
conformer_4	-1796.889035	0.430341	0.335726	-1798.566528	-1798.136187	-1798.230802	13.9	14.2	7.2
conformer_6	-1796.885191	0.430349	0.331057	-1798.563992	-1798.133643	-1798.232935	20.6	20.8	1.6
conforme	-	0.430368	0.330467	-	-	-	20.6	20.9	0

r_7	1796.885224			1798.564001	1798.133633	1798.233534			
conformer_9	-1796.890345	0.430259	0.337393	-1798.568176	-1798.137917	-1798.230783	9.6	9.6	7.2
conformer_10	-1796.890676	0.430435	0.337226	-1798.567305	-1798.136870	-1798.230079	11.9	12.4	9.1
conformer_11	-1796.893134	0.430516	0.338571	-1798.570123	-1798.139607	-1798.231552	4.5	5.2	5.2
conformer_12	-1796.890478	0.430360	0.337961	-1798.567892	-1798.137532	-1798.229931	10.4	10.6	9.5
conformer_13	-1796.890007	0.430289	0.336582	-1798.568012	-1798.137723	-1798.231430	10.0	10.1	5.5
conformer_14	-1796.891141	0.430218	0.337231	-1798.568434	-1798.138216	-1798.231203	8.9	8.8	6.1
conformer_16	-1796.889674	0.430223	0.337087	-1798.567761	-1798.137538	-1798.230674	10.7	10.6	7.5
conformer_17	-1796.889712	0.430239	0.337176	-1798.567871	-1798.137632	-1798.230695	10.4	10.4	7.5
conformer_18	-1796.891089	0.430169	0.337204	-1798.568743	-1798.138574	-1798.231539	8.1	7.9	5.2

[a]: Single-point calculation in the gas phase.

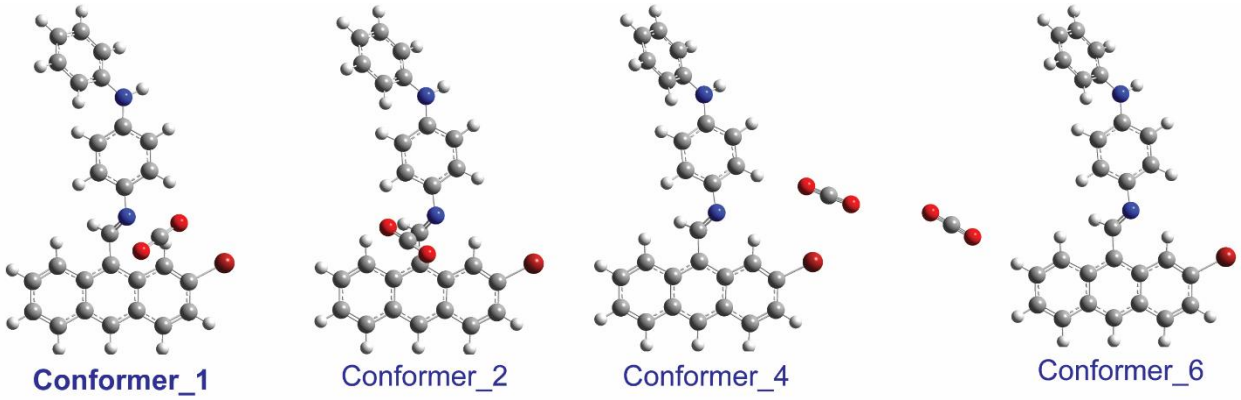

Figure 4.9. M06-2X/def2-SVPP optimized geometries of representative conformers for the W-A-Br-CO_2 complex with the optimum marked bold.

Table 4.4. Conformers of gas-phase optimized W-A-Br-CO_2 at the M06-2X/def2-SVPP level of theory followed by single-point calculation at the M06-2X/def2-TZVPP level of theory. The columns display total energy (E_{Tot}), thermal correction to enthalpy (δH), Gibbs free energy (δG), and total energy calculated at the M06-2X/def2-TZVPP level of theory ($E_{Tot,TZ}$), along with their corrected enthalpy (H_{298}), and Gibbs free energy (G_{298}). ΔE, ΔH_{298}, and ΔG_{298} representing the respective energy difference to the lowest structure. Only conformers within the 24 kJ/mol (6 kcal/mol) energy window above the lowest in CREST are included in initial

conformer sampling. Duplicates of the same structure are excluded. The overall optimum is marked bold.

	M06-2X/def2-SVPP			M06-2X/def2-TZVPP[a]					
W-A-Br-CO_2	**E_{Tot}**	**δH**	**δG**	**$E_{Tot,TZ}$**	**H_{298}**	**G_{298}**	**ΔE**	**ΔH_{298}**	**ΔG_{298}**
No.	(Hartree)	(Hartree)	(Hartree)	(Hartree)	(Hartree)	(Hartree)	(kJ/mol)	(kJ/mol)	(kJ/mol)
conformer_1	**-3910.737328**	**0.429932**	**0.337830**	**-3912.565097**	**-3912.135165**	**-3912.227267**	**0**	**0**	**2.6**
conformer_2	-3910.735272	0.429846	0.335432	-3912.563490	-3912.133644	-3912.228058	4.2	4.0	0.5
conformer_4	-3910.730811	0.430069	0.334081	-3912.559145	-3912.129076	-3912.225064	15.6	16.0	8.4
conformer_5	-3910.731172	0.429971	0.334209	-3912.559968	-3912.129997	-3912.225759	13.5	13.6	6.6
conformer_6	-3910.727747	0.430026	0.328975	-3912.557238	-3912.127212	-3912.228263	20.6	20.9	0
conformer_7	-3910.727726	0.430032	0.329727	-3912.557229	-3912.127197	-3912.227502	20.7	20.9	2.0
conformer_8	-3910.737223	0.430037	0.337516	-3912.564966	-3912.134929	-3912.227450	0.3	0.6	2.1

[a]: Single-point calculation in the gas phase.

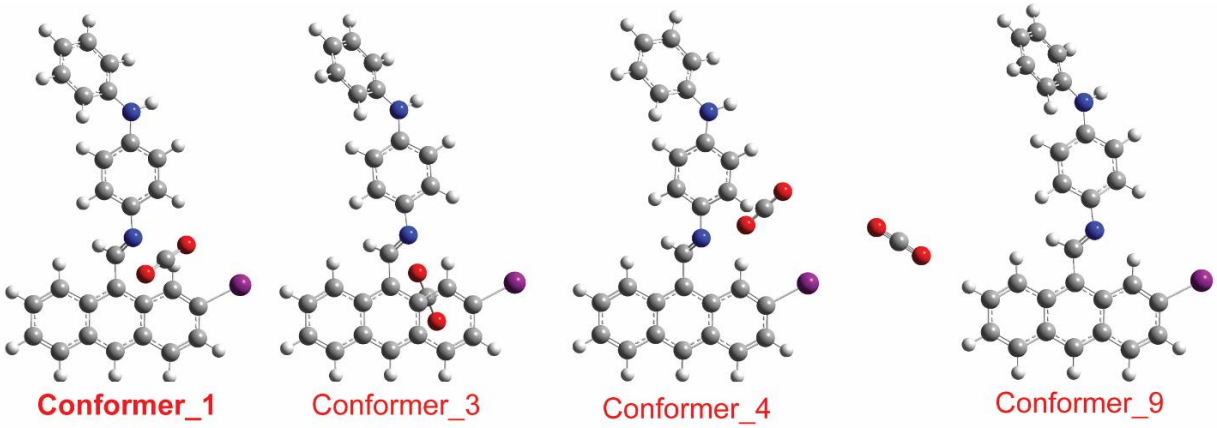

Figure 4.10. M06-2X/def2-SVPP optimized geometries of representative conformers for the W-A-I-CO_2 complex with the optimum marked bold.

Table 4.5. Conformers of gas-phase optimized W-A-I-CO_2 at the M06-2X/def2-SVPP level of theory followed by single-point calculation at the M06-2X/def2-TZVPP level of theory. The columns display total energy (E_{Tot}), thermal correction to enthalpy (δH), Gibbs free energy (δG), and total energy calculated at the M06-2X/def2-TZVPP level of theory ($E_{Tot,TZ}$), along

with their corrected enthalpy (H_{298}), and Gibbs free energy (G_{298}). ΔE, ΔH_{298}, and ΔG_{298} representing the respective energy difference to the lowest structure. Only conformers within the 24 kJ/mol (6 kcal/mol) energy window above the lowest in CREST are included in initial conformer sampling. Duplicates of the same structure are excluded. The overall optimum is marked bold.

	M06-2X/def2-SVPP			**M06-2X/def2-TZVPP[a]**					
W-A-I-CO_2	**E_{Tot}**	**δH**	**δG**	**$E_{Tot,TZ}$**	**H_{298}**	**G_{298}**	**ΔE**	**ΔH_{298}**	**ΔG_{298}**
No.	(Hartree)	(Hartree)	(Hartree)	(Hartree)	(Hartree)	(Hartree)	(kJ/mol)	(kJ/mol)	(kJ/mol)
conformer_1	**-1634.471138**	**0.429694**	**0.336661**	**-1635.999798**	**-1635.570104**	**-1635.663137**	**0**	**0**	**3.3**
conformer_3	-1634.467423	0.429645	0.334811	-1635.996617	-1635.566972	-1635.661806	8.4	8.2	6.8
conformer_4	-1634.466387	0.429506	0.333271	-1635.996071	-1635.566565	-1635.662800	9.8	9.3	4.2
conformer_5	-1634.464341	0.429750	0.332905	-1635.994516	-1635.564766	-1635.661611	13.9	14.0	7.3
conformer_6	-1634.462312	0.429682	0.329466	-1635.992532	-1635.562850	-1635.663066	19.1	19.1	3.5
conformer_8	-1634.461442	0.429774	0.328064	-1635.991779	-1635.562005	-1635.663715	21.1	21.3	1.8
conformer_9	-1634.461474	0.429817	0.327403	-1635.991812	-1635.561995	-1635.664409	21.0	21.3	0
conformer_10	-1634.466234	0.429661	0.334563	-1635.995632	-1635.565971	-1635.661069	10.9	10.9	8.8
conformer_12	-1634.465897	0.429675	0.334278	-1635.995558	-1635.565883	-1635.661280	11.1	11.1	8.2
conformer_13	-1634.465941	0.429669	0.334458	-1635.995670	-1635.566001	-1635.661212	10.8	10.8	8.4
conformer_14	-1634.467661	0.429723	0.334863	-1635.996474	-1635.566751	-1635.661611	8.7	8.8	7.3
conformer_15	-1634.466294	0.429661	0.334664	-1635.995723	-1635.566062	-1635.661059	10.7	10.6	8.8
conformer_16	-1634.468006	0.429771	0.334410	-1635.996669	-1635.566898	-1635.662259	8.2	8.4	5.6
conformer_17	-1634.467218	0.429615	0.334074	-1635.996290	-1635.566675	-1635.662216	9.2	9.0	5.8
conformer_18	-1634.465904	0.429683	0.333950	-1635.995587	-1635.565904	-1635.661637	11.1	11.0	7.3
conformer_19	-1634.467300	0.429650	0.333727	-1635.996311	-1635.566661	-1635.662584	9.2	9.0	4.8

[a]: Single-point calculation in the gas phase.

Table 4.6. Comparative energetic properties of gas-phase optimized reactants at the M06-2X/def2-SVPP level of theory. The columns display total energy (E_{Tot}), thermal correction to enthalpy (δH), and Gibbs free energy (δG), along with their corrected enthalpy (H_{298}), and Gibbs free energy (G_{298}). ΔE_{Ads}, ΔH_{Ads}, and ΔG_{Ads} represent the respective energies for the gas adsorption.

	M06-2X/def2-SVPP			**M06-2X/def2-TZVPP[a]**					
	E_{Tot}	**δH**	**δG**	**$E_{Tot,TZ}$**	**H_{298}**	**G_{298}**			
Reactant	(Hartree)	(Hartree)	(Hartree)	(Hartree)	(Hartree)	(Hartree)			
CO_2	-188.370469	0.015688	-0.008550	-188.596927	-188.581239	-188.605477			
W-A-H	-1149.062382	0.421619	0.344177	-1150.362009	-1149.940390	-1150.017832			
W-A-Cl-(c1)	-1608.512810	0.413107	0.332115	-1609.966470	-1609.553363	-1609.634355			
W-A-Cl-(c2)	-1608.512329	0.413142	0.332539	-1609.966016	-1609.552874	-1609.633477			
W-A-Br-(c1)	-3722.355331	0.412806	0.330852	-3723.959708	-3723.546902	-3723.628856			
W-A-Br-(c2)	-3722.354747	0.412806	0.330839	-3723.959252	-3723.546446	-3723.628413			
W-A-I-(c1)	-1446.089051	0.412554	0.329312	-1447.394276	-1446.981722	-1447.064964			
W-A-I-(c2)	-1446.088424	0.412567	0.329156	-1447.393851	-1446.981284	-1447.064695			
	E_{Tot}	**δH**	**δG**	**$E_{Tot,TZ}$**	**H_{298}**	**G_{298}**	**ΔE_{Ads}**	**ΔH_{Ads}**	**ΔG_{Ads}**
Product	(Hartree)	(Hartree)	(Hartree)	(Hartree)	(Hartree)	(Hartree)	(kJ/mol)	(kJ/mol)	(kJ/mol)
W-A-H-CO_2	-1337.444625	0.438710	0.351089	-1338.967696	-1338.528986	-1338.616607	-23.0	-19.3	17.6
W-A-Cl-(c1)-CO_2	-1796.894722	0.430258	0.339349	-1798.571835	-1798.141577	-1798.232486	-22.2	-18.3	19.3
W-A-Cl-(c2)-CO_2	-1796.894523	0.430241	0.339177	-1798.571656	-1798.141415	-1798.232479	-22.9	-19.2	17.0
W-A-Br-(c1)-CO_2	-3910.737328	0.429932	0.337830	-3912.565097	-3912.135165	-3912.227267	-22.2	-18.4	18.6
W-A-Br-(c2)-CO_2	-3910.736955	0.429945	0.337684	-3912.564852	-3912.134907	-3912.227168	-22.8	-19.0	17.6
W-A-I-(c1)-CO_2	-1634.471138	0.429694	0.336661	-1635.999798	-1635.570104	-1635.663137	-22.6	-18.8	19.2
W-A-I-(c2)-CO_2	-1634.470659	0.429658	0.336541	-1635.999429	-1635.569771	-1635.662888	-22.7	-19.0	19.1

[a]: Single-point calculation in the gas phase.

4.6.8. Proton affinity studies for the imine bonds in adsorption units of W-A-X

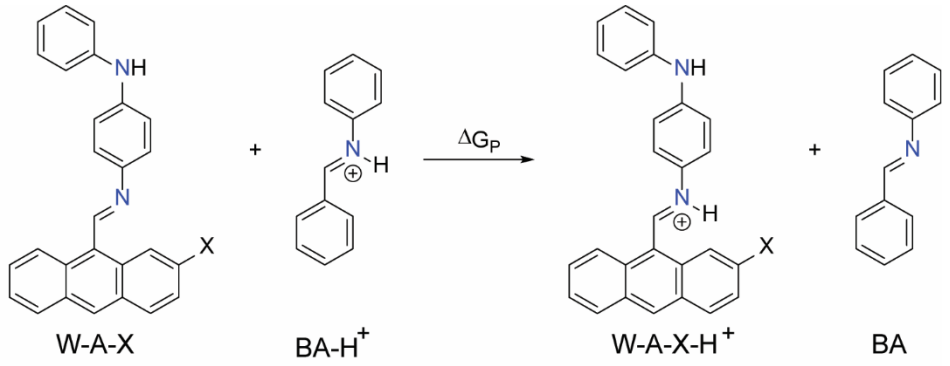

Scheme 4.2. Model reaction used to evaluate the local basicity of the imine bond in the adsorption unit of W-A-X (X = H, Cl, Br, I). A proton is transferred from protonated N-benzylideneaniline ($BA\text{-}H^+$) to WA to form $W\text{-}A\text{-}X\text{-}H^+$ and BA.

Local proton affinity calculations

Local proton affinity is reflected in the reaction free energy ΔG_P (eq. (4.1)).

$$\Delta G_P = \sum G^{Product} - \sum G^{Reactant} \qquad (4.1)$$

The enthalpy and Gibbs free energy at standard state in the gas phase, H_{298} and G_{298}, were obtained as the sum of $E_{Tot,TZ}$ and the thermal correction to enthalpy δH (eq. (2)) or Gibbs free energy δG (eq. (4.3)).

$$H_{298} = E_{Tot,TZ} + \delta H \qquad (4.2)$$

$$G_{298} = E_{Tot,TZ} + \delta G \qquad (4.3)$$

Table 4.7. Comparative energetic properties of gas-phase optimized reactants and products at the M06-2X/def2-SVPP level of theory followed by single-point calculation at the M06-2X/def2-TZVPP level of theory. The columns display total energy (E_{Tot}), thermal correction to enthalpy (δH), Gibbs free energy (δG), and total energy calculated at the M06-2X/def2-TZVPP level of theory ($E_{Tot,TZ}$), along with their corrected enthalpy (H_{298}), and Gibbs free energy (G_{298}). ΔE_P, ΔH_P, and ΔG_P represent the respective energies changes for the reaction.

	M06-2X/def2-SVPP			M06-2X/def2-TZVPP[a]					
	E_{Tot}	δH	δG	$E_{Tot,TZ}$	H_{298}	G_{298}			
Reactants	(Hartree)	(Hartree)	(Hartree)	(Hartree)	(Hartree)	(Hartree)			
$BA\text{-}H^+$	-556.445236	0.230961	0.180141	-557.086947	-556.855986	-556.906806			

W-A-H	-1149.062382	0.421619	0.344177	-1150.362009	-1149.940390	-1150.017832			
W-A-Cl	-1608.512810	0.413107	0.332115	-1609.966470	-1609.553363	-1609.634355			
W-A-Br	-3722.355331	0.412806	0.330852	-3723.959708	-3723.546902	-3723.628856			
W-A-I	-1446.089051	0.412554	0.329312	-1447.394276	-1446.981722	-1447.064964			
	E_{Tot}	**δH**	**δG**	**$E_{Tot,TZ}$**	**H_{298}**	**G_{298}**	**ΔE_P**	**ΔH_P**	**ΔG_P**
Products	(Hartree)	(Hartree)	(Hartree)	(Hartree)	(Hartree)	(Hartree)	(kJ/mol)	(kJ/mol)	(kJ/mol)
BA	-556.076579	0.217090	0.167279	-556.713155	-556.496065	-556.545876	0	0	0
W-A-H-H^+	-1149.451701	0.435651	0.358364	-1150.756030	-1150.320379	-1150.397666	-53.1	-52.7	-49.6
W-A-Cl-H^+	-1608.898989	0.427125	0.346560	-1610.357356	-1609.930231	-1610.010796	-44.9	-44.5	-40.7
W-A-Br-H^+	-3722.741157	0.426771	0.344811	-3724.350325	-3723.923554	-3724.005514	-44.2	-43.9	-41.3
W-A-I-H^+	-1446.475115	0.426525	0.343560	-1447.785323	-1447.358798	-1447.441763	-45.3	-45.0	-41.7
[a]: Single-point calculation in the gas phase.									

4.6.9. ESP of adsorption units of W-A-X

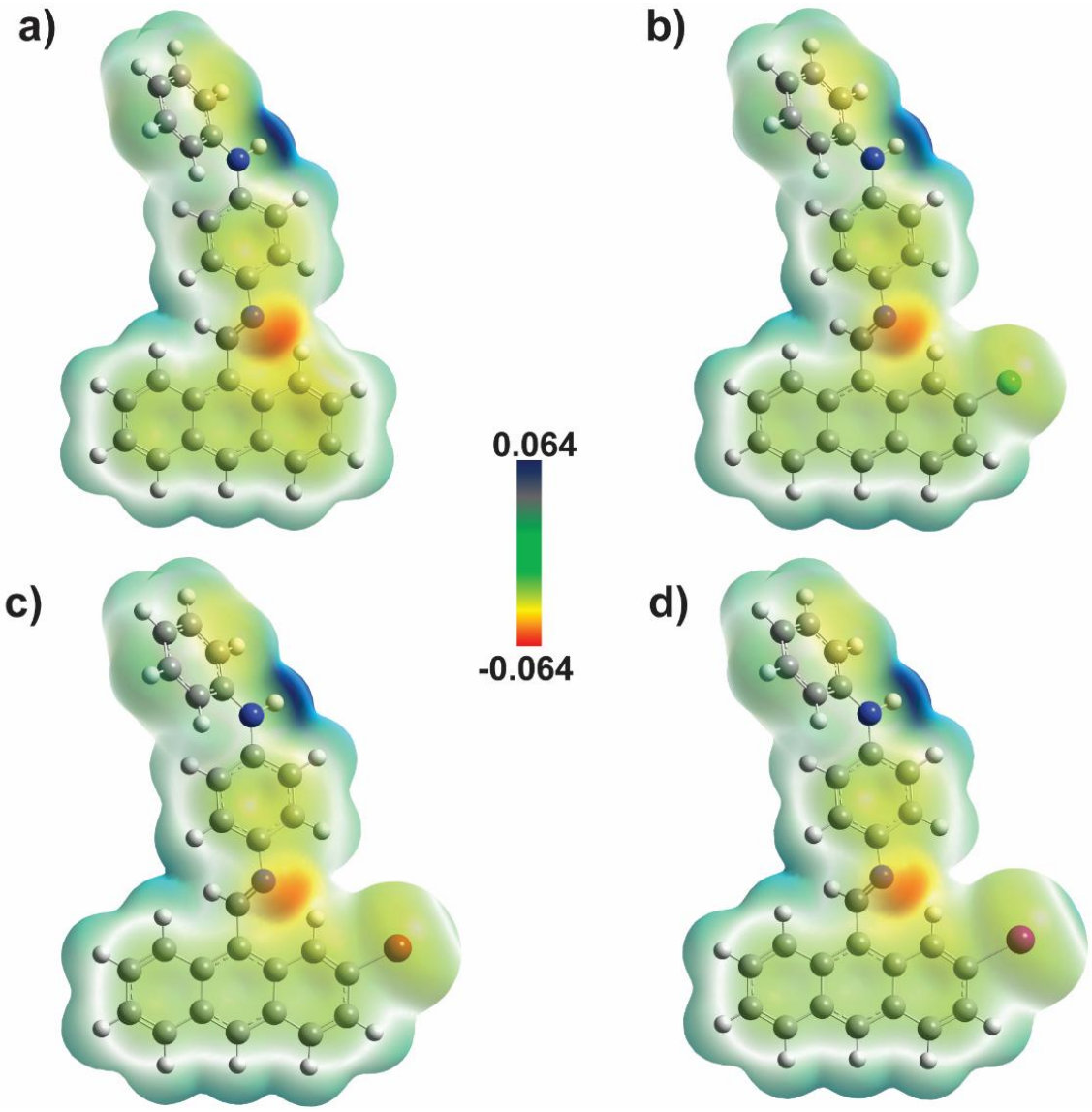

Figure 4.11. ESP maps superimposed on the M06-2X/def2-SVPP optimized geometries of the adsorption unit of (a) W-A-H, (b) W-A-Cl, (c) W-A-Br, (d) W-A-I. The ESP values in atomic units (a.u.) are mapped onto the total electron density surface with an isovalue of 0.001 highlighting electron-rich (red) and electron-deficient (blue) regions.

4.6.10. Visualization of iso-surface, non-covalent interactions and atom-wise contributions for adsorption units of W-A-X

Figure 4.12. Qualitative color scale of visualized non-covalent interactions in IGMH analysis.

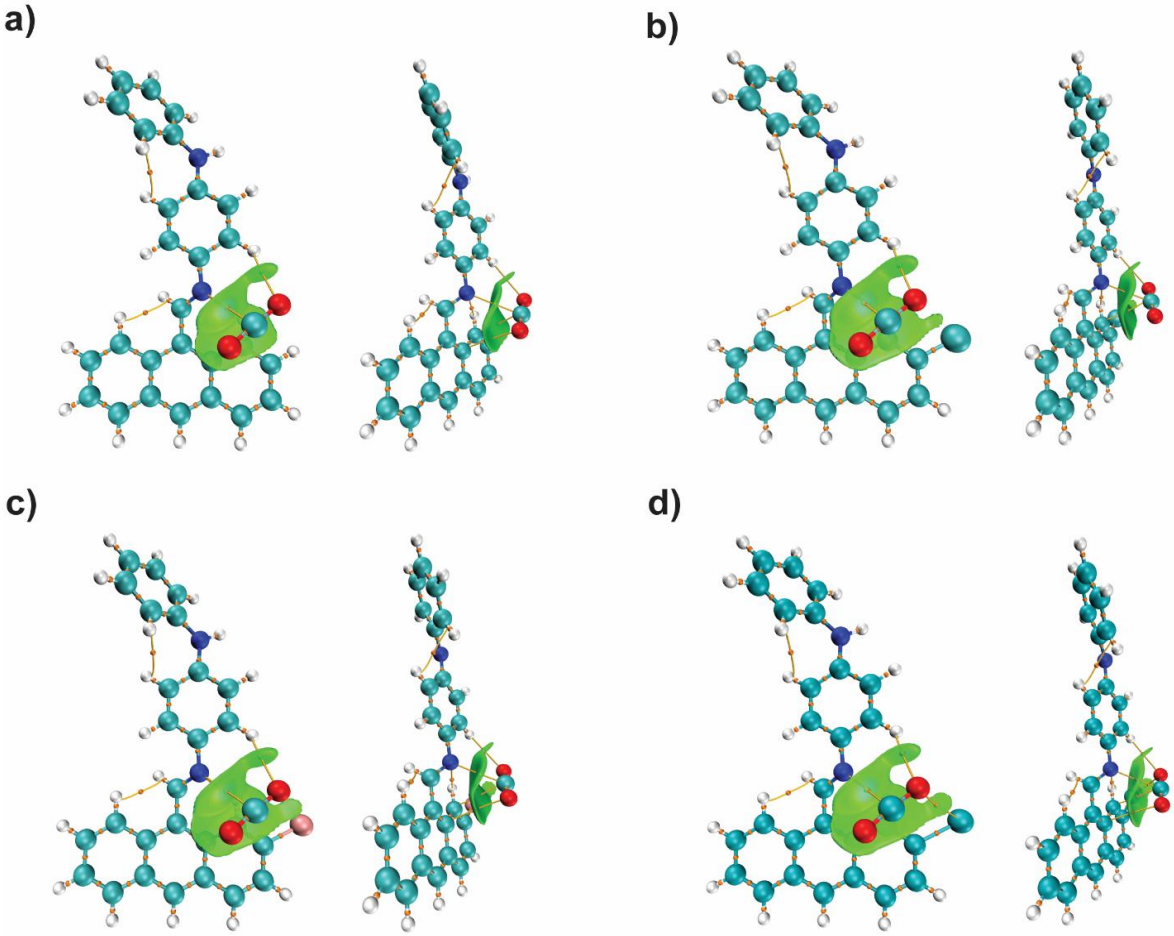

Figure 4.13. Sign(λ_2)ρ colored IGMH δg^{inter} = 0.004 a.u. for representing physical adsorption of benzene. The coloring method of CO_2 on W-A-X adsorption unit: (a) W-A-H, (b) W-A-Cl, (c) W-A-Br and (d) W-A-I. Bond critical points (orange spheres) and bond paths (brown lines) corresponding to bonding interaction are also shown.

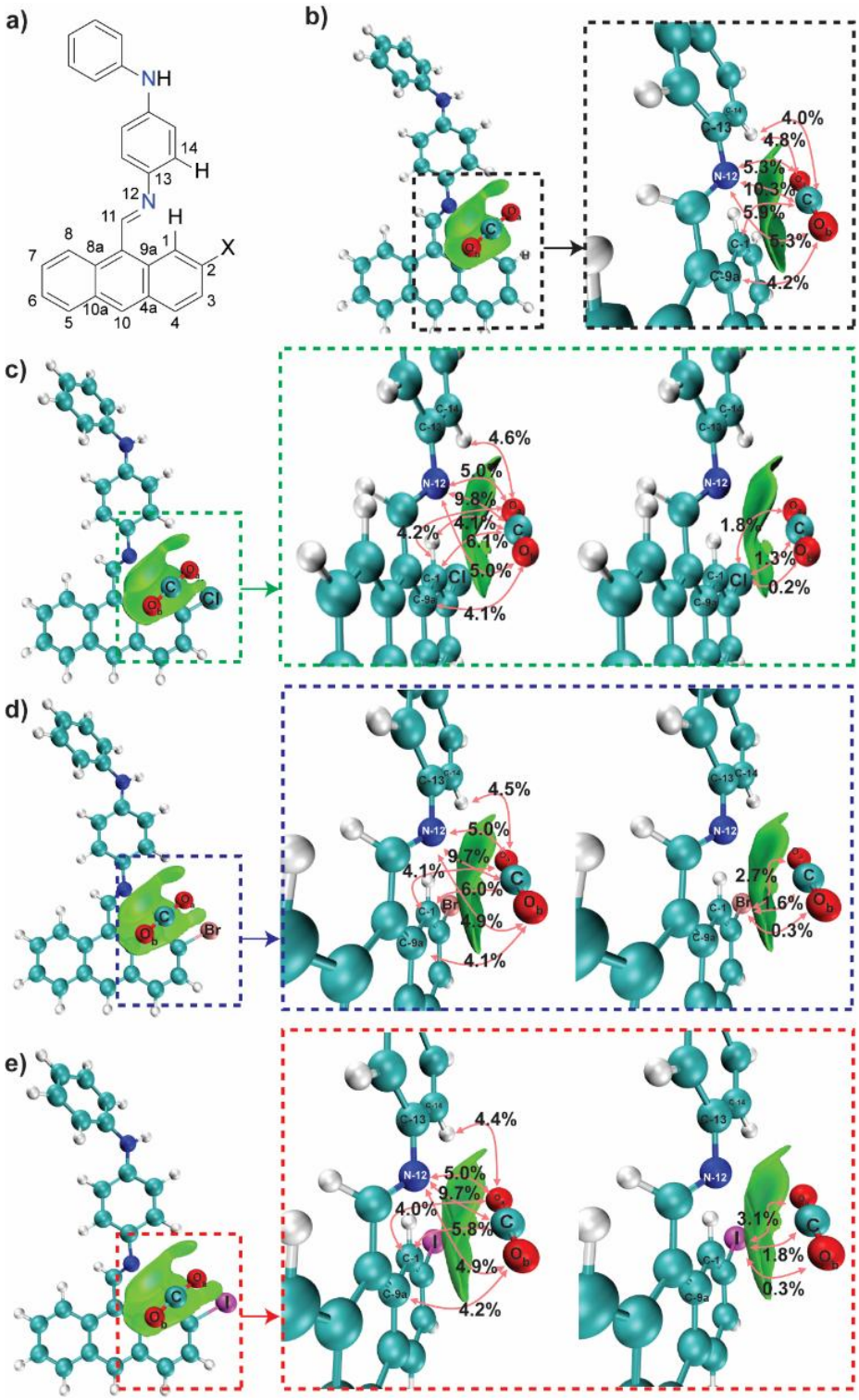

Figure 4.14. (a) W-A-X Adsorption-Unit. Visualization of iso-surface, non-covalent interactions and atom-wise contribution for Adsorption-Units of (b) W-A-H, (c)W-A-Cl, (d) W-A-Br and (e) W-A-I.

4.6.11. Comparative energetic properties of the triangle unit of W-A-X and CO_2 in different adsorption sites

Table 4.8. Comparative energetic properties of gas-phase optimized reactants at the M06-2X/def2-SVPP level of theory at the scale of kagome cell structure. The columns display total energy (E_{Tot}), thermal correction to enthalpy (δH), and Gibbs free energy (δG), along with their corrected enthalpy (H_{298}), and Gibbs free energy (G_{298}). ΔE_{Ads}, ΔH_{Ads}, and ΔG_{Ads} represent the respective energies for the gas adsorption.

	M06-2X/def2-SVPP										
	E_{Tot}	δH	δG	H_{298}	G_{298}						
Reactant	(Hartree)	(Hartree)	(Hartree)	(Hartree)	(Hartree)						
CO_2	-188.370469	0.015688	-0.008550	-188.370469	-188.354781						
W-A-H	-5966.530258	2.102449	1.801024	-5966.530258	-5964.427809						
W-A-Cl	-7344.880511	2.077012	1.764906	-7344.880511	-7342.803499						
W-A-Br	-13686.408083	2.076099	1.761308	-13686.408083	-13684.331984						
W-A-I	-6857.609341	2.075272	1.757366	-6857.609341	-6855.534069						
	E_{Tot}	δH	δG	H_{298}	G_{298}	ΔE_{Ads}	ΔH_{Ads}	ΔG_{Ads}	$\Delta\Delta E_{Ads}$	$\Delta\Delta H_{Ads}$	$\Delta\Delta G_{Ads}$
Product	(Hartree)	(Hartree)	(Hartree)	(Hartree)	(Hartree)	(kJ/mol)	(kJ/mol)	(kJ/mol)	(kJ/mol)	(kJ/mol)	(kJ/mol)
W-A-H-Imine-CO_2	-6154.912348	2.119481	1.806870	-6152.792867	-6153.105478	-30.5	-27.0	7.3			
W-A-H-Triangle-CO_2	-6154.906207	2.119548	1.803869	-6152.786659	-6153.102338	-14.4	-10.7	15.5	16.1	16.3	8.2
W-A-Cl-Imine-CO_2	-7533.262330	2.094197	1.772162	-7531.168133	-7531.490168	-29.8	-25.9	11.7			
W-A-Cl-Triangle-CO_2	-7533.257053	2.094180	1.769795	-7531.162873	-7531.487258	-15.9	-12.1	19.3	13.9	13.8	7.6
W-A-Br-Imine-CO_2	-13874.789952	2.093232	1.767478	-13872.696720	-13873.022474	-29.9	-26.1	8.7			
W-A-Br-Triangle-CO_2	-13874.785218	2.093308	1.765928	-13872.691910	-13873.019290	-17.5	-13.5	17.1	12.4	12.6	8.4
W-A-I-Imine-CO_2	-7045.991332	2.092505	1.764380	-7043.898827	-7044.226952	-30.3	-26.2	10.6			
W-A-I-Triangle-CO_2	-7045.987572	2.092579	1.763839	-7043.894993	-7044.223733	-20.4	-16.1	19.1	9.9	10.1	8.5

4.6.12. References

[1] G. Kupgan, T. P. Liyana-Arachchi, C. M. Colina, *Langmuir* **2017**, *33*, 11138–11145.

[2] P. Pracht, F. Bohle, S. Grimme, *Phys. Chem. Chem. Phys.* **2020**, *22*, 7169–7192.

[3] S. Grimme, *J. Chem. Theory Comput.* **2019**, *15*, 2847–2862.

[4] D. J. Frisch, Michael J., Trucks, George W., Schlegel, H. Bernhard, Scuseria, Gustavo E., Robb, Michael A., Cheeseman, John R., Scalmani, Giovanni, Barone, Vincenzo, Petersson, George A., Nakatsuji, Hiroshi, Li, Xiaosong, Caricato, Marco, Marenich, Aleksandr, B, **2016**.

[5] Y. Zhao, D. G. Truhlar, *Theor. Chem. Acc.* **2008**, *120*, 215–241.

[6] F. Weigend, R. Ahlrichs, *Phys. Chem. Chem. Phys.* **2005**, *7*, 3297.

[7] J. Zhang, T. Lu, *Phys. Chem. Chem. Phys.* **2021**, *23*, 20323–20328.

[8] T. Lu, *J. Chem. Phys.* **2024**, *161*, 082503.

[9] T. Lu, F. Chen, *J. Comput. Chem.* **2012**, *33*, 580–592.

[10] W. Humphrey, A. Dalke, K. Schulten, *J. Mol. Graph.* **1996**, *14*, 33–38.

[11] R. S. Mulliken, *J. Chem. Phys.* **1955**, *23*, 1833–1840.

[12] J. Cioslowski, *J. Am. Chem. Soc.* **1989**, *111*, 8333–8336.

[13] A. E. Reed, R. B. Weinstock, F. Weinhold, *J. Chem. Phys.* **1985**, *83*, 735–746.

[14] F. L. Hirshfeld, *Theor. Chim. Acta* **1977**, *44*, 129–138.

[15] C. M. Breneman, K. B. Wiberg, *J. Comput. Chem.* **1990**, *11*, 361–373.

[16] B. H. Besler, K. M. Merz, P. A. Kollman, *J. Comput. Chem.* **1990**, *11*, 431–439.

[17] T. Lu, F. Chen, *J. Theor. Comput. Chem.* **2012**, *11*, 163–183.

[18] L. Tian, C. Fei-Wu, *Acta Physico-Chimica Sin.* **2012**, *28*, 1–18.

[19] Otto Phanstiel, *Fluorescent Cytotoxic Compounds Specific for the Cellular Polyamine Transport System*, **2013**.

[20] K. I. Yamashita, M. Tsuboi, M. S. Asano, K. I. Sugiura, *Synth. Commun.* **2012**, *42*, 170–175.

[21] A. Nuhnen, C. Janiak, *Dalt. Trans.* **2020**, *49*, 10295–10307.

5. Post-synthetic modification of BDT-ETTA-COF: Linkage conversion

This chapter is based on the following article:

Surface Charge Modulation in Covalent Organic Frameworks for Controlled Pt-Photodeposition and Enhanced Photocatalytic Hydrogen Evolution

Published in "Small". **2025**, *21*, 2500870

Klaudija Paliušytė, Lucas Leão Nascimento, Hannah Illner, Max Wiedmaier, Roman Guntermann, Markus Döblinger, Thomas Bein, Antonio Otavio T. Patrocinio*, and Jenny Schneider*

Department of Chemistry and Center for NanoScience, Ludwig-Maximilians-Universität (LMU) München, Butenandtstraße 5-13, 81377, Munich, Germany, E-mail: jenny.schneider@lmu.de

Laboratory of Photochemistry and Materials Science (LAFOT-CM), Institute of Chemistry Federal University of Uberlandia (UFU) Av. João Naves de Ávila, 2121 38400-902 Uberlandia, Brazil, E-mail: otaviopatrocinio@ufu.br

Centro de Excelência em Hidrogênio e Tecnologias Energéticas Sustentáveis – CEHTES, Parque Tecnológico Samambaia, 74690-631, Goiânia, GO, Brazil

* Corresponding authors

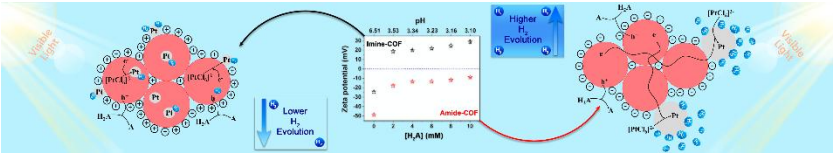

5.1. Abstract

Covalent organic frameworks (COFs) represent a new class of organic photocatalysts for the hydrogen evolution reaction (HER). While the influence of COF structural and optoelectronic properties on HER is well-studied, the role of surface charge in optimizing interfacial

interactions with reactants remains underexplored. In this study, we demonstrate that converting imine to amide linkages in a thiophene-based COF allows for altering surface charge through different protonation behaviour of the linkages. Zeta potential measurements reveal that the amide-linked COF, due to its lower basicity, is deprotonated and negatively charged in the presence of ascorbic acid, while the imine-linked COF is protonated and positively charged. This electrostatic contrast drives the photoreduction of $[PtCl_6]^{2-}$ to Pt, with the imine-linked COF yielding uniformly distributed small Pt particles (1–2 nm), whereas the amide-linked COF forms larger Pt particles (up to 100 nm). The amide-linked COF, acting as an antenna that facilitates interdomain electron transport along COF agglomerates, promotes both Pt growth and subsequent proton reduction demonstrating 300 % increase in photocatalytic HER rate compared to its imine form. This work introduces surface charge modulation as a novel tool for controlling photocatalytic processes in COF-based systems expanding the COF functionality in photocatalysis.

5.2. Introduction

Covalent Organic Frameworks (COFs) have garnered significant attention as promising photocatalysts for H_2 evolution, owing to their crystalline porous structure, high chemical stability, and virtually limitless tunability in terms of both structure and optoelectronic properties.[1] In 2014, B. Lotsch et al. reported the first water-stable hydrazine-based COF for the hydrogen evolution reaction (HER), achieving a reaction rate of 1979.0 μmol g^{-1} h^{-1}.[2] Subsequent studies have focused on the molecular engineering of COFs to enhance their photocatalytic H_2 evolution efficiency by optimizing light-harvesting capabilities, charge carrier separation, thermodynamic driving force, water dispersibility, and photostability.[3–13]

Linkage chemistry has proven to be an effective tool for tuning the physicochemical properties of COFs relevant to photocatalysis. X. Liu et al. demonstrated that fully π-conjugated sp^2 carbon linkages not only broaden the visible-light absorption of COFs but also enhance charge transfer and separation efficiency, compared to imine linkages.[14] Recently, Thomas et al. showed that protonation of a series of imine-linked donor-acceptor COFs enhances photocatalytic H_2 evolution performance, which was attributed to improved light absorption, charge carrier separation efficiency, and hydrophilicity of the COFs upon protonation.[15] In a further study, X. Pan and co-workers investigated the effect of linkage isomerism on

photocatalytic hydrogen evolution.[16] While the influence of linkages on optoelectronic properties has been widely explored, leveraging COF linkage chemistry to modulate interfacial chemical and electrostatic interactions between COFs and reactants for improved photocatalytic H_2 evolution has yet to be reported.

Typical reactants in the photocatalytic H_2 evolution reaction include charged precursors for co-catalyst deposition, such as a H_2PtCl_6, and sacrificial electron donors, which often also serve as proton sources.[17,18] Tuning the surface charge to promote the preferential adsorption of specific compounds at the photocatalyst surface, thereby controlling the photocatalytic reaction mechanism, is a well-established strategy in traditional inorganic photocatalysis.[19] This method relies on modulating the electrostatic interactions between the adsorbate and the adsorbent, either by altering the chemical environment or by tailoring the surface charge of the photocatalyst. However, systematic studies on this approach applied to COFs remain rare.

The present study explores and demonstrates the effect of different protonation behaviors of imine-and amide-linked COFs in acidic conditions on the COF's surface charge and photocatalytic HER. The imine-linked COF was synthesized from benzo[1,2- b:4,5-b′]-dithiophene-2,6-dicarboxaldehyde (BDT) and 4-fold amine functionalized tetraphenylethylene (1,1′,2,2′-tetra-paminophenylethylene) (ETTA) building blocks under solvothermal conditions.[20] A post-modification method was applied to induce imine-to-amide linkage conversion.[21] This approach resulted in a crystalline Amide-BDT-ETTA COF, which demonstrated a 300 % increase in photocatalytic HER rate compared to its imine form. Zeta potential measurements of the suspensions of the COFs in the presence of ascorbic acid serving as an electron donor reveal a switch from positive to negative surface charge of the COF upon imine-to-amide linkage conversion. The influence of the surface charge on the mechanism of the in situ Pt-photodeposition and subsequent proton reduction will be discussed among the observed changes in hydrophilicity, and optoelectronic properties.

5.3. Results and discussion

5.3.1. Structural and morphological characterization

Imine-BDT-ETTA COF was synthesized according to the previously reported procedure using an acceptor-type ETTA building block and a donor-type BDT linker.[20] The obtained Imine-

BDT-ETTA was subsequently post-modified to convert imine to amide linkages using Pinick oxidation reaction[22] where sodium chlorite is used as an oxidizing agent, 2-methyl-2-butene as a free radical scavenger, and acetic acid as a buffer during the oxidation process (

Figure **5.1** a). The powder X-ray diffraction (PXRD) pattern shown in

Figure **5.1** b for Imine-BDT-ETTA COF and in Figure 1c for Amide-BDT-ETTA confirm successful synthesis and post-modification of the COF revealing high crystallinity through the presence of a pronounced and sharp 100 reflection along with well-defined higher-order reflections. The structures of Imine-BDT-ETTA and Amide-BDT-ETTA were simulated using force-field methods[23] comprising a dual-pore Kagome structure in symmetry (Space Group No. 168) (see Figures 5.4 and 5.5, Tables 5.1 and 5.2, Appendix B) with the unit cell parameters being a = b = 4.64 nm, c = 0.446 nm (Rwp = 4.6%, Rp = 3.7%) and a = b = 4.78 nm, c = 0.448 nm (Rwp = 5.7%, Rp = 3.8%), respectively. The increase of a, b, and c parameters for amide-linked COF in in attributed to the bond length change resulting from the conversion of the C = N double bond (0.129 nm from structural simulations) to the C-N single bond (0.135 nm from structural simulations). For comparison, the structure of Amide-BDT-ETTA was also simulated assuming 50% conversion (see Table 5.3, Appendix B). The simulated and experimental PXRD patterns were consistent (Rwp = 7.8%, Rp = 5.2%), demonstrating that regardless of conversion degree to amide bonds, there are no significant changes in the structure of the COF.

Nitrogen physisorption isotherms were used to monitor the changes in porosity of the COF after the linkage conversion. Like the imine counterpart (**Figure 5.10**, Appendix B), Amide-BDT-ETTA exhibits a sorption isotherm of type IV with two steep nitrogen uptake steps (Figure 5.6 b, Appendix B). The Brunauer--Emmett--Teller (BET) surface area of Amide-BDT-ETTA decreased to 688 $m^2 g^{-1}$ in comparison to Imine-BDT-ETTA being 1679 $m^2 g^{-1}$. Previous studies have reported a decrease in the surface area as a result of post-synthetic modification.[21,24,25] However, the linkage conversion of the Imine-BDT-ETTA did not induce substantial changes in the pore sizes. Using the equilibrium QSDFT method with carbon kernel for cylindrical pores, pore sizes for Imine-BDT-ETTA were calculated to be 1.79 nm and 3.68 nm (versus 1.72 nm and 3.58 nm based on structural simulations (**Figure 5.8**, Appendix B)

aligning well with previous reports.[26] Pore sizes for Amide-BDT-ETTA were found to be 1.79 nm and 3.55 nm (1.72 nm and 3.58 nm from structural simulations **Figure 5.9**, Appendix B).

The morphological characteristics of both COFs were further investigated via scanning electron microscopy (SEM) (**Figure 5.11**, Appendix B). SEM images suggest that Imine-BDT-ETTA features a spherical morphology constructed from particles organized in a rose-shaped agglomerates. Notably, Amide-BDT-ETTA shows a more mixed morphology, featuring rod-like agglomerates alongside remaining rose-shaped particles. The chemical conversion of the imine-COF involves a series of processes, including ultrasonication, treatment with different solvents (dioxane, 2-methyl-2-butene), utilization of the inorganic oxidant $NaClO_2$, and exposure to glacial acetic acid which serves as a buffer. To identify the origin of the morphological changes, the following control experiments were conducted: Reference-COF-1 was obtained in the absence of $NaClO_2$, Reference-COF-2 with a fivefold reduction in $NaClO_2$ concentration, and Reference-COF-3 in the absence of acetic acid, while keeping other ingredients consistent with the original conversion procedure (see Appendix B). All three reference samples retained crystallinity after all treatment steps, respectively (**Figure 5.12**, Appendix B). As expected, Fourier transform infrared (FT-IR) analysis reveals that for the linkage conversion, the oxidant is required (**Figure 5.12**, Appendix B). The rod-shaped particles were observed in all three reference samples (**Figure 5.13**, Appendix B), thus indicating that the formation of such structures is not related to the amidization process itself but rather the result of the ultrasonication and the treatment with organic solvents. ^{13}C cross-polarization magic angle spinning (CPMAS) analysis allowed us to determine the local chemical changes of the COF after linkage conversion (

Figure 5.1 d). In the ^{13}C NMR spectrum of Amide-BDT-ETTA, a distinctive peak at 161 ppm appeared, which is not present in the NMR spectrum of Imine-BDT-ETTA prior to the oxidation. This new signal arises from the formation of amide carbonyl C = O moieties.[21] Additionally, a residual signal attributed to C = N bonds at 151 ppm remains detectable in Amide-BDT-ETTA. This observation implies partial oxidation and suggests that the final structural configuration of Amide-BDT-ETTA includes both newly introduced carbonyl C = O functionalities and unreacted imine C = N bonds from its imine precursor COF. We note that harsher conditions, such as prolonged reaction times and increased amount of oxidative agent

to induce a full conversion from imine to amide linkages, resulted in a non-crystalline samples. As demonstrated in previous studies, exposure so to strong oxidizing agents can disrupt the crystalline structure by breaking imine bonds.[27]

FT-IR spectroscopy was applied to further explore the chemical changes induced through linkage conversion (

Figure **5.1** e). Imine-BDT-ETTA exhibits a prominent band at 1611 cm^{-1} corresponding to the stretching vibrations of the C = N functional group.[28,29] Observed vibration peaks in the FT-IR spectra of Imine-BDT-ETTA are in a good agreement with the previously published results.[20,30] The emergence of a new band at 1315 cm^{-1} in the Amide-BDT-ETTA spectrum reveals the formation of the C-N-C moiety, indicative of the amide linkage.[31] Another pronounced band at 1515 cm^{-1} can be attributed to the in-plane N-H bending vibrations of the secondary amide group.[32,33] As previously substantiated by ^{13}C solid-state NMR analysis, the presence of imine bonds is evident in the FT-IR spectrum of Amide-BDT-ETTA as well. Typically, the stretching vibrations of imine and amide bonds are observed in the spectral range of 1600-1690 cm^{-1}.[21,28,29,34–38] However, within the spectral range of Amide-BDT-ETTA, there are multiple overlapping signals, which require more complex analysis. For a deeper analysis of the vibrations associated with the newly formed bonds in the polymeric structure, the FT-IR spectrum of Imine-BDT-ETTA was subtracted from the spectrum of the Amide-BDT-ETTA (**Figure 5.14**, Appendix B). In the resulting FT-IR difference spectrum, the C = O stretching vibration of the amide bond is evident at 1645 cm^{-1}.[21,32,33]

X-ray photoelectron spectroscopy (XPS) analysis was performed to investigate changes in the oxidation states of the elements present in both COFs (**Figure 5.15**, Appendix B). The survey spectra confirm the absence of impurities, with only peaks corresponding to C, S, O, and N atoms detected. High-resolution spectra were acquired for each peak and compared to those of the BDT linker (**Figure 5.16**, Appendix B). Focusing initially on the C 1s spectrum of Imine-BDT-ETTA (**Figure 5.16**, Appendix B), the primary peak observed at 284.6 eV is attributed to carbon atoms integrated within the COF framework. A weaker signal at 289.5 eV is linked to residual, unreacted aldehyde groups present at surface terminations and lattice defects. These

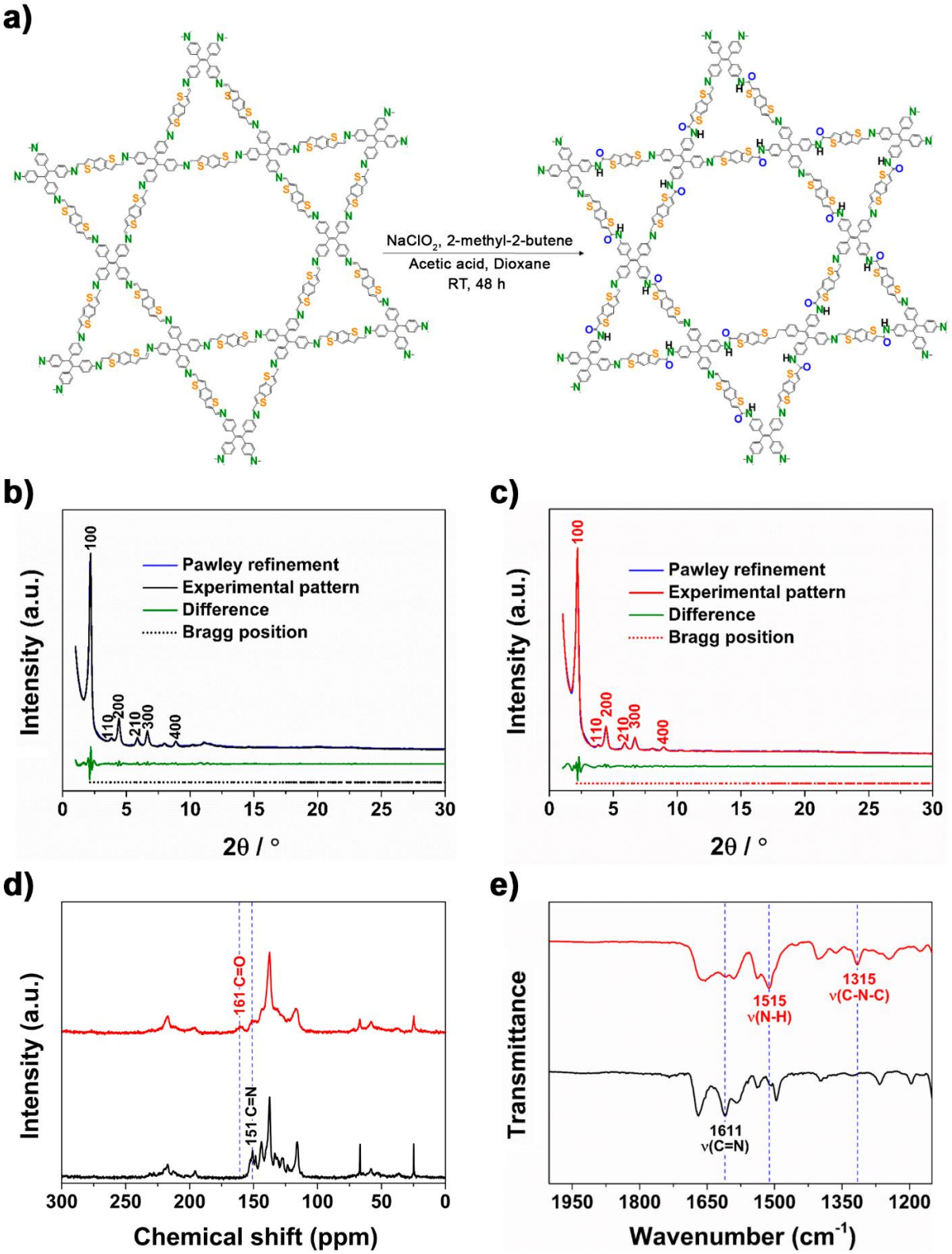

Figure 5.1. (a) Schematic representation of Imine-BDT-ETTA to Amide-BDT-ETTA conversion. Experimental and Pawley refined PXRD patterns of (b) Imine-BDT-ETTA and (c) Amide-BDT-ETTA. (d) 13C NMR spectra and (e) FT-IR spectra of Imine-BDT-ETTA (black) and Amide-BDT-ETTA (red).

groups exhibit a higher binding energy due to the reduced electron density surrounding the carbon atoms.[39,40] In the case of Amide-BDT-ETTA COF, an additional feature appears at 288.1 eV, assigned to the carbonyl (C = O) moiety (**Figure 5.16** b, Appendix B).[41,42]

In the S 2p region, two distinct sulfur environments are observed in both COFs, characterized by S $2p_{3/2}$ binding energy peaks at 164.2 and 169.0 eV (**Figure 5.16** d,e, Appendix B). These peaks correspond to neutral sulfur species (S-S, S-C) and oxidized sulfur species (S = O), respectively.[43–45] Quantitative analysis reveals that Amide-BDT-ETTA contains 20% sulfur in the +VI oxidation state, while Imine-BDT-ETTA has ≈ 15% oxidized sulfur species. Notably, the BDT linker used in the synthesis of Imine-BDT-ETTA COF also exhibits 15% oxidized sulfur species (**Figure 5.16** f, Appendix B). These results indicate that COF amidization does not induce significant sulfur oxidation, thereby establishing that the introduction of the amide functionalities is the dominant factor controlling the changes of in COF properties.

The primary peak in the O 1s spectra of both COFs (Figure 5.12 g,h, Appendix B) is attributed to surface-adsorbed oxygen species.[25] In the Amide-BDT-ETTA COF, this peak appears at 533.6 eV, shifted relative to that of Imine-BDT-ETTA (532.5 eV), indicating differences in surface properties. Additionally, a secondary feature at 531.0 eV is observed for Amide-BDT-ETTA, consistent with previously reported values for C = O bonds formed during the amidization reaction.[46]

In the N 1s region, distinct differences are observed between the two COFs. For Imine-BDT-ETTA COF (Figure 5.12 j, Appendix B), the spectrum can be deconvoluted into two components at 398.7 and 402.8 eV, corresponding to imine groups (- C = N - C-) and unreacted amino groups (-C-NH_2) from the ETTA building block, respectively.[47] The comparison between the N 1s spectra of Imine-BDT-ETTA (Figure 5.12 j, Appendix B) and Amide-BDT-ETTA (Figure 5.12 k, Appendix B) reveals a shift toward higher binding energy after the amidization process (from 398.7 to 399.2 eV, Figure 5.12 l, Appendix B). This shift confirms the efficient conversion, consistent with previously reported binding energy changes associated with imine-to-amide transformation.[25,39]

However, the N 1s peak does not allow for a direct quantification of imine-to-amide conversion yield. Complementary evidence from ^{13}C-NMR and FTIR confirms the presence of residual imine groups in Amide-BDT-ETTA COF. To reliably estimate the conversion yield, we have

taken the ratio between the corresponding area for the peaks attributed to the amide C = O (C1s at 288.1 eV and O1s at 531.0 eV) and the N1s in the survey spectra, which should be ideally 1:1. The calculated C = O/N ratio was 0.9, suggesting an approximate conversion yield of 90%.

5.3.2. Photocatalytic hydrogen evolution

The as-prepared imine and amide COFs were tested for photocatalytic hydrogen evolution. The photocatalytic tests were performed in the presence of 1.0 wt% (Pt/COF) H_2PtCl_6 precursor and ascorbic acid (H_2A) acting as sacrificial electron donor (Equations 5.1-5.4) upon illumination with visible light ($\lambda > 420$ nm, 100 mW cm^{-2}). After excitation of the COFs, photogenerated electrons (e−) and holes (h+) are formed (Equation 5.1). The holes can oxidize H_2A to dehydroascorbic acid, A, either directly by two-electron transfer or by one-electron oxidation via the formation of ascorbyl radical, HA•, as an intermediate • + H+ (Equations 5.2 and Equation 5.3) thus suppressing the undesired recombination. Simultaneously, the photogenerated electrons can reduce 2H+ to H_2 on the surface of in- situ formed Pt particles (Equation 5.4).

$$COF \xrightarrow{h\nu} e^- + h^+ \quad (5.1)$$

$$H_2A + h^+ \rightarrow HA^{\bullet} + H^+ \quad (5.2)$$

$$HA^{\bullet} + h^+ \rightarrow A + H^+ \quad (5.3)$$

$$2H^+ + 2e^- \rightarrow H_2 \quad (5.4)$$

Figure 5.2 a shows the hydrogen evolution obtained with Imine- and Amide-BDT-ETTA COFs in the experiments lasting 13 hours. From the linear increase of H2 production with time, the HER rates for Imine-BDT-ETTA and Amide-BDT-ETTA were quantified to be 0.22 mmol g^{-1} h^{-1} and 0.95 mmol g^{-1} h^{-1}, respectively. These results reveal a pronounced promotion of hydrogen evolution through the linkage conversion. Both COFs were also tested in the absence of light and in the absence of Pt, but no hydrogen evolution was detected. The illumination of the Pt precursor in the presence of ascorbic acid also does not lead to H_2 evolution. Longterm photocatalytic experiments were performed in which hydrogen evolution was monitored over three cycles in total for 39 hours (**Figure 5.2** b). Both COFs were able to continuously sustain an average HER rate of 0.22 mmol g^{-1} h^{-1} for Imine-BDT-ETTA and of 0.95 mmol g^{-1} h^{-1} for Amide-BDT-ETTA. In subsequent three cycles of 3 hours each and in the presence of 2 mM H2A, even higher evolution rates for both COF were detected, with the Amide-COF showing

an average HER rate of 1.7 mmol g^{-1} h^{-1} while Imine-BDT-ETTA delivered 0.40 mmol g^{-1} h^{-1} (**Figure 5.17**, Appendix B).

The HER rate was measured in the presence of various H_2A concentrations using Amide-BDT-ETTA as the photocatalyst to investigate the origin of the increased HER rate observed at lower H_2A concentrations. The increase in H_2A concentration from 2 mM to 6 mM resulted in a gradual increase of HER rate up to 2.6 mmol g^{-1} h^{-1} (**Figure 5.18** a, Appendix B). Further, increase in the H_2A concentration from 8 mM to 10 mM led to a drop in the HER rate. A similar dependence of H_2 evolution on the concentration of the sacrificial electron donor has been already reported and assigned to a Langmuir-type catalytic behavior.[48-50] At low H_2A concentrations, the HER rate is limited by the mass transfer of the H_2A to the Pt/COF surface. At high H_2A concentrations, the coupling of the surface-adsorbed H• radicals on the Pt surface to form H_2 gas might be hindered through competing acid adsorption. It has been reported that H_2A adsorbs at the Pt surface, occupying hydrogen adsorption sites.[51] Moreover, H_2A oxidation is very sensitive to the pH of the reaction media and is favored at higher pH values.[52,53] Photocatalytic tests were also conducted using triethanolamine (TEOA) as a sacrificial electron donor (**Figure 5.18** b, Appendix B). Under these alkaline conditions, Imine-BDT-ETTA exhibited superior performance compared to Amide-BDT-ETTA, with hydrogen evolution rates of 0.63 and 0.39 mmol g^{-1} h^{-1}, respectively. The change in H_2 evolution rates observed when using ascorbic acid H_2A versus TEOA is typically attributed to differences in the suspension pH, which can influence the adsorption and desorption dynamics and equilibria of reactants and products at the photocatalyst surface.[54-56] In addition, the decrease in the H_2 evolution rates for both COFs can be attributed to the higher pH values of the reaction medium (pH = 10.75), thus reducing the availability of protons.[57,58]

5.3.3. Physical characterization

To explore the origin of the enhanced H2 evolution with Amide-BDT-ETTA in comparison to Imine-BDT-ETTA, the optoelectronic features of both COFs were examined using cyclic voltammetry (CV), UV-vis absorption spectroscopy (UV-vis), and photoluminescence spectroscopy (PL). CV measurements allowed us to quantify the energetic positions of the HOMO levels from half wave potentials for both COFs (**Figure 5.19**, Appendix B). Herein, the experiments were conducted using the Fc/Fc+ redox couple as a reference in 0.1 M NBu4PF6

acetonitrile solutions as described elsewhere.[26] The HOMO levels for Imine-BDTETTA and Amide-BDT-ETTA are positioned at -4.94 eV (0.44 V vs SHE) and at -5.31 eV (0.81 V vs SHE), respectively. For a photocatalyst to facilitate photo-oxidation via photogenerated holes, the HOMO or valence band energy must be more positive (higher potential) than the redox potential of the target oxidation reaction. The more positive HOMO potential of Amide-BDT-ETTA compared to its imine counterpart reveals that it is a stronger photooxidizing agent, enhancing its effectiveness in driving photocatalytic oxidation.[59,60]

The optical properties of the COFs were evaluated by UV-vis measurement by applying the Kubelka-Munk function F(R) for solid materials (**Figure 5.2** c). In contrast to Imine-BDT-ETTA, Amide-BDT-ETTA exhibits a strong visible-light absorption in the spectral region above 510 nm. These findings are consistent with prior studies.[61] Assuming direct optical transitions for both polymers, the optical band gap energies were calculated employing Tauc plots, thereby revealing values of 2.25 eV for Imine-BDT-ETTA and 2.20 eV for Amide-BDT-ETTA.[62,63] The stronger optical absorption of the amide-linked COF above 510 nm might originate from the presence of defect states which could reduce the Schottky barrier thus facilitating electron transfer to the Pt and enhancing the proton reduction.[64] A Schottky barrier at the semiconducting polymer/metal interface has been reported to result from the large band offset between the electron affinity of the polymer versus the work function of the metal.[65] Schottky barriers should impede the electron injection into the metal, however, the presence of surface states in the polymer can dramatically reduce the barrier, thus allowing fast electron injection and enhancing the photocatalytic performance.[66,67]

The LUMO energy levels for both COFs were calculated from the HOMO energy levels obtained by the CV measurements and the optical bandgap energies. As evident from Figure 5.2d, the imine to amide linkage conversion has caused a shift in HOMO and LUMO energies to more negative potentials. Xiang et al. reported similar changes upon amidization and attributed the behavior to a more pronounced negative charge accumulation in amide COF as a result of the stronger electron-withdrawing properties of amide linkages.[39] PL spectra of the COFs were recorded by exciting the materials at 375 nm. Imine-BDT-ETTA and Amide-BDTETTA exhibit strong emission bands centered at 617 nm and 608 nm, respectively (**Figure**

5.20, Appendix B). The blueshift for the latter can be explained by the weakened conjugation arising from the oxidation of the imine bonds.[68,69]

Figure 5.2 d shows the band energy levels for both COFs compared to the redox potentials of the studied photocatalytic reactions. **Figure 5.2** d reveals the low thermodynamic driving force for the Imine-BDT-ETTA to induce the one-electron oxidation of H_2A in the pH range of photocatalytic experiments (from 3.10 to 3.53 as shown in **Table 5.4**, Appendix B). On the other hand, Amide-BDT-ETTA can efficiently initiate one and two-electron oxidation of the H_2A, thus enabling more efficient electron accumulation required for the targeted H_2 evolution. Additionally, both COFs are thermodynamically suitable to promote the hydrogen evolution reaction, $2H+ /H_2$ (Equation 5.4). Here, the potential variation of the HOMO and LUMO levels of the COFs as a function of the pH was neglected based on prior studies.[26] Moreover, the difference in the thermodynamic driving force for proton reduction between Imine- and Amide-BDT-ETTA (see **Figure 5.2** d) is less relevant as no H_2 was generated in the absence of Pt. This evidences that the proton reduction proceeds via electron transfer at the metal surface.

5.3.4. Interfacial characterization

Among the thermodynamic driving force for the photocatalytic reaction the interactions at the interface between reactants/products and the photocatalyst is essential. In the photocatalytic hydrogen evolution reaction in aqueous media, the hydrophilic character of the COF might influence the efficiency of the process. Herein, volumetric water sorption experiments were conducted for both COFs. **Figure 5.2** e shows that at lower relative pressures ($P/P_0 < 0.45$) Amide-BDT-ETTA has a greater water vapor sorption in comparison to Imine-BDT-ETTA, thus evincing its higher affinity for adsorbate[70-72] and stronger hydrophilic character. This is most likely arises from the presence of the carbonyl groups of the amide.[73] The total water vapor uptake for Amide-BDT-ETTA was 348 $cm^3\ g^{-1}$ while for Imine-BDT-ETTA a value of 443 $cm^3\ g^{-1}$ was found. For an adequate comparison, the previously determined BET surface area has to be considered (**Figure 5.10**, Appendix B). Accordingly, the water vapor uptake normalized to the BET surface for Amide-BDT-ETTA is higher (0.51 $cm^3\ m^{-2}$) in comparison to Imine-BDTETTA (0.26 $cm^3\ m^{-2}$). Hence, the inherent hydrophilic characteristics and increased polarity arising from the presence of C = O bonds and higher concentration of

oxidized sulfur in Amide-BDT-ETTA contribute to the elevated HER rate and supports the formation of stable

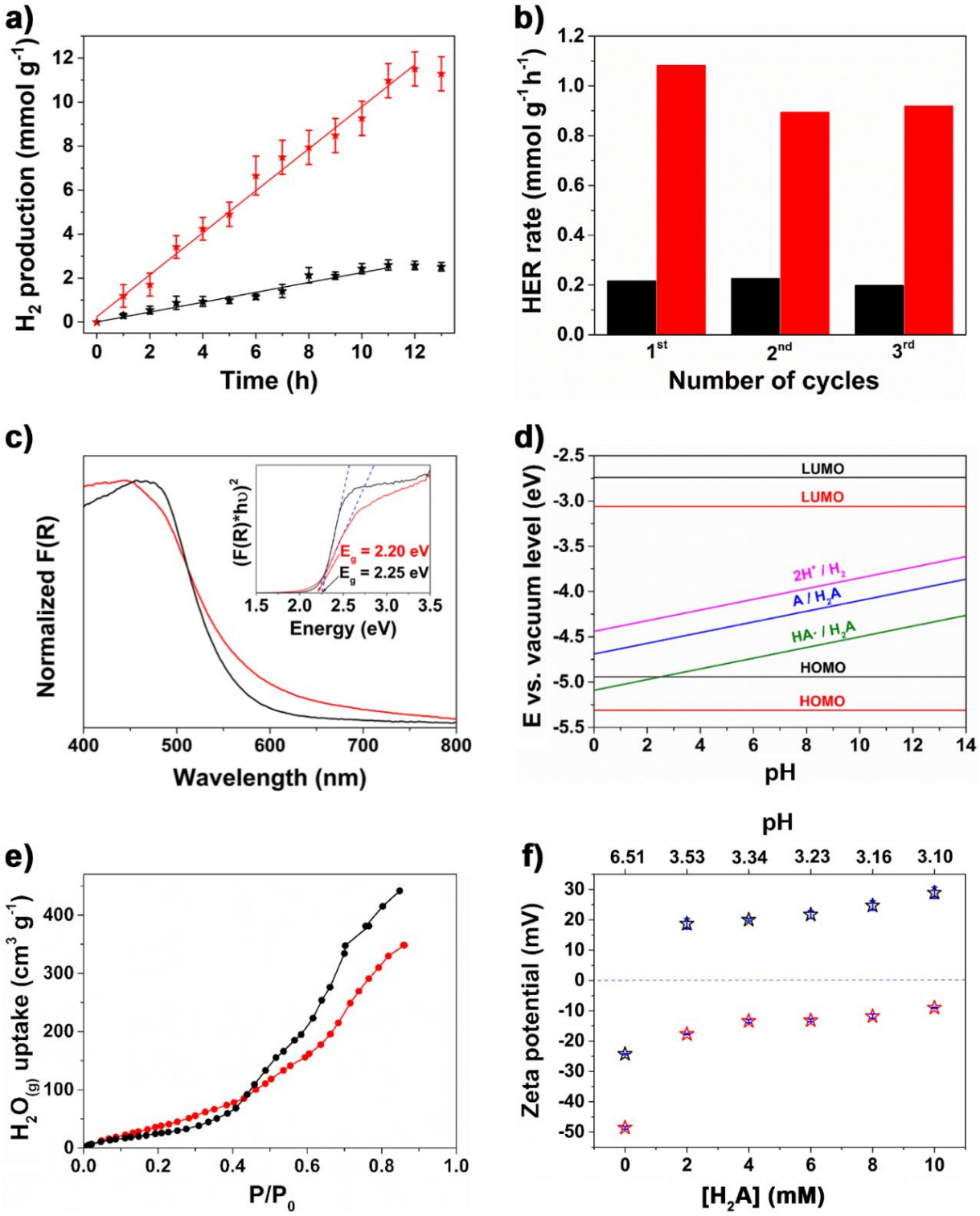

Figure 5.2. (a) Time course of H_2 evolution and (b) hydrogen evolution rates for three cycles, each 13 h obtained with Imine-BDT-ETTA (black) and Amide-BDT-ETTA (red) including the error bars. Solid lines in (a) represent the linear fitting to extract evolution rates. Conditions of photocatalytic tests: $\lambda > 420$ nm, 100 mW cm^{-2}, 1 g/l COF suspension containing 10 mM H_2A and 1.0 wt% (Pt/COF) H_2PtCl_6 precursor. (c) F(R) and Tauc plots (inset) as well as (d)

determined energy levels of Imine-BDT-ETTA (black) and of Amide-BDT-ETTA COF (red) including the redox potentials of the studied photocatalytic reaction. (e) Volumetric water vapor adsorption isotherms of Imine-BDT-ETTA (black) and Amide-BDT-ETTA (red). (f) Zeta potential of Imine-BDT-ETTA (black) and Amide-BDT-ETTA (red) as a function of pH, adjusted using varying concentrations of H_2A (0, 2, 4, 6, 8, and 10 mM) including the error bars (blue).

suspensions in aqueous media in contrast to Imine-BDT-ETTA (**Figure 5.21**, Appendix B).[74]

The observed HER rate dependence on the H_2A concentration for Imine-BDT-ETTA (see **Figure 5.17** a, Appendix B) and Amide-BDT-ETTA (see **Figure 5.17** b, Appendix B) underscores the effect of the COF structure on the hole-driven H_2A oxidation, aiming at the promotion of H_2 evolution. The efficiency of the H_2A oxidation depends on the thermodynamic driving force (discussed above) and its adsorption at the COF surface. In the studied pH region, H_2A is present in a protonated form and it can interact with both COFs only through weak H-bonding formed either with the imine linkage or the C = O bond of amide linkage. Consequently, no adsorption of H_2A onto the surface of either COF was detected in the dark (see **Figure 5.22**, Appendix B). However, Amide-BDT-ETTA has a greater tendency to form stronger H-bonds with water molecules, thereby potentially aiding in the eventual reduction of protons.[75]

The interfacial interactions between the COF and the H_2PtCl_6 precursor present mainly as $[PtCl_6]^{2-}$ are crucial for photocatalytic H_2 evolution, as they dictate Pt growth and distribution on the COF surface. The coordinating sites for metal complexes in the COF structures have been reported to enable the controlled growth of Pt particles.[76] However, the formation of the coordinative bonds may be slower than the charge transfer to the transition metal complexes as the latter is known to happen on nanoseconds to picoseconds timescale.[77] Additionally, coordinative binding often requires thermal treatment.[78] Hence, interactions such as electrostatic attraction and repulsion between charged particles are most likely to govern the in-situ photodeposition of Pt.

For studies of the columbic interactions between the COFs and $[PtCl_6]^{2-}$ precursor, the surface charge of both COFs was determined by measuring the zeta potential in water-based suspensions (0.1 g L^{-1}) with different H_2A concentrations (0 to 10 mM). As shown in **Figure 5.2** f, both COFs have negative surface charge in the absence of H_2A. Imine-BDT-ETTA ($[H_2A]$ = 0 mM) shows a zeta potential of -24.4 ± 0.3 mV, while the zeta potential value for

Amide-BDT-ETTA is -48.6 ± 0.5 mV. The Amide-BDTETTA exhibits more negative zeta potential (below -30 mV), indicating improved stability in aqueous suspensions compared to its imine counterpart.[79] The addition of H2A shifted the zeta potential of Imine-BDT-ETTA to positive values. As shown in previous studies,[80,81] such a shift can be caused by the protonation of functional groups. Imine bonds are known to act as weak bases and are capable of being protonated.[15] In order to calculate the ratio between protonated and non-protonated forms of the COFs, the Henderson-Hasselbalch equation for weak bases was used (Equation 5.5).[82,83]

$$pOH = pK_b + log\frac{[AH^+]}{[A]} \qquad (5.5)$$

pK_b: base dissociation constant; *[A]:* concentration of the base; *[AH+]:* concentration of conjugate acid

Here pK_b values for imine bonds range between 8 to 10, and their conjugate acids (protonated imines) have pK_a (acid dissociation constant) values between 4 and 6 (because $pK_b + pK_a = 14$),[84] suggesting that protonation of imine linkages occurs at pH levels below 6.[85,86] During photocatalytic tests in the presence of H_2A an acidic environment is achieved (pH = 3.10 – 3.53), i.e., Imine-BDT-ETTA-COF is predominantly present in protonated form ([A] < [AH+]). The positive shift of the zeta potential was also observed for Amide-BDT-ETTA, however, it remained in the negative range. The positive shift can be attributed to the protonation of unreacted imine bonds while amide bonds remain non-protonated due to their lower basicity (pK_b values ranging between 13 and 16 while pK_a for conjugate acids (protonated amides) varies between -2 to 1).[87-90] This aligns well with the well-known fact that more acidic functional groups typically exhibit more negative zeta potential than the more basic functional groups.[91] The protonation of amide linkages occurs in the presence of strong acids at pH values below 1. In the experimental conditions employed for the photocatalytic tests, the amide linkages are in the non-protonated form ([A] > [AH+]) causing negative zeta potential and negatively charged COF particles. These results suggest the electrostatic attraction of negatively charged Pt-precursor $[PtCl_6]^{2-}$ with positively charged Imine-BDT-ETTA and electrostatic repulsion with negatively charged Amide-BDT-ETTA. Further analysis requires post-characterization of both COFs.

5.3.5. Post-Characterization and Proposed Reaction Mechanism

The consistent and stable rates of hydrogen production observed during the illumination lasting 48 hours reveal fair photochemical stability of both COFs. Accordingly, structural characterization of both COFs was conducted after 13 and 56 hours of illumination in the presence of 10 mM H_2A and 1 wt% Pt loading. The PXRD patterns presented in Figure 5.3 a,b reveals that after 13 and after 56 hours of illumination, both COFs exhibit retention of crystalline structure.

To gain insights into the structural distribution of Pt particles, scanning transmission electron microscopy (STEM) analysis was performed for both COFs following 13 hours photocatalytic test. **Figure 5**.3 c and **Figure 5.23** a,b (Appendix B) reveal a random distribution of small Pt particles dispersed within the matrix of Imine-BDT-ETTA. Statistical analysis of the Pt size distribution, **Figure 5.24** a (Appendix B), establishes an average Pt particle size of 3.9 nm with a full width at half maximum (FWHM) of the distribution of 3.6 nm. In contrast, Amide-BDT-ETTA (**Figure 5**.3 d and **Figure 5.23** c,d, Appendix B) displays large Pt particles with a much broader size distribution. As shown in **Figure 5.24** b (Appendix B), the size of the Pt particles grown on the amide-linked COF lies within two distinct size ranges, i.e., a broad distribution centered around an average size of 90 nm (FWHM = 35 nm), and a narrower distribution with an average size of 12 nm (FWHM = 4 nm). Statistical analysis reveals that ≈ 90% of Pt particles on Amide-BDT-ETTA are larger than those observed on Imine-BDT-ETTA. These findings also correlate with the quantified imine-to-amide conversion degree of 90% and strongly suggest that the Pt growth mechanism is influenced by the nature of the COF linkage, which modulates the interaction between the COF framework and the Pt precursor during photodeposition.

The attractive interaction between positively charged Imine-BDT-ETTA with the negatively charged Pt-precursor $[PtCl_6]^{2-}$ should promote the high Pt nucleation rate at numerous sites and resulting in a homogeneous distribution of small (1-2 nm) Pt particles in the framework (**Figure 5**.3 e). In contrast, Amide-BDT-ETTA is negatively charged in the acidic environment, leading to repulsion between the COF and the $[PtCl_6]^{2-}$ anions, which is proposed to cause the formation of larger Pt particles. Hereby, the interparticle electron transport along the BDT-

ETTA agglomerates to pre- formed metal particles enables the formation of larger particles (**Figure 5**.3 f).

These results reveal the ability of the COF to serve as an antenna for electron transport. The effect of COF surface charge on Pt particle formation and photocatalytic performance is further supported by experiments conducted in the presence of TEOA as a sacrificial agent. Under these conditions, the medium becomes alkaline, and both COFs are non-protonated[85-90] and acquire a negative surface charge. Notably, the Imine-BDT-COF outperforms the Amide-COF in this scenario. These results highlight the critical role of surface charge modulation in controlling the efficiency of photocatalytic hydrogen production. Hence, the linkage conversion allowed for tuning of the surface charges of the COF through different protonation behavior of the imine and amide linkage, which had a direct impact on the growth of the Pt particles on the COF surface. Hence, an additional tool for controlling the photocatalytic process was demonstrated.

The influence of the Pt particle size on the hydrogen evolution reaction remains a topic of ongoing debate in the literature.[92-95] In general, the overall photocatalytic performance is governed by a sequence of key steps (omitting here the role of the sacrificial donor): i) light absorption, charge separation, and charge transport within the (COF) photocatalyst to the metal cocatalyst, ii) interfacial electron transfer between the photocatalyst and the metal co-catalyst, and iii) proton reduction to form hydrogen atoms on the metal surface, followed by H_2 formation and desorption. While the first step is primarily determined by the intrinsic electronic properties of the (COF) photocatalyst, the second and third steps are influenced by the nature and distribution of the metal particles, particularly their size and interfacial characteristics, including electronic coupling to the COF. The efficiency of charge separation and interfacial electron transfer can indeed be modulated by the Pt particle size, which plays a critical role in facilitating or hindering these processes.[94,96] However, the Volmer step - the initial formation of adsorbed hydrogen atoms (H•) on the Pt surface is the rate-limiting step in catalytic hydrogen evolution. Bard and co-workers demonstrated that the kinetics of this step are accelerated as Pt particle size increases on Bi and Pb substrates.[97] In light of these findings, we propose that the larger Pt particles formed on Amide-BDT-ETTA may enhance H_2 production due to improved kinetics of the Volmer step. However, we emphasize that systematic studies on

the relationship between Pt particle size, charge separation efficiency, interfacial electron transfer, and hydrogen formation kinetics in COF-based systems are still lacking and warrant further investigation.

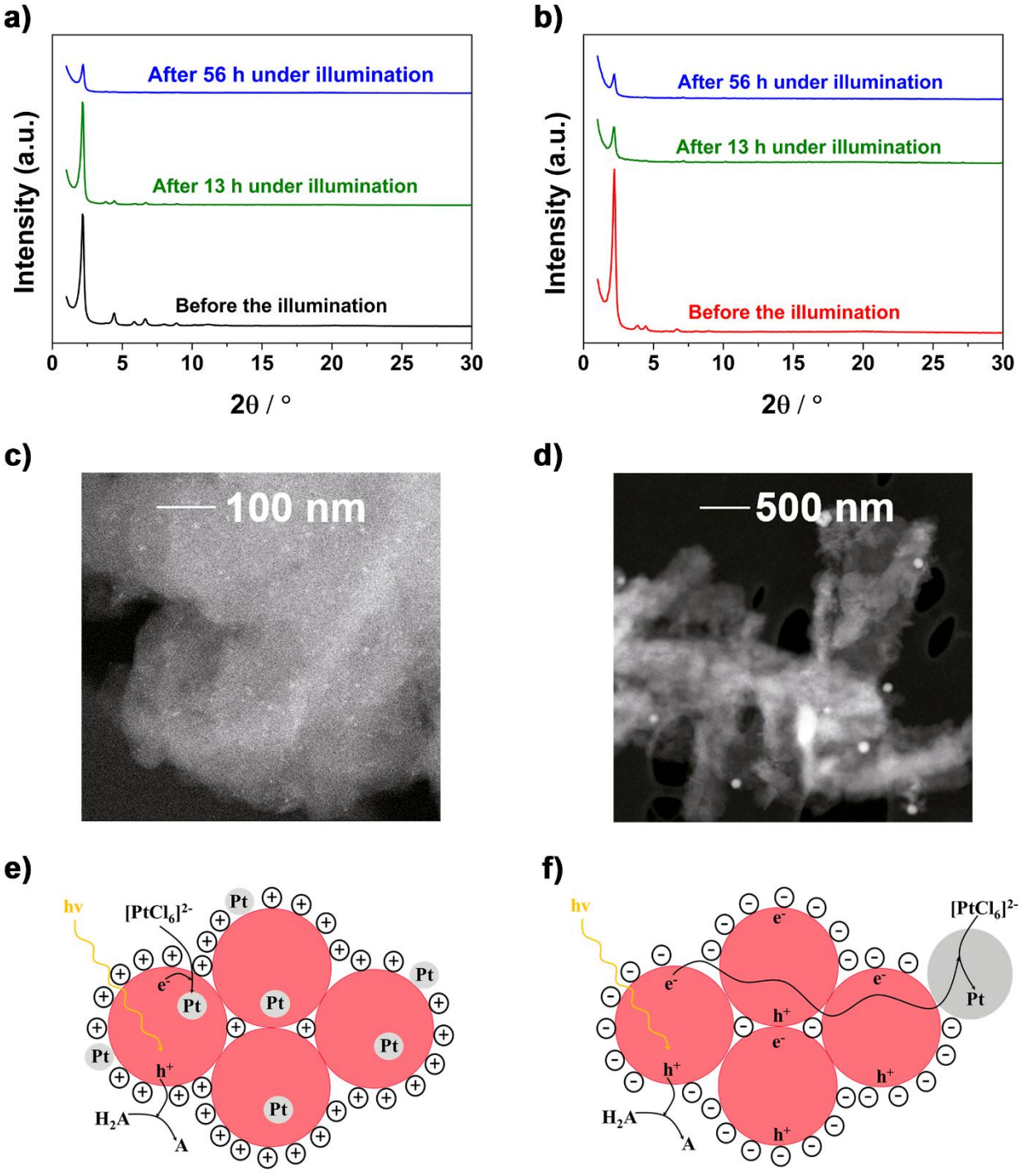

Figure 5.3. PXRD patterns of (a) Imine-BDT-ETTA and (b) Amide-BDT-ETTA before and after 13 h and 56 h of photocatalytic test. STEM-HAADF images showing distribution of Pt

particles in the polymeric structure of (c) Imine-BDT-ETTA and (d) Amide-BDT-ETTA after 13 h of photocatalytic test. Conditions of photocatalytic test: $\lambda > 420$ nm, 100 mW cm^{-2}, 1 g/l COF suspension containing 10 mM H_2A and 1.0 wt% (Pt/COF) H_2PtCl_6 precursor. Schematic representation of interparticle electron transport along agglomerates of (e) Imine-BDT-ETTA and (f) Amide-BDT-ETTA towards the Pt particles (red: COF domains, grey: Pt particles).

5.4. Conclusions

This study demonstrates how the structural, optoelectronic, and interfacial properties of the BDT-ETTA COF are modulated through linkage conversion from imine to amide and their resulting influence on photocatalytic performance. Retaining its crystallinity upon amidization, the amide-linked COF exhibits a shift in energy levels toward more positive potentials (E vs SCE), enhancing its oxidizing power. This stronger oxidation capability facilitates more efficient hole scavenging, thereby promoting proton reduction while suppressing charge carrier recombination. Additionally, the increased hydrophilicity of Amide-BDT-ETTA, attributed to the presence of C = O bonds, leads to an improved HER rate and enhances the stability of its suspensions in aqueous media compared to Imine-BDT-ETTA. Notably, our findings reveal, for the first time, that surface charge modulation, driven by the distinct protonation behavior of imine and amide linkages, plays a critical role in photocatalytic performance. This interfacial modification strategy effectively switches the surface charge of COFs and alters the in-situ Pt-photodeposition mechanism. Specifically, the negatively charged Amide-BDT-ETTA promotes proton adsorption and facilitates the formation of large Pt particles (up to 100 nm), which are highly effective for proton reduction. By highlighting the impact of interfacial properties on reaction mechanisms and photocatalytic hydrogen evolution, this study expands the functional versatility of COFs in photocatalysis. We anticipate that this approach can be further applied to a wide range of photocatalytic reactions and diverse linkage motifs, offering new pathways for designing advanced COF-based photocatalysts.

5.5. References

[1] A. P. Côté, A. I. Benin, N. W. Ockwig, M. O'Keeffe, A. J. Matzger, O. M. Yaghi, *Science* **2005**, *310*, 1166.

[2] L. Stegbauer, K. Schwinghammer, B. V. Lotsch, *Chem. Sci.* **2014**, *5*, 2789.

[3] X. Li, Q. Gao, J. Aneesh, H. Sen Xu, Z. Chen, W. Tang, C. Liu, X. Shi, K. V. Adarsh, Y. Lu, K. P. Loh, *Chem. Mater.* **2018**, *30*, 5743.

[4] H. Y. Yu, J. S. Wang, F. Y. Xie, Q. Yang, Y. Chen, L. Zhao, Y. Li, W. J. Ruan, *Chem. Eng. J.* **2022**, *445*, 136713.

[5] T. Shi, H. Wang, L. Li, Z. Zhao, C. Wang, X. Zhang, Y. Xie, *Matter* **2022**, *5*, 1004.

[6] S. Ghosh, A. Nakada, M. A. Springer, T. Kawaguchi, K. Suzuki, H. Kaji, I. Baburin, A. Kuc, T. Heine, H. Suzuki, R. Abe, S. Seki, *J. Am. Chem. Soc.* **2020**, *142*, 9752.

[7] X. Song, Y. Wu, X. Zhang, X. Li, Z. Zhu, C. Ma, Y. Yan, P. Huo, G. Yang, *Chem. Eng. J.* **2021**, *408*, 127292.

[8] L. Stegbauer, S. Zech, G. Savasci, T. Banerjee, F. Podjaski, K. Schwinghammer, C. Ochsenfeld, B. V. Lotsch, *Adv. Energy Mater.* **2018**, *8*, 1703278.

[9] G. Zhang, X. Li, Q. Liao, Y. Liu, K. Xi, W. Huang, X. Jia, *Nat. Commun.* **2018**, *9*, 2785.

[10] R. Chen, Y. Wang, Y. Ma, A. Mal, X. Y. Gao, L. Gao, L. Qiao, X. B. Li, L. Z. Wu, C. Wang, *Nat. Commun.* **2021**, *12*, 1534.

[11] Y. Xiao, K. Wang, W. Dong, L. Li, *Polymer* **2024**, *300*, 126980.

[12] S. Karak, K. Dey, R. Banerjee, *Adv. Mater.* **2022**, *34*, 2202751.

[13] Z. Li, T. He, Y. Gong, D. Jiang, *Acc. Chem. Res.* **2020**, *53*, 1672.

[14] Z. Li, T. Deng, S. Ma, Z. Zhang, G. Wu, J. Wang, Q. Li, H. Xia, S.-W. Yang, X. Liu, *J. Am. Chem. Soc.* **2023**, *145*, 8364.

[15] J. Yang, A. Acharjya, M. Y. Ye, J. Rabeah, S. Li, Z. Kochovski, S. Youk, J. Roeser, J. Grüneberg, C. Penschke, M. Schwarze, T. Wang, Y. Lu, R. van de Krol, M. Oschatz, R. Schomäcker, P. Saalfrank, A. Thomas, *Angew. Chem., Int. Ed.* **2021**, *60*, 19797.

[16] M. Zhang, X. Wu, Y. Xie, X. Hao, Q. Wang, Y. Zhao, J. Wu, X. Pan, *Mater. Chem. Front.* **2023**, *7*, 5399.

[17] Y. Wang, A. Vogel, M. Sachs, R. S. Sprick, L. Wilbraham, S. J. A. Moniz, R. Godin, M. A. Zwijnenburg, J. R. Durrant, A. I. Cooper, J. Tang, *Nat. Energy* **2019**, *4*, 746.

[18] F. Costantino, P. V. Kamat, *ACS Energy Lett.* **2022**, *7*, 242.

[19] M. R. Hoffmann, S. T. Martin, W. Choi, D. W. Bahnemann, *Chem. Rev.* **1995**, *95*, 69.

[20] J. M. Rotter, S. Weinberger, J. Kampmann, T. Sick, M. Shalom, T. Bein, D. D. Medina, *Chem. Mater.* **2019**, *31*, 10008.

[21] P. J. Waller, S. J. Lyle, T. M. Osborn Popp, C. S. Diercks, J. A. Reimer, O. M. Yaghi, *J. Am. Chem. Soc.* **2016**, *138*, 15519.

[22] M. A. Mohamed, K. Yamada, K. Tomioka, *Tetrahedron Lett.* **2009**, *50*, 3436.

[23] A. K. Rappé, C. J. Casewit, K. S. Colwell, W. A. Goddard, W. M. Skiff, *J. Am. Chem. Soc.* **1992**, *114*, 10024.

[24] X. Han, J. Huang, C. Yuan, Y. Liu, Y. Cui, *J. Am. Chem. Soc.* **2018**, *140*, 892.

[25] Z. B. Zhou, X. H. Han, Q. Y. Qi, S. X. Gan, D. L. Ma, X. Zhao, *J. Am. Chem. Soc.* **2022**, *144*, 1138.

[26] T. Sick, A. G. Hufnagel, J. Kampmann, I. Kondofersky, M. Calik, J. M. Rotter, A. Evans, M. Döblinger, S. Herbert, K. Peters, D. Böhm, P. Knochel, D. D. Medina, D. Fattakhova-Rohlfing, T. Bein, *J. Am. Chem. Soc.* **2018**, *140*, 2085.

[27] J.-R. Wang, K. Song, T.-X. Luan, K. Cheng, Q. Wang, Y. Wang, W. W. Yu, P.-Z. Li, Y. Zhao, *Nat. Commun.* **2024**, *15*, 1267.

[28] P. J. Waller, Y. S. Alfaraj, C. S. Diercks, N. N. Jarenwattananon, O. M. Yaghi, *J. Am. Chem. Soc.* **2018**, *140*, 9099.

[29] Y. Zhang, W. Shi, Y. Zhao, C. Zhang, Y. Zhi, *Macromol. Rapid Commun.* **2023**, *44*, 2200787.

[30] J. Feijoo, K. Paliušyte, J. Schneider, ˙ *JPhys Energy* **2024**, *6*, 025018.

[31] H. L. Nguyen, C. Gropp, O. M. Yaghi, *J. Am. Chem. Soc.* **2020**, *142*, 2771.

[32] B. C. Smith, *Spectroscopy*, CRC Press, Boca Raton, Florida, **2020**.

[33] M. di Foggia, P. Taddei, A. Torreggiani, M. Dettin, A. Tinti, *Proteomics Res. J.* **2011**, *2*, 231.

[34] T. M. Magalhães, R. C. Guerra, R. A. da, S. San, A. P. Gil, R. A. Valente, B. G. Simão, T. Soares, C. de, A. Mendes dos, S. Pyrrho, V. P. de Sousa, V. L. Rodrigues-Furtado, *J. Nanoparticle Res.* **2017**, *19*, 1.

[35] E. A. Gendy, A. I. Khodair, A. M. Fahim, D. T. Oyekunle, Z. Chen, *J. Mol. Liq.* **2022**, *358*, 119191.

[36] C. Krishnaraj, H. S. Jena, K. S. Rawat, J. Schmidt, K. Leus, V. Van Speybroeck, P. Van Der Voort, *ACS Appl. Mater. Interfaces* **2022**, *14*, 50923.

[37] C. Krishnaraj, A. M. Kaczmarek, H. S. Jena, K. Leus, N. Chaoui, J. Schmidt, R. Van Deun, P. Van Der Voort, *ACS Appl. Mater. Interfaces* **2019**, *11*, 27343.

[38] R. Xue, Y. S. Liu, M. Y. Wang, H. Guo, W. Yang, J. X. Guo, G. Y. Yang, *ChemSusChem* **2024**, *17*, 202400732.

[39] W. Wang, D. Huang, W. Zheng, X. Zhao, K. He, H. Pang, Y. Xiang, *Chem. Mater.* **2023**, *35*, 7154.

[40] S. Nagakura, *Bull. Chem. Soc. Jpn.* **1952**, *25*, 164.

[41] J. Kettle, Z. Ding, M. Horie, G. C. Smith, *Org. Electron.* **2016**, *39*, 222.

[42] M. A. Leich, N. M. Mackie, K. L. Williams, E. R. Fisher, *Macromolecules* **1998**, *31*, 7618.

[43] C. Zhang, A. Yan, H. Guo, Y. Lei, H. Hao, F. Liu, *Fuel* **2022**, *317*, 123482.

[44] M. Descostes, F. Mercier, N. Thromat, C. Beaucaire, M. GautierSoyer, *Appl. Surf. Sci.* **2000**, *165*, 288.

[45] E. Cato, A. Rossi, N. C. Scherrer, E. S. B. Ferreira, *J. Cult. Herit.* **2018**,*29*, 30.

[46] B. Gieroba, A. Sroka-Bartnicka, P. Kazimierczak, G. Kalisz, A. Lewalska-Graczyk, V. Vivcharenko, R. Nowakowski, I. S. Pieta, A. Przekora, *Int. J. Biol. Macromol.* **2020**, *159*, 911.

[47] M. Šetka, R. Calavia, L. Vojkuvka, E. Llobet, J. Drbohlavová, S. Vallejos, *Sci. Rep.* **2019**, *9*, 8465.

[48] S. Hamid, R. Dillert, D. W. Bahnemann, *J. Phys. Chem. C* **2018**, *122*, 12792.

[49] X. J. Zheng, L. F. Wei, Z. H. Zhang, Q. J. Jiang, Y. J. Wei, B. Xie, M. B. Wei, *Int. J. Hydrogen Energy* **2009**, *34*, 9033.

[50] S. Mozia, A. Heciak, A. W. Morawski, *Catal. Today* **2011**, *161*, 189.

[51] M. Bˇrezina, J. Koryta, T. Louˇcka, D. Maršíková, *Electroanal. Chem. Inerfacial Electrochem.* **1972**, *40*, 13.

[52] M. G. Roig, Z. S. Rivera, J. F. Kennedy, *Int. J. Food Sci. Nutr.* **1995**, *46*, 107.

[53] M. Salki´c, *J. Anal. Chem.* **2016**, *71*, 153.

[54] A. Xie, Z. H. Pan, M. Yu, G. G. Luo, D. Sun, *Chinese Chem. Lett.* **2019**, *30*, 225.

[55] Y. Z. Yayun Wang, H. Wang, Y. Li, M. Zhang, *Molecules* **2022**, *27*, 6286.

[56] J. Zhang, J. Wang, Y. Tang, K. Liu, B. Zhang, G. Ma, *ACS Appl. Mater. Interfaces* **2022**, *14*, 34656.

[57] Y. Pellegrin, F. Odobel, *Comptes Rendus Chim* **2017**, *20*, 283.

[58] P. Du, J. Schneider, G. Luo, W. W. Brennessel, R. Eisenberg, *Inorg. Chem.* **2009**, *48*, 4952.

[59] A. Kumar, M. D. Sevilla, *J. Phys. Chem. B* **2018**, *122*, 98.

[60] I. Dance, *Inorg. Chem.* **2006**, *45*, 5084.

[61] Y. Zhu, D. Huang, W. Wang, G. Liu, C. Ding, Y. Xiang, *Angew. Chem., Int. Ed.* **2024**, *63*, 202319909.

[62] P. Makuła, M. Pacia, W. Macyk, *J. Phys. Chem. Lett.* **2018**, *9*, 6814.

[63] J. Tauc, R. Grigorovici, A. Vancu, *Phys. status solidi* **1966**, *627*, 627.

[64] R. Ghosh, F. Paesani, *Chem. Sci.* **2021**, *12*, 8373.

[65] G. L. J. A. Rikken, D. Braun, E. G. J. Staring, R. Demandt, *Appl. Phys. Lett.* **1994**, *65*, 219.

[66] Y. Wang, S. Nasreen, D. Kamal, Z. Li, C. Wu, J. Huo, L. Chen, R. Ramprasad, Y. Cao, *ACS Appl. Mater. Interfaces* **2021**, *13*, 46142.

[67] P. Khanchaitit, K. Han, M. R. Gadinski, Q. Li, Q. Wang, *Nat. Commun.* **2013**, *4*, 2845.

[68] N. Keller, T. Sick, N. N. Bach, A. Koszalkowski, J. M. Rotter, D. D. Medina, T. Bein, *Nanoscale* **2019**, *11*, 23338.

[69] C. B. Meier, R. S. Sprick, A. Monti, P. Guiglion, J. S. M. Lee, M. A. Zwijnenburg, A. I. Cooper, *Polymer* **2017**, *126*, 283.

[70] K. J. Korman, G. E. Decker, M. R. Dworzak, M. M. Deegan, A. M. Antonio, G. A. Taggart, E. D. Bloch, *ACS Appl. Mater. Interfaces* **2020**, *12*, 40318

[71] G. De Luca, A. Arbouznikov, A. Goursot, P. Pullumbi, *J. Phys. Chem.* B **2001**, *105*, 4663.

[72] N. C. Burtch, H. Jasuja, D. Dubbeldam, K. S. Walton, *J. Am. Chem. Soc.* **2013**, *135*, 7172.

[73] Y. Ge, H. Zhou, Y. Ji, L. Ding, Y. Cheng, R. Wang, S. Yang, Y. Liu, X. Wu, Y. Li*, J. Phys. Chem. C* **2018**, *122*, 27495.

[74] S. Ma, Z. Li, J. Jia, Z. Zhang, H. Xia, H. Li, X. Chen, Y. Xu, X. Liu, *Chinese J. Catal.* **2021**, *42*, 2010.

[75] J. Z. Marinho, L. L. Nascimento, A. L. R. Santos, A. M. Faria, A. E. H. Machado, A. O. T. Patrocinio, *Photochem. Photobiol. Sci.* **2022**, *21*, 1659.

[76] Y. Li, L. Yang, H. He, L. Sun, H. Wang, X. Fang, Y. Zhao, D. Zheng, Y. Qi, Z. Li, W. Deng, *Nat. Commun.* **2022**, *13*, 1355.

[77] W. Yang, R. Godin, H. Kasap, B. Moss, Y. Dong, S. A. J. Hillman, L. Steier, E. Reisner, J. R. Durrant, *J. Am. Chem. Soc.* **2019**, *141*, 11219.

[78] Q. J. Wu, D. H. Si, S. Ye, Y. L. Dong, R. Cao, Y. B. Huang, *J. Am. Chem. Soc.* **2006**, *145*, 19856.

[79] V. Gupta, P. Trivedi, *Lipid Nanocarriers for Drug Targeting*, Elsevier, Norwich, **2018**.

[80] S. Bocian, E. Dziubakiewicz, B. Buszewski, *J. Sep. Sci.* **2015**, *38*, 2625.

[81] A. Serrano-Lotina, R. Portela, P. Baeza, V. Alcolea-Rodriguez, M. Villarroel, P. Ávila, *Catal. Today* **2023**, *423*, 113862.

[82] R. Mioni, G. Mioni, Scand. *J. Clin. Lab. Invest.* **2015**, *75*, 452.

[83] N. Radi´c, A. Prki´c, *Rev. Anal. Chem.* **2012**, *31*, 93.

[84] R. S. Treptow, *J. Chem. Educ.* **1986**, *63*, 938.

[85] G. fa Long, K. Wan, M. yao Liu, Z. xing Liang, J. hua Piao, P. Tsiakaras, *J. Catal.* **2017**, *348*, 151.

[86] J. E. Rice, *Organic Chemistry Concepts and Applications for Medicinal Chemistry*, Elsevier, San Diego, CA, **2017**.

[87] B. Lotina-Hennsen, B. King, M. Albores, R. Pozas, *Photochem. Photobiol.* **1987**, *46*, 287.

[88] K. V. Raman, M. M. Mortland, *Soil Sci. Soc. Am. J.* **1969**, *33*, 313.

[89] N. R. Ayyangar, K. V. Srinivasan, *Can. J. Chem.* **1984**, *62*, 1292.

[90] S. Morsch, L. Farmer, *Organic Chemistry III*, LibreTexts, Northampton, MA, **2021**.

[91] M. P. M. Poschmann, K. P. Lillerud, N. Stock, *Chem. – A Eur. J.* **2023**, *29*, 202301760.

[92] S. Chen, A. Kucernak, *J. Phys. Chem. B* **2003**, 107, 8392.

[93] N. Cheng, S. Stambula, D. Wang, M. N. Banis, J. Liu, A. Riese, B. Xiao, R. Li, T. K. Sham, L. M. Liu, G. A. Botton, X. Sun, *Nat. Commun.* **2016**, *7*, 13638.

[94] Y. Nakibli, Y. Mazal, Y. Dubi, M. Wächtler, L. Amirav, *Nano Lett.* **2018**, *18*, 357.

[95] I. Vamvasakis, B. Liu, G. S. Armatas, *Adv. Funct. Mater.* **2016**, *26*, 8062.

[96] Y. Liu, W. Yang, Q. Chen, D. A. Cullen, Z. Xie, T. Lian, *J. Am. Chem. Soc.* **2022**, *144*, 2705.

[97] M. Zhou, S. Bao, A. J. Bard, *J. Am. Chem. Soc.* **2019**, *141*, 7327.

5.6. Appendix A

This section presents preliminary investigations and additional experimental work that informed the development of the main study described in Chapter 5. While not central to the final results, these experiments provided critical insights that shaped the overall research strategy. They offer context regarding the initial hypotheses, synthetic challenges, and early

characterization efforts that preceded the optimized conditions and analyses detailed in the main text.

5.6.1. Initial idea and hypotheses

The initial phase of linkage conversion project started with Pt photodeposition experiment on Imine-BDT-ETTA COF. Imine-BDT-ETTA COF has been previously established and used as photocathodes for light-driven water splitting.[1] Although the photocurrent reported was relatively low, the study highlights the significant potential of BDT-ETTA COF films as stable and active photocathodes for light-driven water reduction. These findings pave the way for a new class of photoabsorber materials with tunable optical and electronic properties. For this reason we decided to investigate Imine-BDT-ETTA COF further in order to discover its full photocatalytic potential. For this reason, we decided to further investigate the Imine-BDT-ETTA COF to explore its full photocatalytic potential. Our focus was to incorporate Pt nanoparticles within the pores of the COF to generate catalytically active sites.

5.6.2. Platinum photodeposition

For the photodeposition of platinum, 2 mg of Imine-BDT-ETTA COF was first dispersed in 20 mL of acetonitrile. The dispersion was then centrifuged and concentrated to 1 mL. Subsequently, 1 mL of a 1.5 M aqueous triethanolamine (TEOA) solution was added as a sacrificial electron donor. The resulting suspension was degassed by bubbling argon for 20 minutes. A calculated amount of H_2PtCl_6 solution was then added to achieve an approximate platinum loading of 9 wt%. The mixture was further bubbled under argon for 10 minutes, followed by sonication for 30 minutes to ensure uniform distribution of the precursor. Photodeposition was carried out under constant stirring using an LED light source (420 nm cut-off filter, intensity adjusted to 100 mW cm^{-2} using a Newport 1916-C powermeter equipped with an 818-UV/DB optical detector) for 4 hours. After illumination, the suspension was centrifuged to isolate the solid material, which was washed three times with acetonitrile and dried under vacuum, producing Imine-BDT-ETTA@Pt.

5.6.3. Results and investigation

Crystallinity before and after Pt photodeposition was evaluated by Powder X-ray diffraction (PXRD). PXRD spectra illustrated in **Figure 5.4** a shows that after photodeposition

crystallinity for Imine-BDT-ETTA COF remains but decrement is observed. This is a regular observation also reported in other studies that Pt photodeposition as long as other post-modifcation processes often results in reduced crystallinity. [2] The signal at 40° 2Θ in **Figure 5.4** b indicates the presence of elemental platinum, corresponding to the (111) plane of Pt.[3,4]

To further investigate the localization of Pt clusters within the COF matrix, we performed transmission electron microscopy (TEM) analysis. Scanning transmission electron microscopy (STEM) images show the homogenous Pt distribution throughout the polymeric matrix. Due to its high atomic number, Pt scatters electrons strongly and appears white comparing to surrounding lighter elements in the COF matrix.[5] High-resolution transmission electron microscopy (HRTEM) images reveal the periodic structure of the COF, along with the relative positioning of Pt clusters, which appear as dark spots due to their strong electrons scattering contrast.[6] By comparing corresponding STEM and HRTEM images, we conclude that the Pt distribution follows the periodicity of the COF, suggesting that the Pt clusters are incorporated inside the pores of the COF and are particularly visible near grain boundaries.

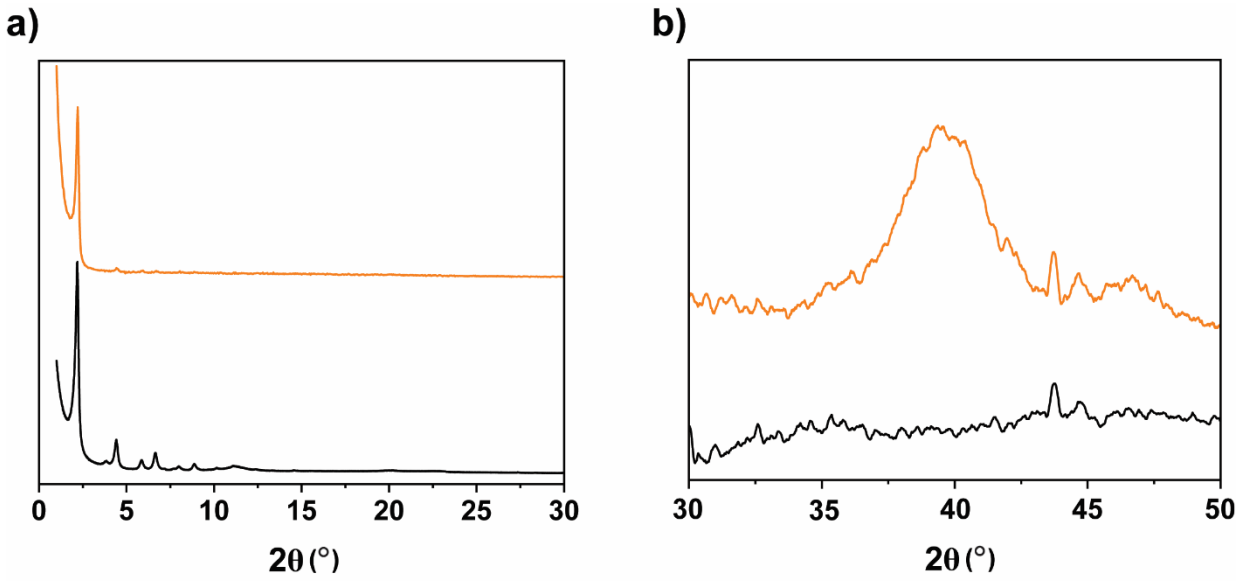

Figure 5.4. PXRD results of Imine-BDT-ETTA (black) and Imine-BDT-ETTA@Pt (orange) at (a) low and (b) high 2Θ values.

To estimate the active sites of the COF involved in the Pt photodeposition process, it is essential to investigate the changes in the oxidation states of the constituent elements. For this

purpose, X-ray photoelectron spectroscopy (XPS) analysis was performed on the Imine-BDT-ETTA@Pt sample (**Figure 5.6** a,c,e). The Pt 4f spectrum reveals the presence of two distinct Pt species: Pt(+II) (66.5%) and Pt(+IV) (33.5%). Pt(+II) is observed at lower binding energies, below 75 eV, while Pt(+IV) appears at higher energies, around 78 eV.[7,8] The characteristic binding energy for metallic Pt(0) is typically found at 71.4 ± 0.1 eV.[9] The absence of this peak initially suggests that Pt in the Imine-BDT-ETTA@Pt sample is not fully reduced to the metallic state but is instead predominantly present in oxidized forms, likely as coordination complexes.

However, TEM analysis, as previously discussed, clearly demonstrates the presence of metallic Pt(0) in the sample. If Pt(+II) and Pt(+IV) were solely present as part of coordination complexes with lighter atoms, the resulting low atomic contrast would significantly diminish its visibility in STEM images.[10,11] It is important to note that XPS is a surface-sensitive technique, and the detection of Pt(0) can be hindered by subsurface location, size-dependent binding energy shifts, and positive charging effects during photoemission.[12,13] Therefore, TEM observations are considered more reliable and conclusive for identifying the presence and oxidation state of Pt in this context.

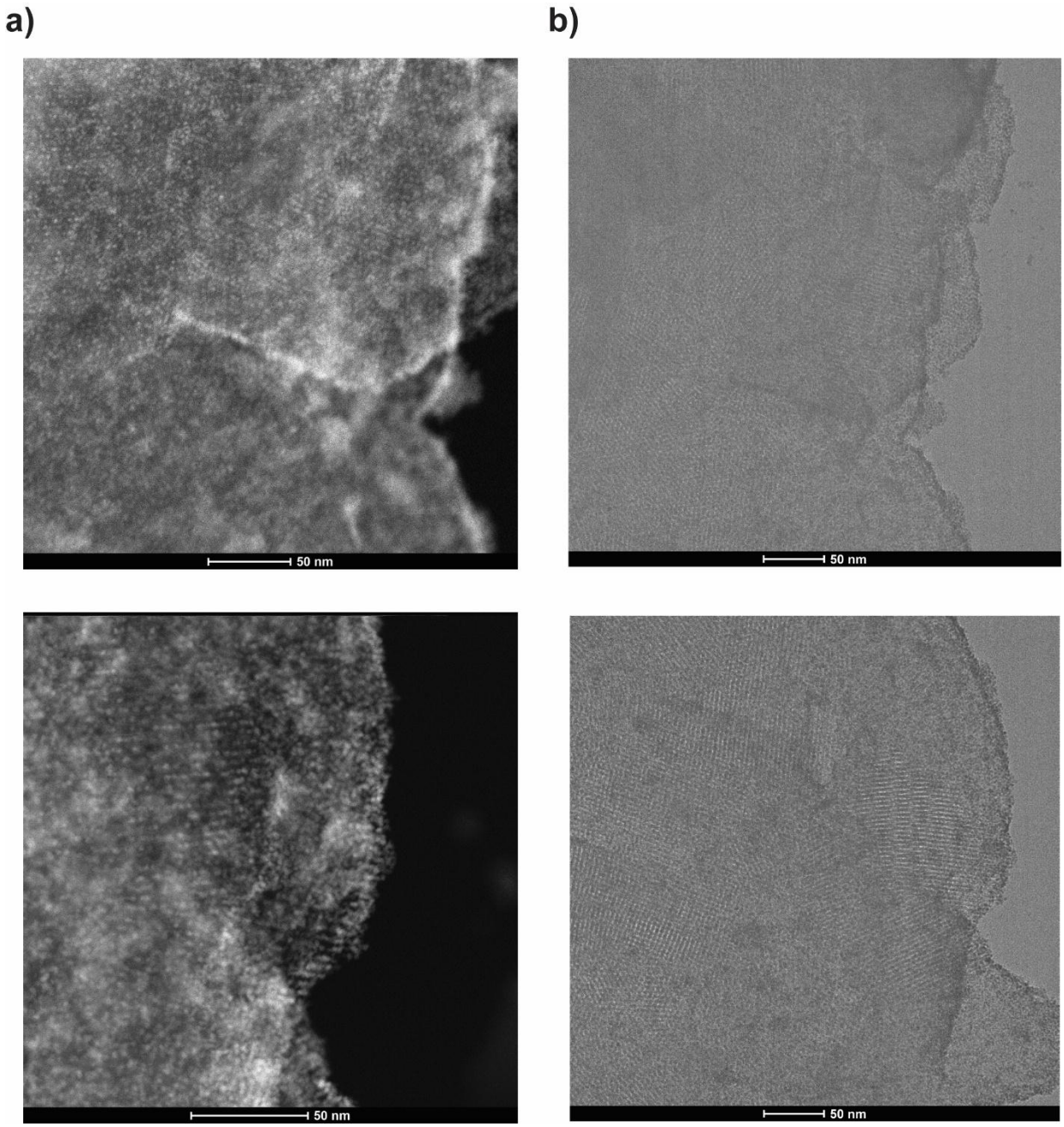

Figure 5.5. (a) Scanning transmission electron microscopy (STEM) images showing localization of Pt clusters within the COF matrix. (b) High-resolution transmission electron microscopy (HRTEM) images revealing lattice fringes of the COF structure.

Another notable observation was the change in the sulfur oxidation state in the Imine-BDT-ETTA@Pt sample. As described in Section 5.3.1, partial sulfur oxidation in the BDT unit was already observed in the untreated Imine-BDT-ETTA sample, with approximately 15% of the sulfur present in an oxidized state (**Figure 5.16**, Appendix B). After the photodeposition, Imine-

BDT-ETTA@Pt exhibited a significantly higher proportion - 46.5% - of oxidized sulfur species, while the remaining sulfur atoms were found in "neutral" forms such as S–S, S–C bonds.[14–16] Such a significant change strongly implies that sulfur atom directly participates in Pt formation. This substantial increase strongly suggests that sulfur atoms are directly involved in the photodeposition process of Pt.

To determine whether sulfur oxidation in the BDT unit is directly caused by photogenerated electrons as part of the photodeposition process or whether it occurs naturally due to exposure to the alkaline TEOA solution, a control experiment was performed. The Imine-BDT-ETTA COF was treated with the same mixture of solvents under identical conditions, as describe in 5.6.2, but in the absence of light, thereby preventing the generation of photogenerated electrons. The resulting material, referred to as Imine-BDT-ETTA reference, was analyzed by XPS. The XPS results showed only trace amounts of platinum, indicating that no significant Pt photodeposition occurred. Furthermore, no oxidized sulfur species were detected in this sample, suggesting that sulfur oxidation is directly induced by light-driven processes rather than by exposure to TEOA alone. In the carbon XPS spectra, peaks were shifted to lower binding energies, which may be attributed to the sample's exposure to the alkaline TEOA medium. This shift could be due to increased electron density or sample charging effects resulting from interactions in the basic environment.[17]

Based on these observations, we conclude that Pt formation within the pores of Imine-BDT-ETTA-COF is a complex process that requires both a light source to excite electrons and a sacrificial electron donor (TEOA). The substantial fraction of sulfur species undergoing a change in oxidation state (46.5%) after photodeposition indicates that the sulfur atoms in the BDT unit play a key role, likely attracting photogenerated holes and serving as sites for oxidation reactions. As the most alkaline and electron-rich site in the framework, the imine bond of the COF is likely involved in the reduction process and coordinates the Pt precursor. The proposed Pt photodeposition mechanism is presented in the **Figure 5.7**.

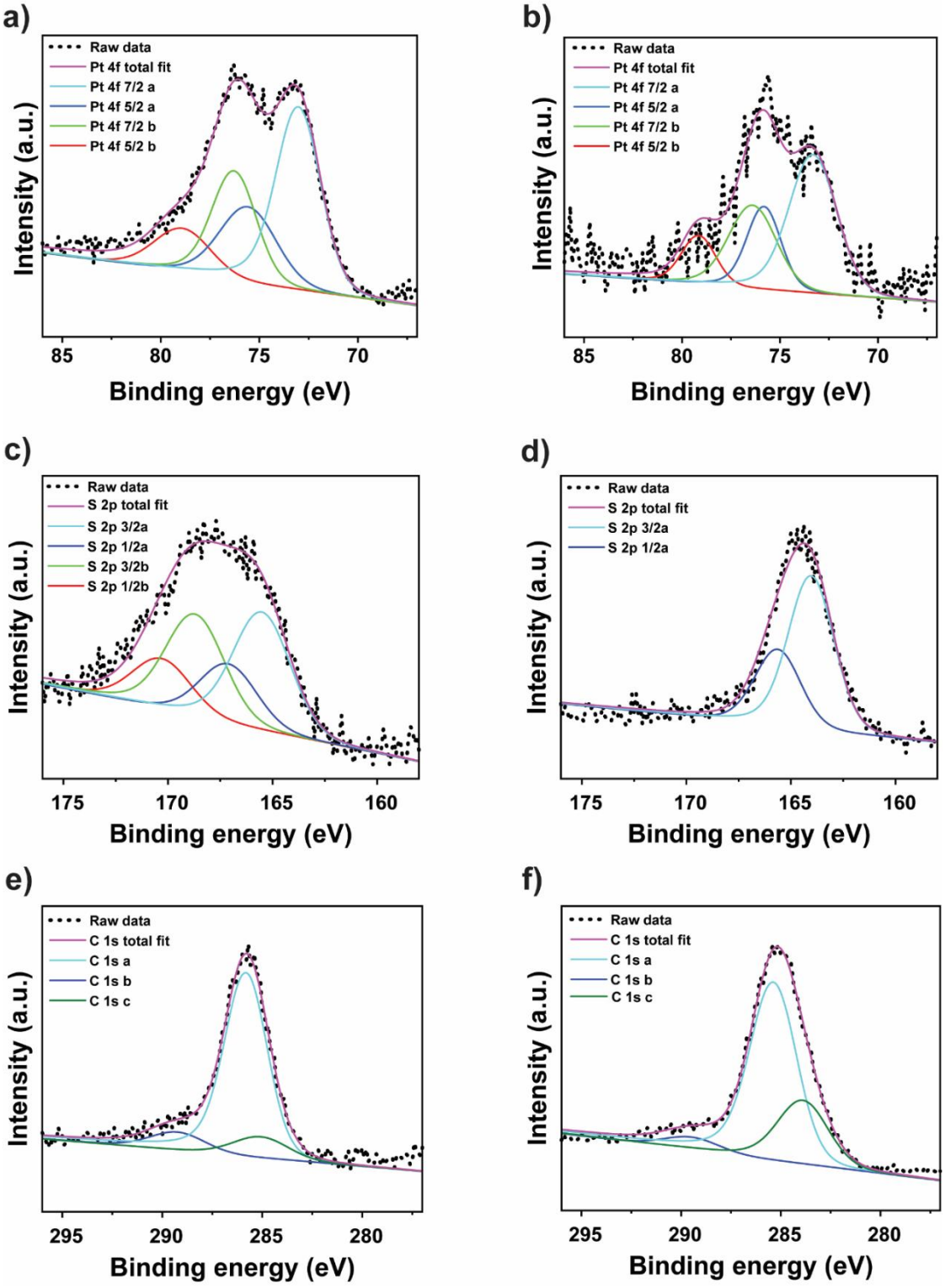

Figure 5.6. Platinum 4f XPS spectra of (a) Imine-BDT-ETTA@Pt and (b) Imine-BDT-ETTA-reference. Sulfur 2p XPS spectra of (c) Imine-BDT-ETTA@Pt and (d) Imine-BDT-ETTA-

reference. Carbon 1s XPS spectra of (e) Imine-BDT-ETTA@Pt and (f) Imine-BDT-ETTA-reference.

Due to reproducibility limitations, the present study is primarily based on experimental observations and an initial mechanistic hypothesis. The results indicate that Pt formation within the pores of Imine-BDT-ETTA-COF is a multistep process requiring both photoexcitation of electrons and the presence of a sacrificial electron donor (TEOA). The substantial proportion of sulfur species exhibiting changes in oxidation state (46.5%) after photodeposition suggests that the sulfur atoms in the BDT unit serve as active sites for hole trapping and subsequent oxidation reactions. In parallel, the imine bonds, as the most alkaline and electron-rich sites in the framework, are likely involved in coordinating and reducing the Pt precursor, thereby facilitating its effective integration into the framework.[18] Although this work was not brought to full completion, it has provided valuable mechanistic insight and opened a complementary research direction focused on linkage conversion.

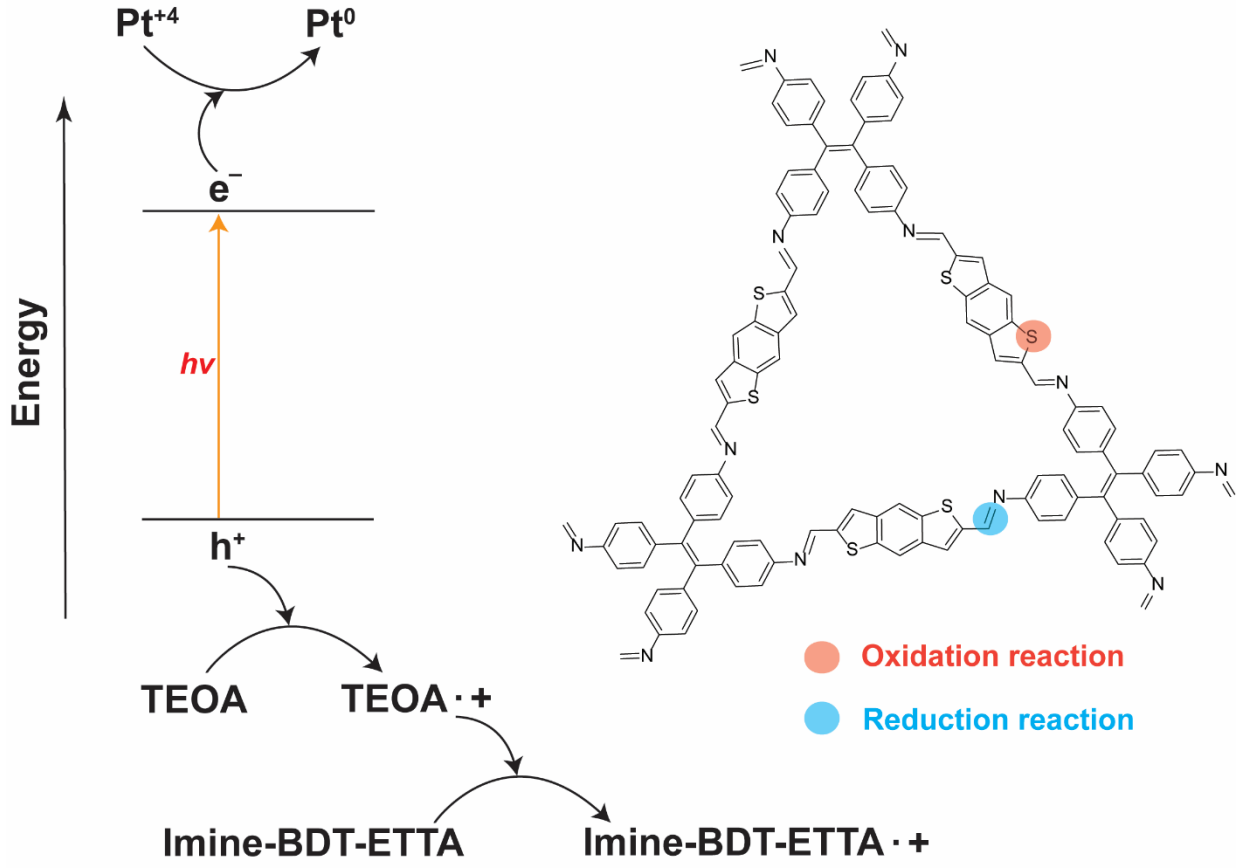

Figure 5.7. Proposed mechanism on Pt formation in Imine-BDT-ETTA COF.

5.6.4. References

[1] T. Sick, A. G. Hufnagel, J. Kampmann, I. Kondofersky, M. Calik, J. M. Rotter, A. Evans, M. Döblinger, S. Herbert, K. Peters, D. Böhm, P. Knochel, D. D. Medina, D. Fattakhova-Rohlfing, T. Bein, *J. Am. Chem. Soc.* **2018**, *140*, 2085.

[2] Y. Li, L. Yang, H. He, L. Sun, H. Wang, X. Fang, Y. Zhao, D. Zheng, Y. Qi, Z. Li, W. Deng, *Nat. Commun.* **2022**, *13*, 1355.

[3] G.-X. Tian, Y. Yang, R.-H. Zhang, L.-Y. Yan, Z. Cheng, D.-H. Lin, X.-W. Zhou, *Adv. Energy Sustain. Res.* **2023**, *4*, 2300058.

[4] C. Rodríguez-Proenza, J. Palomares-Báez, M. Chávez-Rojo, A. García-Ruiz, C. Azanza-Ricardo, A. Santoveña-Uribe, G. Luna-Bárcenas, J. Rodríguez-López, R. Esparza, *Materials* **2018**, *11*, 1882.

[5] J. C. Yang, S. Bradley, J. M. Gibson, *MRS Proc.* **1998**, *549*, 191.

[6] C. Poidevin, P. Paciok, M. Heggen, A. A. Auer, *J. Chem. Phys.* **2019**, *150*, 040901.

[7] M.-C. J. Chun Kim, *Jpn. J. Appl. Phys.* **1999**, *38*, 4872.

[8] M. Peucert, *Chem. Informationsd.* **1985**, *16*, 1315.

[9] S. K. Shaikhutdinov, M. Schildenberger, M. Noeske, G. Mestl, *React. Kinet. Catal. Lett.* **1999**, *67*, 129.

[10] Y. Zhang, P. Yan, Y. Zhou, Q. Xu, *Phys. Chem. Chem. Phys.* **2022**, *24*, 27515.

[11] R. Sugimoto, Y. Segawa, A. Suzuta, Y. Kunisada, T. Uchida, K. Yamazaki, K. Gohara, *J. Phys. Chem. C* **2021**, *125*, 2900.

[12] A. Norman, R. Sporken, A. Galtayries, F. Mirabella, K. Keveney, M. Pijolat, R. Baker, S. Bernal, *MRS Proc.* **1999**, *581*, 345.

[13] D. E. Ramaker, M. K. Oudenhuijzen, D. C. Koningsberger, *J. Phys. Chem. B* **2005**, *109*, 5608.

[14] C. Zhang, A. Yan, H. Guo, Y. Lei, H. Hao, F. Liu, *Fuel* **2022**, *317*, 123482.

[15] M. Descostes, F. Mercier, N. Thromat, C. Beaucaire, M. Gautier-Soyer, *Appl. Surf. Sci.*

2000, *165*, 288.

[16] E. Cato, A. Rossi, N. C. Scherrer, E. S. B. Ferreira, *J. Cult. Herit.* **2018**, *29*, 30.

[17] B. B. Rath, L. Fuchs, F. Stemmler, A. Rodríguez-Camargo, Y. Wang, M. F. X. Dorfner, J. Olbrich, J. van Slageren, F. Ortmann, B. V. Lotsch, *J. Am. Chem. Soc.* **2025**, *147*, 18492.

[18] Z. Almansaf, J. Hu, F. Zanca, H. R. Shahsavari, B. Kampmeyer, M. Tsuji, K. Maity, V. Lomonte, Y. Ha, P. Mastrorilli, S. Todisco, M. Benamara, R. Oktavian, A. Mirjafari, P. Z. Moghadam, A. R. Khosropour, H. Beyzavi, *ACS Appl. Mater. Interfaces* **2021**, *13*, 6349.

[19] D. Wöhrle, D. Meissner, *Adv. Mater.* **1991**, *3*, 129.

[20] A. P. Côté, A. I. Benin, N. W. Ockwig, M. O'Keeffe, A. J. Matzger, O. M. Yaghi, *Science* **2005**, *310*, 1166.

[21] M. S. Lohse, T. Bein, *Adv. Funct. Mater.* **2018**, *28*, 1705553.

[22] F. J. Uribe-Romo, J. R. Hunt, H. Furukawa, C. Klöck, M. O'Keeffe, O. M. Yaghi, *J. Am. Chem. Soc.* **2009**, *131*, 4570.

[23] S. Bi, C. Yang, W. Zhang, J. Xu, L. Liu, D. Wu, X. Wang, Y. Han, Q. Liang, F. Zhang, *Nat. Commun.* **2019**, *10*, 2467.

[24] X. Xu, R. Ray, Y. Gu, H. J. Ploehn, L. Gearheart, K. Raker, W. A. Scrivens, *J. Am. Chem. Soc.* **2004**, *126*, 12736.

[25] A. Sciortino, A. Cannizzo, F. Messina, *C* **2018**, *4*, 67.

[26] Q. Gao, X. Li, G.-H. Ning, K. Leng, B. Tian, C. Liu, W. Tang, H.-S. Xu, K. P. Loh, *Chem. Commun.* **2018**, *54*, 2349.

[27] S. Dalapati, E. Jin, M. Addicoat, T. Heine, D. Jiang, *J. Am. Chem. Soc.* **2016**, *138*, 5797.

[28] X. Ma, Y. Yang, R. Ma, Y. Zhang, X. Zou, S. Zhu, X. Ge, Y. Yuan, W. Zhang, G. Zhu, *Chem. Sci.* **2020**, *11*, 12187.

[29] S. Wang, L. Guo, L. Chen, L. Wang, Y. Song, *ACS Appl. Nano Mater.* **2022**, *5*, 1339.

[30] Y. Song, L. Guo, Y. Du, L. Yang, L. Wang, *Chem. Commun.* **2020**, *56*, 14913.

[31] J. Cui, L. Kan, Z. Li, L. Yang, M. Wang, L. He, Y. Lou, Y. Xue, Z. Zhang, *Talanta* **2021**, *228*, 122060.

[32] J. Liang, W. Li, J. Chen, X. Huang, Y. Liu, X. Zhang, W. Shu, B. Lei, H. Zhang, *J. Mater. Chem. A* **2022**, *10*, 23384.

[33] H. Zhong, R. Sa, H. Lv, S. Yang, D. Yuan, X. Wang, R. Wang, *Adv. Funct. Mater.* **2020**, *30*, 2002654.

[34] A. C. Jakowetz, T. F. Hinrichsen, L. Ascherl, T. Sick, M. Calik, F. Auras, D. D. Medina, R. H. Friend, A. Rao, T. Bein, *J. Am. Chem. Soc.* **2019**, *141*, 11565.

[35] S. Bhattacharyya, F. Ehrat, P. Urban, R. Teves, R. Wyrwich, M. Doeblinger, J. Feldmann, A. Urban, J. Stolarczyk, *Nat. Commun.* **2017**, *8*, 1401.

[36] M. K. Barman, S. Bhattacharyya, A. Patra, *Phys. Chem. Chem. Phys.* **2013**, *15*, 16834.

[37] J. H. Gorvin, *J. Chem. Soc.* **1959**, *0*, 678.

[38] J. Lu, J. Zhang, *J. Mater. Chem. A* **2014**, *2*, 13831.

[39] G. Koßmehl, P. Beimling, G. Manecke, *Die Makromol. Chemie* **1983**, *184*, 627.

[40] B. C. M. Martindale, G. A. M. Hutton, C. A. Caputo, S. Prantl, R. Godin, J. R. Durrant, E. Reisner, *Angew. Chemie Int. Ed.* **2017**, *56*, 6459.

[41] H. Peng, J. Travas-Sejdic, *Chem. Mater.* **2009**, *21*, 5563.

[42] A. Bruno, M. Alfe, B. Apicella, C. de Lisio, P. Minutolo, *Opt. Lasers Eng.* **2006**, *44*, 732.

[43] M. Chenchiliyan, H. K. Sadhanala, K. Sharma, A. Le Marois, A. Gedanken, D. Fixler, *Fluorescence depolarization studies of heteroatom-doped CDs*, in *Proc. SPIE* **2019**, *10891*, 108911J.

[44] K. Bramhaiah, R. Bhuyan, S. Mandal, S. Kar, R. Prabhu, N. S. John, M. Gramlich, A. S. Urban, S. Bhattacharyya, *J. Phys. Chem. C* **2021**, *125*, 4299.

[45] X. Zhao, J. Zhang, L. Shi, M. Xian, C. Dong, S. Shuang, *RSC Adv.* **2017**, *7*, 42159.

[46] F. Kubelka, P. and Munk, *Zeitschrift für Tech. Phys.* **1931**, *12*, 593.

[47] M. Fu, F. Ehrat, Y. Wang, K. Z. Milowska, C. Reckmeier, A. L. Rogach, J. K. Stolarczyk, A. S. Urban, J. Feldmann, *Nano Lett.* **2015**, *15*, 6030.

[48] Y. Wang, A. Hu, *J. Mater. Chem. C* **2014**, *2*, 6921.

[49] A. K. Saini, C. M. Carlin, H. H. Patterson, *J. Polym. Sci. Part A Polym. Chem.* **1993**, *31*, 2751.

[50] T. Sick, J. M. Rotter, S. Reuter, S. Kandambeth, N. N. Bach, M. Döblinger, J. Merz, T. Clark, T. B. Marder, T. Bein, D. D. Medina, *J. Am. Chem. Soc.* **2019**, *141*, 12570.

[51] M. Calik, T. Sick, M. Dogru, M. Döblinger, S. Datz, H. Budde, A. Hartschuh, F. Auras, T. Bein, *J. Am. Chem. Soc.* **2016**, *138*, 1234.

[52] S. Chen, T. Sun, M. Zheng, Z. Xie, *Adv. Funct. Mater.* **2020**, *30*, 2004680.

5.7. Appendix B

5.7.1. Materials and Methods

General: All chemicals and materials were purchased from Aldrich, Fluka, Acros, Activate Scientific, or TCI Europe in the common purities purum, puriss, or reagent grade. Materials were used as received without additional purification and handled under air unless noted otherwise. All used solvents were anhydrous and purged with inert gas.

Nitrogen sorption measurement. Nitrogen sorption isotherms were recorded on a Quantachrome Autosorb 1 at 77 K within a pressure range from P/P_0 = 0.001 to 0.98. Prior to the measurement of the sorption isotherms, the samples were heated for 24 h at 120 °C under turbo-pumped vacuum. For the evaluation of the surface area the BET model was applied between 0.05 and 0.28 P/P_0. Pore size distributions were calculated using the QSDFT equilibrium model with a carbon kernel for cylindrical pores.

Powder X-ray diffraction (PXRD) measurements. Powder X-ray diffraction measurements were performed on a Bruker D8 Discover diffractometer using Ni-filtered Cu Kα radiation and a position sensitive LynxEye detector in Bragg-Brentano geometry.

The **structure models of the COFs** were constructed on the basis of the previously reported Imine-BDT-ETTA COF structure[3] using the Accelrys Materials Studio software package. For each COF *P6* symmetry was applied. The structure models were optimized using the Forcite module with the Dreiding force-field. Structure refinements using the Pawley method were carried out as implemented in the Reflex module of the Materials Studio software. Thompson-Cox-Hastings peak profiles were used, and peak asymmetry was corrected using the Berar-Baldinozzi method.

Solid state ^{13}C NMR analysis. The solid state ^{13}C cross-polarization magic angle spinning (CP/MAS) spectra were obtained on a Bruker Avance III-500 solid state NMR spectrometer with a 4 mm double resonance MAS probe and at a MAS rate of 10.0 kHz with a contact time of 2-5 ms and a pulse delay of 4 s.

Infrared (IR) spectra. Infrared (IR) spectra were recorded on a Perkin Elmer Spectrum BX II FT-IR system and a Thermo Scientific Nicolet™ 6700 FT-IR spectrometer in transmission mode. IR data are reported in wavenumbers (cm^{-1}).

Ultraviolet–Vis–infrared absorption spectra. Ultraviolet–Vis–infrared absorption spectra were recorded on a Perkin-Elmer Lambda 1050 spectrometer equipped with a 150 mm integrating sphere.

Scanning electron microscopy (SEM) images. SEM images were recorded with an FEI Helios NanoLab G3 UC scanning electron microscope equipped with a field emission gun operated at 3 kV. Prior to the measurements, the samples were sputtered with carbon.

Transmission electron microscopy (TEM) images. TEM images were recorded with an FEI Titan Themis 60 - 300 equipped with a field emission gun operated at 300 kV.

X-ray photoelectron spectroscopy (XPS) measurement. The XPS measurements were performed with a VSW TA10 X-ray source providing non-monochromatized Al Kα radiation ($h\nu$ = 1486.6 eV) set at 15 mA and 12 kV and a VSW HA100 hemispherical analyzer. The spectra were recorded with a pass energy of 22 eV and a dwell time of 0.1 s per measurement

point. The samples were prepared by drop-casting a dispersion of the respective COF powder in acetonitrile on a silicon wafer. After drying the samples by 60 ºC for 24 h they were transferred to the UHV chamber. The obtained spectra were fitted in Igor Pro 6.0.2.4 using a convolution of Doniach-Ŝunjić and Gaussian functions after a linear background subtraction. For advanced data analysis we applied CasaXPS 2.3.15 processing software based on the survey spectra of the samples.[4]

Photodeposition of Pt and photocatalytic setup. For each photocatalytic assay, 5 mg of the as-prepared COFs were dispersed in 50 mL of ascorbic acid (H_2A) aqueous solution with concentration varying from 2 to 10 mM. Following, a proper amount of platinum precursor (H_2PtCl_6) was added to the suspension in order to obtain 1.0 wt% of platinum loading. The suspension was sonicated for 30 minutes. A custom-made jacketed borosilicate reactor was used to conduct the photocatalytic reactions, which was kept at 20 ºC through a circulating bath. The reactor was illuminated by a Newport 300 W arc Xe lamp, using a 420 nm LP filter. The irradiation intensity was adjusted to 100 mW cm^{-2} using a Newport 1916-C powermeter equipped with an 818-UV/DB optical detector.

Photocatalytic H_2 production tests. During the H_2 evolution experiments, aliquots of 500 µL were sampled from the headspace of the reactor, using a gas-tight syringe, and then injected in a PerkinElmer Clarus 580 gas chromatograph equipped with a thermal conductivity detector (GC-TCD). A molecular sieve coupled with a Porapak N column was used to separate the gas products. Argon was used as carrier gas at 10 mL min^{-1} and the TCD filament was kept at 250 ºC.

The generated H_2 was quantified using a calibration curve established by sampling known concentrations of analytical standard H_2 under the same experimental conditions as the photocatalytic assays. Control experiments conducted in the absence of light, platinum precursor, or sacrificial agent showed no H_2 evolution, confirming the necessity of these components for the reaction.

The photonic efficiency of a photocatalytic system is determined by the ratio between the number of reacted molecules and the number of incident photons. It is expressed as follows:

$$\xi = \frac{v_{H2}}{I_0} \times 100\% \qquad (5.1)$$

ξ is the photonic efficiency (%), v_{H2} is the H_2 evolution rate (mol s^{-1}), I_0 is the photon flux at 450 nm (einstein s^{-1}), the wavelength at which both samples exhibit maximum absorption.

For amide-COF, the highest H_2 evolution rate obtained was $1.7x10^{-3}$ mol g^{-1} h^{-1}, which corresponds to:

$$\frac{1.7 \times 10^{-3}\ \text{mol g}^{-1}\ \text{h}^{-1} \times 0.005\ \text{g}}{3600\ \text{s}} = 2.4 \times 10^{-9}\ \text{mol s}^{-1}$$

The photon flux at 450 nm, considering a 3.0 cm diameter round-shaped beam with intensity of 100 mW cm^{-2}, is approximately $2.67x10^{-6}$ einstein s^{-1}. Thus, the photonic efficiency is calculated as follows:

$$\xi = \frac{2.4\times10^{-9}}{2.67\times10^{-6}} \times 100\% = 0.09\%$$ (Amide-BDT-ETTA COF)

Similarly, for imine-COF, the highest H_2 evolution rate was $5.6x10^{-10}$ mol s^{-1}, resulting in photonic efficiency of:

$$\xi = \frac{2.4\times10^{-9}}{2.67\times10^{-6}} \times 100\% = 0.02\%$$ (Imine-BDT-ETTA COF)

Cyclic voltammetry (CV) measurements. COF working electrodes were prepared using an ink made by mixing 5 mg of COF and 3 mg of carbon black in 50 uL of Nafion (~5 % in a mixture of lower aliphatic alcohols and water) and 450 uL of dimethylformamide. The mixture was then sonicated for 30 minutes. Subsequently, the prepared ink was drop-cast onto the surface of clean FTO glass. The obtained films were dried under vacuum and then used as anodes for the electrochemical experiments. The electrochemical setup was made of a single chamber electrochemical cell, filled with 0.1 M NBu_4PF_6 in acetonitrile, using a Pt wire as counter electrode and Ag as pseudo-reference standardized to the ferrocene/ferrocenium couple. The CV measurements were carried out on an Autolab PGSTAT204 potentiostat/galvanostat at 0.1 V s^{-1} scan speed. The pH dependent absolute potential for the HER was calculated as follows:

$$E_{Abs,\,pH} = -4.5\ \text{eV} + 0.059 \cdot \text{pH} \qquad (5.2)$$

The band edges of the studied COFs were calculated considering that the absolute energy of the Fc/Fc^+ redox couple is -5.14 eV relative to the vacuum level, as described elsewhere.[3]

Zeta potential measurements. Zeta potential measurements were recorded using a Malvern Zetasizer instrument at room temperature using 10 mm path length cuvettes by determining the electrophoretic mobility and then applying the Henry equation. The electrophoretic mobility is obtained by performing an electrophoresis experiment on the sample and measuring the velocity of the particles using Laser Doppler Velocimetry (LDV).

Henry equation:

$$\zeta = \frac{3\eta U_e}{2\varepsilon f(\kappa a)} \qquad (5.3)$$

ζ is zeta potential, calculated from electrophoretic mobility (mV), η is the viscosity of the medium (in this study 0.8872 mPa s), U_e is electrophoretic mobility, measured directly in a given sample in each round of experiment ($m^2\ V^{-1}\ s^{-1}$), ε is dielectric constant (in this study 78.5), $f(\kappa a)$ is Henry's function. According to the Smoluchowski approximation, which is typically used for aqueous samples, $f(\kappa a)$ = 1.5.

The samples for the measurement were prepared as follows. 1 mg of the COF was dispersed in 20 ml water following by adding the appropriate amount of H_2A to achieve 2 to 10 mM in the final suspensions. Measurements were performed in three independent rounds, with each round consisting of 50 measurement cycles.

5.7.2. Synthetic procedures

Benzo[1,2-*b*:4,5-*b*']dithiophene-2,6-dicarboxaldehyde (BDT).

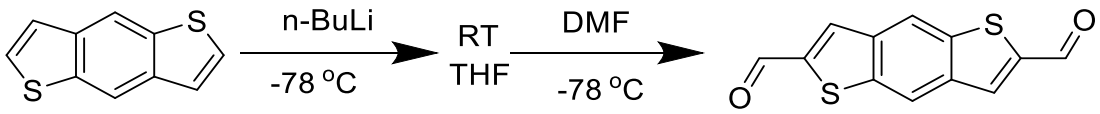

2,6-benzo[1,2-b:4,5-b′]dithiophene dialdehyde (BDT) was synthesized as reported in the literature.[1] Benzo[1,2-*b*:4,5-*b*']dithiophene (1.0 g, 5.3 mmol) was dissolved in 100 mL anhydrous, inhibitor-free THF in an outgassed 250 mL flask under nitrogen atmosphere. The

stirred solution was cooled to -78°C in a dry ice/acetone cooling bath. A solution of *n*-butyl lithium (5.0 mL, 2.5 M in *n*-hexane, 12.5 mmol) was added dropwise within 10 minutes. The solution was stirred for 30 minutes at -78°C and after removal of the cooling bath for 1 h at room temperature. The solution was then cooled again to -78°C and DMF (1.0 mL, 13.0 mmol) was added dropwise. After stirring overnight, the solution was poured into ice water and filtered. The yellow precipitate was washed with water several times and further treated with small amounts of MeOH and Et_2O. The solid was dried under reduced pressure, giving a yellow solid with 46% yield. ^{1}H NMR (400 MHz, DMSO-*d6*) δ (ppm): 8.53 (s, 2H), 8.89 (s, 2H), 10.20 (s, 2H); ^{13}C NMR (100 MHz, DMSO-*d6*) δ (ppm): 121.6, 135.3, 138.4, 138.9, 144.9, 186.6.

Imine-BDT-ETTA COF.

Under argon atmosphere, BDT (benzo[1,2-b:4,5- b′]dithiophene-2,6-dicarboxaldehyde, 74 mg, 0.30 mmol) and ETTA (1,1,2,2-tetra(p-aminophenyl)ethylene, 58.6 mg, 0.15 mmol) were suspended in a solvent mixture of benzyl alcohol and mesitylene (v/v 9:1, 5 mL) in a 25 mL Schott-Duran vial. Acetic acid (6 M, 500 μL) was added to the vessel, and the mixture was placed in a preheated oven at 120 °C for 3 days. The resulting orange precipitate was suction filtered, Soxhlet-extracted with dry THF, and dried under reduced pressure, yielding 70 mg of the final material (53% yield).

Amide-BDT-ETTA COF.

Conversion of BDT-ETTA from imine to amide linkages was adapted from the literature.[2] 10 mg of Imine-BDT-ETTA was dispersed in 10 ml of dioxane and the mixture was ultrasonicated for 30 min to obtain a uniform dispersion. The mixture was then centrifuged to separate the solid and liquid phases, and the excess dioxane was removed to obtain a final volume of 1 ml. To a suspension of Imine-BDT-ETTA (10 mg, 0.025 mmol by imine) in dioxane (1 mL) was added 2-methyl-2-butene (1274 μL, 12.0 mmol, 480 equiv), aqueous sodium chlorite solution (200 μL, 3.3 M, 0.66 mmol, 26.4 equiv), and glacial acetic acid (68.8 μL, 1.2 mmol, 48 equiv) in sequence. The biphasic suspension was let stand without stirring at room temperature in the dark for 48 h, after which an additional portion of sodium chlorite solution (200 μL, 3.3 M, 0.66 mmol, 26.4 equiv) was added. Thereafter, Amide-BDT-ETTA was isolated by filtration and washed with water (10 mL), then 10% sodium thiosulfate (10 mL), then water (10 mL) and

finally acetone (10 mL). This resulting powder was Soxhlet-extracted with methanol and dry THF in sequence, followed by drying under reduced vacuum at room temperature for 16 h, yielding 4 mg of the final material (40% yield).

Reference-COF-1.

10 mg of Imine-BDT-ETTA was dispersed in 10 ml of dioxane and the mixture was ultrasonicated for 30 min to obtain a uniform dispersion. The mixture was then centrifuged to separate the solid and liquid phases, and the excess dioxane was removed to obtain a final volume of 1 ml. To a final suspension of Imine-BDT-ETTA (10 mg, 0.025 mmol by imine) in dioxane (1 mL) was added 2-methyl-2-butene (1274 μL, 12.0 mmol, 480 equiv), and glacial acetic acid (68.8 μL, 1.2 mmol, 48 equiv) in sequence. The biphasic suspension was let stand without stirring at room temperature in the dark for 48 h, after which Reference-COF-1 was isolated by filtration and washed with water (10 mL), then 10% sodium thiosulfate (10 mL), then water (10 mL) and finally acetone (10 mL). The resulting material was Soxhlet-extracted with methanol and dry THF in sequence, followed by drying under reduced vacuum at room temperature for 16 h.

Reference-COF-2.

10 mg of Imine-BDT-ETTA was dispersed in 10 ml of dioxane and the mixture was ultrasonicated for 30 min to obtain a uniform dispersion. The mixture was then centrifuged to separate the solid and liquid phases, and the excess dioxane was removed to obtain a final volume of 1 ml. To a final suspension of Imine-BDT-ETTA (10 mg, 0.025 mmol by imine) in dioxane (1 mL) was added 2-methyl-2-butene (1274 μL, 12.0 mmol, 480 equiv), aqueous sodium chlorite solution (40 μL, 3.3 M, 0.66 mmol, 26.4 equiv), and glacial acetic acid (68.8 μL, 1.2 mmol, 48 equiv) in sequence. The biphasic suspension was let stand without stirring at room temperature in the dark for 48 h, after which Reference-COF-2 was isolated by filtration and washed with water (10 mL), then 10% sodium thiosulfate (10 mL), then water (10 mL) and finally acetone (10 mL). The resulting material was Soxhlet-extracted with methanol and dry THF in sequence, followed by drying under reduced vacuum at room temperature for 16 h.

Reference-COF-3.

10 mg of Imine-BDT-ETTA was dispersed in 10 ml of dioxane and the mixture was ultrasonicated for 30 min to obtain a uniform dispersion. The mixture was then centrifuged to separate the solid and liquid phases, and the excess dioxane was removed to obtain a final volume of 1 ml. To a final suspension of Imine-BDT-ETTA (10 mg, 0.025 mmol by imine) in dioxane (1 mL) was added 2-methyl-2-butene (1274 µL, 12.0 mmol, 480 equiv), and aqueous sodium chlorite solution (200 µL, 3.3 M, 0.66 mmol, 26.4 equiv in sequence. The biphasic suspension was let stand without stirring at room temperature in the dark for 48 h, after which Reference-COF-3 was isolated by filtration and washed with water (10 mL), then 10% sodium thiosulfate (10 mL), then water (10 mL) and finally acetone (10 mL). The resulting material was Soxhlet-extracted with methanol and dry THF in sequence, followed by drying under reduced vacuum at room temperature for 16 h.

5.7.3. Structural analysis

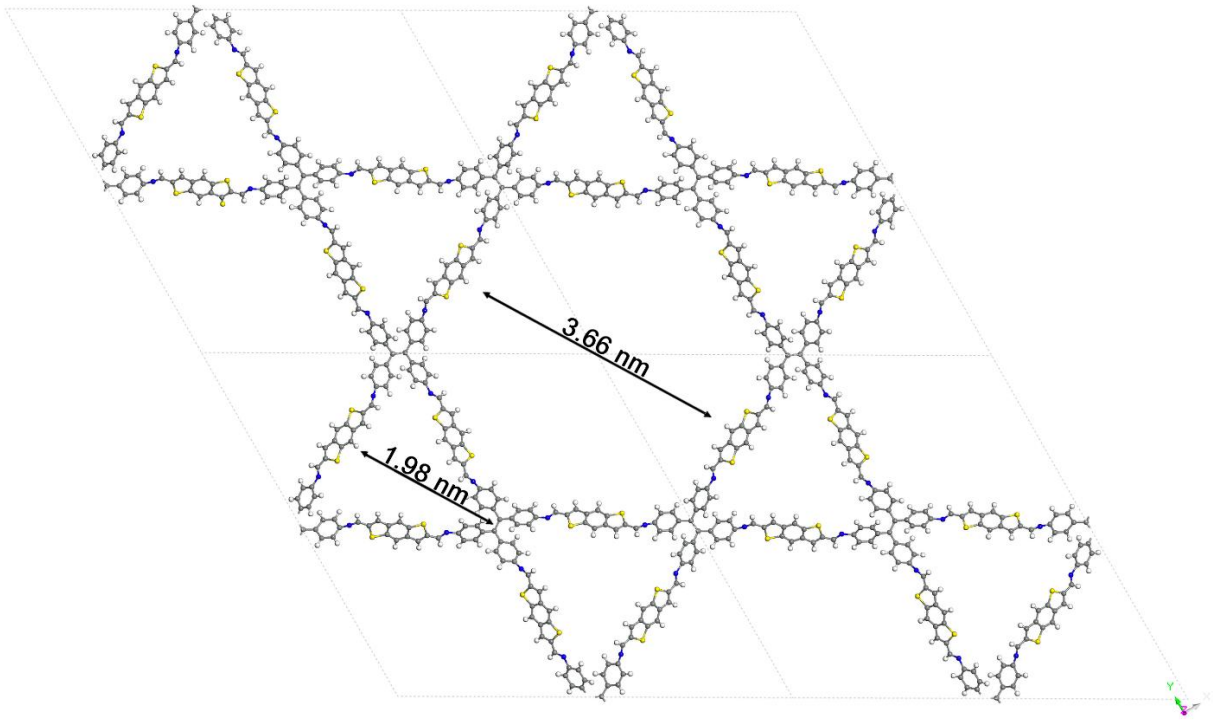

Figure 5.8. Simulated Kagome structure of Imine-BDT-ETTA.

Structural parameters of Imine-BDT-ETTA:

Unit Cell Parameters (*P6*):

$a = b = 4.641$ nm, $c = 0.447$ nm

$\alpha = \beta = 90$ º, $\gamma = 120$ º

Table 5.1. Fractional coordinates of Imine-BDT-ETTA.

C1	C	0.48488	148.320	0.27866
C2	C	0.51472	0.54810	0.28876
C3	C	0.54703	0.52009	0.32098
C4	C	0.57525	0.54268	0.15422
C5	C	0.60616	0.54449	0.19731
C6	C	0.60923	0.52384	0.41010
C7	C	0.58184	0.50322	0.58725
C8	C	0.55167	0.50259	0.55024
C9	C	0.46020	0.42402	0.44830
C10	C	0.46340	0.39632	0.52071
C11	C	0.49111	0.39437	0.43094
C12	C	0.51510	0.41916	0.25108
C13	C	0.51285	0.44705	0.17380
N14	N	0.50224	0.62709	0.55696
C15	C	0.49283	0.64461	0.69314

N16	N	0.63889	0.52197	0.45301
C17	C	0.66745	0.53819	0.31775
C18	C	0.49687	0.32253	0.61467
S19	S	0.46352	0.29767	0.34968
C20	C	0.47186	0.26430	0.42403
C21	C	0.49747	0.27299	0.62728
C22	C	0.51131	0.30666	0.73550
C23	C	0.50801	0.25069	0.71007
C24	C	0.49177	0.21909	0.58145
C25	C	0.46596	0.20993	0.37917
C26	C	0.45541	0.23242	0.29525
C27	C	0.45299	0.17604	0.27100
C28	C	0.46890	0.16145	0.39059
S29	S	0.50186	0.18726	0.65424
H30	H	0.43913	0.42443	0.54517
H31	H	0.44527	0.37716	0.66617
H32	H	0.53703	0.41799	0.18828
H33	H	0.53437	0.46629	0.06758
H34	H	0.53125	0.31766	0.89847
H35	H	0.52801	0.25749	0.86879
H36	H	0.43562	0.22572	0.13452
H37	H	0.43324	0.16431	0.10728

H38	H	0.44331	0.11526	0.14900
H39	H	0.52604	0.36730	0.86435
H40	H	0.62692	0.56104	0.05796
H41	H	0.57300	0.55797	0.01601
H42	H	0.58421	0.48774	0.75540
H43	H	0.53060	0.48739	0.68770

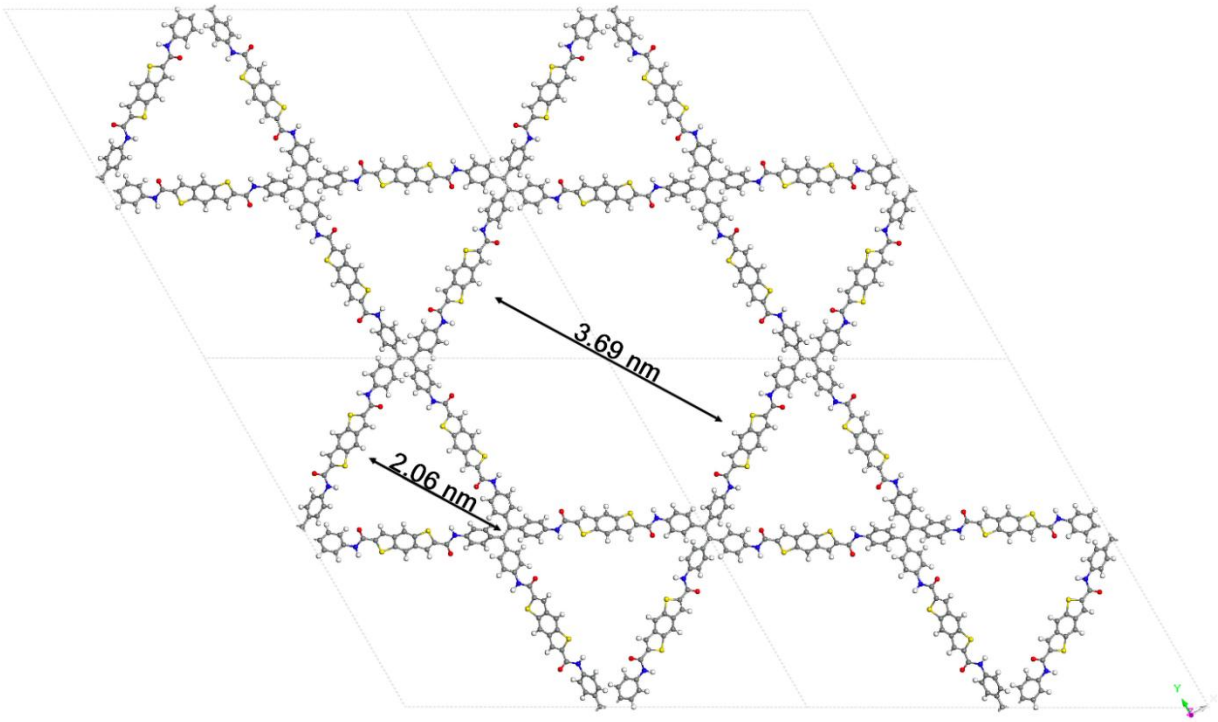

Figure 5.9. Simulated Kagome structure of Amide-BDT-ETTA.

Structural parameters of fully (100%) amidized Amide-BDT-ETTA

Unit Cell Parameters (*P6*):

$a = b = 4.781$ nm, $c = 0.448$ nm

$\alpha = \beta = 90$ º, $\gamma = 120$ º

Table 5.2. Fractional coordinates of fully (100%) oxidized Amide-BDT-ETTA.

C1	C	0.48369	148.521	0.33321
C2	C	0.52241	0.54821	0.33528
C3	C	0.54474	0.51214	0.36387
C4	C	0.57274	0.53115	0.18995
C5	C	0.60124	0.52990	0.23550
C6	C	0.60253	0.50973	0.45772
C7	C	0.57461	0.49027	0.62587
C8	C	0.54663	0.49256	0.58555
C9	C	0.44904	0.42667	0.47581
C10	C	0.44250	0.39460	0.49319
C11	C	0.46443	0.38614	0.37885
C12	C	0.49242	0.40972	0.23659
C13	C	0.49889	0.44180	0.21559
N14	N	0.54176	0.64639	0.41138
C15	C	0.51749	0.65345	0.51616
N16	N	0.63138	0.50794	0.51263
C17	C	0.66389	0.53407	0.46122
C18	C	0.47741	0.31317	0.49350
S19	S	0.44395	0.28097	0.27960
C20	C	0.45949	0.25512	0.39199

C21	C	0.48703	0.27049	0.56985
C22	C	0.49700	0.30428	0.62475
C23	C	0.50238	0.25383	0.67696
C24	C	0.48894	0.22113	0.59735
C25	C	0.46130	0.20576	0.42078
C26	C	0.44601	0.22243	0.31316
C27	C	0.45132	0.17203	0.36452
C28	C	0.47111	0.16316	0.49127
S29	S	0.50475	0.19529	0.70394
H30	H	0.43167	0.43159	0.58390
H31	H	0.42081	0.37645	0.60634
H32	H	0.50947	0.40309	0.14583
H33	H	0.52183	0.45829	0.12074
H34	H	0.51780	0.32048	0.75988
H35	H	0.52386	0.26560	0.81602
H36	H	0.42461	0.21069	0.17309
H37	H	0.43047	0.15590	0.22962
H38	H	0.62193	0.54404	0.09179
H39	H	0.57246	0.54692	0.01774
H40	H	0.57499	0.47426	0.79612
H41	H	0.52558	0.47877	0.71954
O42	O	0.13911	0.50733	0.62913

O43	O	0.89245	0.33146	0.39605
H44	H	0.56552	0.66565	0.38945
H45	H	0.62882	0.48690	0.61184

Structural parameters of partially (50%) oxidized Amide-BDT-ETTA

Unit Cell Parameters (P6):

$a = b = 4.749$ nm, $c = 0.447$ nm

$\alpha = \beta = 90$ º, $\gamma = 120$ º

Table 5.3. Fractional coordinates of partially (50%) oxidized Amide-BDT-ETTA.

C1	C	0.48432	148.461	0.38418
C2	C	0.51927	0.54774	0.38439
C3	C	0.54538	0.51508	0.40932
C4	C	0.57251	0.53551	0.23115
C5	C	0.60187	0.53578	0.26161
C6	C	0.60481	0.51526	0.47096
C7	C	0.57813	0.49539	0.65177
C8	C	0.54930	0.49634	0.62704
C9	C	0.45327	0.42585	0.52296
C10	C	0.44866	0.39449	0.53153
C11	C	0.47148	0.38751	0.41026
C12	C	0.49915	0.41204	0.27012
C13	C	0.50448	0.44361	0.25494

N14	N	0.53394	0.64495	0.43012
C15	C	0.50887	0.65207	0.50951
N16	N	0.63381	0.51315	0.50190
C17	C	0.66179	0.53232	0.37952
C18	C	0.48554	0.31470	0.47330
S19	S	0.45191	0.28421	0.25146
C20	C	0.46618	0.25691	0.35089
C21	C	0.49346	0.27083	0.53285
C22	C	0.50438	0.30459	0.59932
C23	C	0.50760	0.25287	0.63550
C24	C	0.49327	0.22033	0.54624
C25	C	0.46604	0.20650	0.36336
C26	C	0.45191	0.22443	0.26118
C27	C	0.45508	0.17281	0.29547
C28	C	0.47361	0.16255	0.42326
S29	S	0.50726	0.19275	0.64687
H30	H	0.43491	0.42906	0.63342
H31	H	0.42727	0.37546	0.64170
H32	H	0.51695	0.40680	0.17385
H33	H	0.52742	0.46109	0.16548
H34	H	0.52517	0.31964	0.73954
H35	H	0.52878	0.26368	0.77909

H36	H	0.43071	0.21362	0.11768
H37	H	0.43443	0.15785	0.15331
H38	H	0.44718	0.11295	0.24398
H40	H	0.62149	0.55131	0.11336
H41	H	0.57082	0.55106	0.06511
H42	H	0.57985	0.47951	0.81549
H43	H	0.52904	0.48174	0.76732
H44	H	0.55792	0.66413	0.42032
O45	O	0.56058	0.89147	0.58254

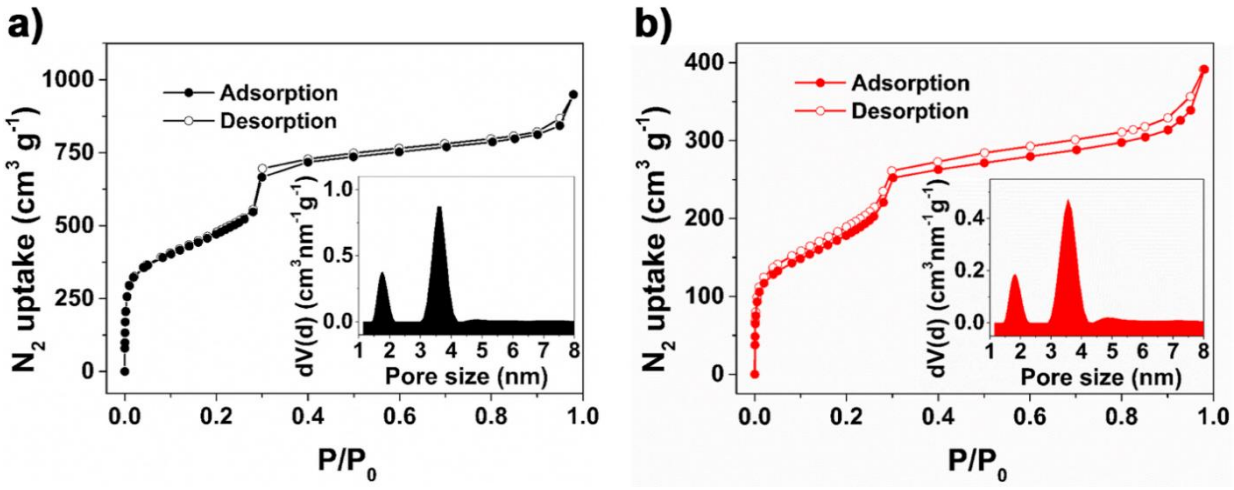

Figure 5.10. Nitrogen sorption isotherms with resulting pore size distribution of (a) Imine-BDT-ETTA and (b) Amide-BDT-ETTA.

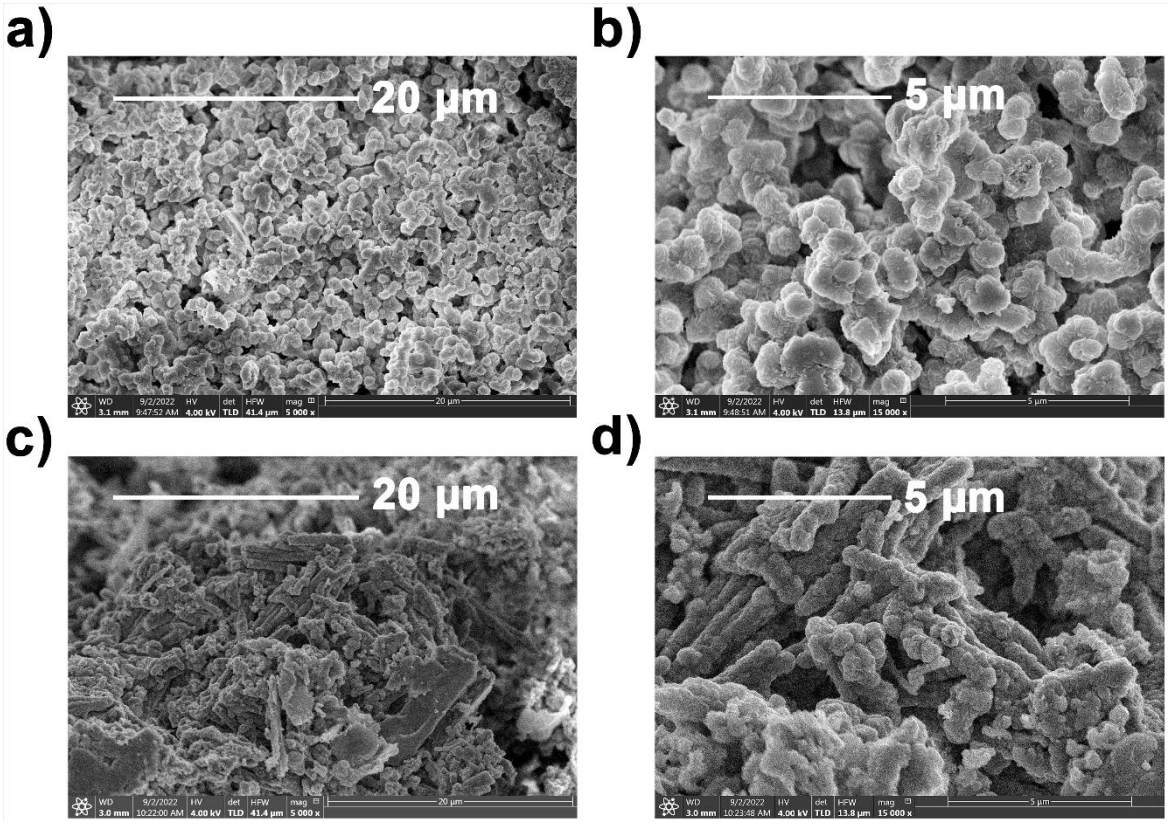

Figure 5.11. SEM images of (a,b) Imine-BDT-ETTA and (c,d) Amide-BDT-ETTA.

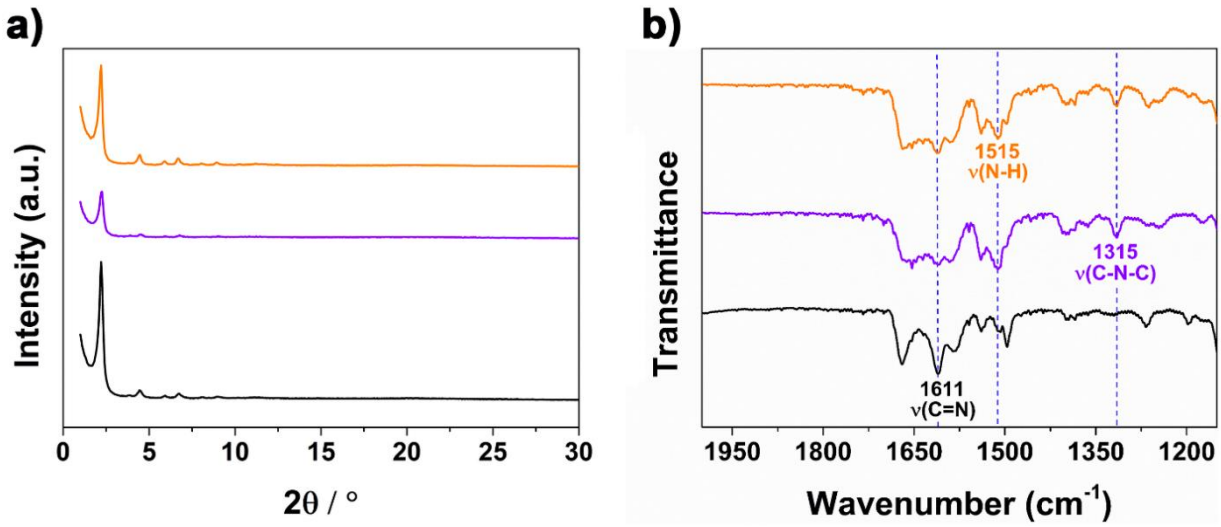

Figure 5.12. (a) PXRD pattern and (b) FT-IR spectra of three reference samples: Reference-COF-1 (black), Reference-COF-2 (purple) and Reference-COF-3 (orange).

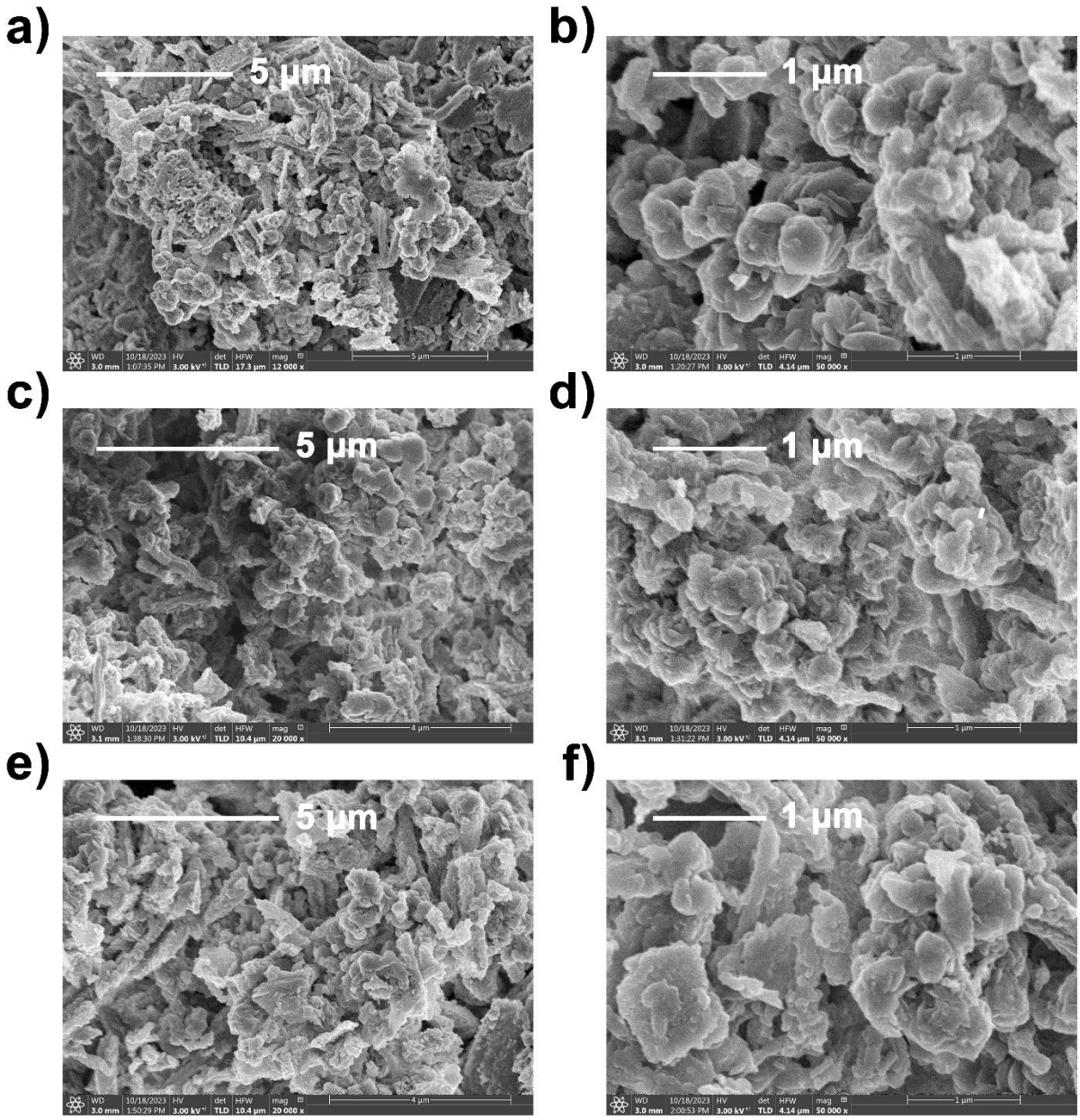

Figure 5.13. SEM images of three reference samples: (a,b) Reference-COF-1, (c,d) Reference-COF-2 and (e,f) Reference-COF-3.

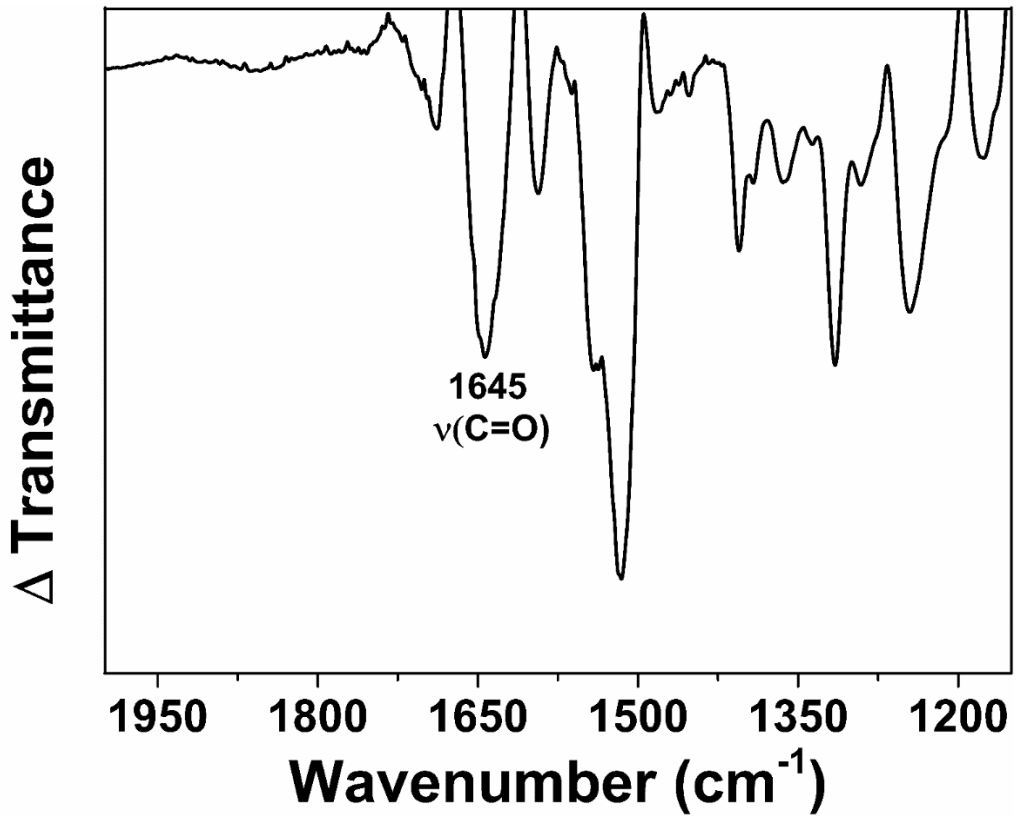

Figure 5.14. FT-IR difference spectrum obtained through the subtraction of the Imine-BDT-ETTA spectrum from Amide-BDT-ETTA spectrum.

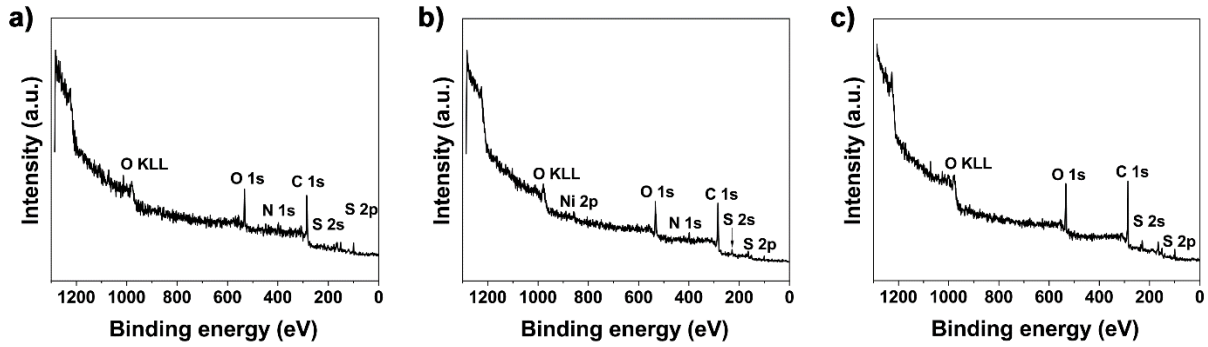

Figure 5.15. Full XPS spectrum of (a) Imine-BDT-ETTA COF, (b) Amide-BDT-ETTA COF and (c) BDT linker. O KLL Auger lines correspond to oxygen Auger transitions with an initial K-shell vacancy and a final double L-shell vacancy. Their kinetic energies remain independent of the ionizing radiation. Ni peak originates from the screws or the sample holder.

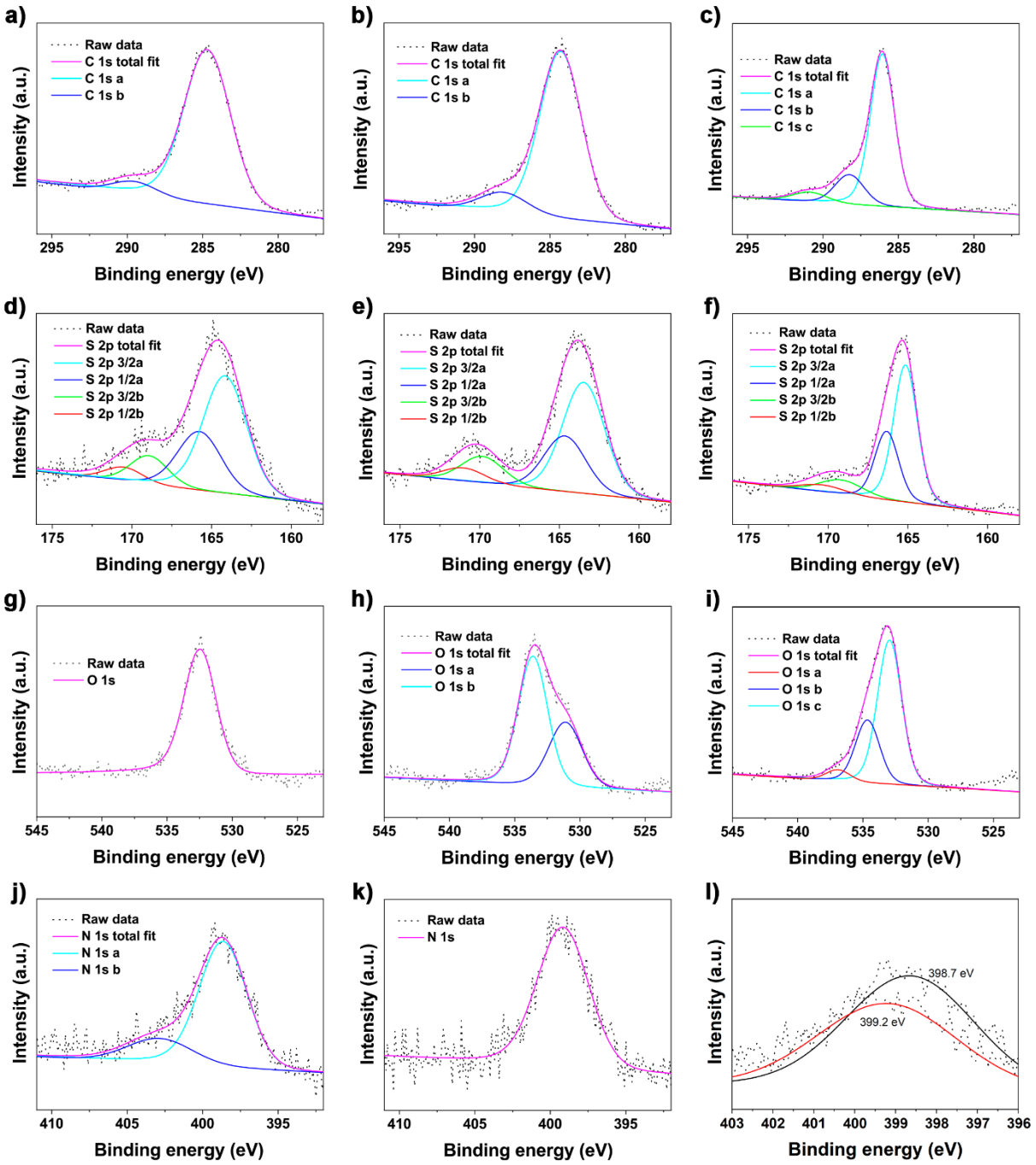

Figure 5.16. Carbon 1s XPS spectra of (a) Imine-BDT-ETTA, (b) Amide-BDT-ETTA and (c) BDT linker. Two carbon environments for both COFs: 284.7 eV and 289.5 eV for Imine-BDT-ETTA, and 284.3 eV and 288.1 eV for Amide-BDT-ETTA. The carbon signals 284.7 eV and 284.3 eV corresponds to overlapping C=C, C–N, and C=N bonds.[5] The higher binding energy peaks indicate oxidized carbon species from surface oxidation. The 288.1 eV peak in Amide-BDT-ETTA suggests a carbonyl (C=O) moiety, while weaker signal at 289.5 eV is assigned to unreacted aldehyde groups at surface terminations and lattice defects. These groups exhibit a higher binding energy due to the reduced electron density surrounding the carbon atoms.[6,7] S 2p XPS spectra of (d) Imine-BDT-ETTA, (e) Amide-BDT-ETTA and (f) BDT linker. Oxygen

1s XPS spectra of (g) Imine-BDT-ETTA COF, (h) Amide-BDT-ETTA COF and (i) BDT linker. Oxygen species between 532 eV and 536 eV correspond to carbonyl groups, amide bonds and sulfonyl groups.[8,9] Nitrogen 1s XPS spectra of (j) Imine-BDT-ETTA and (k) Amide-BDT-ETTA. For Imine-BDT-ETTA revealed two nitrogen species at 398.6 eV (C=N and C–N bonds)[5] and 402.8 eV (ammonium salts).[10] The presence of 402.8 eV signal exclusively in Imine-BDT-ETTA suggests the presence of unreacted (surface-terminating) amino groups remaining after COF formation. For Amide-BDT-ETTA, one nitrogen species was observed at 399.0 eV, which implies in the existence of the C=N and C–N bonds. (l) The comparison between the N 1s spectra of Imine-BDT-ETTA (black) and Amide-BDT-ETTA (red) reveals a shift toward higher binding energy after the amidization process (from 398.7 to 399.2 eV), confirming the efficient conversion of imine to amide.

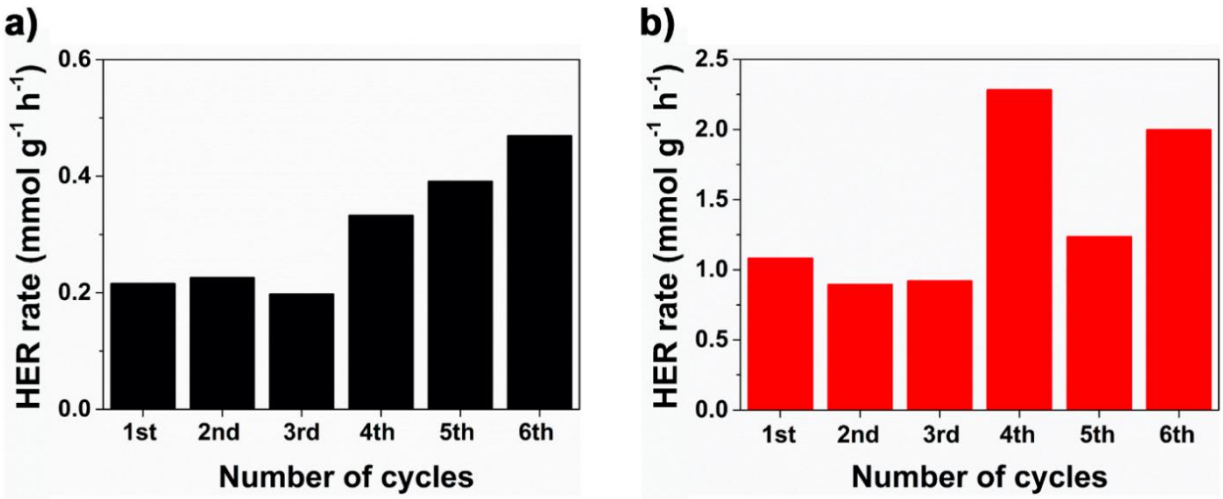

Figure 5.17. HER rates using 10 mM H_2A (1st-3rd cycles) and 2 mM H_2A (4th-6th cycles) for (a) Imine-BDT-ETTA and (b) Amide-BDT-ETTA. Conditions of photocatalytic tests: $\lambda > 420$ nm, 100 mW cm^{-2}, 1 g/L COF suspension in H_2A, 1.0 wt% (Pt/COF) using H_2PtCl_6 precursor.

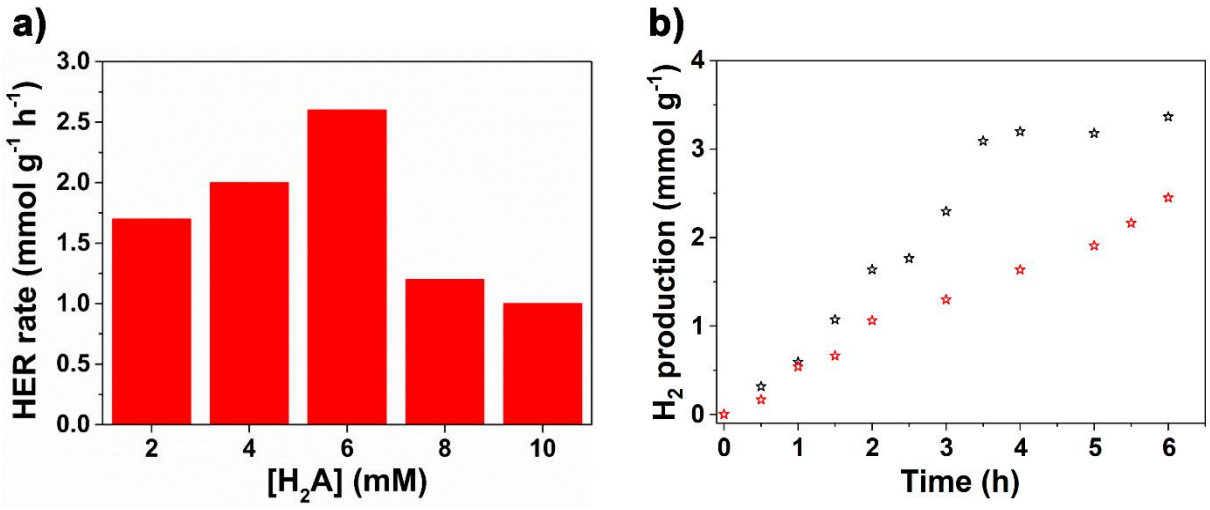

Figure 5.18. (a) HER rates depending on the concentration of H_2A for the Amide-BDT-ETTA. (b) H_2 evolution using 0.75 M TEOA suspension for the Imine-BDT-ETTA (black) and Amide-BDT-ETTA (red). Conditions of photocatalytic tests: $\lambda > 420$ nm, 100 mW cm^{-2}, 1 g/L COF suspension, 1.0 wt% (Pt/COF) using H_2PtCl_6 precursor.

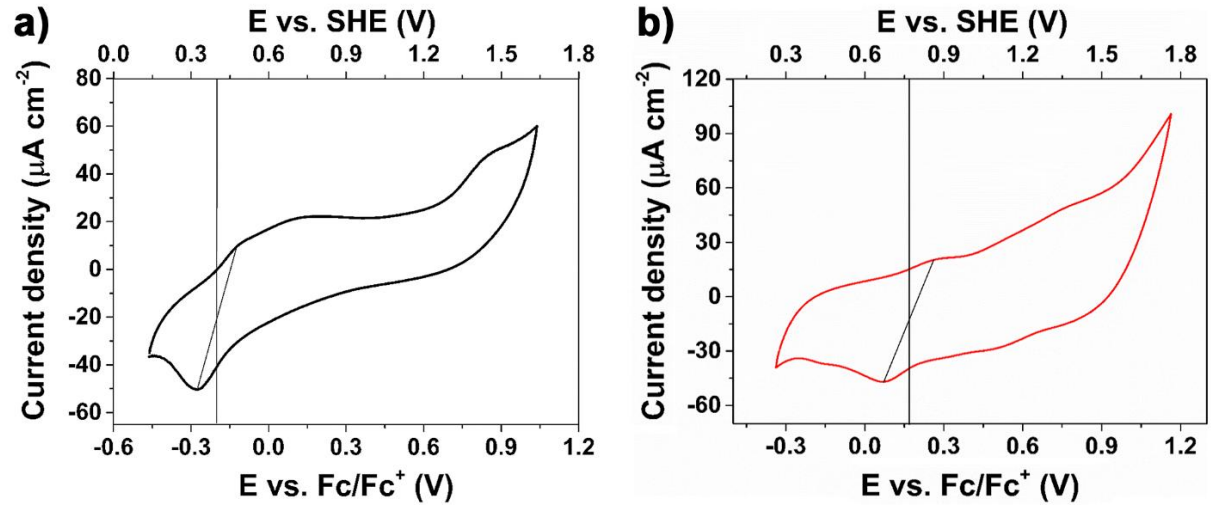

Figure 5.19. CV plot of (a) Imine-BDT-ETTA and of (b) Amide-BDT-ETTA recorded in 0.1 M NBu4PF6 in acetonitrile.

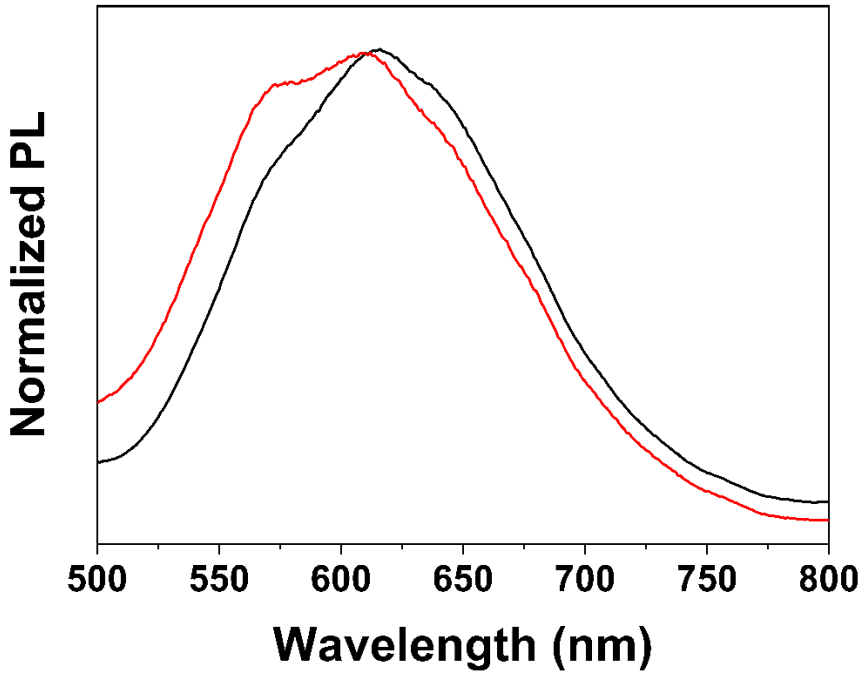

Figure 5.20. PL spectra for Imine-BDT-ETTA (black) and Amide-BDT-ETTA (red).

Table 5.4. pH Values measured at different concentrations of H_2A.

Concentration of H_2A (mM)	**pH value**
0	6.51
2	3.53
4	3.34
6	3.23
8	3.16
10	3.10

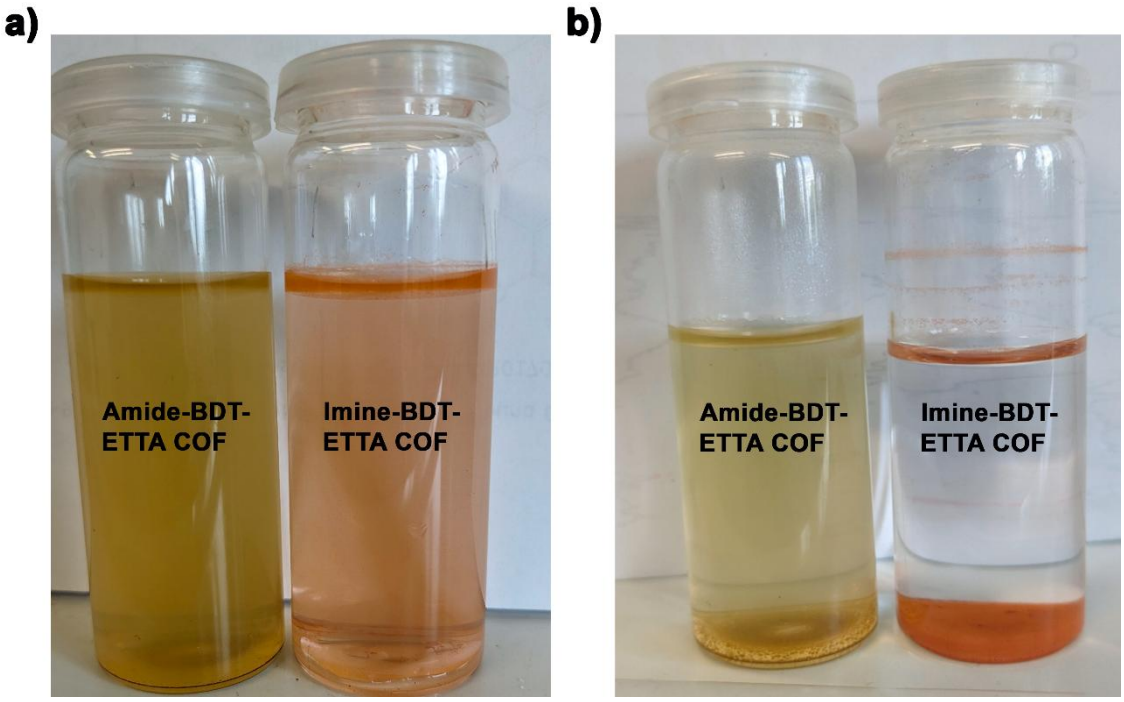

Figure 5.21. Suspensions in water of Amide-BDT-ETTA and Imine-BDT-ETTA (a) after the ultrasonication and (b) one hour after the ultrasonication.

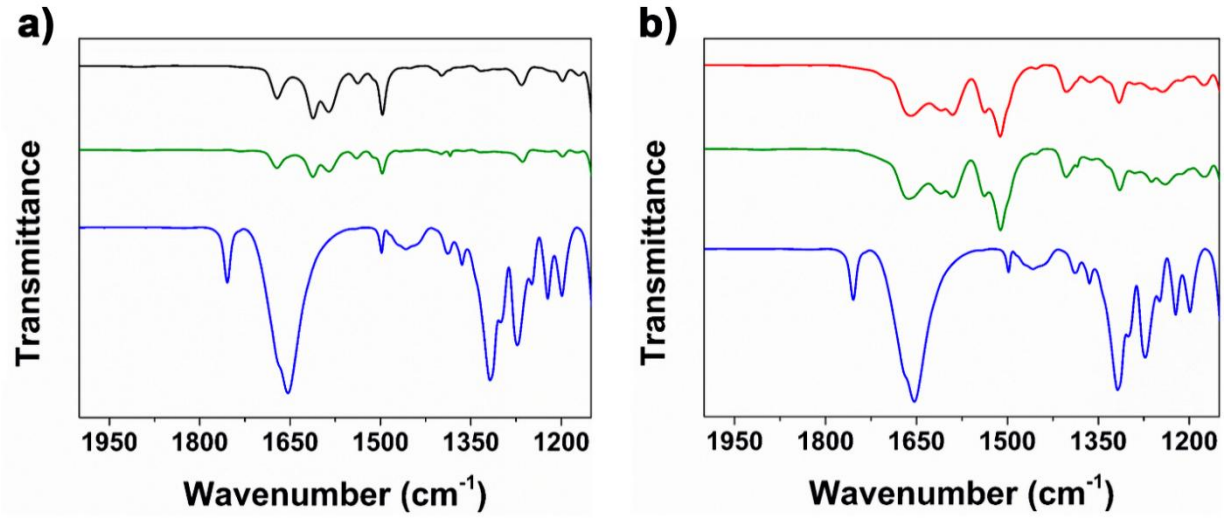

Figure 5.22. FT-IR spectra of (a) Imine-BDT-ETTA (black), Imine-BDT-ETTA treated with H_2A (green) and H_2A (blue) and (b) Amide-BDT-ETTA (red), Amide-BDT-ETTA treated with H_2A (green) and H_2A (blue).

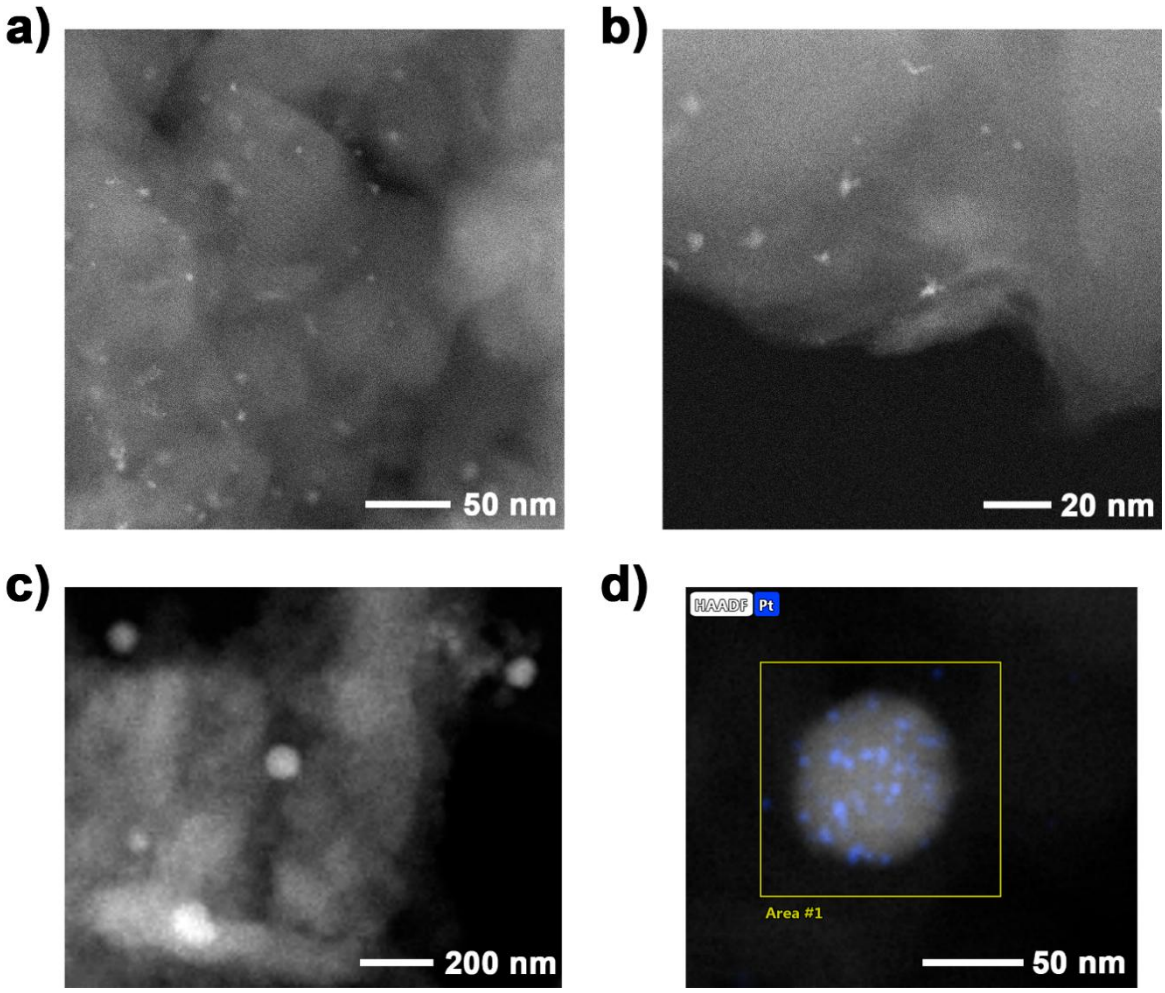

Figure 5.23. Images of Pt particles within (a,b) Imine-BDT-ETTA-COF and (c,d) Amide-BDT-ETTA structure obtained after 13 h illumination. Conditions of illumination: $\lambda > 420$ nm, 100 mW cm^{-2}, 1 g/L COF suspension containing 10 mM H_2A, 1.0 wt% (Pt/COF) using H_2PtCl_6 precursor.

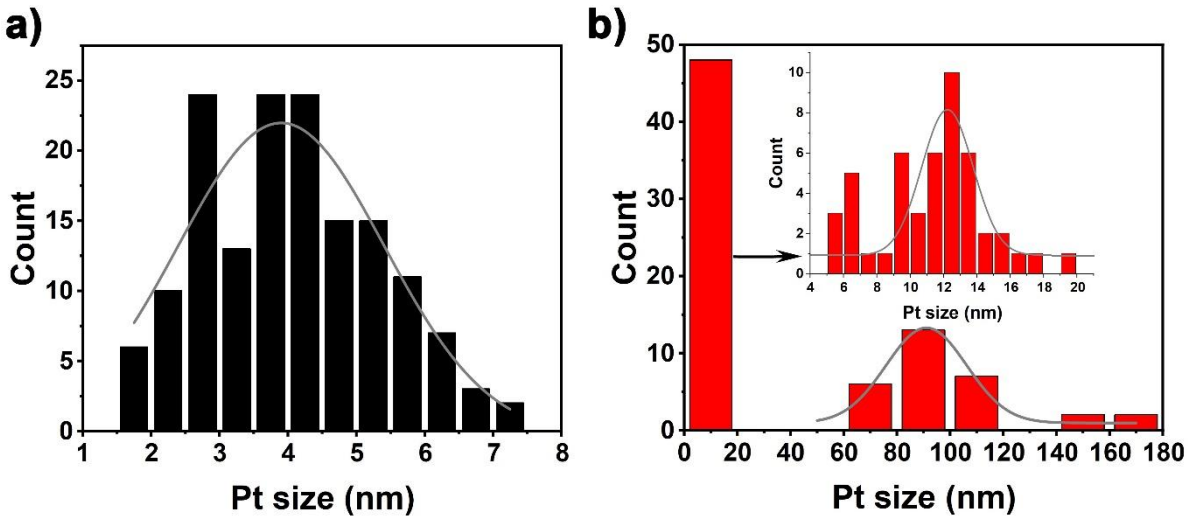

Figure 5.24. Pt size distribution in the (a) Imine-BDT-ETTA-COF and in the (b) Amide-BDT ETTA-COF obtained after 13 h illumination. Conditions of illumination: $\lambda > 420$ nm, 100 mW cm^{-2}, 1 g/L COF suspension containing 10 mM H_2A, 1.0 wt% (Pt/COF) using H_2PtCl_6 precursor.

5.7.4. References

[1] J. M. Rotter, S. Weinberger, J. Kampmann, T. Sick, M. Shalom, T. Bein, D. D. Medina, *Chem. Mater.* **2019**, *31*, 10008.

[2] P. J. Waller, S. J. Lyle, T. M. Osborn Popp, C. S. Diercks, J. A. Reimer, O. M. Yaghi, *J. Am. Chem. Soc.* **2016**, *138*, 15519.

[3] T. Sick, A. G. Hufnagel, J. Kampmann, I. Kondofersky, M. Calik, J. M. Rotter, A. Evans, M. Döblinger, S. Herbert, K. Peters, D. Böhm, P. Knochel, D. D. Medina, D. Fattakhova-dRohlfing, T. Bein, *J. Am. Chem. Soc.* **2018**, *140*, 2085.

[4] G. Greczynski, L. Hultman, *J. Appl. Phys.* **2022**, *132*, 011101.

[5] M. Kehrer, J. Duchoslav, A. Hinterreiter, M. Cobet, A. Mehic, T. Stehrer, D. Stifter, *Plasma Process. Polym.* **2019**, *16*, 1800160.

[6] W. Wang, D. Huang, W. Zheng, X. Zhao, K. He, H. Pang, Y. Xiang, *Chem. Mater.* **2023**, *35*, 7154.

[7] S. Nagakura, *Bull. Chem. Soc. Jpn.* **1952**, *25*, 164.

[8] G. P. López, D. G. Castner, B. D. Ratner, *Surf. Interface Anal.* **1991**, *17*, 267.

[9] B. Folkesson, *Spectrosc. Lett.* **1982**, *15*, 165.

[10] M. Šetka, R. Calavia, L. Vojkůvka, E. Llobet, J. Drbohlavová, S. Vallejos, *Sci. Rep.* **2019**, *9*, 8465

6. Hydrid modification of BDT-ETTA-COF: Carbon Dots doping

This chapter is based on the following article:

Synthetic Control over the Energy Transfer and Charge Transfer between Carbon Dots and Covalent Organic Framework

Published in "Journal of Physics: Energy". **2024**, *6(2)*, 025018.

Julian Feijoo, **Klaudija Paliušytė**, Jenny Schneider*

Department of Chemistry and Center for NanoScience, Ludwig-Maximilians-Universität (LMU) München, Butenandtstraße 5-13, 81377, Munich, Germany, E-mail: jenny.schneider@lmu.de

* Corresponding authors

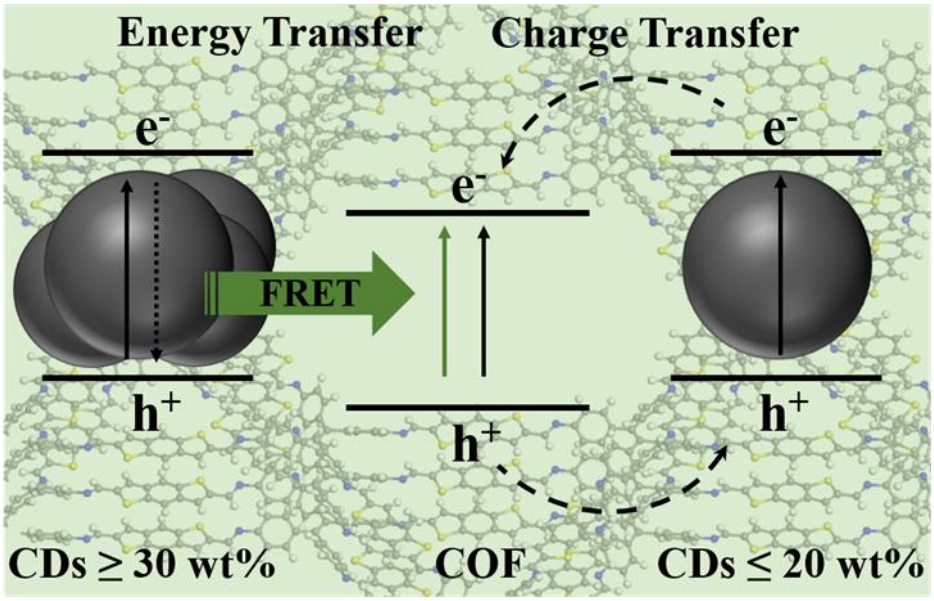

6.1. Abstract

Carbon dots (CDs) are environmentally benign, strongly photoluminescent, metal free nanoparticles. Interfacing them with tailor-made organic semiconductors such as covalent organic frameworks (COFs) promises to yield multifunctional materials. In this study, microwave-derived CDs are successfully incorporated into the porous structure of COF in a

one-pot method in which BDT-ETTA COF is synthesized by the amine and aldehyde condensation between 1,1,2,2-Tetra(p-aminophenyl)ethylene (ETTA) and Benzo[1,2-b:4,5-b']dithiophene-2,6-dicarboxaldehyde (BDT) in the presence of CDs. A detailed structural and optoelectronic characterization of the COF/CDs composite reveals that upon tuning the CDs loadings encapsulated in COF the interaction between both components can be controlled allowing the switch between energy and charge transfer. At CDs loadings ≤ 20 wt%, strong binding of CDs to the COF enables charge transfer evinced from the quenched photoluminescence of both components and accelerated exciton decay kinetics of the COF. At CDs loadings ≥ 30 wt% Förster resonance energy transfer from CDs to COF prevails, leading to enhanced COF photoluminescence. Our study underlines the interaction mechanism in organic composites and provides the knowledge required for the design of novel functional materials with applications in photocatalysis, optoelectronics and sensing.

6.2. Introduction

For a long time, inorganic semiconductors were at the forefront of the functional materials for energy and sensing applications. Since then, the focus of the search for cheap materials that can be produced *via* simple modular construction has shifted toward organic materials.[19] In acknowledgment of these materials, the 2000 Nobel Prize in Chemistry was jointly awarded to Heeger, MacDiarmid and Shirakawa for the discovery of conducting polymers. Recently, a new class of organic semiconductors, namely, Covalent organic frameworks (COFs), has emerged.[20,21] COFs are built by rigid organic building blocks that are covalently connected *via* various reversible reactions, *e.g.,* imine condensation[22] or Knoevenagel condensation[23] By rational selection of the building block's symmetry, three-dimensional or two-dimensional frameworks featuring long-range order and porosity are formed. In addition to their modular structure, COFs are tailor-made materials from the perspective of chemical and physical properties. COFs with specific properties can be designed by installing reactive functional groups or semiconducting organic segments into the building blocks. An intriguing structural property of two-dimensional COFs is their defined, uniform and continuous channels in which guest molecules or particles can be embedded and thus providing a platform for the formation of multifunctional composites.

In this regard, carbon dots (CDs) are an intriguing option.[24] These nanoparticles are made up entirely of abundant, environmentally friendly elements – usually carbon, oxygen, hydrogen and nitrogen – with a wide spectrum of possible applications ranging from optoelectronics, photocatalysis, biomedical imaging, and sensing.[25] The design of the composite materials based on COF and CDs has attracted a lot of attention since by combining two materials with highly tunable properties countless promising applications can be envisioned. Herein, the interactions between the COF and CDs determine the final functionality of the composite. COFs usually have weak emission because of π–π stacking between layers and intramolecular bond rotation.[26,27] Encapsulation of the CDs in the COF's porous structure can lead to an enhanced emission yield of the COF *via* energy transfer from CDs to COF. Ma *et al.* showed that when the emission spectra of CDs overlap with the absorption spectra of the COF, Förster resonance energy transfer (FRET) occurs resulting in a strong COF PL.[28] The PL was dynamically quenched in the presence of Cu^{2+}, allowing the sensitive detection of this metal. Song *et al.* prepared a similar system that allowed the detection of Fe^{3+} and Cu^{2+}.[29,30] Cui *et al.* developed an aptasensor employing COF and CDs.[31] The CDs were non-covalently bound to COF and their PL were quenched due to energy transfer to COF. The presence of a certain biomolecule causes the detachment of CDs from the surface and recovery of their original emission. In the case of strong interactions between COF and CDs charge transfer (CT) at the interface of the composite might occur thus suppressing the undesired recombination of the photogenerated charge carriers. Interactions involving charge transfer are crucial in the photocatalytic and optoelectronic applications. Zhang *et al.* reported the construction of the COF/CDs composite promoting high-flux CT and efficient photocatalytic activity for antibacterial photocatalytic therapy.[32] Zhong *et al.* reported COF/CDs composite system for efficient photocatalytic CO_2 to CO reduction.[33] Although the proof of principle for CT and FRET in COF/CDs composites has been demonstrated the control over these two processes *via* the concentration of embedded CDs in COF has not been yet reported.

In this study, a two-dimensional COF constructed from 1,1,2,2-Tetra(p-aminophenyl)ethylene (ETTA) and Benzo[1,2-b:4,5-b']dithiophene-2,6-dicarboxaldehyde (BDT) is combined with CDs synthesized by a simple and quick microwave approach. BDT-ETTA COF exhibits suitable features for the studies on energy and charge transfer in COF/CDs composite. BDT-ETTA COF possesses high crystallinity and porosity, photoluminescence and efficient charge

separation due to the acceptor and donor character of the ETTA and BDT units, respectively, so that the charge transport to CDs can compete with the recombination.[34] Carbon dots synthesized from citric acid (CA) and branched polyethyleneimine (BPEI) have previously shown both photocatalytic activity and strong luminescence.[35] Detailed spectroscopic and structural analysis reveals that the energetic interactions between COF and CDs depend on the structural arrangement of the composite, which was controlled *via* adjusting the CDs loading.

6.3. Methods

6.3.1. Synthesis of CDs

The CDs were synthesized according to the literature reports.[35,36] A branched Polyethylenimine (BPEI) purchased from Sigma-Aldrich and anhydrous citric acid purchased from Merck served as precursors for the CDs synthesis. Herein, citric acid (1 g) and BPEI (2 g) were dissolved in 20 mL of milli-Q water and stirred at 60 °C for 10 minutes. The volume was adjusted to 50 mL with water and transferred to the microwave reactor. The sample was then heated at 190 °C for 30 minutes. The maximum heating rate was set to 900 W. The resulting yellow solution was purified by centrifugation at 25000 RCF, followed by filtering through a 0.2 µm pore size syringe filter, and freeze drying. The obtained brownish powder was ground with pestle and mortar before use in the COF syntheses.

6.3.2. Synthesis of BDT-ETTA COF and COF/CDs composite

6.3.2.1 Synthesis of ETTA

1,1,2,2-Tetraphenylethylene (3.0 g, 9.0 mmol) was slowly added with stirring at 0 °C to a mixture of 30 mL nitric acid (≥ 99%) and 30 mL glacial acetic acid followed by stirring for three hours at room temperature. Then the solution was diluted with cold water. The resulting precipitate was filtered and dried under reduced pressure. Recrystallization from 1,4-dioxane, filtration and drying resulted in a yellow solid of 1,1,2,2-Tetra(p-nitrophenyl)ethylene (TNPE) with 69 % yield.[37] 1H NMR (400 MHz, $CDCl_3$) δ (ppm): 8.055-8.100 (m, 8H), 7.16-7.21 (m, 8H).

20 mL of anhydrous THF was used to dissolve TNPE (1.0 g, 1.9 mmol) under nitrogen atmosphere. Under further stirring 4 g of Raney-nickel catalyst slurry was added.[38] Followed by the dropwise addition of Hydrazine monohydrate (1.3 mL, 26 mmol) to the mixture. The

mixture was heated to reflux for two hours. After cooling to room temperature and filtration, the filtrate was dried under reduced pressure leading to a yellow solid of ETTA with 79% yield. 1H NMR (400 MHz, DMSO-d6) δ (ppm): 6.60-6.55 (m, 8H), 6.29-6.24 (m, 8H), 4.84 (s, 8H).

6.3.2.2 Synthesis of BDT

The synthesis of BDT was adapted from ref.[39] Herein, Benzo[1,2-b:4,5-b']dithiophene (1.0 g, 5.3 mmol) was dissolved in 100 mL anhydrous THF in an outgassed flask under nitrogen atmosphere. The cooling to -78°C of the stirred mixture was conducted in a dry ice/acetone cooling bath. A solution of n-butyl lithium (5.0 mL, 2.5 M in n-hexane, 12.5 mmol) was added dropwise within 10 minutes. Stirring for 30 min at -78°C and then for one hour at room temperature were performed. The cooling to -78°C was repeated followed by the dropwise addition of DMF (1.0 mL, 13.0 mmol) and stirring overnight. The solution was then transferred into ice water and filtered. The yellow precipitate was washed with water several times and further treated with MeOH and Et_2O. The solid was dried under reduced pressure leading to a yellow solid of BDT with 46% yield. 1H NMR (400 MHz, DMSO-d6) δ(ppm): 8.53 (s, 2H), 8.89 (s, 2H), 10.20 (s, 2H).

6.3.2.3 Synthesis of BDT-ETTA COF and COF/CDs composite

BDT (4.94 mg, 0.0201 mmol), ETTA (3.94 mg, 0.0100 mmol) and CDs (between 0 and 17.76 mg) were added to a culture tube. Benzyl alcohol and mesitylene (V/V 9:1, 500 μL) were added. The mixture was mixed with a pipette before adding acetic acid (6M, 50 μL). The tube was sealed and kept at 120 °C for 3 days. The resulting precipitate was filtered, washed and extracted with THF.

6.3.3. PXRD

Powder X-ray diffraction measurements were performed on a Bruker D8 Discover with Ni-filtered Cu-Kα radiation and a LynxEye position-sensitive detector. (scan speed of 4 s per 0.01 degree 2θ).

6.3.4. Physisorption

Nitrogen sorption isotherms were recorded on a Quantachrome Autosorb 1 at 77 K within a pressure range of p/p_0 = 0.001 to 0.98. Prior to the measurement of the sorption isotherms the samples were heated for 24 h at 120°C under turbo-pumped vacuum. For evaluating of the

surface area the BET model was applied between 0.05 and 0.2 p/p_0. Pore size distributions were calculated using the QSDFT equilibrium model (desorption branch) with a carbon kernel for cylindrical pores.

6.3.5. UV-vis spectroscopy

UV-Vis spectra were recorded using a Perkin-Elmer Lambda 1050 spectrometer equipped with a 150 mm integrating sphere. For powder measurements $BaSO_4$ was applied as a reference.

6.3.6. Steady-state and time-resolved photoluminescence measurements

PL and PL anisotropy measurements were performed with a FluoTime 300 from PicoQuant GmbH. The samples were photo-excited using a laser with a wavelength of 378 nm (LDH-P-C-375 from PicoQuant GmbH) and 510 nm (LDH-P-C510 from PicoQuant GmbH) pulsed at 500 kHz, with a pulse duration of ~100 ps and fluence of ~300 μJ cm^{-2}/pulse. The PL was collected using a high-resolution monochromator and photomultiplier detector assembly (PMAC 192-N-M, PicoQuant GmbH).

6.3.7. Cyclic Voltammetry

Electrochemistry measurements were recorded using 0.1 M NBu_4PF_6 (Aldrich, 99.9 %) in acetonitrile (Aldrich, anhydrous) as the electrolyte. The cell was assembled in an argon-filled glove box ($c(O_2) < 0.1$ ppm, $c(H_2O) < 0.1$ ppm). A silver wire served as a reference electrode, that had been kept in concentrated hydrochloric acid for half an hour. Ferrocene potential versus the silver electrode was established to be 440 mV. (see **Figure 6.6**). CDs were measured as a solution, using ITO substrate as working electrode. When measuring COF thin films, the films themselves were used as the working electrodes. Platinum wire served as the counter electrode. A Metrohm Autolab PGStat302N was used for the measurements.

6.4. Results

This study aimed to design a multifunctional composite material *via* functionalization of covalent organic frameworks with carbon dots and to explore the structural and optoelectronic interactions between the components in the composite. For the synthesis of CDs, the microwave approach reported in Ref.[35] was adapted. Herein, citric acid and branched polyethyleneimine were treated in a microwave at 200 °C and under pressure of 20 mbar.

Powder X-ray diffractograms (PXRD) of the obtained CDs (**Figure 6.1** a) show two very broad, overlapping reflections extending from approximately 5 to 25 2θ. Zhang *et al.* reported a similar broad reflection for the CDs prepared by condensing citric acid and ethylenediamine using a hydrothermal method.[32] The broad PXRD reflection indicates low graphitization of the sample. The CDs were further subjected to calcination in an oven at 200 and 350 °C. The samples will be referred to as CDs_150 °C and CDs_200 °C. For both samples reflection at 27 2θ occurred, as shown in Figure 1 a, indicating the formation of crystalline particles with a lattice spacing similar to that of graphite.[40,41]

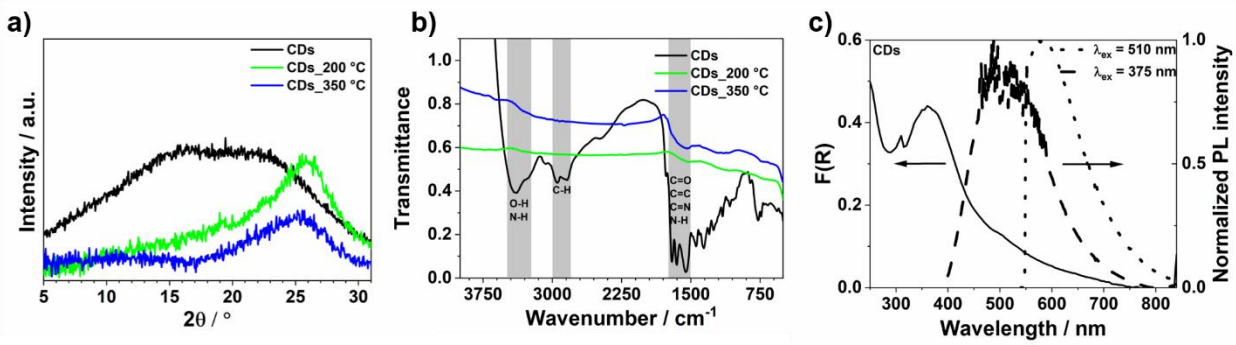

Figure 6.1. (a) PXRD diffraction patterns and (b) FT-IR spectra (prominent features are highlighted in gray) of untreated CDs (black) and after calcination at 200 °C (green) and 350 °C (blue). (c) F(R) spectrum and PL spectra (at λ_{ex} = 375 nm (dashes) and at λ_{ex} = 510 nm (dots)) of untreated CDs.

For the quantification of the particle size, the diffractograms were fitted with multiple Gaussian functions to extract FWHM values required for the calculation of the crystallite size *via* the Scherrer equation. The function closest to 27 2θ was selected to obtain the size of graphitic domains. The fits are shown in **Figure 6.7** and all relevant values obtained from the fits and the calculated using the Scherrer equation are given in **Table 6.2**. In the case of the untreated CDs, the center of the Gaussian function is not at 27 2θ in contrast to the tempered CDs. Hence, to estimate the particle size of the CDs photoluminescence (PL) anisotropy measurements were performed.[42,43] This method applies the Einstein-Stokes relationship to calculate the hydrodynamic diameter. Herein, the depolarization of the PL is related to the Brownian motion of the particles, which in turn is related to the size of the particles. The fitting is presented in the **Figure 6.8**. The particle diameters of the tempered CDs obtained from the Scherrer equation and the PL anisotropy are similar, being 1.9 nm for CDs_200°C, and 2.3 nm for CDs_350°C.

For untreated CDs, only PL anisotropy allowed the accurate particle size quantification of 2.5 nm.

The surface functionality of the CDs was characterized by means of Fourier Transformation - Infrared Spectroscopy (FT-IR) spectroscopy. The FT-IR spectra of the precursors are presented in **Figure 6.9** and the corresponding signal assignments in **Table 6.3**. **Figure 6.1** b shows the FT-IR spectra of untreated and tempered CDs. Measurements were carried out in transmission on pellets containing the samples and KBr. Untreated CDs show a broad signal at around 3400 cm^{-1} with a shoulder at lower frequencies, which has been ascribed to O-H and N-H stretching vibrations, respectively.[35,44] This indicates the presence of alcohol and amine groups. The doublet band at around 2950 and 2850 cm^{-1} has previously been assigned to alkyl C-H bond stretching vibration, indicating the presence of sp^3 carbon domains.[45] In addition, there are many absorption bands in the fingerprint region below 2000 cm^{-1}. Most prominently, bands at around 1700 cm^{-1}, 1650 cm^{-1} and 1550 cm^{-1} are associated with C=O, C=C and C=N stretches, as well as N-H bending.[35,45] After calcination at 200 °C and 350 °C most IR bands disappeared evincing the loss of the surface functionalization. Although untreated CDs have low crystallinity they possess the suitable size and surface functionalization for the planned incorporation into the porous structure of the COF. Further in-depth characterization is presented for untreated CDs denoted as CDs.

One of the most prominent properties of CDs is their strong photoluminescence. UV-vis and PL spectra of the precursors differ from the spectra of CDs as presented in **Figure 6.10**. The recorded diffuse reflectance UV-vis and PL spectra of CDs powder are shown in **Figure 6.1** c. The measured UV-VIS reflectance was converted into the Kubelka-Munk function which is proportional to the absorption according to the following equations:[46]

$$F(R) = \frac{(1-R(\lambda))^2}{2R(\lambda)} = \frac{\alpha(\lambda)}{S(\lambda)} \qquad (6.1)$$

where *F(R)*, *R(λ)*, *α(λ)* and *S(λ)* are the Kubelka-Munk function, reflectance referred to $BaSO_4$ standard, absorption coefficient and scattering coefficient at each wavelength, respectively. Apart from an absorption below 300 nm there is a prominent absorption band at 360 nm, as well as a weak shoulder at around 500 nm. The features in the visible wavelength range were previously shown to be caused by different polycyclic aromatic hydrocarbons.[47] Specifically, this involves π-π* transitions of C=C bonds and n-π* transitions of C=O groups.[44,48] The

bandgap energy was estimated to be 2.80 eV by means of the Tauc method, as shown in Figure 6.**11**. When exciting CDs at λ_{ex} = 375 nm, a broad and intense PL band centered at around 500 nm with a long tail toward longer wavelengths is observed. The large stokes-shift of around 160 nm is due to exciton self-trapping in the form of excimer formation.[47] The tail toward longer wavelengths has been previously explained by energy transfer between different chromophores within the CDs. Upon excitation at λ_{ex} = 510 nm, a less intense PL band is observed with a maximum at around 570 nm. This excitation-dependent emission is a characteristic feature of CDs.[48] This is often ascribed to the multichromophoric nature of CDs which comprises different molecular species as well as defects and surface states.[44]

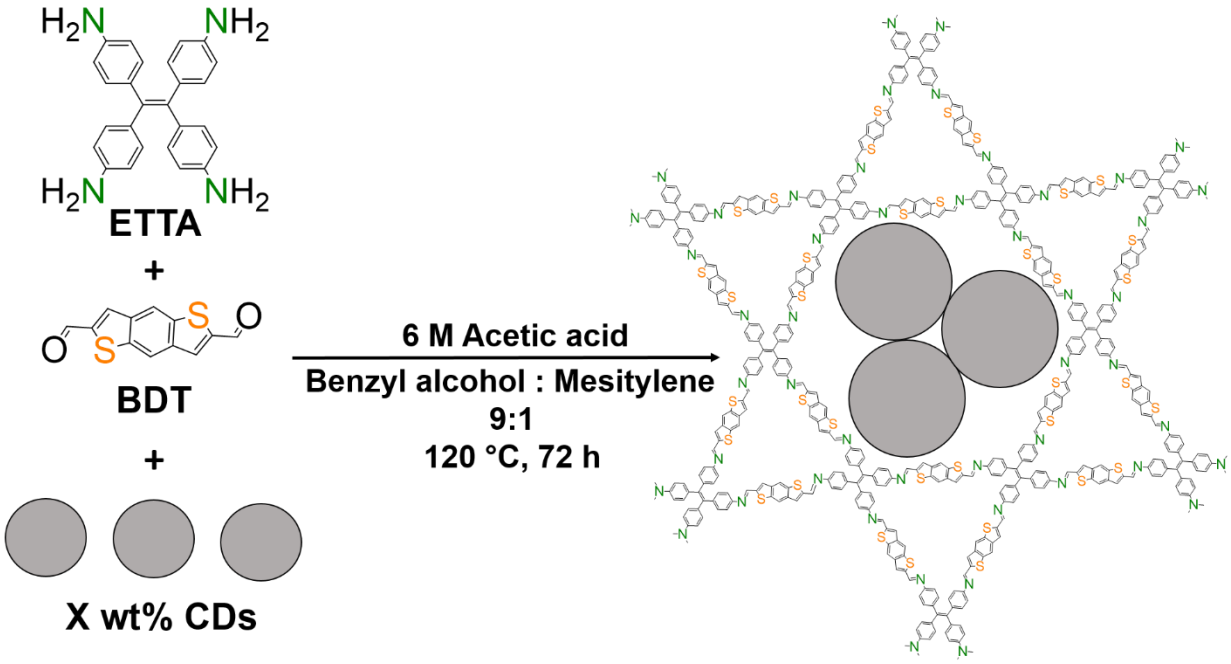

Scheme 6.1. Schematic representation of the BDT-ETTA COF synthesis in the presence of CDs, X was varied between 0 and 100 wt%. Note: The exact position of the CDs within the COF structure is not known.

For the synthesis of the COF functionalized with CDs, BDT-ETTA COF was selected. BDT-ETTA was synthesized solvothermally according to a literature report.[1] The appearance of an intense (100) reflection as well as several higher order reflections in the diffractogram confirm the successful formation of the COF (**Figure 6.2** a). The obtained structure of BDT-ETTA-COF is in a good agreement with the simulated a dual-pore Kagome structure in P6 symmetry (see **Figure 6.12**). The inset of the **Figure 6.2** a shows a magnification of the smaller reflections at slightly higher angles, including the stacking reflection at around 20 2θ which corresponds to a

π-π stacking distance of 0.44 nm. For the preparation of COF/CDs composite BDT-ETTA COF was synthesized in the presence of CDs (**Scheme 6.1**). This approach allows the linkers to be arranged around the CDs as the COF grows. PXRD measurements demonstrate high crystallinity of samples with up to 20 wt% CDs loadings, as shown in Figure 6**.2** a. Less intense higher order reflections can be observed up to 50 wt% loadings, although relative intensities decrease significantly above CDs loading of 20 wt%. Stacking reflection is present for samples with CDs loadings up to 20 wt%, whereas for higher CDs loadings broad reflections at these angles are caused by the presence of CDs.

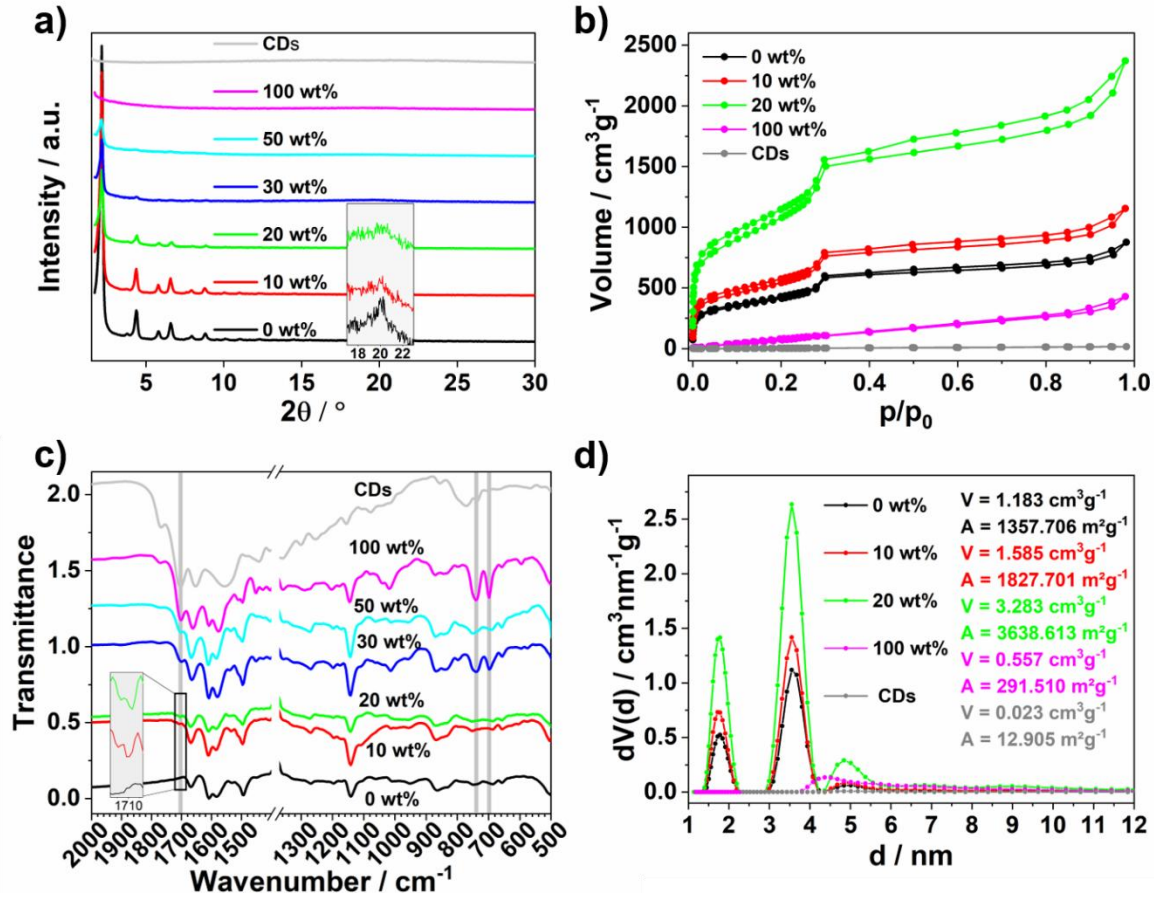

Figure 6.2. (a) PXRD diffraction patterns with inset showing the stacking peak for the samples with high crystallinity, (b) Nitrogen sorption isotherms, (c) FT-IR-spectra with gray highlighted bands, which intensify after CDs addition, of BDT-ETTA COF synthesized in the presence of different CDs loadings: 0 wt% (black) 10 wt% (red), 20 wt% (green), 30 wt% (blue), 50 wt% (turquoise), 50 wt% (pink), and CDs (grey). (d) calculated PSD,

Nitrogen sorption measurements were conducted to confirm the formation of a porous COF structure and to monitor the changes upon CDs loading. The isotherms and the corresponding

pore size distribution (PSD) are shown in **Figure 6.2** b and d, respectively. For BDT-ETTA COF two sharp volume increases in the isotherm were observed, corresponding to pore sizes of 1.8 and 3.6 nm. These can be assigned to the trigonal and hexagonal cavities of the Kagome structure, respectively. The surface area and pore volume were found to be around 1360 $m^2 g^{-1}$ and 1.2 $cm^3 g^{-1}$, respectively. Composites with up to 20 wt% CDs loadings show similar behavior with two maxima at about 1.8 nm and 3.6 nm, as expected of a Kagome structure. However, both pore volume and surface area increase with increasing CDs loading, without any change in the shape of the PSD. In contrast, the pore structure of the 100 wt% sample changes significantly, along with a drastic decrease in pore volume and surface area. CDs exhibit no porosity.

Scanning electron microscopy (SEM) micrographs of the BDT-ETTA COF synthesized in the presence of 0 wt%, 30 wt% and 100 wt% CDs loadings revealed that the morphology of the BDT-ETTA COF changes from the closely packed distinct particles (0 wt%) to less-defined agglomerates as CDs loading increases (**Figure 6.13**). These morphological changes are consistent with the PXRD data shown in **Figure 6.2**a. The transmission electron microscopy (TEM) image shown in **Figure 6.14** a reveals a high degree of crystallinity and order for pristine BDT-ETTA COF. For the composite containing 30 wt% CDs loading crystalline areas among amorphous areas could be detected as presented in **Figure 6.14** b. However, no CDs could be detected most likely due to the small dimensions (around 2 nm), low Z-contrast (made up entirely of C, N, O, H), and low crystallinity.

To prove the incorporation of the CDs into the porous structure of the COF and to study the interaction in the composite on the molecular level the FT-IR measurements were conducted (**Figure 6.2** c). The observed FT-IR band at 1668 cm^{-1} in the pristine COF, which is still visible in all COF/CDs composites, can be assigned to the imine-bond.[49] This indicates that the COF layers remain intact in the presence of the CDs loadings up to 100 wt%. The decreased crystallinity for COF samples with high CDs loadings observed in PXRD is a result of less ordered layer stacking.[50] Further changes in FT-IR spectra can be observed as the CDs loading increases. The corresponding sections of the spectra are highlighted in grey. New, weak bands appear at 1780 cm^{-1}, 1700 cm^{-1} and 1360 cm^{-1}, which closely match the bands observed in the pristine CDs. As shown in the inset, the appearance of the signal at 1700 cm^{-1} is observable for

samples with low CDs loadings. The presence of CDs features in the COF spectra confirms the co-existence of CDs and COF. However, no shift or appearance of the new FT-IR bands were observed, which excludes the possibility of the covalent bond formation between COF and CDs.

For the additional characterization of the pristine BDT-ETTA COF and of the corresponding composites with CDs elemental analysis was performed. The corresponding data are presented in the **Table 6.1**. Such elements as C, N, H are present in both components of the composites while S is only present in the BDT unit of the COF and not in the CDs. Hence, a gradual decline of S with increasing CDs:COF ratio and an increase of the C and N in the composites compared to the pristine BDT-ETTA COF evince the successful incorporation of the CDs into the COF structure.

Table 6.1. Material composition obtained from theoretical calculations of BDT-ETTA COF and from elemental analysis of pristine BDT-ETTA COF and BDT-ETTA/CDs composites.

BDT-ETTA COF/CDs (CDs loading in wt%)	N / %	C / %	H / %	S / %
0 (from simulations)	6.79	73.76	3.91	15.54
0 (synthesized)	5.49	61.47	3.35	13.04
10	6.47	69.9	4.05	12.76
20	6.09	68.36	4.52	11.85
30	6.31	68.48	4.81	11.97
50	7.19	66.13	4.55	9.96
100	8.89	60.21	4.63	7.82

For the investigations of the optoelectronic interactions between COF and CDs the UV-vis diffuse reflectance and PL measurements were conducted on powders. Compared to the building blocks, ETTA and BDT (**Figure 6.15**), the absorption of the COF is red-shifted as a result of conjugation between the molecular units (**Figures 6.3** a). The bandgap energy of the pristine BDT-ETTA COF was determined *via* the Tauc plot method being 2.09 eV. The Tauc plot is shown in **Figure 6.16**. Upon increasing CDs loading, the color of the COF changes gradually from bright orange to brown. The F(R) spectra shown in Figure 6.3 a reveal an increase in absorbance in the wavelength range between 600 and 750 nm as the CDs loading increases from 0 to 100 wt%. Furthermore, the absorption onset in the wavelength region

between 400 nm and 700 nm shows a different slope for 100 wt% samples in comparison to the pristine COF. The band gap energies of all samples were determined using the Tauc plot method assuming a direct transition. The corresponding graphs are shown in **Figure 6.16Figure 6.11**. As evident from **Figure 6.3** b, E_g does not show any trend with the CDs loading. Figure 6.3 c shows the change in the PL of the COF induced by the presence of CDs. For PL spectra, the assumption is made that the penetration depth of the excitation light is less than the thickness of the sample, thus the difference in intensity can be related. Pristine BDT-ETTA COF shows a very broad PL with a maximum at around 690 nm when excited at 375 nm. Compared to the PL spectra of the building blocks shown in **Figure 6.17**, there is a significant redshift, which can be explained by enhanced conjugation in the crystalline COF. Upon increasing of the CDs loading up to 20 wt% a decline in PL intensity of the COF occurs indicating a quenching process. For the CDs loadings higher than 20 wt% the PL intensity of the COF increases gradually with CDs loading. For the samples with CDs loadings from 10 to 50 wt% no shift of the PL maxima occurred, while the sample with 100 wt% shows a blue-shift of the emission. The latter results from the loss of crystallinity and thus in conjugation of the COF. The PL spectra of amorphous and crystalline synthesized BDT-ETTA COF are shown in **Figure 6.18**. The PL band of the CDs is absent in the PL spectra of the composite for all CDs loadings.

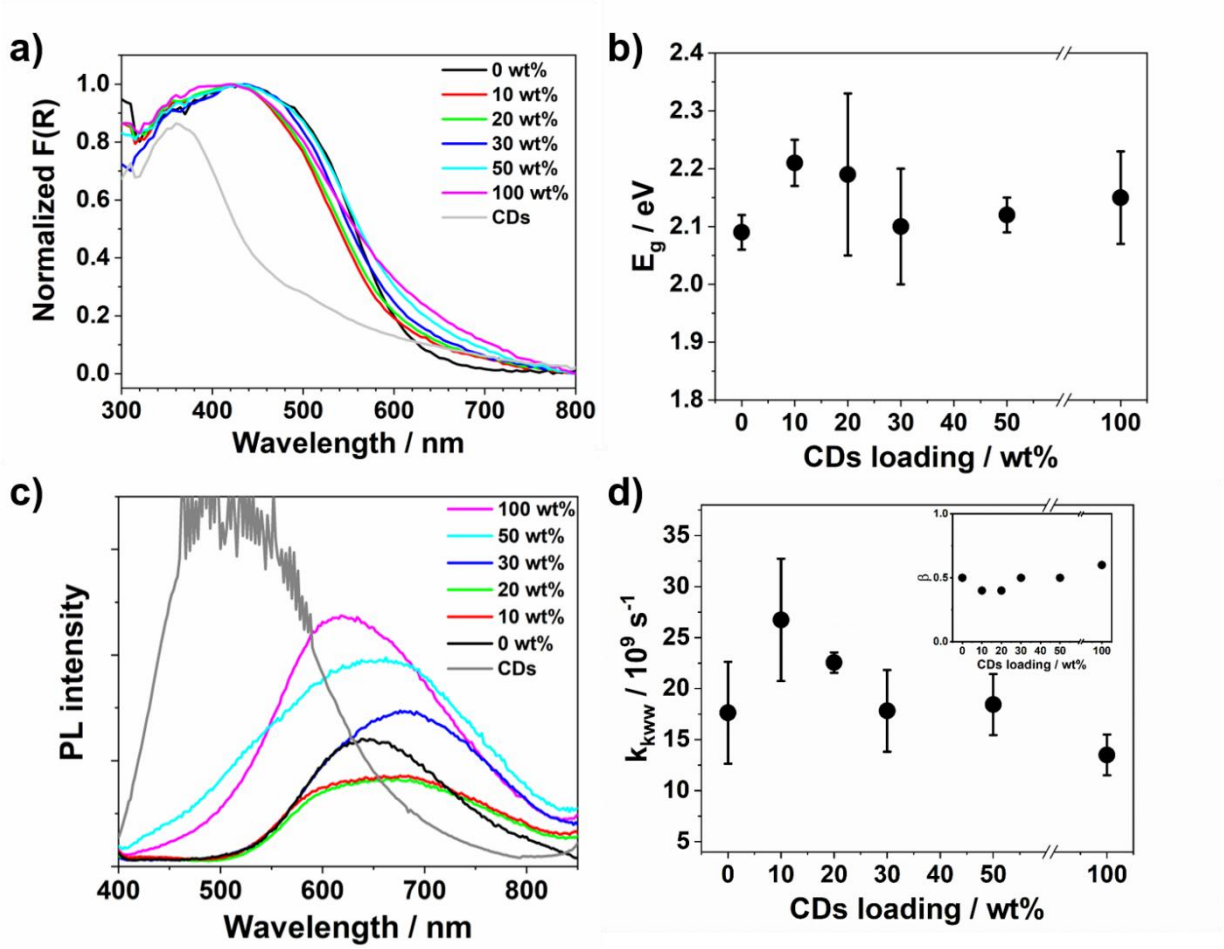

Figure 6.3. (a) F(R) and c) PL spectra (λ_{ex} = 375 nm) of BDT-ETTA COF synthesized in the presence of different CDs loadings: 0 wt% (black) 10 wt% (red), 20 wt% (green), 30 wt% (blue), 50 wt% (turquoise), 50 wt% (pink), and CDs (grey). (b) Optical bandgap energies E_g determined *via* Tauc method and (c) PL decay constants k_{kww} extracted from the stretched exponential fitting according to Kohlrausch-Williams-Watts (KWW) model as a function of CDs loading. (d) The inset shows the distribution breadth β of the decay constant k_{kww}.

Time-resolved PL decays were recorded to identify whether charge transfer between COF and CDs occurs. The observed decay dynamics represent the recombination between photogenerated electron-hole pairs. Due to the low dielectric constant of the COF the electron-hole pair remains bound as an exciton. Hence, it is expected that the decay dynamics follow first order kinetics. However, since the COF contains defects and other irregularities in the structure the photogenerated excitons are not homogeneously distributed in three dimensions. This causes a dispersion of the decay rate constants. The Kohlrausch-Williams-Watts (KWW) model provides mathematical description of the dispersive kinetics. It assumes a Lévy-

distribution of first-order rate constants. As shown in equation (6.2), this results in a stretched-exponential decay of the involved species. Fitting experimental data allows the estimation of the observed rate constant k_r and the distribution width β. From these parameters, the average decay rate constant k_{KWW} is calculated according to equation (6.3).

$$[A](t) = [A]_0 e^{-(k_r t)^{\beta}} \qquad (6.2)$$

[A](t) and *[A]₀* are initial and time dependent concentrations, k_r is observed decay rate constant, t is time, β is distribution breadth.

$$k_{KWW} = \frac{k_r \beta}{\Gamma\left(\frac{1}{\beta}\right)} \qquad (6.3)$$

k_{KWW} is average decay rate constant, Γ is gamma function.

The fitted decays are shown in the **Figure 6.19**. **Figure 6.3** d demonstrates that the decay rate constant k_{kww} increases with CDs loadings up to 10 wt% and 20 wt% compared to pristine BDT-ETTA COF, while at loadings of 30 wt% and 50 wt% k_{kww} remains unchanged, and decreases at CDs loading of 100 wt%. Herein, an inverse relationship exists between the decay constants and the PL intensities. The β values presented in the inset of **Figure 6.3** d lie at around 0.5 thus indicating a good agreement between the experimental values and the fitting model.

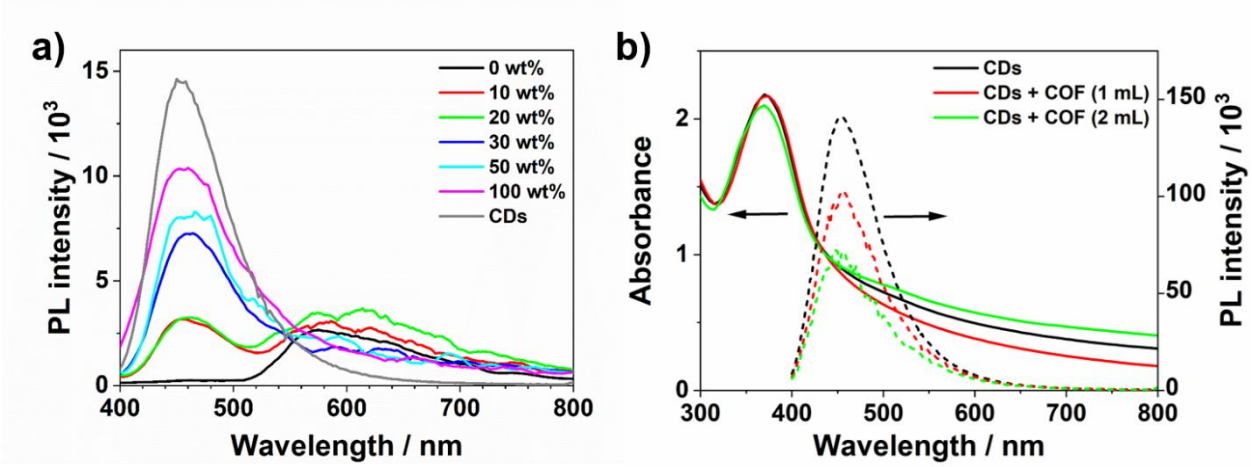

Figure 6.4. (a) PL spectra of COF suspensions in ACN synthesized in the presence of different CDs loadings: 0 wt% (black) 10 wt% (red), 20 wt% (green), 30 wt% (blue), 50 wt%

(turquoise), 50 wt% (pink), and CDs (grey). (b) PL spectra of CDs suspensions in acetonitrile with increasing volume of COF suspension. The total volume was kept constant.

To gain further insight into the interactions between the COF and CDs mechanical strength was applied to the composite to initiate the separation between the two components. Herein, the samples were treated in acetonitrile by ultrasonication. As opposed to dry powder samples, two distinct PL bands with a maxima at 460 nm and at 580 nm appear in the PL spectra, **Figure 6.4** a. The former feature belongs to the PL of CDs while the latter feature belongs to the PL of the BDT-ETTA COF. These results reveal that sonication power causes partial separation between COF and CDs. The quenching of CDs PL is prevented and the original emission can be observed. Additionally, from **Figure 6.4** a it is evident that CDs PL intensity increases with higher CDs loadings thus revealing that the amount of the CDs included in the COF structure increased gradually with the amount of CDs added to the reaction mixture of COF. In further experiment, CDs suspensions of equal concentration were exposed to the different volumes of the COF suspension, herein, the total volume was kept constant. While the absorbance of CDs did not change as the COF concentration was increased, a gradual decline in the CDs PL intensity with higher COF concentration occurred, see **Figure 6.4** b.

6.5. Discussion

The results presented above allow the construction of a detailed picture of the physicochemical interaction in COF/CDs composite. The appearance of CDs bands alongside the typical COF bands in FT-IR spectra and the elemental analysis confirm the coexistence of the two materials (**Figure 6.2** c, **Table 6.1**). The increased pore volume found in sorption experiments has already been reported in previous studies and has been assigned to the reduction of the interlayer interaction through the insertion of CDs, which transforms the original stacked structure into a thinner 2D-layered structure through self-exfoliation.[29] However, the self-exfoliation is less likely since the PXRD reflections typical for the COF arranged in three dimensions through π-π stacking are still present (**Figure 6.2** a). The CDs can act as a diffusion barrier for ETTA and BDT units, leading to slow and controlled growth of the COF. Moreover, due to the high surface functionalization, the CDs can serve as a modulator promoting the growth of the COF. Calik *et al.* studied the effect of the modulators on the COF synthesis.[51] The modulator has been found to react reversibly with the COF building blocks thus allowing

more controlled growth. The authors observed that addition of small amount of the modulator led to increased crystallinity, pore volume and surface area of COF-5, which they ascribed to the formation of larger crystallites with few defects. Addition of high modulator concentration, however, resulted in crystallinity decline. This is well in line with the above presented observations: Samples with CDs loadings of up to 20 wt% showed high crystallinity and increased pore volume and surface area compared to bare COF. On the other hand, CDs loadings of ≥ 30 wt% hampered the COF formation leading to loss in crystallinity as shown in **Figure 6.2** a). It can be concluded from the above discussion that the chosen method to obtain the composite via growth of COF in the presence of the CDs has limitations. On the one side, the presence of the functional groups on the surface of the CDs enables the incorporation of the CDs into the porous structure of the COF. On the other side, CDs can impede the crystallization process of the COF resulting in the amorphous product. For example, CDs with their functional groups can act as the COF building block and exchange the linker.[52] Additionally, we have tested different synthetic methods in which COF served as a template for the CDs synthesis, however, the BDT-ETTA COF did not survive the harsh conditions of the synthesis.

The observed structural interactions between BDT-ETTA COF and CDs imposes the evolution of the novel photophysical features which were not present in the single components. The main observations in this regard are: 1. For all CDs loadings the PL band of the CDs disappeared; 2. For CDs loadings ≤ 20 wt% a decrease in PL intensity and acceleration of the PL decay rate of functionalized COF compared to pristine COF occurred; 3. For CDs loadings ≥ 30 wt% an increase in PL intensity and deceleration of the PL decays of COF compared to pristine COF occurred. The first observation reveals a quenching process of the CDs PL operating either *via* charge or/and energy transfer. The second observation indicates the quenching of the COF PL features *via* charge transfer, while the third observation can originate from the FRET between COF and CDs. To validate these hypotheses, the energetics of the COF and CDs have been analyzed. For an efficient charge transport among the strong structural interaction an alignment of the energetics is required. The energetic positions of the HOMO were determined by cyclic voltammetry from the onset potentials of the oxidative features (**Figure 6.20**). The position of the LUMO was calculated from the HOMO and the band gap energy. The HOMO and LUMO positions for COF are -5.29 eV and -3.20 eV, respectively, and for CDs -4.96 eV and -2.16 eV, respectively. Accordingly, HOMO and LUMO positions of the CDs are at less negative

potentials than those of BDT-ETTA COF. This configuration can result in either a type II or a Z-scheme band alignment. In **Figure 6.5** a, we have schematically illustrated the type II band alignment: CT can occur via hole transfer from the COF to CDs and electron transfer from CDs to COF. In the case of a Z-scheme alignment, an electron from the COF would recombine with a hole from the CDs. In both cases, acceleration of the PL decay through charge transfer will occur as demonstrated in **Figure 6.3** d.

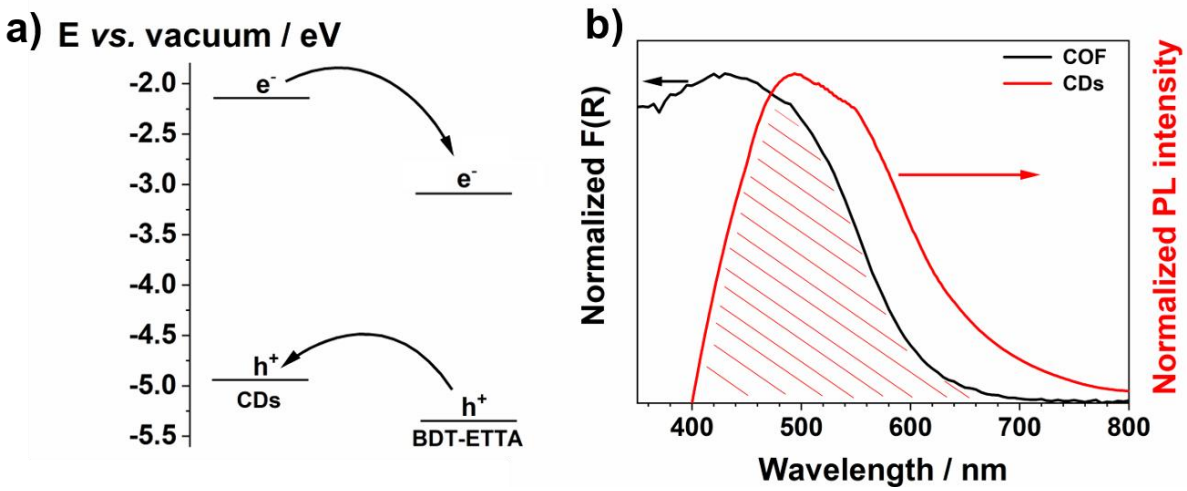

Figure 6.5. Illustration of the two processes that occur between CDs and BDT-ETTA COF in a corresponding composite: a) charge transfer and b) Förster resonance energy transfer.

For the energy transfer an overlap between the emission of the CDs and the absorption of BDT-ETTA COF is required according to the Förster resonance energy transfer theory. Apart from the spectral overlap, close proximity of energy donor and energy acceptor, typically on the order of 1 to 10 nm is needed. **Figure 6.5** b demonstrates the energetic overlap between COF and CDs. Both CT and FRET will quench the PL of CDs. Most obviously, this was shown by the systematic decrease of the PL of a CDs suspension with increasing COF concentration (**Figure 6.4** b). In the bulk samples, the close association of CDs with COF leads to complete disappearance of CDs PL, substantiating the operation of both CT and FRET. Furthermore, the control experiment, shown in Figure 4 a, demonstrates that the CDs did not become a part of the COF as through the application of the external force the CDs were separated from the COF leading to the recovery of its original emission. The emission of COF is quenched only by the CT process at CDs loadings $\leq$ 20 wt%, while FRET causes enhanced PL at CDs loadings $\geq$ 30 wt%. The appearance of two different mechanisms dependent on CDs loading can be

explained as follows: Stronger contact and interaction between CDs and COF can be assumed at low CDs loading. In that situation, the CT process dominates, leading to complete quenching of PL of CDs, as well as of the COF. As the CDs ratio increases, a thin layer starts to form around the COF crystallites. Once completed, additional CDs cannot directly interact with the COF, but are instead attached to the previous CDs layer. Here, CT is prohibited. However, the CDs meet the spatial distance requirements for FRET to occur. As mentioned before, FRET occurs at the distances between donor and acceptor of up to around 10 nm. As result of FRET, enhanced PL of COF is obtained. FRET from CDs to COF has already been reported.[28,30,31] These conclusions are further supported by the kinetic data obtained from the time-resolved PL measurements. The COF decay rate constant increases for 10 and 20 wt% samples as a result of the additional decay pathway *via* CT (see **Figure 6.5** a). At higher loadings, FRET from CDs repopulates the excited state of COF, slowing the overall observed decay. These observations have also been demonstrated by another group.[28]

6.6. Conclusions

COF/CDs composites were successfully prepared by solvothermal synthesis of BDT-ETTA COF in the presence of different CDs concentrations. CDs with their high surface functionalization affect the crystallization process of the COF. For CDs loadings up to 20 wt%, they served as the modulator promoting the growth of the BDT-ETTA COF, while at higher CDs loadings the crystallization of COF was hindered. The incorporation of the CDs into the porous structure of the COF was demonstrated for all CDs loadings by FT-IR spectroscopy. Elemental analysis revealed that the amount of CDs encapsulated in COF increased gradually with the concentration of the CDs present during the COF synthesis. This synthetic control over the COF:CDs ratio in the composite enabled systematic study of the optoelectronic interactions between the two components. Close contact between the two materials at low CDs loadings enabled interfacial charge transfer evinced by the PL quenching of the BDT-ETTA COF and CDs as well as by the acceleration of the PL decay kinetics of COF. At CDs loadings ≥ 30 wt%, the contact between both components decreased, however, spatial distance requirements for FRET to occur were fullfilled and the energy transfer prevailed leading to the increased PL of the BDT-ETTA COF. This study demonstrates the structure-property realtionship in COF/CDs composites and provides important insights for the applications in photocatalysis and sensing.

6.7. References

[1] T. Sick, A. G. Hufnagel, J. Kampmann, I. Kondofersky, M. Calik, J. M. Rotter, A. Evans, M. Döblinger, S. Herbert, K. Peters, D. Böhm, P. Knochel, D. D. Medina, D. Fattakhova-Rohlfing, T. Bein, *J. Am. Chem. Soc.* **2018**, *140*, 2085–2092.

[2] Y. Li, L. Yang, H. He, L. Sun, H. Wang, X. Fang, Y. Zhao, D. Zheng, Y. Qi, Z. Li, W. Deng, *Nat. Commun.* **2022**, *13*, 1355.

[3] G.-X. Tian, Y. Yang, R.-H. Zhang, L.-Y. Yan, Z. Cheng, D.-H. Lin, X.-W. Zhou, *Adv. Energy Sustain. Res.* **2023**, *4*, DOI 10.1002/aesr.202300058.

[4] C. Rodríguez-Proenza, J. Palomares-Báez, M. Chávez-Rojo, A. García-Ruiz, C. Azanza-Ricardo, A. Santoveña-Uribe, G. Luna-Bárcenas, J. Rodríguez-López, R. Esparza, *Materials (Basel).* **2018**, *11*, 1882.

[5] J. C. Yang, S. Bradley, J. M. Gibson, *MRS Proc.* **1998**, *549*, 191.

[6] C. Poidevin, P. Paciok, M. Heggen, A. A. Auer, *J. Chem. Phys.* **2019**, *150*, DOI 10.1063/1.5047666.

[7] M.-C. J. Chun Kim, *Jpn. J. Appl. Phys.* **1999**, *38*, 4872.

[8] M. PEUCKERT, *Chem. Informationsd.* **1985**, *16*, DOI 10.1002/chin.198503015.

[9] S. K. Shaikhutdinov, M. Schildenberger, M. Noeske, G. Mestl, *React. Kinet. Catal. Lett.* **1999**, *67*, 129–135.

[10] Y. Zhang, P. Yan, Y. Zhou, Q. Xu, *Phys. Chem. Chem. Phys.* **2022**, *24*, 27515–27523.

[11] R. Sugimoto, Y. Segawa, A. Suzuta, Y. Kunisada, T. Uchida, K. Yamazaki, K. Gohara, *J. Phys. Chem. C* **2021**, *125*, 2900–2906.

[12] A. Norman, R. Sporken, A. Galtayries, F. Mirabella, K. Keveney, M. Pijolat, R. Baker, S. Bernal, *MRS Proc.* **1999**, *581*, 345.

[13] D. E. Ramaker, M. K. Oudenhuijzen, D. C. Koningsberger, *J. Phys. Chem. B* **2005**, *109*, 5608–5617.

[14] C. Zhang, A. Yan, H. Guo, Y. Lei, H. Hao, F. Liu, *Fuel* **2022**, *317*, 123482.

[15] M. Descostes, F. Mercier, N. Thromat, C. Beaucaire, M. Gautier-Soyer, *Appl. Surf. Sci.* **2000**, *165*, 288–302.

[16] E. Cato, A. Rossi, N. C. Scherrer, E. S. B. Ferreira, *J. Cult. Herit.* **2018**, *29*, 30–35.

[17] B. B. Rath, L. Fuchs, F. Stemmler, A. Rodríguez-Camargo, Y. Wang, M. F. X. Dorfner, J. Olbrich, J. van Slageren, F. Ortmann, B. V. Lotsch, *J. Am. Chem. Soc.* **2025**, *147*,

18492–18503.

[18] Z. Almansaf, J. Hu, F. Zanca, H. R. Shahsavari, B. Kampmeyer, M. Tsuji, K. Maity, V. Lomonte, Y. Ha, P. Mastrorilli, S. Todisco, M. Benamara, R. Oktavian, A. Mirjafari, P. Z. Moghadam, A. R. Khosropour, H. Beyzavi, *ACS Appl. Mater. Interfaces* **2021**, *13*, 6349–6358.

[19] D. Wöhrle, D. Meissner, *Adv. Mater.* **1991**, *3*, 129–138.

[20] A. P. Côté, A. I. Benin, N. W. Ockwig, M. O'Keeffe, A. J. Matzger, O. M. Yaghi, *Science.* **2005**, *310*, 1166–1170.

[21] M. S. Lohse, T. Bein, *Adv. Funct. Mater.* **2018**, *28*, 1705553.

[22] F. J. Uribe-Romo, J. R. Hunt, H. Furukawa, C. Klöck, M. O'Keeffe, O. M. Yaghi, *J. Am. Chem. Soc.* **2009**, *131*, 4570–4571.

[23] S. Bi, C. Yang, W. Zhang, J. Xu, L. Liu, D. Wu, X. Wang, Y. Han, Q. Liang, F. Zhang, *Nat. Commun.* **2019**, *10*, 2467.

[24] X. Xu, R. Ray, Y. Gu, H. J. Ploehn, L. Gearheart, K. Raker, W. A. Scrivens, *J. Am. Chem. Soc.* **2004**, *126*, 12736–12737.

[25] A. Sciortino, A. Cannizzo, F. Messina, *C* **2018**, *4*, DOI 10.3390/c4040067.

[26] Q. Gao, X. Li, G.-H. Ning, K. Leng, B. Tian, C. Liu, W. Tang, H.-S. Xu, K. P. Loh, *Chem. Commun.* **2018**, *54*, 2349–2352.

[27] S. Dalapati, E. Jin, M. Addicoat, T. Heine, D. Jiang, *J. Am. Chem. Soc.* **2016**, *138*, 5797–5800.

[28] X. Ma, Y. Yang, R. Ma, Y. Zhang, X. Zou, S. Zhu, X. Ge, Y. Yuan, W. Zhang, G. Zhu, *Chem. Sci.* **2020**, *11*, 12187–12193.

[29] S. Wang, L. Guo, L. Chen, L. Wang, Y. Song, *ACS Appl. Nano Mater.* **2022**, *5*, 1339–1347.

[30] Y. Song, L. Guo, Y. Du, L. Yang, L. Wang, *Chem. Commun.* **2020**, *56*, 14913–14916.

[31] J. Cui, L. Kan, Z. Li, L. Yang, M. Wang, L. He, Y. Lou, Y. Xue, Z. Zhang, *Talanta* **2021**, *228*, 122060.

[32] J. Liang, W. Li, J. Chen, X. Huang, Y. Liu, X. Zhang, W. Shu, B. Lei, H. Zhang, *J. Mater. Chem. A* **2022**, *10*, 23384–23394.

[33] H. Zhong, R. Sa, H. Lv, S. Yang, D. Yuan, X. Wang, R. Wang, *Adv. Funct. Mater.* **2020**, *30*, 2002654.

[34] A. C. Jakowetz, T. F. Hinrichsen, L. Ascherl, T. Sick, M. Calik, F. Auras, D. D. Medina, R. H. Friend, A. Rao, T. Bein, *J. Am. Chem. Soc.* **2019**, *141*, 11565–11571.

[35] S. Bhattacharyya, F. Ehrat, P. Urban, R. Teves, R. Wyrwich, M. Doeblinger, J. Feldmann, A. Urban, J. Stolarczyk, *Nat. Commun.* **2017**, *8*, DOI 10.1038/s41467-017-01463-x.

[36] M. K. Barman, S. Bhattacharyya, A. Patra, *Phys. Chem. Chem. Phys.* **2013**, *15*, 16834–16840.

[37] J. H. Gorvin, *J. Chem. Soc.* **1959**, 678–682.

[38] J. Lu, J. Zhang, *J. Mater. Chem. A* **2014**, *2*, 13831–13834.

[39] G. Koßmehl, P. Beimling, G. Manecke, *Die Makromol. Chemie* **1983**, *184*, 627–650.

[40] B. C. M. Martindale, G. A. M. Hutton, C. A. Caputo, S. Prantl, R. Godin, J. R. Durrant, E. Reisner, *Angew. Chemie Int. Ed.* **2017**, *56*, 6459–6463.

[41] H. Peng, J. Travas-Sejdic, *Chem. Mater.* **2009**, *21*, DOI 10.1021/cm901593y.

[42] A. Bruno, M. Alfe, B. Apicella, C. de Lisio, P. Minutolo, *Opt. Lasers Eng.* **2006**, *44*, 732–746.

[43] M. Chenchiliyan, H. K. Sadhanala, K. Sharma, A. Le Marois, A. Gedanken, D. Fixler, in *Nanoscale Imaging, Sensing, Actuation Biomed. Appl. XVI* (Eds.: D. V Nicolau, D. Fixler, E.M. Goldys), SPIE, **2019**, p. 108911J.

[44] K. Bramhaiah, R. Bhuyan, S. Mandal, S. Kar, R. Prabhu, N. S. John, M. Gramlich, A. S. Urban, S. Bhattacharyya, *J. Phys. Chem. C* **2021**, *125*, 4299–4309.

[45] X. Zhao, J. Zhang, L. Shi, M. Xian, C. Dong, S. Shuang, *RSC Adv.* **2017**, *7*, 42159–42167.

[46] F. Kubelka, P. and Munk, *Zeitschrift für Tech. Phys.* **1931**, *12*, 593–601.

[47] M. Fu, F. Ehrat, Y. Wang, K. Z. Milowska, C. Reckmeier, A. L. Rogach, J. K. Stolarczyk, A. S. Urban, J. Feldmann, *Nano Lett.* **2015**, *15*, 6030–6035.

[48] Y. Wang, A. Hu, *J. Mater. Chem. C* **2014**, *2*, 6921–6939.

[49] A. K. Saini, C. M. Carlin, H. H. Patterson, *J. Polym. Sci. Part A Polym. Chem.* **1993**, *31*, 2751–2758.

[50] T. Sick, J. M. Rotter, S. Reuter, S. Kandambeth, N. N. Bach, M. Döblinger, J. Merz, T. Clark, T. B. Marder, T. Bein, D. D. Medina, *J. Am. Chem. Soc.* **2019**, *141*, 12570–12581.

[51] M. Calik, T. Sick, M. Dogru, M. Döblinger, S. Datz, H. Budde, A. Hartschuh, F. Auras, T. Bein, *J. Am. Chem. Soc.* **2016**, *138*, 1234–1239.

[52] S. Chen, T. Sun, M. Zheng, Z. Xie, *Adv. Funct. Mater.* **2020**, *30*, 2004680.

6.8. Appendix

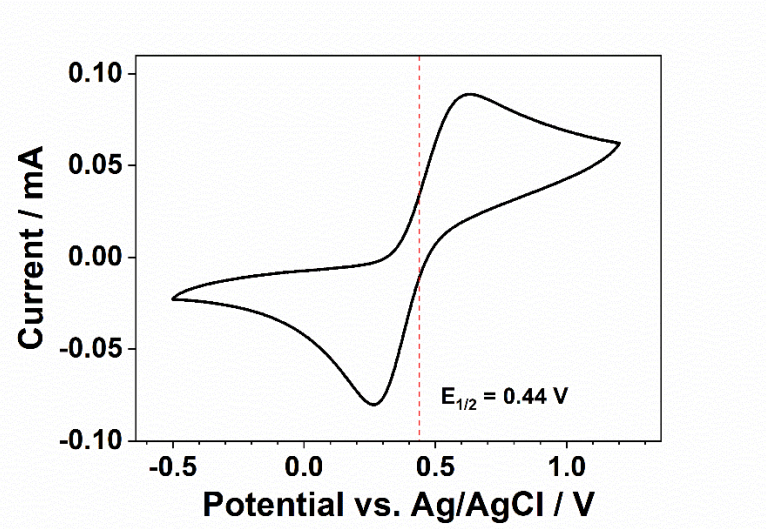

Figure 6.6. Cyclic voltammogram of ferrocene ($FeCp_2$) in acetonitrile recorded at a scan rate of 100 mVs^{-1} versus Ag/AgCl electrode.

Scherrer equation:

$$\tau = \frac{K\lambda}{\beta cos\theta} \qquad (6.4)$$

τ is crystallite size, K is shape factor, λ is x-ray wavelength, β is full width at half maximum, θ is Bragg angle.

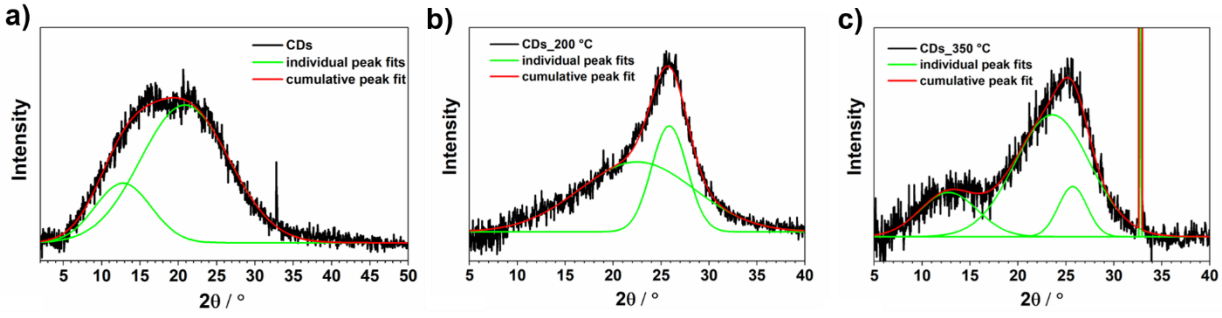

Figure 6.7. Fitting of XRD diffraction patterns for (a) non-treated CDs, (b) CDs_200°C, and (c) CDs_350°C.

Table 6.2. Reflection angles and widths obtained from fitting of CDs diffraction patterns, as well as lattice constants and particle diameters calculated using the Scherrer equation (eq. 6.4).

.Sample	2θ	FWHM	Lattice constant / Å	Particle diameter / nm
CDs	12.81	8.2	6.90	0.97
	20.88	14.92	4.25	0.54
CDs_200 °C	22.49	14.18	3.95	0.57
	25.85	4.37	3.44	1.86
CD_350 °C	25.71	3.54	3.46	2.30
	23.59	9.2	3.77	0.88
	12.78	7.03	6.92	1.14

6.8.1. Photoluminescence (PL) anisotropy approach to estimate the CDs particle size

This approach is based on the Einstein-Stokes relationship (eq. 6.5) which allows to correlate the depolarization of the PL to the Brownian motion of the particles, which in turn is related to the size of the particles (taking into consideration also the temperature and solvent viscosity). The calculated anisotropy values can then be fitted with eq. 6.6 to extract the rotational correlation time θ. The calculated and fitted anisotropy values are shown in

$$\theta = \frac{\eta V}{k_B T} \qquad (6.5)$$

θ is rotational correlation time, η is solvent viscosity, V is hydrodynamic volume, k_B is Boltzman constant, T is temperature.

$$r(t) = (r_0 - r_\infty)e^{-\frac{t}{\theta}} + r_\infty \qquad (6.6)$$

$r(t)$ is fluorescence anisotropy, r_0 is initial anisotropy, r_∞ is factor accounting for hindered rotation, t is time.

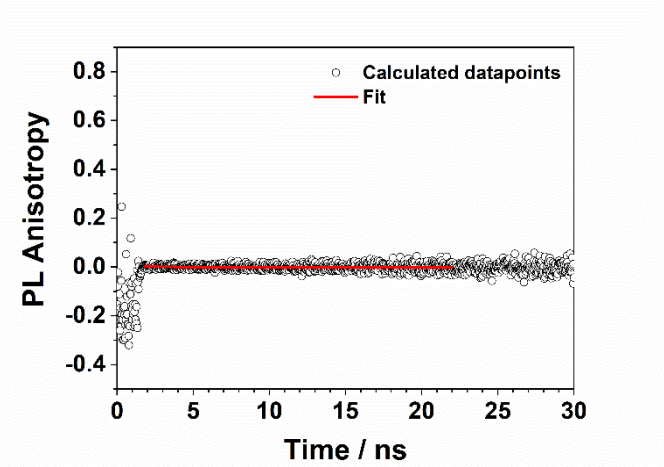

Figure 6.8. PL anisotropy values calculated from photoluminescence measurements and the fit with *eq.* S3 to the data points.

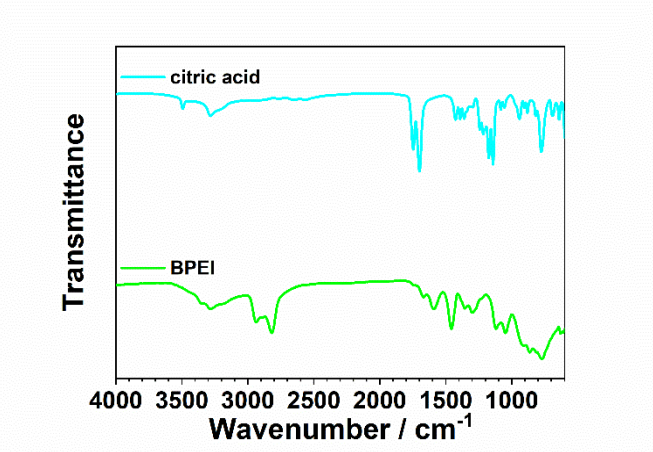

Figure 6.9. FT-IR spectra of CDs precursors.

Table 6.3. FT-IR band assignment for the BPEI precursor.

FT-IR Band / cm^{-1}	Assignment
3350	N-H stretch, primary Amine
3283	N-H stretch, secondary Amine
1589	N-H bend
1457	C-H bend
1298	C-N stretch

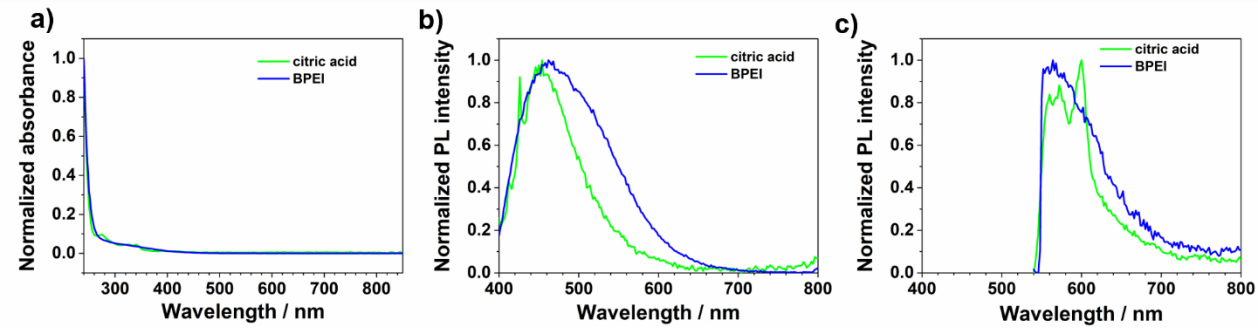

Figure 6.10. UV-vis and PL spectra of CDs precursors dissolved in acetonitrile (citric acid) and water (BPEI).

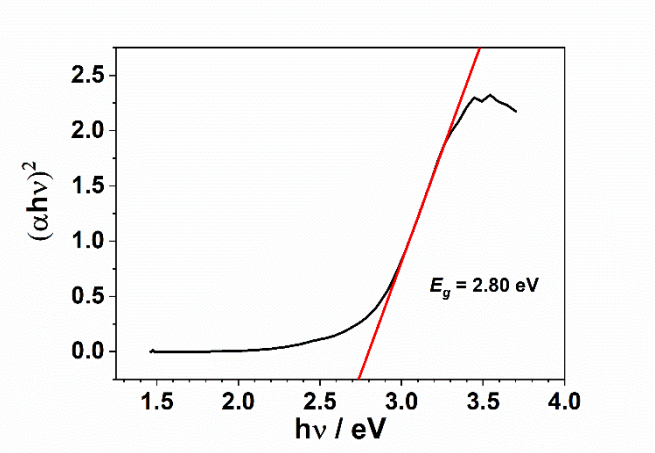

Figure 6.11. Tauc plot of CDs. A direct allowed bandgap was assumed, giving E_g = 2.8 eV.

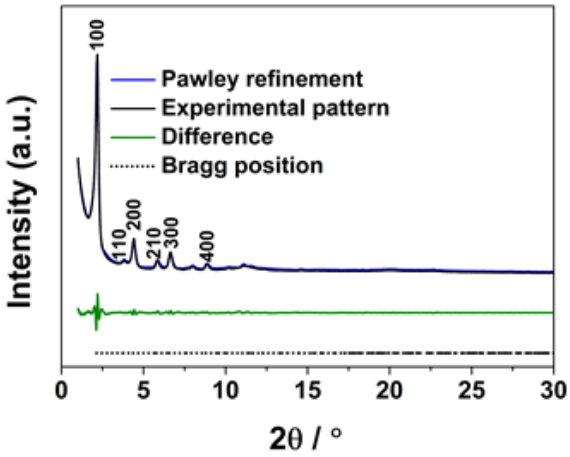

Figure 6.12. PXRD patterns of the experimentally observed (black) and Pawley refined (blue) BDT-ETTA COF with their refinement differences (green), and Bragg position (dotted).

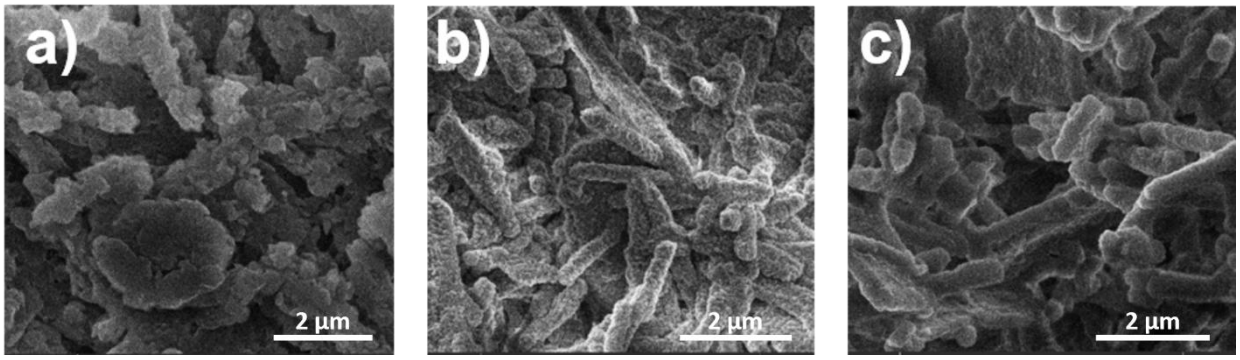

Figure 6.13. SEM images of BDT-ETTA COF synthesized in the presence of different CDs loadings: (a) 0 wt%; (b) 30 wt%; (c) 100 wt%.

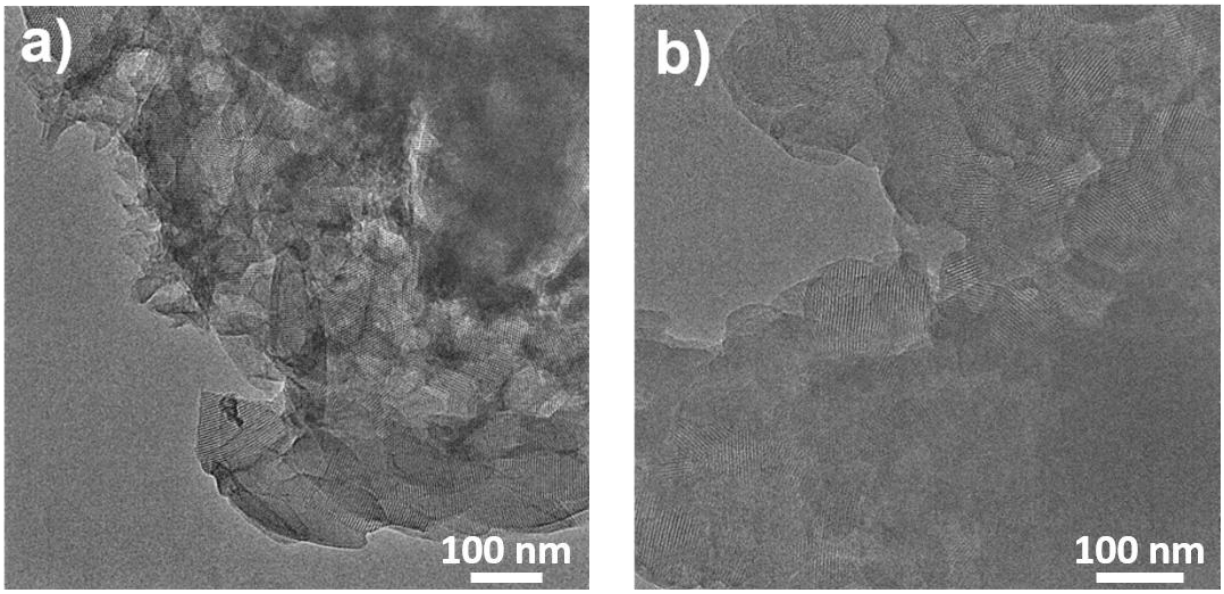

Figure 6.14. TEM images of BDT-ETTA synthesized in the presence of different CDs loadings: (a) 0 wt% and (b) 30 wt%.

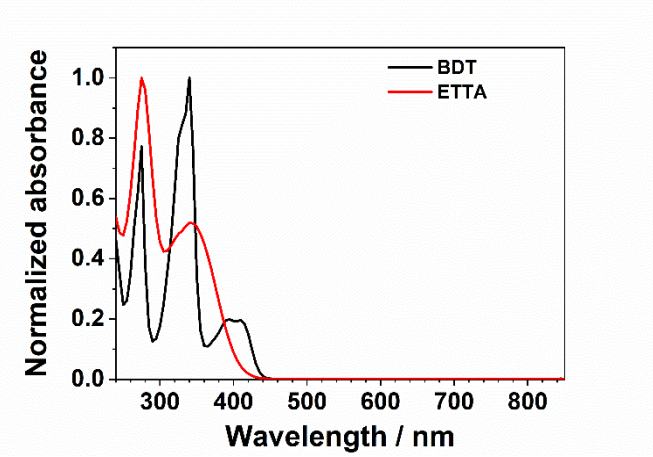

Figure 6.15. UV-vis spectra of BDT and ETTA building blocks.

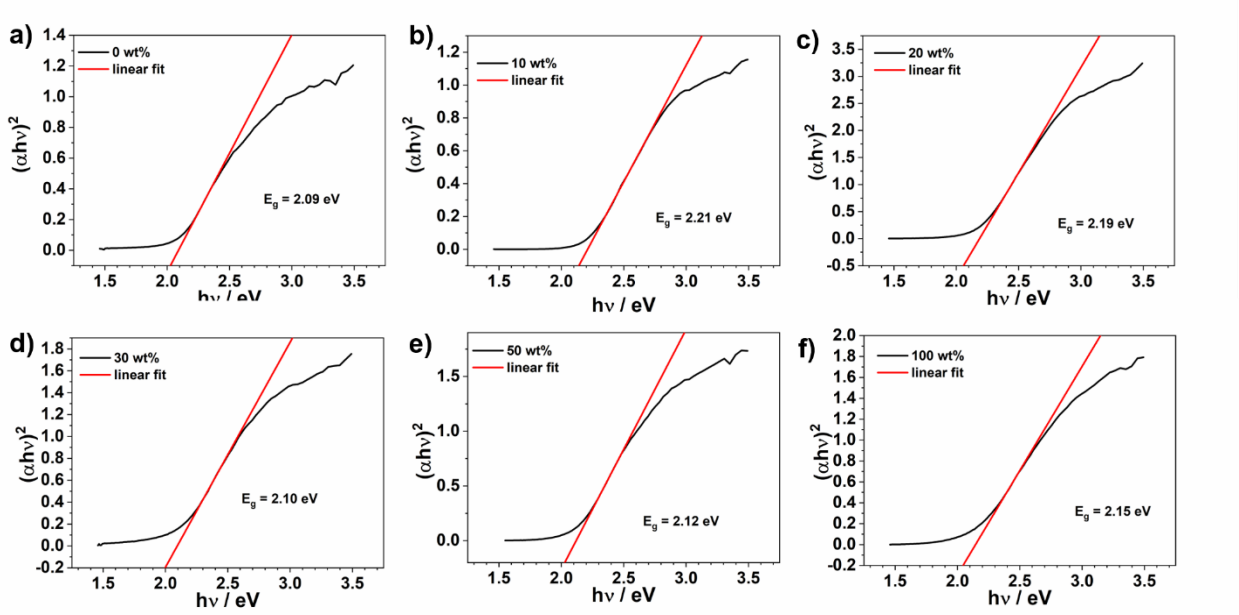

Figure 6.16. Tauc plots of BDT-ETTA synthesized in the presence of different CDs loadings.

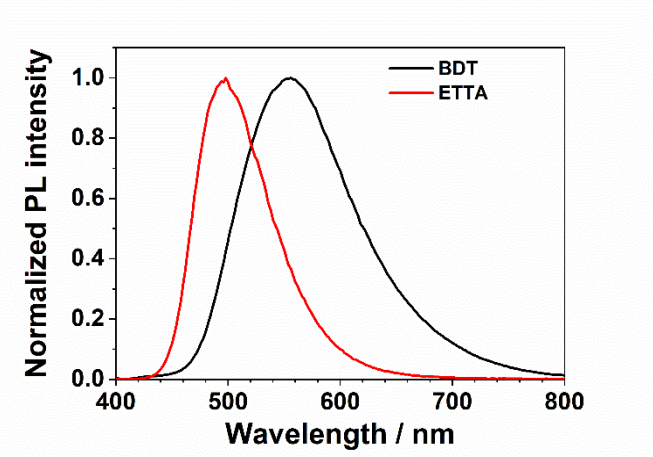

Figure 6.17. PL spectra of BDT and ETTA building blocks.

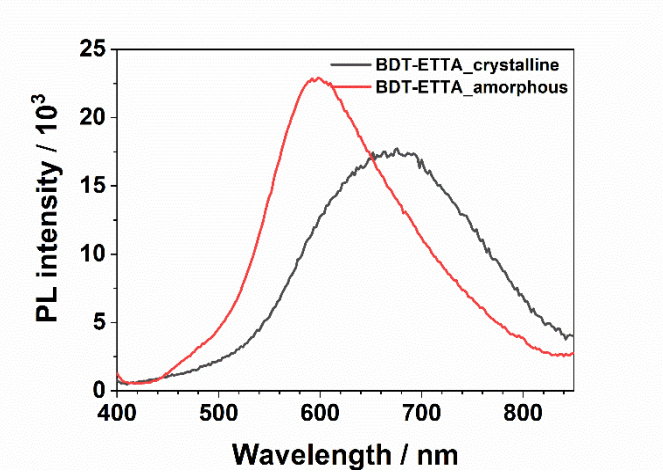

Figure 6.18. PL spectra of BDT-ETTA synthesized at different conditions to obtain crystalline (black) and amorphous (red) phases.

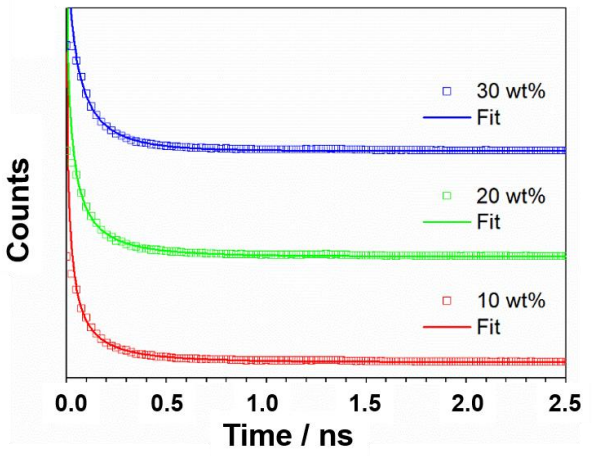

Figure 6.19. Photoluminescence decay of BDT-ETTA COF synthesized in the presence of different CDs loadings: 10 wt% (red), 20 wt% (green), 30 wt% (blue), as well as stretched exponential fits.

6.8.2. Electrochemical characterization

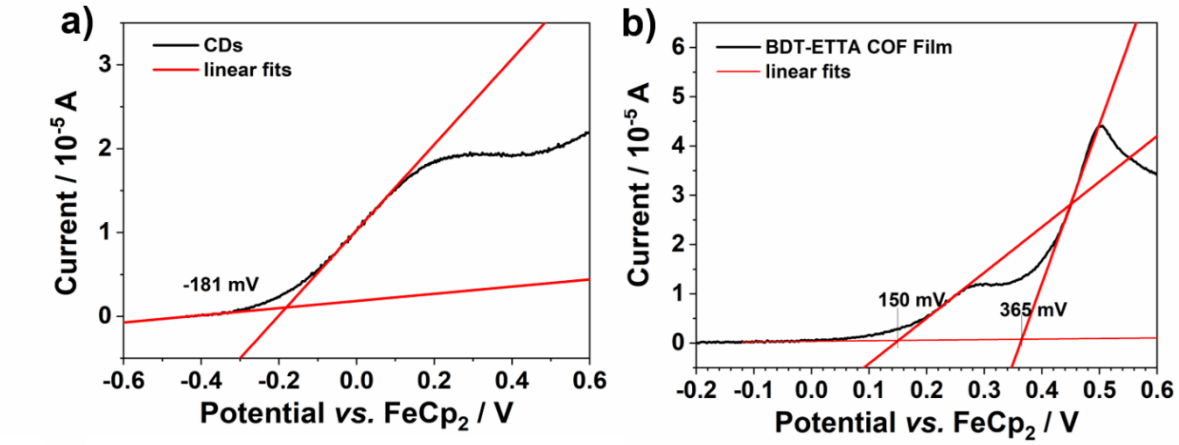

Figure 6.20. a) Cyclic voltammograms and the determination of the onset potentials of (a) CDs and (b) BDT-ETTA versus $FeCp_2$ in 0.1 M TBAHFP in acetonitrile.

The energetic position of the HOMO versus vacuum were determined from the oxidation potentials versus the reference potential and the potential of the reference versus the vacuum. Conversion from V to eV by multiplying with the elementary charge *e*, as shown below:

$$E_{X\ vs.\ vac} = E_{ref\ vs.\ vac} - eU_{X\ vs.\ ref} \qquad (6.7)$$

As an example, we calculate the potential on the vacuum scale of CDs below:

$$E_{CDs\ vs.\ vac} = E_{FeCp2\ vs.\ vac} - eU_{CDs\ vs.\ FeCp2} = \qquad (6.8)$$

$$= -5.14\ \text{eV} - \text{e} \cdot (-0.18\ \text{V}) = -4.96\ \text{Ev}$$

$1.602 \cdot 10^{-19}$ Coulombs $\cdot$ 1V = $1.602 \cdot 10^{-19}$ Joule = 1 eV. $E_{FeCp2\ vs.\ vac}$= -5.14 V was calculated using literature.[1,2]

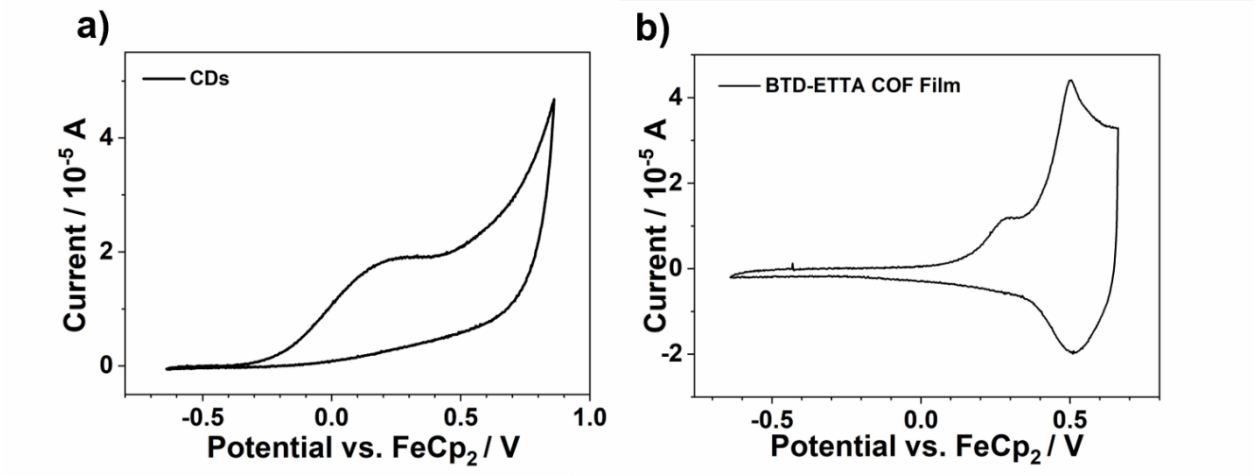

Figure 6.21. Complete anodic and cathodic scans of (a) CDs and of (b) BDT-ETTA thin film versus $FeCp_2$ in 0.1 M TBAHFP in acetonitrile.

6.8.3. References

[1] Connelly NG, Geiger WE 1996 Chemical Redox Agents for Organometallic Chemistry *Chem. Rev.* **96**, 877.

[2] Bard AJ, Faulkner LR Electrochemical Methods: Fundamentals and Applications. 2nd ed.; Wiley: New York, **2001**.

7. Conclusion and outlook

This thesis investigates pre-synthetic, post-synthetic and hybrid modification strategies to tailor the structure, optoelectronic properties, intermolecular interactions, and photocatalytic performance of COFs. Achieving this goal required a comprehensive approach involving organic monomer synthesis, structural and optoelectronic characterization, Density Functional Theory (DFT) analysis of optoelectronic properties and host-gas interactions as well as evaluation of photocatalytic and gas sorption abilities.

The first part of the thesis (Chapters 3 and 4) focused on the design and synthesis of a family of Wurster-Anthracene-based COFs, denoted as W-A-X (X = H, Cl, Br, I), where systematic pre-synthetic halogen functionalization of the anthracene unit was employed to modulate their properties. Chapter 3 presented a detailed synthesis and structural analysis of W-A-X COFs, where only one atom (X) at the 2-position of the anthracene core differentiates the chemical structure of these four systems. Using a combination of experimental and theoretical approaches, it was demonstrated that even minimal pre-synthetic modifications at the molecular level can lead to significant changes in the framework's crystallinity, morphology, and photophysical response. The introduction of heavier halogens promoted the formation of larger crystalline domains and induced a systematic redshift in optical absorption and emission, consistent with increased polarizability and extended π-conjugation. Electrostatic potential mapping and band structure calculations confirmed that these effects originate from halogen-mediated modulation of local charge distribution and anthracene-centered electronic transitions. This chapter therefore explored how single-atom halogen substitution influences the structural and optoelectronic characteristics of the frameworks.

Chapter 4 extended the functionality of W-A-X COFs by linking halogenation to CO_2 sorption behavior, providing the first systematic evidence that single-atom halogen substitution can precisely tune CO_2 adsorption in COFs through σ-hole interactions. A σ-hole represents a region of localized positive electrostatic potential (δ^+) on the outer side of a covalently bonded halogen atom, which enables attractive noncovalent interactions with electron-rich (δ^-) regions of CO_2 molecules. The introduction of electronegative halogens into the anthracene unit weakened conventional adsorption at imine sites by reducing their basicity through electron-

withdrawing effects, while simultaneously generating new, energetically favorable adsorption sites near the halogen atoms. Density functional theory calculations revealed that CO_2 binding in the non-halogenated W-A-H occurs exclusively at the imine linkage, whereas in halogenated analogues CO_2 is additionally stabilized through X-σ(δ^+)···O(δ^-) interactions. The interaction strength followed the trend I > Br > Cl, consistent with increasing halogen polarizability. Experimentally, this was reflected in significantly increased CO_2 uptake and higher isosteric heats of adsorption for all halogenated COFs compared to W-A-H. Within the series, W-A-Br achieved the best balance between strong σ-hole interactions and high crystallinity, resulting in the highest CO_2 adsorption performance. This study demonstrated the utility of σ-hole engineering as a strategy for programming host-guest interactions in porous frameworks and underscored the importance of using structurally representative extended COF models in theoretical analyses. Combined with the findings from Chapter 3, these results highlight halogenation as a powerful design strategy for modulating intermolecular interactions in COFs, offering a versatile concept for the development of functional materials where such interactions play a crucial role, such as in molecular adsorption or photocatalysis.

Chapter 5 focused on the post-synthetic modification of the thiophene-based imine BDT-ETTA COF through linkage conversion from imine to amide. This conversion demonstrated how chemical transformation at the framework linkage can influence both the electronic structure and photocatalytic performance. Under the experimental conditions employed for photocatalytic tests, the imine-linked COF exhibited a positive surface charge due to partial protonation of the imine sites, whereas the amide-linked COF remained negatively charged. These contrasting surface charges governed the interaction with the negatively charged Pt precursor $[PtCl_6]^{2-}$ during photodeposition. In the imine-linked COF, electrostatic attraction facilitated rapid nucleation at multiple sites, resulting in a homogeneous distribution of small Pt nanoparticles across the framework. In contrast, electrostatic repulsion in the amide-linked COF suppressed uniform nucleation, leading instead to the formation of larger Pt particles that acted as electron-collecting centers. This behavior, combined with the amide-linked COF's enhanced oxidizing power and hydrophilicity, led to enhanced photocatalytic H_2 evolution. Complementary mechanistic studies on the imine-based COF further revealed that Pt photodeposition is a multistep process requiring photoexcitation and a sacrificial electron donor, with sulfur atoms in the BDT unit serving as active sites for hole trapping and oxidation,

and the imine bonds coordinating and reducing the Pt precursor. These findings reveal the critical role of interfacial electrostatics and linkage chemistry in directing charge transfer and catalytic dynamics, underscoring post-synthetic linkage conversion as a versatile strategy for controlling photocatalytic behavior in COFs.

Chapter 6 introduced a hybrid modification for the imine-linked BDT-ETTA COF, employing CDs to construct COF/CD composites with tunable interfacial interactions. Incorporation of CDs during solvothermal COF synthesis modulated crystallization behavior and allowed precise control over the COF-to-CD ratio within the composite. At low CD loadings, intimate interfacial contact promoted efficient charge transfer between the COF and CDs, whereas higher loadings enhanced COF emission by altering exciton dynamics. These results underscore the delicate interplay between composition, morphology, and optoelectronic coupling in hybrid COF-based systems. The study demonstrates that integrating nanocarbon materials offers a versatile platform to tune light harvesting, charge transport, and energy flow, broadening the functional potential of COFs for applications in photocatalysis, sensing, and energy conversion.

Altogether, this work shows that pre-synthetic, post-synthetic and hybrid modifications are complementary strategies for tuning COF properties. Our study provides the first demonstration of σ-hole effects in COFs and highlights their influence on crystallization and nucleation behavior as well as intermolecular interactions, suggesting that σ-hole engineering could become a valuable direction for further investigation, for instance in *in situ* crystallization studies. Beyond the σ-hole effects, halogenation or other heteroatom functionalization of extended π-systems such as anthracene or larger aromatic building blocks offers a powerful means to tune optoelectronic properties while simultaneously shaping host-guest interactions. This combination is particularly important for photocatalysis, where both the electronic structure of the framework and its interfacial behavior affect overall performance. The importance of interfacial behavior for photocatalytic activity was further confirmed by our linkage conversion studies, which demonstrated that the surface charge of a COF can be systematically tailored and plays a central role in controlling interactions between the COF, sacrificial electron donors and metal precursors. In this context, deeper exploration of surface chemistry, including how different charge states, for example positively versus negatively

charged metal precursors or sacrificial electron donors, influence photocatalytic activity represents a promising direction for the rational design of next-generation COF-based systems.

8. Appendix

8.1. Publications

1. *Single-Atom Tuning of Structural and Optoelectronic Properties in Halogenated Anthracene-Based Covalent Organic Frameworks*

   Submitted to "*Journal of Materials Chemistry A*"

   Klaudija Paliušytė, Laura Fuchs, Zehua Xu, Kuangjie Liu, Kornel Roztocki, Shuo Sun, Hendrik Zipse, Achim Hartschuh, Frank Ortmann* and Jenny Schneider*

2. *Single-Atom Halogen Substitution in Covalent Organic Frameworks Enables σ-Hole–Driven CO_2 Adsorption*

   Submitted to "*Chemistry of Materials*"

   Klaudija Paliušytė, Kuangjie Liu, Kornel Roztocki, Shuo Sun, Hendrik Zipse, and Jenny Schneider*

3. *Surface Charge Modulation in Covalent Organic Frameworks for Controlled Pt-Photodeposition and Enhanced Photocatalytic Hydrogen Evolution*

   Published in "Small". **2025**, *21*, 2500870

   Klaudija Paliušytė, Lucas Leão Nascimento, Hannah Illner, Max Wiedmaier, Roman Guntermann, Markus Döblinger, Thomas Bein, Antonio Otavio T. Patrocinio*, and Jenny Schneider*

4. *Synthetic Control* over *the Energy Transfer and Charge Transfer between Carbon Dots and Covalent Organic Framework*

Published in "Journal of Physics: Energy". **2024**, *6(2)*, 025018.

Julian Feijoo, **Klaudija Paliušytė**, Jenny Schneider*

8.2. Conference Contributions

28.02.2024 – 01.03.2024	**German Zeolite Conference**	*Jena, Germany*
24.09.2023 – 27.09.2023	**European Conference of Metal-Organic Frameworks and Porous Polymers**	*Granada, Spain*
14.10.2022	**"Chemistry and Chemical Technology 2022". International Scientific Conference**	*Kaunas, Lithuania*
04.09.2022 – 07.09.2022	**International Conference of Metal-Organic Frameworks and Open Framework Compounds**	*Dresden, Germany*
23.03.2022 – 25.03.2022	**German Zeolite Conference**	*Frankfurt, Germany*